First full-magnetic storage of ultracold neutrons in the τSPECT experiment for measuring the neutron lifetime

Dissertation zur Erlangung des Grades

„Doktor der Naturwissenschaften“

am Fachbereich Physik, Mathematik und Informatik
der Johannes Gutenberg-Universität in Mainz

vorgelegt von

Jan Kahlenberg

geboren in Koblenz

Mainz, den 2. Juli 2020

Abstract

The lifetime of the free neutron, τ_n, not only affects the helium-4 abundance shortly after the Big Bang. It also provides an experimental determination of the first element of the Cabibbo-Kobayashi-Maskawa (CKM) matrix, V_{ud}, free of nuclear structure effects. Probing unitarity of the CKM matrix is an attractive way to trace Beyond the Standard Model physics, as a violation of unitarity would call for additional fermion generations. The value of τ_n and therefore the corresponding conclusion for unitarity currently depends on the measurement method, with a $\sim 4\sigma$ deviation found between beam- and bottle-type experiments.

In beam-type experiments, τ_n is determined by detecting the decay products of a neutron beam, while bottle-type experiments are based on a direct measurement of neutrons. For bottle-type experiments, neutrons with especially low kinetic energies of $\lesssim 200\,\mathrm{neV}$ are required, which are termed 'ultracold' neutrons (UCN). The UCN are kept inside a storage volume, in which their decay according to τ_n and additional loss terms τ_{loss} sets in. Instead of storing UCN in material bottles, modern bottle-type experiments rely on the magnetic confinement of UCN due to their magnetic moment. Magnetic confinement offers severely reduced loss mechanisms compared to material confinement and can therefore yield unprecedented accuracies of $\Delta\tau_n \leq 1\,\mathrm{s}$. As a drawback, magnetic bottle-type experiments require more intense UCN sources due to lower storage depths $\lesssim 60\,\mathrm{neV}$ compared to material storage ($\lesssim 200\,\mathrm{neV}$).

Being the first neutron lifetime experiment based on full-magnetic storage, the τSPECT experiment relies on storing UCN with a maximum energy of $\sim 47\,\mathrm{neV}$ inside a storage volume of $\sim 6.8\,\mathrm{l}$. As part of this work, τSPECT has been successfully set up for phase I at the research reactor TRIGA Mainz, which aims at measuring τ_n with an uncertainty of $\Delta\tau_n = 1\,\mathrm{s}$. A Halbach octupole inserted into the former aSPECT cryostat provides the radial magnetic confinement, which along with the cryostat's longitudinal magnetic field forms a 3D magnetic trap. For filling UCN prepared to their storable spin state into the trap, a movable neutron guide was designed, which is retracted after the filling process to prevent material interaction. A detection of 'surviving', *i.e.,* non-decayed UCN after varying storage times is required for determining τ_n. Moved into the magnetic trap after the storage time, a custom UCN detector counts these 'surviving' UCN. It comprises a boron-10-coated silver-doped zinc sulfide scintillator for converting captured UCN to photons and a silicon photomultiplier array for photon detection and has been thoroughly characterised to allow for the reconstruction of UCN events from the pulse height spectra.

Prior to the final commissioning of the τSPECT experiment, the pulsed UCN source at beamport D was upgraded to provide a 3.5 times higher UCN density, which corresponds to $\sim 8.5\,\mathrm{cm}^{-3}$ in a material bottle of $\sim 32\,\mathrm{l}$. Additional to detailed characterisations of the source performance, the upgraded source was used to characterise central τSPECT components before the installation. Finally, a first full-magnetic UCN storage was demonstrated.

Contents

List of Figures

List of Tables

1 Introduction

> Don't adventures always have an end? I suppose not.
> Someone else always has to carry on the story.
>
> J. R. R. Tolkien, *The Fellowship of the Ring*

Throughout the 20$^{\text{th}}$ century, several advances in modern physics have been made. Our present understanding of nature phenomena is based on the Standard Model of Particle Physics (SM), which has been developed throughout the 1960s and 1970s and is of $\mathrm{SU}(3)_C \times \mathrm{SU}(2)_L \times \mathrm{U}(1)_Y$ structure [Sch16]. The Higgs boson discovery in 2012 at LHC [AAA$^+$12, CKS$^+$12] led to an experimental confirmation of all elementary particles postulated in the SM. Despite its apparent completeness, several phenomena observed in the Universe cannot be explained by solely referring to the SM. Thus, numerous attempts have been made to extend the SM, which are commonly known as 'Physics beyond the Standard Model' (BSM) approaches. Among others, the SM does not account for experimentally-detected neutrino oscillations [FHI$^+$98] and the cosmologically-observed dark matter [RFT80]. A common approach in BSM physics is to look for new elementary particles. Presently, an active search for dark matter candidates is ongoing.

The experimental discovery of new particles calls for detection methods employed in not-yet accessed energy ranges. In principle, two possibilities exist, *i.e.*, going towards even higher energies or performing extremely high-precision low energy experiments. While considering the low-energy range has not been the primary interest over the past decades, it is now gaining momentum again [DS11]. More accurate theoretical computations and refined experimental methods now offer various convincing tests of the SM. At the low-energy frontier, precise measurements on decays governed by the weak interaction are very promising and could provide answers to *e.g.* the number of fermion generations [MS86]. Free neutron decay as the prototype semileptonic decay is an elegant tool to investigate the weak interaction and is theoretically well understood due to the absence of nuclear corrections [Poc17]. Governed by the neutron lifetime τ_n, it decays into a proton while releasing an electron/electron-antineutrino pair.

The value of τ_n is not only an important input parameter for the helium-4 abundance resulting from the Big Bang nucleosynthesis (BBN) [BBF89], but also allows for testing the unitarity of the Cabibbo–Kobayashi–Maskawa (CKM) matrix [KM73]. The unitarity

of the CKM matrix is essential to SM physics, since it predicts the observed three quark generations. Due to the involved $d - u$ quark transition, free neutron decay is sensitive to the first matrix element of the first row, V_{ud}. Its value is determined by independently measuring τ_n and the ratio of the vector-to-axialvector coupling constants, $\lambda = \left|\frac{g_{\mathrm{A}}}{g_{\mathrm{V}}}\right|$ [DS11] [CMS19]:

$$|V_{\mathrm{ud}}|^2 = \frac{4906.4(1.7)\ \mathrm{s}}{\tau_n \left(1 + 3\,|\lambda|^2\right)}\ . \tag{1.1}$$

The current best value for V_{ud} is derived from superallowed $0^+ \to 0^+$ nuclear decays, which however involves possibly error-prone nuclear corrections [HT15]. Taking recent experiments based on neutron decay into account, a ~ 3 times worse precision is reached despite recent advances [MMS$^+$19]. Thus, measurements of λ and τ_n with increasing precision are needed to compete with the $0^+ \to 0^+$ decays without including nuclear corrections.

Neutron lifetime experiments are actively performed and have recently gained momentum after the onset of the 'neutron lifetime puzzle' [Pau09, Mum18, Ber19a], which refers to a 4.1σ deviation between the average values extracted from bottle-type and beam-type measurement methods [Wie18]. Bottle-type experiments determine τ_n by counting 'surviving' neutrons after storage for varying times, while in beam-type experiments, τ_n is inferred from the decay products of a neutron beam [Byr11]. The 4.1σ deviation most likely results from non-determined systematic effects. Upcoming experiments are underway to clarify this issue and further improve the precision.

Unlike beam-type experiments, which were carried out since the 1950s, bottle-type experiments require ultracold neutrons (UCN) with typical energies below 350 neV. Since UCN production requires a complicated moderation process, first UCN sources were engineered at the end of the 1960s [Ste69, LPSS69], leading to the first precise bottle-type measurement in 1989 [MAB$^+$89]. Modern bottle-type experiments relying on material storage cannot reach a significantly better precision than $\Delta\tau_n \sim 1$ s due to loss mechanisms upon wall collisions [SKF$^+$18]. Using magnetic storage, UCN are no longer exposed to material interactions. Instead, UCN are stored by taking advantage of the interaction between their magnetic moment and a magnetic field. In 2018, promising results on τ_n could be determined by combining magnetic and gravitational storage [PCCW$^+$18, EAB$^+$18].

Being the first full-magnetic neutron lifetime experiment at a pulsed UCN source, the τSPECT experiment is set up at the superthermal UCN D source at the research reactor TRIGA Mainz. The upgrade of the UCN D source [KRR$^+$17], which has been part of this work, yields a ~ 3.5 times higher UCN density. Thus, the statistics for the first phase of the experiment is improved, which aims at measuring τ_n with an uncertainty of $\Delta\tau_n = 1$ s. During the measurement process, spin-flipped UCN, *i.e.,* UCN spin-prepared to their low energy state, are stored in a volume of $V_{\mathrm{storage}} \sim$ 6.8 l with a maximum potential of 47 neV. After a first prototype measurement demonstrated the successful magnetic UCN storage in longitudinal direction using the superconducting coils of the former aSPECT cryostat [Kar17], full-magnetic storage is achieved by installing a permanent magnetic Halbach octupole, which accounts for the magnetic field in radial direction.

Several modifications were needed to convert the aSPECT cryostat into the τSPECT experiment with full-magnetic UCN storage. The addition of the 150 kg heavy Halbach

octupole has led to several engineering challenges. Great care had to be taken to provide the cryogenic conditions to operate the superconducting coils. Further modifications included the design of a movable neutron guide section, since the neutron guide must be retracted after filling UCN into the storage volume to avoid material interactions. To provide a high UCN extraction efficiency, a boron-10-coated UCN detector was developed and characterised, which drives into the storage volume to count the stored UCN. Due to the environments inside the cryostat, the detector was designed to work at low temperatures while being exposed to magnetic fields up to $\sim 1.7\,\mathrm{T}$. All relevant components were designed to achieve a high vacuum inside the storage volume, which is required to reduce the density of residual gas atoms interacting with the stored UCN.

Prior to the commissioning of the τSPECT experiment, preparatory studies at the upgraded UCN D source have been carried out. The studies involved detailed characterisations of the UCN D source, during which fluctuations of the UCN yield were discovered. These fluctuations call for a normalisation of the stored UCN counts in τSPECT, with different normalisation methods having been evaluated in dedicated test measurements. Moreover, the conditions found in τSPECT were emulated using an aluminium storage bottle offering similar properties to the full-magnetic storage volume. The related measurements were used to optimise the UCN transmission from the source to the τSPECT storage volume and to predict the number of full-magnetically storable UCN. The predicted amount has been used to estimate how many measurement days were required to reach a precision of $\Delta\tau_n = 1\,\mathrm{s}$.

Finally, τSPECT was successfully set up for phase I of data taking. In the September 2019 beam time, UCN were fully-magnetically stored. In phase II, τ_n shall be inferred from decay protons. For this, the detector movement mechanics has been modularly designed, which allows for a unique comparison of the τ_n values extracted from both UCN and decay proton detection.

First, Ch. 2 provides a general overview on the weak interaction, explains the role of τ_n for BBN, views neutron decay from a particle physics perspective, and reviews the involvement of τ_n in astrophysical processes. Chapter 3 outlines the history of neutron lifetime experiments, reports on the current status and motivates the necessity of using UCN for measuring τ_n. Also, the fundamental interactions to which UCN are sensitive are presented, along with UCN production mechanisms. Preparatory studies performed at the upgraded UCN D source at TRIGA Mainz which have led to crucial implications for τSPECT are analysed in Ch. 4. Chapter 5 introduces the reader to the modifications required for the implementation of full-magnetic storage. After giving a simplified insight into the measurement sequence and the involved components, technical and physical details are discussed. The first successful UCN storage and the experienced drawbacks are given in Ch. 6. Chapter 7 summarises the main results and provides an outlook on the future of the τSPECT experiment.

For further details, the appendix contains extensive information on the upgraded UCN source (cf. Ch. A), on various details regarding the setup process (cf. Ch. B) as well as the temperature conditions during the first τSPECT measurements (cf. Ch. C).

2 Neutron β-decay

This chapter introduces the reader to the nature of the weak interaction (cf. Ch. 2.1). Several implications of neutron decay properties for various astrophysical phenomena and tests of the Standard Model (SM) are discussed in Ch. 2.2.

2.1 The weak interaction

In the weak interaction, a massive boson is exchanged [Mar07]. In total, three bosons W^+, W^-, Z^0 exist, with the superscript denoting its positive, negative and neutral charge. Beta (β)-decay refers to interactions involving the exchange of a W^+/W^- boson, as a consequence of which two leptons are released. A typical example is the decay of the free neutron, in which a neutron (n) decays into a proton (p) by W^- exchange, releasing a electron/electron-antineutrino ($e^-/\bar{\nu}_e$) pair[1]:

$$n \rightarrow p + e^- + \bar{\nu}_e \; . \tag{2.1}$$

To current knowledge and in line with the SM, the weak interaction maximally violates parity and is purely left-handed [PRS+09]. Due to its complicated nature, the development of a coherent quantum field theory which led to the unification of the electromagnetic and weak interaction ('electroweak unification') has been a challenge to theory in the past century. In the following, the $V-A$ theory is presented to the reader (cf. Ch. 2.1.1), which is complemented by giving a brief insight into electroweak unification (cf. Ch. 2.1.2). The last section refers to different types of β-transitions (cf. Ch. 2.1.3).

2.1.1 The path to V-A theory

The theoretical description of the weak interaction started with Fermi's assumption to view β-decay analogous to electromagnetic processes [Fer34]. The SM describes the weak interaction according to the 'vector minus axialvector' ($V-A$) theory [FGM58, GM58], which has emerged after several considerations in both experimental and theoretical physics. In the following, a short review on the path to the $V-A$ theory is provided.

[1] Details on the decay of the free neutron will be given in Ch. 2.2.3.

Fermi's analogy to electromagnetism

In 1934, Enrico Fermi succeeded in giving a description of β-decay, which is commonly known as the 'Fermi theory' [Fer34]. The theory is still successful today, even after a quantum field description has been found[2]. As Fig. 2.1 shows, Fermi recognised a resemblance to the electromagnetic interaction and assumed that the electron and the electron-antineutrino released in neutron decay are similar to a photon emitted by a proton or electron, respectively [Raj14].

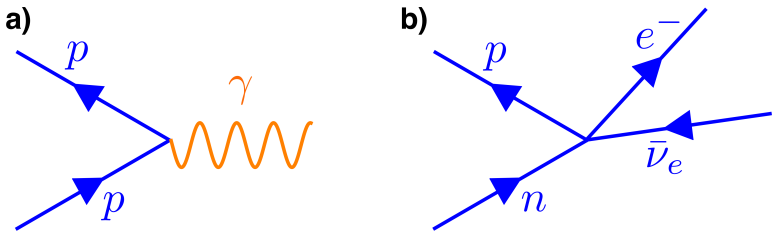

Figure 2.1: Analogy of electromagnetism and Fermi theory. (a) Feynman diagram of a photon emission by a proton ($p \to p + \gamma$). (b) In Fermi theory, neutron decay ($n \to p + e^- + \bar{\nu}_e$) is regarded as a four-point interaction between neutron (n), proton (p), electron (e^-), and electron-antineutrino ($\bar{\nu}_e$). The time axis points from left to right. Figure based on [Raj14].

The radiative process of a photon emitted by a proton ($p \to p + \gamma$) is represented in Quantum Electrodynamics (QED) by the Lagrangian density[3] [Les09]

$$\mathcal{L}_{\text{QED}} = e j_\mu^{\text{em}} A^\mu = e \left(\bar{\psi}_p \gamma_\mu \psi_p \right) A^\mu \ , \quad \mu = 1, \cdots, 4 \ , \tag{2.2}$$

with the electrical charge e representing the interaction strength, the proton's electromagnetic current j_μ^{em}, the proton Dirac spinor ψ_p, the four-vector γ_μ containing the Dirac matrices, and the photon Dirac spinor A^μ.

Using its analogy to neutron β-decay, Fermi substituted the terms found in the QED Lagrangian density [Les09]:

$$e \to G \ , \tag{2.3}$$

$$j_\mu^{\text{em}} \to j_\mu^{n \to p} = \bar{\psi}_p \gamma_\mu \psi_n \ , \tag{2.4}$$

$$A^\mu \to j_{\nu \to e}^\mu = \bar{\psi}_e \gamma^\mu \psi_\nu \ . \tag{2.5}$$

Thus, neutron β-decay could now be described by the two currents $j_\mu^{n \to p}$ describing the neutron with Dirac spinor ψ_n transitioning into a proton (ψ_p), and $j_{\nu \to e}^\mu$ referring to the emitted electron (ψ_e) and electron-antineutrino (ψ_ν). Fermi introduced a new coupling constant G, which is commonly known as the Fermi coupling constant G_{F} (see further

[2] In nuclear β-decay, low momentum transfers with $q^2 \to 0$ permit calculations based on Fermi theory at the current level of precision. This assumption states that reactions should be independent of reaction energy, which implies that phenomena can be observed at both low- and high-energy scales in the same way [DS11].

[3] Note that according to Einstein convention, a summation over $\mu = 1, \ldots, 4$ is performed.

content of this section). The resulting Lagrangian density for β-decay reads [Les09]:

$$\mathcal{L}_{\text{Fermi}} = G \underbrace{\left(\bar{\psi}_p \gamma_\mu \psi_n\right)}_{j_\mu^{n\to p}} \underbrace{\left(\bar{\psi}_e \gamma^\mu \psi_\nu\right)}_{j_\mu^{\nu\to e}} . \tag{2.6}$$

Due to the analogy to electromagnetism, Fermi described the weak interaction using a vector matrix operator. Contrary to electromagnetic interactions, β-decay is described by currents interacting at one point, whereby the electric charges of the respective lepton and baryon change[4]. Therefore, β-decays of this type are known as charged current interactions [Kra88].

Considerations beyond Fermi's analogy

Taking locality and Lorentz invariance into account, the Lagrangian density reads[5] [Kle16],

$$\begin{aligned}\mathcal{L}_{\text{Lorentz}} = & C_S \bar{\psi}_p \psi_n \bar{\psi}_e \psi_\nu \\ & + C_P \bar{\psi}_p i\gamma_5 \psi_n \bar{\psi}_e i\gamma_5 \psi_\nu \\ & + C_V \bar{\psi}_p \gamma^\mu \psi_n \bar{\psi}_e \gamma^\mu \psi_\nu \\ & + C_A \bar{\psi}_p \gamma^\mu \gamma_5 \psi_n \bar{\psi}_e \gamma^\mu \gamma_5 \psi_\nu \\ & + \frac{1}{2} C_T \bar{\psi}_p \sigma^{\lambda\kappa} \psi_n \bar{\psi}_e \sigma^{\lambda\kappa} \psi_\nu + c.c.\end{aligned} \tag{2.7}$$

Additional to combinations of Dirac matrices (1, $i\gamma_5$, γ^μ, $\gamma^\mu\gamma_5$ with $\gamma_5 \equiv i\gamma_1\gamma_2\gamma_3\gamma_4$, and $\sigma^{\mu\nu}/\sqrt{2}$) defining the interaction type, Eq. (2.7) contains the coupling constants C_i, with the index i representing scalar (S), pseudoscalar (P), vector (V), axial vector (A), and tensor (T) interaction types. The coupling constants represent the interaction strength and need to be determined experimentally.

In the following, the reader is introduced to the concept of matrix elements. As a weak perturbation, the matrix element $\mathcal{M}_{fi}$ is contained in Fermi's Golden Rule, which in general describes the transition between an initial (i) and a final state (f). The associated transition rate, $\Gamma_{i\to f}$, is given by [Mar07]

$$\Gamma_{i\to f} = \frac{2\pi}{\hbar} \left|\mathcal{M}_{fi}\right|^2 \cdot \frac{dn}{dE_f} , \tag{2.8}$$

with transition amplitude $|\mathcal{M}_{fi}|^2$ (squared absolute value of $\mathcal{M}_{fi}$) and final state density, dn/dE_f. In general, the transition matrix element equates to [Mar07]

$$\mathcal{M}_{fi} = \int dV \bar{\Psi}_f \left(gO\right) \Psi_i , \tag{2.9}$$

with states $\bar{\Psi}_f$ and Ψ_i, integration over volume V, coupling constant g, and operator O. In the nonrelativistic limit, the matrix element for neutron decay can either be [MK02, Kle16]

$$\mathcal{M}_{\text{V,S}} = \int dV \bar{\psi}_p \mathbf{1} \psi_n , \tag{2.10}$$

[4] In these interactions, which are mediated by a W^+ or by a W^- boson, the electric charges change by one unit.

[5] The term *c.c.* refers to the complex conjugate.

for V- and S-type interactions, or [MK02, Kle16]

$$\mathcal{M}_{\mathrm{A,T}} = \int dV \bar{\psi}_p \vec{\sigma} \psi_n \ , \tag{2.11}$$

for interactions of A and T type. with pseudoscalar interactions (P) being neglected since they are suppressed by the ratio of momentum transfer to nucleon mass, q/M [VWT15]. Only after several experimental evidences, interactions of type S, and T could be ruled out[6], which is still valid within the present experimental precision. Following the discussion in [Per82], the following consideration will thus be limited to V- and A-type interactions.

Summing over operators O_i of V and A type ($i = V, A$), the parity-conserving matrix element for neutron decay is written as [Per82]:

$$\mathcal{M}_{pn} = G \sum_{i=V,A} C_i \left(\bar{\psi}_p O_i \psi_n\right) \left(\bar{\psi}_e O_i \psi_\nu\right) \tag{2.12}$$

The matrix element in Eq. (2.12) is of scalar type. After Lee and Yang questioned the parity conservation in 1956 [LY56], parity violation was experimentally discovered in 1957 by Wu et al. [WAH$^+$57]. The addition of parity violation calls for a pseudoscalar quantity. This is achieved by adding the matrix γ_5 to the expression, yielding[7] [Per82]

$$\mathcal{M}_{pn} = \frac{G}{\sqrt{2}} \sum_{i=V,A} \left(\bar{\psi}_p O_i \psi_n\right) \left(\bar{\psi}_e O_i \left(C_i - C_i' \gamma_5\right) \psi_\nu\right) \ , \tag{2.13}$$

which for normalisation reasons has also changed the coupling constant ($G \to G/\sqrt{2}$). Goldhaber's conclusion of the neutrino left-handedness in 1958 [GGS58] determined the operator $(1 \pm \gamma_5)$ to be $(1 - \gamma_5)$. Maximum parity violation leads to $C_i' \equiv C_i$. As a result, the matrix element can be written as [Per82]

$$\mathcal{M}_{pn} = \frac{G}{\sqrt{2}} \sum_{i=V,A} C_i \left(\bar{\psi}_p O_i \psi_n\right) \left(\bar{\psi}_e O_i \left(1 - \gamma_5\right) \psi_\nu\right) \ , \tag{2.14}$$

and with operators $O_V = \gamma_\mu$, $O_A = i\gamma_\mu\gamma_5$, and ratio of axial vector and vector coupling constants, $\lambda = -C_A/C_V$, the equation is expressed by

$$\mathcal{M}_{pn} = \frac{G}{\sqrt{2}} C_V \left(\bar{\psi}_p \gamma_\mu \left(1 - \lambda\gamma_5\right) \psi_n\right) \left(\bar{\psi}_e \gamma_\mu \left(1 - \gamma_5\right) \psi_\nu\right) \ , \tag{2.15}$$

which clearly shows its vector minus axial vector ($V - A$) nature. The associated $V - A$ theory was developed by Feynman and Gell-Mann in 1958[8] [FGM58, GM58].

In its internal structure, the neutron consists not only of the three valence quarks (udd), but also of virtual $q\bar{q}$ pairs ('sea quarks') and gluons, g. For describing its internal structure, nuclear form factors $f_i(q^2)$ and $g_i(q^2)$ are used, with $i = 1, \cdots, 3$ and q^2 denoting the momentum transfer[9]. The problem simplifies since due to negligible momentum transfer,

[6] For a detailed historical overview over the experiments eventually leading to the $V - A$ theory, consider [Bod78, Wei09].

[7] The equations extracted from [Per82] were adapted to correspond to Dirac notation.

[8] Sudarshan and Marshak also postulated the $V - A$ theory in 1957 [SM57]. For a detailed historical overview, consider [Byr11].

[9] The following discussion is based on [DS11]. For further details, refer to the named source and the references therein. Note that given equations have been adapted to represent standard Dirac notation.

$(pc)^2 \ll (m_\mathrm{W}c^2)^2$, q^2 is set to zero ($q^2 \to 0$). Furthermore, due to the SM property to constrain currents to 'first class', f_3 and g_2 ('second class currents') are ignored. The factor g_3 contained in the 'induced pseudoscalar' term can be neglected due to the low energies found in neutron decay [DS11].

The coupling constant G in Eq. (2.15) is not equal to the Fermi coupling constant G_F, but $\sim 3\,\%$ smaller. This is due to the suppression by the Cabibbo-Kobayashi-Maskawa (CKM) matrix element V_ud, which is linked to the quark mixing involved in the process (further details are given in Ch. 2.2.3.1). With the resulting replacement $G \to G_\mathrm{F}V_\mathrm{ud}$, conventions $f_1(0) \equiv f_1(q^2=0)$, $f_2(0) \equiv f_2(q^2=0)$, $g_1(0) \equiv g_1(q^2=0)$, and the sum of proton/neutron mass $2M = m_p + m_n$, the transition element can be written as [DS11]:

$$\mathcal{M}_\mathrm{pn} = \frac{G_\mathrm{F}}{\sqrt{2}} V_\mathrm{ud} \left(\bar{\psi}_p(x) \left(\underbrace{f_1(0)}_{=1} \gamma_\mu + g_1(0)\gamma_\mu\gamma_5 - i \underbrace{f_2(0)}_{\equiv \kappa_p - \kappa_n} \frac{\sigma_{\mu\nu} q^\nu}{2M} \right) \psi_n(x) \right) \cdot \left(\bar{\psi}_e(x) \gamma^\mu \left(1 - \gamma_5\right) \psi_\nu(x) \right) \,. \tag{2.16}$$

Next, the remaining form factors can be summarised by the ratio of the axial vector and vector coupling constants,

$$\lambda \equiv \frac{g_\mathrm{A}}{g_\mathrm{V}} = \frac{g_1(0)}{f_1(0)} = \frac{|g_1(0)| \cdot e^{i\pi}}{1} = -\,|g_1(0)| \,, \tag{2.17}$$

and $f_2(0)$ can be replaced by the difference between the anomalous magnetic moments of the proton and the neutron, respectively ($\kappa_p - \kappa n = 3.706$, 'weak magnetism' [DS11]), which gives:

$$\mathcal{M}_\mathrm{pn} = \frac{G_\mathrm{F}}{\sqrt{2}} V_\mathrm{ud} \left(\bar{\psi}_p(x) \left(\gamma_\mu \left(1 + \lambda\gamma_5\right) + \frac{\kappa_p - \kappa_n}{2M} \sigma_{\mu\nu} q^\nu \right) \psi_n(x) \right) \cdot \left(\bar{\psi}_e(x) \gamma^\mu \left(1 - \gamma_5\right) \psi_\nu(x) \right) \tag{2.18}$$

Note that the simplifications for $f_1(0)$ and $f_2(0)$ stem from conserved vector current (CVC) theory [Wu64], which implies [DS11]

(i) $f_1(0) = 1$, since the vector coupling is independent of the neutron's interacting quark constituents, *i.e.,* the strong interaction does not influence weak charges,

(ii) $f_2(0) = \kappa_p - \kappa_n$, due to fact that strong interactions also do not influence the higher multipoles of the weak and electromagnetic hadronic couplings[10].

Likewise, the leading order Standard Model (SM) Lagrangian density for neutron decay[11] is given by[12] [VWT15]

$$\mathcal{L}_\mathrm{SM} = \frac{G_\mathrm{F} V_\mathrm{ud}}{\sqrt{2}} g_V(q^2) \bar{\psi}_e \gamma_\mu \left(1 - \gamma_5\right) \psi_\nu \bar{\psi}_p \gamma^\mu \left(1 - \frac{|g_A(q^2)|}{g_V} \gamma_5 \right) \psi_n + h.c. \,. \tag{2.19}$$

[10] The neutron β-spectrum is affected by 'weak magnetism' when considering the recoil expansion in first order [GANCS19]. The neutron decay spectrum is thus expected to be distorted by $\sim 1\,\%$ [GP13], which has not been measured to date.

[11] The given leading order Lagrangian density does not include weak magnetism, which will be relevant for next-generation neutron decay experiments. The PERC experiment aims to measure weak magnetism directly [DAB+08].

[12] The term *h.c.* denotes the Hermitian conjugate.

For the low momentum transfer limit ($q^2 \to 0$), the vector charge becomes essentially $g_V(q^2 = 0) = 1$ according to CVC theory. In contrast, the axial vector charge is partially conserved (PCAC [Suz66]), with $|g_A| = 1.27641(56)$ [MMS$^+$19]. A conservation of the axial vector charge would imply $|g_A| = 1$, which has not been observed experimentally[13].

Expressing the ratio of the axial vector and the axial vector coupling constants in terms of $\lambda \equiv \frac{g_A}{g_V}$ [DS11], the Lagrangian density of free neutron decay reads

$$\mathcal{L}_{\text{n-decay}} = \frac{G_\text{F} V_\text{ud}}{\sqrt{2}} \bar{\psi}_e \gamma_\mu \left(1 - \gamma_5\right) \psi_\nu \bar{\psi}_p \gamma^\mu \left(1 - \lambda\gamma_5\right) \psi_n + h.c. \tag{2.20}$$

The Fermi constant G_F is determined from measuring the muon lifetime [WTP$^+$11] and is nowadays given in the form $G_\text{F}/\left(\hbar c\right)^3 = 1.1663787(6) \times 10^{-5}$ GeV^{-2} [THH$^+$18][14]. With the mass of the W boson (m_W), the Fermi constant is related to the weak coupling constant g_W by [Byr11]

$$\frac{G_\text{F}}{\left(\hbar c\right)^3} = \sqrt{2} \frac{g_\text{W}^2}{8\left(m_\text{W} c^2\right)^2}. \tag{2.21}$$

2.1.2 Electroweak unification

According to the SM, the W^- boson mediates the decay of the neutron into a proton (cf. Eq. (2.20) for the Lagrangian density). It only couples to left-handed fermions, which is due to the principle of maximum parity violation [PRS$^+$09]. While right-handed neutrinos are not contained in the SM, the neutrino mass is considered to be zero.

Salam/Ward, Glashow and Weinberg [Gla61, SW59, Wei67] succeeded in the unification of the electromagnetic and weak interaction in the late 1960s ('electroweak unification'), which is an integral part of the SM. Based on a $\text{SU}(2)_L \times \text{U}(1)_Y$ gauge group[15], they postulated four massive spin-1 vector bosons $W_\mu^+, W_\mu^0, W_\mu^-, B_\mu^0$. Sufficiently low energies cause a symmetry breaking of the electromagnetic and the weak interaction, upon which the massive weak bosons (W^+, W^- for charged current interactions, Z^0 for neutral current interactions) and the massless photon (γ) mediate the respective interaction [Kra88]. Consequently, the photon (A_μ) and the Z^0 boson (Z_μ) are different combinations of the vector bosons B_μ^0 and W_μ^0, with θ_W being the Weinberg angle [KMM$^+$13]:

$$A_\mu = B_\mu^0 \cos\theta_\text{W} + W_\mu^0 \sin\theta_\text{W} \,, \tag{2.22}$$

$$Z_\mu = W_\mu^0 \cos\theta_\text{W} - B_\mu^0 \sin\theta_\text{W} \,. \tag{2.23}$$

Taking the Higgs mechanism into account, the Weinberg angle furthermore allows for relating the mass of the W^+/W^- boson, m_W, to the Z^0 boson mass, m_Z [KMM$^+$13],

$$m_\text{W} = m_\text{Z} \cos\theta_\text{W} \,. \tag{2.24}$$

Equation 2.21 has shown the relation of the weak coupling constant g_W to the Fermi constant G_F, taking the mass m_W of the gauge bosons W^+/W^- in charged current interactions

[13] For more details, refer to the Goldberger-Treiman relation, *e.g.* in [JS75, EK94].

[14] In Eq. (2.20), the dimension of G_F is GeV $\cdot$ m^3. For G_F determined from muon decay, the dimension is GeV^{-2}. The conversion is made by the factor $(\hbar c)^3$.

[15] The index L exhibits the model's application to left-handed particles, while Y denotes the weak hypercharge.

into account. This relation can be used to compare the strength of the weak to the electromagnetic interaction. Using $m_{\mathrm{W}} = 80.379(12)\,\mathrm{GeV}$ [THH$^+$18], the weak coupling constant becomes ~ 0.653. The (dimensionless) electromagnetic coupling constant, e, is related to the fine structure constant $\alpha = 1/137$ by $e = \sqrt{4\pi\alpha}$, giving

$$\frac{g_{\mathrm{W}}^2}{e^2} = \frac{0.653}{4\pi\,(1/137)} \sim 4.649\ . \tag{2.25}$$

Thus, the weak interaction is more than 4 times stronger than the electroweak interaction in the limit $Q^2 \gg M^2$ with M being the mass of the heavy bosons. A similar factor is obtained when the relation between both constants is expressed depending on the Weinberg angle θ_{W} [DS11],

$$g_{\mathrm{W}} \sin\theta_{\mathrm{W}} = e\ , \tag{2.26}$$

with $\sin^2\theta_{\mathrm{W}} \sim 0.231\,22(4)$ [THH$^+$18].

2.1.3 Fermi and Gamow-Teller transitions

Two β-decay transition types exist, which are referred to as Fermi and Gamow-Teller[16] transitions, respectively. The transition matrix elements for Fermi ($\mathcal{M}_{\mathrm{F}}$) transitions correspond to the matrix elements for vector or scalar (V, S) interactions (cf. Eq. (2.10)) [Kle16]. Since Gamow-Teller (GT) transitions require axial vector or tensor (A, T) interactions, they are described by the matrix element in Eq. (2.11). Thus, the following matrix elements result [MK02, Kle16],

$$\mathcal{M}_{\mathrm{F}} = \int dV \bar{\psi}_p \mathbf{1} \psi_n\ , \tag{2.27}$$

$$\mathcal{M}_{\mathrm{GT}} = \int dV \bar{\psi}_p \vec{\sigma} \psi_n\ . \tag{2.28}$$

The operators involved demonstrate the nature of the transition. In case of a Gamow-Teller transition, the spin operator $\vec{\sigma}$ containing the Pauli matrices acts on the nuclear spin, while the Fermi transition's identity operator $\mathbf{1}$ leaves the spin unchanged.

The implication of a Fermi transition is demonstrated in Fig. 2.2 a). Since no change in the total angular momentum of the nucleus occurs ($\Delta I = 0$), the proton remains in the same spin state as the neutron [MK02]. To account for the conservation of angular momentum, the electron-electron-antineutrino pair ($e, \bar{\nu}_e$) is thus emitted in a singlet state, with total spin 0. An example would be the $0^+ \to 0^+$ transition[17] of ^{14}O decaying into ^{14}N. In Gamow-Teller transitions, the spin operator $\vec{\sigma}$ acts on the nuclear spin, yielding transitions with $\Delta I = 0, \pm 1$ while excluding $I = 0 \to 0$ transitions [MK02]. Figure 2.2 b) shows a Gamow-Teller transition leading to the proton spin being found in the opposite state of the neutron spin. Thus, the ($e, \bar{\nu}_e$) pair is emitted in a triplet state with total spin 1. The $0^+ \to 1^+$ transition of ^{6}He decaying into ^{6}Li is a typical example [MK02].

In β-decay, different decay types occur, which are depending on their decay products either purely leptonic, purely hadronic or semileptonic. While purely leptonic decays are only sensitive to the axial vector current and are therefore classified as Gamow-Teller transitions, semileptonic decays can either have a contribution of only the vector current (Fermi transitions, *e.g.,* $0^+ \to 0^+$, $\pi^+ \to \pi^0 + e^+ + \nu_e$) or be governed by a mixture between vector and axial vector current (*e.g.,* $n \to p + e^- + \bar{\nu}_e$, $\Lambda \to p + e^- + \bar{\nu}_e$) [CGH13].

[16] Gamow-Teller transitions were posulated in 1936 by Gamow and Teller [GT36].

[17] The notation 0^+ refers to I^P, with I indicating the total angular momentum of the nucleus and P the parity.

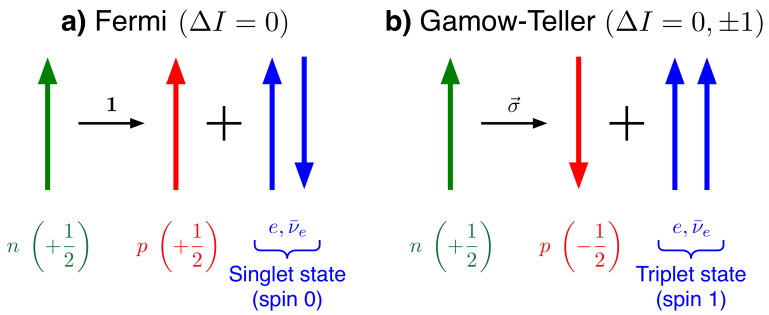

Figure 2.2: Fermi and Gamow-Teller transitions compared, with the arrows denoting the spins' z-components. (a) Fermi transitions with no change in total angular momentum of the nucleus ($\Delta I = 0$, neutron and proton spin given in brackets) due to the acting of the identity operator, $\mathbf{1}$ (cf. Eq. (2.10)). Electron (e) and electron-antineutrino ($\bar{\nu}_e$) are emitted in a singlet state with total spin 0. (b) In Gamow-Teller transitions ($\Delta I = 0, \pm 1$), the spin operator $\vec{\sigma}$ (cf. Eq. (2.11)) acts on the spin state of the proton, leading to an opposite spin state of the proton in the depicted case. Due to angular momentum conservation, the electron and the electron-antineutrino are emitted in a triplet state with total spin 1. Figure based on [MK02].

2.2 Implications of neutron β-decay

After introducing the reader to the weak interaction, the implications of neutron β-decay are laid out. First, Ch. 2.2.1 presents the relation of the neutron lifetime to the Big Bang and further astrophysical phenomena, which is followed by a discussion on further astrophysical phenomena (cf. Ch. 2.2.2). The last section deals with a detailed description of neutron decay from a particle physics perspective (cf. Ch. 2.2.3).

2.2.1 Neutron lifetime and the Big Bang

In the following, the relation of τ_n to BBN is explained, which has affected the primordial helium-4 (^{4}He) abundance[18].

Shortly after Big Bang ($t_b \sim 10^{-4}\,\mathrm{s}$), leptons (electron/positron, e^-/e^+, and (anti-) neutrinos, $\nu/\bar{\nu}$), photons (γ), and a $\sim 10^{-9}$ fraction of baryons (neutrons, n, and protons, p) were present at a high energy of $\sim 100\,\mathrm{MeV}$. Invoked by rapid collisions, all particles were in thermal equilibrium due to the reactions [BBF89]

$$\nu_e + n \longleftrightarrow p + e^- \,, \tag{2.29}$$
$$e^+ + n \longleftrightarrow p + \bar{\nu}_e \,, \tag{2.30}$$
$$n \longleftrightarrow p + e^- + \bar{\nu}_e \,, \tag{2.31}$$

which also led to a chemical equilibrium of all baryons. Thus, the neutron-proton ratio R_{np} can be expressed in terms of the Boltzmann law with temperature T, Boltzmann constant k_B, and the difference of the neutron and proton mass, $\Delta m = m_n - m_p$ [DS11],

$$R_{np}(T) = \frac{n(T)}{p(T)} = \exp\left(\frac{-\Delta m}{k_\mathrm{B} T}\right) \,. \tag{2.32}$$

[18] The reasoning is based on [BBF89], with additions from [DS11] and [CFO+16]. For a more detailed discussion, refer to named sources.

Conventionally, the expression is rewritten to express the ratio of n to all baryons [BBF89],

$$X(T) = \frac{n(T)}{n(T)+p(T)} = \frac{1}{1+\frac{p(T)}{n(T)}} = \frac{1}{1+\exp\left(\Delta m/k_{\mathrm{B}}T\right)} \,. \tag{2.33}$$

After $t_f \sim 2\,\mathrm{s}$, the freeze-out temperature $T_f \sim 8\times10^9\,\mathrm{K}$ is reached, which corresponds to an energy of $k_{\mathrm{B}}T_f \sim 0.7\,\mathrm{MeV}$. With the universe expanding, the decoupling of baryons and leptons sets in, which causes the reactions in Eqs. (2.29) and (2.30) to stop, with a significant fraction of neutrons ($R(T_F) \sim 1/5$ [CFO$^+$16]) remaining. At T_f, the light nuclei deuterium (^{2}H), tritium (^{3}H), and helium-4 (^{4}He) are forced in thermal and chemical equilibrium by the following reactions [BBF89]:

$$n + p \longleftrightarrow {}^2\mathrm{H} + \gamma \,, \tag{2.34}$$

$${}^2\mathrm{H} + \ \longleftrightarrow {}^3\mathrm{H} + p \,, \tag{2.35}$$

$${}^2\mathrm{H} + {}^3\mathrm{H} \longleftrightarrow {}^4\mathrm{He} + n \,. \tag{2.36}$$

Photodissociation caused by the large number density of photons prevents the nucleosynthesis starting with deuterium production at this point ('deuterium bottleneck' [CFO$^+$16]).

The point in time when freeze-out sets in depends on the energy density ρ at temperature T, which for $k_{\mathrm{B}}T > 1\,\mathrm{MeV}$ is given by [BBF89, CFO$^+$16]

$$\rho = \frac{\pi^2 T^4}{30}\left(\underbrace{2}_{\gamma} + \underbrace{\frac{7}{2}}_{e^-/e^+} + \underbrace{\frac{7}{4}\mathcal{N}_\nu}_{\nu/\bar{\nu}}\right) \,, \tag{2.37}$$

with the available degrees of freedom resulting from photons (γ), electrons/positrons (e^-/e^+), and neutrinos ($\nu_e/\bar{\nu}_e$) encapsulated inside the bracket. The influence of the number of neutrino flavours, *i.e.*, $\mathcal{N}_\nu = 3$, is relevant, since a higher $\mathcal{N}_\nu$ value would have led to an earlier freeze-out and therefore a higher number of free neutrons at T_f [DS11].

Nucleosynthesis starts with deuterium formation (cf. Eq. (2.34)) when the baryon-photon ratio $\eta = n_b/n_\gamma$ meets the condition [CFO$^+$16]

$$\eta^{-1}\exp\left(\frac{-E_{\mathrm{B},\,{}^2\mathrm{H}}}{k_{\mathrm{B}}T_c}\right) \sim 1 \,, \tag{2.38}$$

with deuterium binding energy $E_{\mathrm{B},\,{}^2\mathrm{H}} = 2.2\,\mathrm{MeV}$. This condition is met following a further cooldown to $k_{\mathrm{B}}T_c \sim 0.09\,\mathrm{MeV}$ after $t_c \sim 180\,\mathrm{s}$, which leads to the formation of light nuclei (cf. Eqs. (2.34) - (2.36), with $\longleftrightarrow$ replaced by $\rightarrow$). Due to its large binding energy of $E_{\mathrm{B},\,{}^4\mathrm{He}} \sim 28.3\,\mathrm{MeV}$, the majority of free neutrons available at t_f are bound in ^{4}He after the reactions given in Eqs. (2.34) to (2.36). The amount of ^{4}He (^{4}He abundance Y_{p}) produced in the nucleosynthesis after a cooldown to temperature $T \sim 0$,

$$Y_{\mathrm{p}} \sim 2X(T\sim0) = \frac{2(n(T\sim0)/p(T\sim0))}{1+(n(T\sim0)/p(T\sim0))} \,, \tag{2.39}$$

can be approximated by $Y_{\mathrm{p}} \sim 0.25$ [CFO$^+$16].

Upon closer look, the number of free neutrons available for nucleosynthesis decreases due to the decay into protons between t_f and t_c, which is determined by the neutron lifetime,

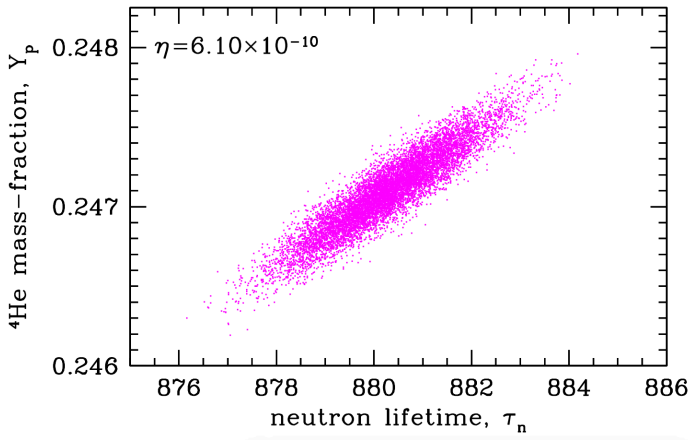

Figure 2.3: Monte carlo simulation on the relation between the neutron lifetime τ_n and helium-4 abundance, Y_p. Plot taken from [CFO+16].

τ_n. Thus, the ^{4}He abundance depends on τ_n. In fact, τ_n causes the neutron/proton ratio to decrease from $R_{np}(T_f) \sim \frac{1}{5}$ at freeze-out temperature to $R_{np}(T_c) \sim \frac{1}{7}$ until nucleosynthesis sets in [CFO+16].

After a detailed derivation, the following equation gives the dependence of Y_p on $\mathcal{N}_\nu$, τ_n, and the baryon-to-photon ratio ($\eta = n_b/n_\gamma$) [BS85]:

$$Y_\mathrm{p} = 0.230 + 0.013\,(\mathcal{N}_\nu - 3) + 0.014\,(\tau_n \cdot \ln(2) - 10.6) + 0.011 \ln\left(\eta \times 10^{10}\right) \tag{2.40}$$

The dependence of Y_p on τ_n for $\eta = 6.10 \times 10^{-10}$ is plotted in Fig. 2.3.

2.2.2 Astrophysical aspects of the neutron lifetime

In astroparticle physics, τ_n determines the so-called '*pp* chain' in the sun [AGR+11], which eventually leads to the production of helium-4 (^{4}He). The reaction chain starts with the fusion of two protons (p) into deuterium (^{2}H) [Sal52],

$$p + p \rightarrow {}^2\mathrm{H} + \nu_e + 0.42\,\mathrm{MeV}\ . \tag{2.41}$$

This fusion process is very slow (mean reaction time $\sim 8 \times 10^9$ y [Sal52]) and is mediated by the weak interaction ('inverse neutron decay' with spectator proton [Byr02]). Thus, the neutron lifetime τ_n affects the primary reaction in the solar *pp* chain.

Due to the processes in BBN (cf. Ch. 2.2.1), the cosmic microwave background (CMB) is also related to τ_n. CMB is the background γ radiation remaining from big bang [Dur15] with temperature $T_\mathrm{CMB} = 2.725\,48(57)\,\mathrm{K}$ [Fix09]. Analyses of the CMB temperature and polarisation anisotropies were carried out by the Planck satellite in 2015 [SPC+16]. Observed anisotropies are expressed in terms of angular power spectra (C_l) as a function of multipole moment l (cf. Fig. 2.4). With higher l, the description of the spectrum becomes increasingly sensitive to τ_n, as can be seen in the damping tail at $l \gtrsim 1500$ for the extreme cases $\tau_n = 1080\,\mathrm{s}$ (magenta line) and $\tau_n = 680\,\mathrm{s}$ (blue dashed line).

Furthermore, the CMB analyses allow to constrain the τ_n value to $907(69)\,\mathrm{s}$ (68 % confidence level, [SPC+16]). Combining the CMB measurements with recent measurement

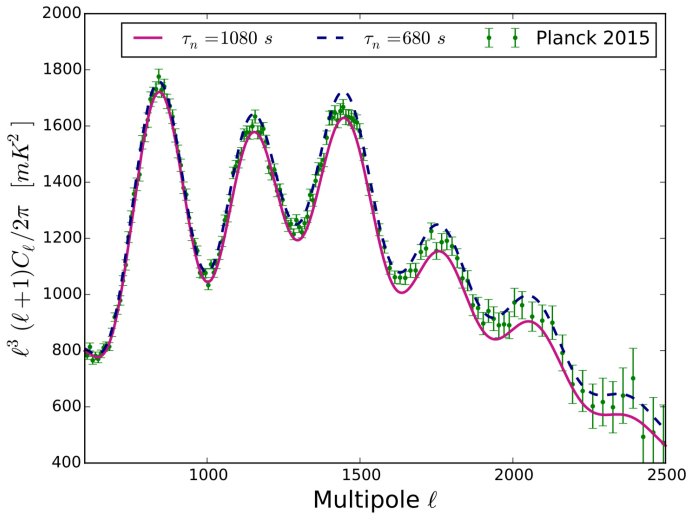

Figure 2.4: Power spectrum of the cosmic microwave background temperature measured by the Planck satellite in 2015 (green data points), with angular power spectrum C_l and multipole moment l. Precisely knowing τ_n is required to describe the spectrum, as is shown for the extreme cases $\tau_n = 1080\,\mathrm{s}$ (magenta line) and $\tau_n = 680\,\mathrm{s}$ (blue dashed line). Figure taken from [SPC+16].

of the ^{4}He abundance $Y_\mathrm{p} = 0.2449(40)$ [AOS15] has been used to further constrain τ_n to $875(19)\,\mathrm{s}$[19], which would neither rule out bottle- nor beam-type results (cf. Ch. 3.1.1).

2.2.3 Neutron decay in the context of particle physics

Let us now turn to the example of free neutron decay in more detail. In its non-bound state, the neutron with mass $m_\mathrm{n} = 939.565\,413\,3(58)\,\mathrm{MeV}$ [THH+18] decays after $\tau_n \sim 15\,\mathrm{min}$ to its lighter isospin-counterpart, the proton ($m_p = 938.272\,081\,3(58)\,\mathrm{MeV}$ [THH+18])[20]. This occurs due to the quark transition $d \to u$, which is mediated by the exchange of a W^- boson, which in turn leads to the production of an electron/electron-antineutrino pair. The associated Feynman diagram is shown in Fig. 2.5.

Viewed on the quark level, the Lagrangian density [NCGA13]

$$\mathcal{L}_\mathrm{ud} = \frac{G_\mathrm{F} V_\mathrm{ud}}{\sqrt{2}} \bar{\psi}_e \gamma_\mu \left(1 - \gamma_5\right) \psi_\nu \bar{\psi}_u \gamma^\mu \left(1 - \gamma_5\right) \psi_d + h.c.\,, \tag{2.42}$$

is similar to the already discussed $\mathcal{L}_\text{n-decay}$ (cf. Eq. (2.20)). The equation contains the Cabibbo-Kobayashi-Maskawa (CKM) matrix element, V_ud, which can be determined in free neutron decay to search for violations of the CKM matrix unitarity. Details on the concept of quark mixing and the unitarity of the CKM matrix are discussed in Ch. 2.2.3.1, which is followed by summarising the available observables in neutron decay (cf. Ch. 2.2.3.2). Additionally, Ch. 2.2.3.3 gives the current status on the SM conformity and possible hints towards 'Physics beyond the Standard Model' (BSM).

[19] Taking other Y_p measurement into account, constraints on τ_n of $916(15)\,\mathrm{s}$ and $921(11)\,\mathrm{s}$ were calculated [SPC+16], which would contradict recent measurements of τ_n.

[20] The I_3 isospin vector components of neutron and proton are $I_{3,\,\mathrm{neutron}} = -\frac{1}{2}$, and $I_{3,\,\mathrm{proton}} = +\frac{1}{2}$.

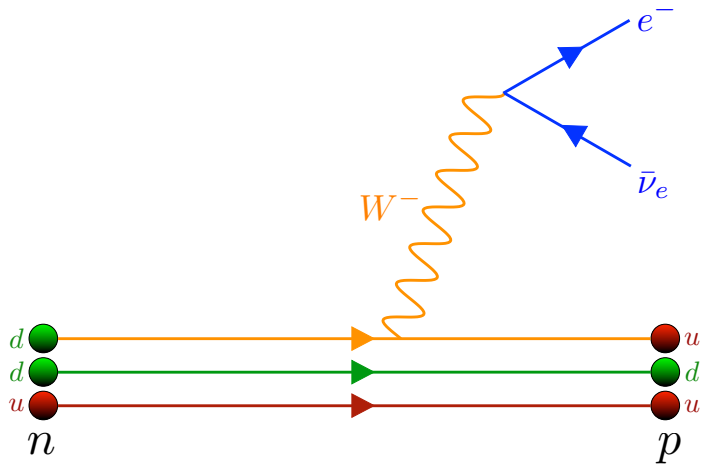

Figure 2.5: Feynman diagram of semileptonic free neutron decay. The free neutron with quark content udd decays into a proton (uud) under quark transformation $d \rightarrow u$ (orange line). The process is mediated by the exchange of a virtual W^- boson, which leads to the release of a electron/electron-antineutrino ($e^-/\bar{\nu}_e$) pair (indicated in blue). Given colours are only used for demonstration purposes and do not *e.g.* represent the quark colour charge. The time axis points from left to right.

2.2.3.1 Quark mixing and unitarity

According to Eq. (2.42), $\mathcal{L}_{\mathrm{ud}}$ depends on V_{ud}, which as the first element of the Cabibbo-Kobayashi-Maskawa (CKM) matrix [KM73] describes the quark mixing of u and d. In experimental observations in the 1960s, it was found that purely leptonic and semileptonic β-decays exhibit different 'strenghts' in relation to G_{F}^2, *i.e.*, $\sim G_{\mathrm{F}}^2$ (purely leptonic), $\sim 0.95 G_{\mathrm{F}}^2$ (semileptonic, strangeness change $\Delta S = 0$), $\sim 0.05 G_{\mathrm{F}}^2$ (semileptonic, $\Delta S = 1$) [DS11]. Cabibbo concluded that there was a 'mixture' of 'down-type' quark states with charge $-1/3$ in weak interaction, so that the quark states $|d'\rangle$ and $|s'\rangle$ were related to each other by the Cabibbo angle θ_C [Cab63]:

$$|d'\rangle = |d\rangle \cos\theta_C + |s\rangle \sin\theta_C \tag{2.43}$$
$$|s'\rangle = |d\rangle \sin\theta_C + |s\rangle \cos\theta_C \,. \tag{2.44}$$

This postulate succeeded in explaining the observed 'strengths' in different β-decay types, since in purely leptonic (e.g. muon decay), no quark mixing occurs, while in semileptonic it affects the process in two different manners ($\Delta S = 0 : \cos^2\theta_C \sim 0.95$, $\Delta S = 1 : \sin^2\theta_C \sim 0.05$). The CKM matrix extended this theoretical concept to all three quark generations and added a complex phase $e^{i\delta}$ to account for CP violation. According to the matrix, quark state transformations $|q'\rangle$ are decribed by [KM73]:

$$\begin{pmatrix} |d'\rangle \\ |s'\rangle \\ |b'\rangle \end{pmatrix} = \begin{pmatrix} V_{\mathrm{ud}} & V_{\mathrm{us}} & V_{\mathrm{ub}} \\ V_{\mathrm{cd}} & V_{\mathrm{cs}} & V_{\mathrm{cb}} \\ V_{\mathrm{td}} & V_{\mathrm{ts}} & V_{\mathrm{tb}} \end{pmatrix} \cdot \begin{pmatrix} |d\rangle \\ |s\rangle \\ |b\rangle \end{pmatrix} \tag{2.45}$$

Several parametrisations of the CKM matrix exist, *e.g.* the Wolfenstein parametrisation [Wol83]. The CKM matrix is unitary and therefore fulfils the condition $\sum_k V_{ki}^* V_{kj} = \delta_{ij}$, which implies for the neutron decay-relevant first row ('unitarity condition', with i = d, s,

b) [AHB$^+$02, ABD$^+$04, Gar06]:

$$\sum_i V_{\mathrm{ui}}^2 = V_{\mathrm{ud}}^2 + V_{\mathrm{us}}^2 + V_{\mathrm{ub}}^2 \equiv 1 \tag{2.46}$$

This unitarity condition is fundamental to the Standard Model, as it reflects its three fermion generations.

2.2.3.2 Available observables in neutron decay

Due to the absence of nuclear structure effects in neutron decay [Poc17], only nucleus-independent radiative corrections need to be included, which underlines its capability to 'purely' access λ and V_{ud}. The absence of complicated nuclear structure-related corrections is not the only advantage of neutron decay, as it additionally offers many different observables for extracting λ. Overall, more than 20 parameters are available for the determination of λ and - considering an additional measurement of the neutron lifetime τ_n - the calculation of V_{ud} [DS11].

Angular correlation coefficients

Among the observables are the angular correlation coefficients a, A, B, D, which correlate several decay properties. They are contained in the differential decay rate $d^3\Gamma$ with electron/electron-antineutrino energies E_e, E_ν, momenta $\vec{p}_e, \vec{p}_\nu$, and neutron spin $\vec{\sigma}_n$ [JTW57],

$$\begin{aligned} d^3\Gamma \sim\, & dE_e d\Omega_e d\Omega_\nu \; G_{\mathrm{F}}^2 V_{\mathrm{ud}}^2 (1+3\lambda^2) p_e E_e (E_0 - E_e)^2 \\ & \cdot \left(1 + a\frac{\vec{p}_e \cdot \vec{p}_\nu}{E_e E_\nu} + \underbrace{b\frac{m}{E_e}}_{=0 \text{ (SM)}} + \frac{\vec{\sigma}_n}{\sigma_n} \cdot \left[A\frac{\vec{p}_e}{E_e} + B\frac{\vec{p}_\nu}{E_\nu} + D\frac{\vec{p}_e \times \vec{p}_\nu}{E_e E_\nu} \right] \right) . \end{aligned} \tag{2.47}$$

Note that given equation only considers momenta $\vec{p}_e, \vec{p}_\nu$ and spin $\vec{\sigma}_n$. In the SM, the Fierz interference term b vanishes ($b \equiv 0$). Finding $b \neq 0$ would allow the introduction of S and T type interactions [ERM05, GANCS19, IHT$^+$19].

Among all observables, the focus should be on a ($\beta - \bar{\nu}_e$ angular correlation), A (β-asymmetry) and B ($\bar{\nu}_e$-asymmetry). Of all angular correlation coefficients, a and A exhibit the highest sensitivity to λ, while B shows a ~ 40 times lower sensitivity [Abe08, DS11, MPB$^+$13]:

$$a = \frac{1 - |\lambda|^2}{1 + 3\,|\lambda|^2} \tag{2.48}$$

$$A = -2\frac{\left(|\lambda|^2 - |\lambda|\right)}{1 + 3\,|\lambda|^2} \tag{2.49}$$

$$B = 2\frac{|\lambda|\,(|\lambda| - 1)}{1 + 3\,|\lambda|^2} \tag{2.50}$$

Lifetime of the free neutron

The neutron lifetime, τ_n, is essentially the neutron decay rate and contains the electroweak radiative correction term RC, which refers to the contribution of 'weak magnetism' [Mar09, DS11, CMS19]:

$$\frac{1}{\tau_n} = \frac{c}{2\pi^3} \frac{\left(m_e c^2\right)^5}{(\hbar c)^7} G_{\mathrm{F}}^2 \,|V_{\mathrm{ud}}|^2 \left(1 + 3\,|\lambda|^2\right) (1 + RC) \cdot f \; . \tag{2.51}$$

Additional to the Fermi constant $G_\mathrm{F} = 1.166\,378\,7(6) \times 10^{-5}\,\mathrm{GeV}^{-2}$ resulting from the muon lifetime [CMS19], the equation contains the electron mass, m_e, and the phase space factor $f = 1.6887(1)$ [CMS18], which contains a contribution of the Fermi function of $\sim 5.6\,\%$ and additional corrections [CMS04][21]. The radiative corrections for neutron decay at lowest order yield [MS06, CMS19]

$$RC = \frac{\alpha}{2\pi}\left(\underbrace{\bar{g}(E_m)}_{\mathrm{I}} + \underbrace{3\ln\left(\frac{m_Z}{m_p}\right)}_{\mathrm{II}} + \underbrace{\ln\left(\frac{m_Z}{m_A}\right)}_{\mathrm{III}} + \underbrace{2C_\mathrm{Born} + A_g}_{\mathrm{IV}}\right) = 0.03947(32)\ , \tag{2.52}$$

where I relates to bremsstrahlung effects and long-distance loop corrections (with neutron β-decay end point energy E_m), II is a QCD-independent correction, and III and IV are QCD corrections (m_p denotes the proton mass, m_Z refers to the mass of all protons and m_A to the mass of all protons and neutrons found in the respective atomic nucleus).

All updated corrections are included in the neutron decay 'master formula', which relates τ_n and V_ud directly by using Eq. (2.51) and Eq. (2.52). The relation has first been stated in 2006 [MS06] and has been recently updated due to notable advances in the calculation of the radiative corrections[22] [CMS19]:

$$\tau_n = \frac{4906.4(1.7)\ \mathrm{s}}{|V_\mathrm{ud}|^2\left(1 + 3\,|\lambda|^2\right)} \tag{2.53}$$

Consequently, measurements of λ and τ_n determine V_ud in neutron decay.

2.2.3.3 Current status and possible hints for BSM physics

A determination of the parameters $\tau_n, V_\mathrm{ud}, \lambda$ in Eq. (2.53), of which only τ_n and λ can be measured in neutron decay, allows for testing the SM from different perspectives.

Status on CKM unitarity and λ

Considering the unitarity of the CKM matrix in the first row (cf. Eq. (2.46), the element V_ub can still be ignored, as current predictions and measurements limit its contribution to $\sim 1.7 \times 10^{-5}$ [THH$^+$18]. Several advances have been made on the measurement of V_us, which is currently determined with highest precision in Kaon decays (weighted average over K_{l3} and $K_{\mu 2}$ decays[23] [THH$^+$18]):

$$V_\mathrm{us} = 0.2244(6)\ . \tag{2.54}$$

Given value is taking lattice quantum chromodynamics (QCD) corrections for $2 + 1$ quark flavous N_f into account, while calculations with $N_f = 2 + 1 + 1$ result in a slightly deviated value of $V_\mathrm{us} = 0.2243(5)$ [THH$^+$18]. Furthermore, V_us can be determined with lower precision from hyperon ($V_\mathrm{us} = 0.2250(27)$) and τ decays ($V_\mathrm{us} = 0.2216(15)$[24]) [THH$^+$18]. The

[21] For further information on the phase space factor f, consider [Wil82].

[22] In their recent recalculation, Czarnecki, Marciano and Sirlin [CMS19] have responded to an updated calculation by Seng et al. in 2018 [SGPRM18]. The calculations by Seng et al. yielded a $\sim 3.3\sigma$ deviation from CKM unitarity, which would call for BSM physics. Using the recalculations by Czarnecki et al., the resulting V_ud value confirms the SM, since it agrees with CKM unitarity at the $\sim 1\sigma$ level.

[23] K_{l3} refers to Kaon decay into three leptons, $K_{\mu 2}$ implies Kaon decay into two muons.

[24] Taking the current recommended PDG value for V_ud [THH$^+$18] into account, V_us from τ decays would violate unitarity by $\sim 2.4\ \sigma$. Due to experimental uncertainties, this value is currently not considered.

Particle Data Group (PDG) currently takes the Kaon decay-extracted value in Eq. (2.54) into account for the CKM unitarity.

Now, the current status on the neutron decay-relevant matrix element V_{ud} is revealed. Highest-accuracy measurements are performed evaluating nuclear $0^+ \rightarrow 0^+$ transitions. The $0^+ \rightarrow 0^+$ transition is a 'superallowed' semileptonic decay with conserved total angular momentum ($\Delta J = 0$) and exclusive contribution of the vector current. Despite the well-developed experimental techniques including nuclei ranging from ^{10}C to ^{74}Rb, the determination of V_{ud} requires additional correction factors to the radiative corrections (RC) which are also considered in free neutron decay. These additional correction factors comprise nuclear structure-dependent corrections and isospin-breaking corrections [HT05], which are potentially error-prone. With respect to 14 $0^+ \rightarrow 0^+$ decays, a corrected ft value of $\overline{\mathcal{F}t} = 3072.27(72)\,\mathrm{s}$ gives $V_{\mathrm{ud},\,0^+} = 0.9720(10)_{\mathrm{exp}}(18)_{RC}$ [HT15]. This value is translated into the present PDG average, which reads [THH$^+$18]

$$V_{\mathrm{ud,\,PDG}} = 0.974\,20(21)\ . \tag{2.55}$$

Pion decay ($\pi^+ \rightarrow \pi^0 + e^+ + \nu_e$) provides another possibility to obtain V_{ud}. As with free neutron decay, the $0^- \rightarrow 0^-$ transition is free of nuclear structure and isospin-breaking corrections. However, the small branching ratio $\mathcal{O}(10^{-8})$ implies challenges for the detection [SBNC06]. The most precise value measured 2004 in the PIBETA experiment [PFB$^+$04] yields [THH$^+$18]:

$$V_{\mathrm{ud},\,\pi^+} = 0.9749(26)\ . \tag{2.56}$$

For free neutron decay, V_{ud} is determined from measurements of λ and τ_n (cf. Eq. (2.53)). The standard approach to obtain V_{ud} is to take individual and/or averaged measurement results of one parameter into account, while fixing the other. With respect to λ, for instance, τ_n is inserted as a fixed parameter. It is decided to follow the recommendation in [Wie18], in which τ_n is derived from the average of the most recent nine 'bottle-type' measurements[25]:

$$\bar{\tau}_{n,\,\mathrm{bottle}} = 879.37(58)\,\mathrm{s}\ . \tag{2.57}$$

The PERKEO III collaboration has recently published an updated λ result based on the measurement of the β-asymmetry A, [MMS$^+$19],

$$\lambda_{\mathrm{PERKEOIII}} = -1.27641(56)\ . \tag{2.58}$$

This result confirms the PDG average of all λ measurements from 2002 onwards [THH$^+$18], $\lambda_{\mathrm{PDG}} = -1.2762(5)$. Taking both individual λ values and the τ_n value of Eq. (2.57) into account for a determination of V_{ud} shows that the values extracted from π^+ decay and A correspond to the PDG average (cf. Fig. 2.6). Considering V_{us} from Eq. (2.54), given λ values would imply for unitarity:

$$|V_{\mathrm{ud}}(\lambda_{\mathrm{PDG}})|^2 + |V_{\mathrm{us}}|^2 + \underbrace{|V_{\mathrm{ub}}|^2}_{\rightarrow 0} = 0.9994(4)(2) \lesssim 1.0000\ , \tag{2.59}$$

$$|V_{\mathrm{ud}}(\lambda_{\mathrm{PERKEOIII}})|^2 + |V_{\mathrm{us}}|^2 + \underbrace{|V_{\mathrm{ub}}|^2}_{\rightarrow 0} = 0.9976(69) \sim 1.0000\ , \tag{2.60}$$

[25] A discussion on the determination of the neutron lifetime in bottle- and beam-type experiments is provided in Ch. 3.1.1.

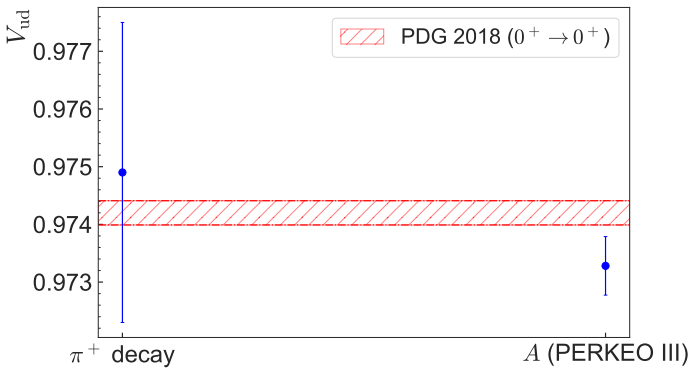

Figure 2.6: Current status on V_{ud}. Shown are extracted V_{ud} values from pion (π^+) decay [PFB+04] and the calculated value taking the most recent λ measurement of the angular correlation coefficient A into account (cf. Eq. (2.58)). The shaded red area depicts the recent PDG value [THH+18], determined by $0^+ \to 0^+$ consideration (cf. Eq. (2.55)). The low error in the PDG value emphasises the high accuracy achieved in $0^+ \to 0^+$ transitions, despite the inclusion of additional correction factors.

which confirms the SM prediction. Taking Eq. (2.59) into account, constraints on the branching ratio of exotic muon decay ($\mathrm{BR}_{\mu,\,\mathrm{exotic}} \leq 1 - 0.9986 \leq 0.0014$) and a fourth quark generation V_{uD} ($1 - |V_{uD}|^2 \geq 0.9986 \Rightarrow V_{uD} \leq 0.04$) [THH+18] can be made.

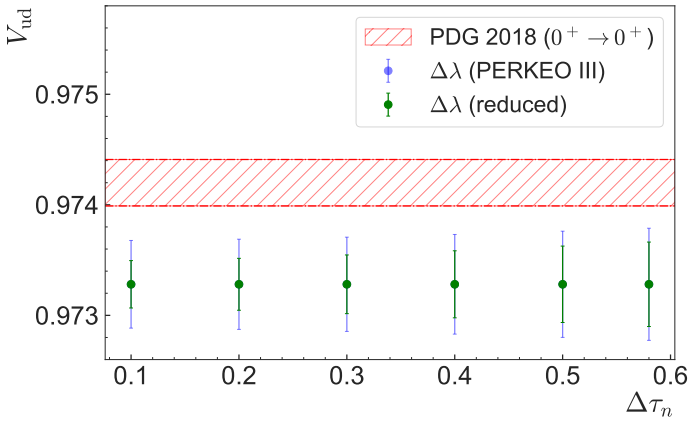

Figure 2.7: Dependency of the V_{ud} precision on the accuracy of τ_n and λ. With the current accuracy in λ determined from the PERKEO III experiment ($\Delta\lambda_{\mathrm{PERKEOIII}} = 0.00056$ [MMS+19]), the $V_{ud,\,\mathrm{PDG}}$ precision inferred from $0^+ \to 0^+$ decays (shaded red area, cf. Eq. (2.55)) cannot be reached, even when reducing $\Delta\tau_n$ from 0.58 s (cf. Eq. (2.57)) to 0.1 s (light blue data points). Along with a reduction of the error in λ by a factor of 3, a similar precision in V_{ud} can be reached for $\Delta\tau_n \sim 0.1$ s (green data points).

Also, deviations from unitarity might lead to the following conclusions [HT77, SBNC06, RM09, Mar12, Ber19b]:

(i) Right-handed currents and - along with Fierz interference - non-V, A contributions,

(ii) existence of an additional Z boson,

(iii) SUSY particles.

Using $\lambda_{\text{PERKEOIII}}$ of Eq. (2.58) and $V_{\text{ud, PDG}}$ (cf. Eq. (2.55)), the expectable value of the neutron lifetime can be calculated:

$$\tau_n = 878.06(80)\,\text{s}\,. \tag{2.61}$$

The value agrees with the current mean derived from bottle-type experiments ($\bar{\tau}_{n,\text{bottle}} = 879.4(6)\,\text{s}$, cf. Ch. 3.1.1). To reach a precision in V_{ud} comparable to $0^+ \rightarrow 0^+$ nuclear decays, a high accuracy in λ and τ_n is needed. With the current accuracy in $\lambda_{\text{PERKEOIII}}$, even a value of $\Delta\tau_n = 0.1\,\text{s}$ would not lead to a precision comparable to the $V_{\text{ud, PDG}}$ result inferred from $0^+ \rightarrow 0^+$ decays (cf. Fig. 2.7). Therefore, the accuracy in λ also needs to be improved. Reducing the error $\Delta\lambda_{\text{PERKEOIII}}$ by a factor of 3 would require an accuracy of $\tau_n \sim 0.1\,\text{s}$ for reaching a precision similar to $V_{\text{ud, PDG}}$.

3 Neutron lifetime experiments and ultracold neutrons

After reviewing neutron beta decay and identifying the important role of the neutron lifetime in the previous chapter, an overview over the history of neutron lifetime experiments and the current status is provided (cf. Ch. 3.1). Additionally, the usage of ultracold neutrons (UCN) for modern neutron lifetime experiments is motivated (cf. Ch. 3.2.2), along with a detailed discussion on the fundamental interactions being available for storage (cf. Ch. 3.2.1). Furthermore, the reader is briefly introduced to UCN production (cf. Ch. 3.2.3).

3.1 History, current status and future directions of neutron lifetime experiments

In this section, a historical overview on the neutron lifetime from the 1950s until today is given while also providing an outlook on upcoming experiments. For a detailed overview over the history of neutron lifetime experiments, refer to [Byr11] and [Wie18].

3.1.1 History of neutron lifetime experiments and the 'neutron lifetime puzzle'

The neutron lifetime τ_n can be determined from both beam- and bottle-type experiments. Between both measurement types, several considerable differences exist. While beam-type experiments rely on the measurement of the decay rate of decay products (electron/proton detection), bottle-type experiments infer τ_n from storing neutrons and measuring the 'surviving' neutrons after different storage times.

Beam-type experiments

As Fig. 3.1 shows, the first measurements of the neutron lifetime were beam-type measurements using a thermal or cold neutron beam. In general, beam-type measurements use charged decay particles (electrons/protons) emitted from a certain neutron beam decay volume filled with an average number of neutrons, N_n. The charged decay particles (N_c) are counted in detectors installed near the neutron beam at a rate of [Byr11]

$$\frac{dN_c(t)}{dt} = \frac{-N_n(t)}{\tau_n} \,, \tag{3.1}$$

which yields an absolute measurement of τ_n. Among others, an experimental challenge is the accurate determination of the respective detection efficiencies and the effective decay volume.

Fig. 3.1 gives an overview over the beam-type measurements (red data points). Leading to the first determination of $\tau_n = 1108(216)\,\mathrm{s}$, Robson used a collimated thermal neutron beam provided by the Chalk River reactor in Canada [Rob51]. The neutron beam activated a manganese foil to determine the integral neutron flux for a defined time. Inferring τ_n additionally required measuring the number of decay products in a defined beam volume. To reduce the strong $\gamma-$ray background, Robson used a electron-proton coincidence method. However, the decay position impacted the decay proton counting efficiency (ε_p), which was a strong systematic effect in Robson's experiment [Wie18]. The notable 1956 and 1959 beam experiments by Spivak [SSP$^+$56] ($\tau_n = 1039(130)\,\mathrm{s}$) and Sosnovki [SSP$^+$59] ($\tau_n = 1013(26)\,\mathrm{s}$) performed at the Moscow I. Y. Kurchatov Atomic Energy Institute improved ε_p by electrostatically extracting the decay protons [Wie12].

Over time, the measured value for τ_n was becoming smaller and increasingly more precise over time, with an impressive accuracy reached by Sosnovki over only some years. In 1972, Christensen [CNB$^+$72] performed a new beam-type measurement in Denmark which relied on two plastic scintillators surrounding the neutron decay volume for decay electron detection, leading to a new best - and again smaller - value of $\tau_n = 919(14)\,\mathrm{s}$. Returning to proton detection, Byrne [BMS$^+$80] developed the idea to store the decay protons in a Penning trap. The 1980 measurement led to $\tau_n = 937(18)\,\mathrm{s}$. In 1988, an updated proton detection measurement by Spivak [Spi88] gave an even more precise value of $\tau_n = 891(9)\,\mathrm{s}$.

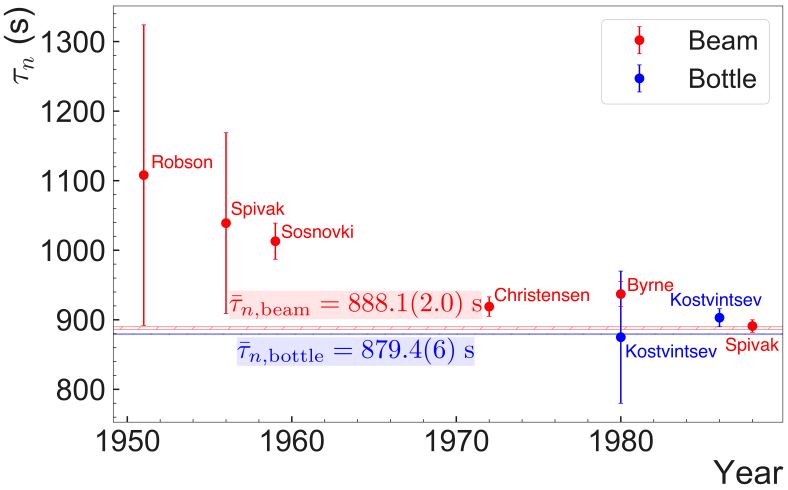

Figure 3.1: Early selected measurements of the neutron lifetime, τ_n. The earliest measurements starting in 1951 are beam-type experiments (red data points). When UCN become usable in the 1980s, they offer the possibility to perform bottle-type measurements (blue data points). The horizontal shaded areas represent the current mean values for beam- ($\bar{\tau}_{n,\mathrm{beam}} = 888.1(2.0)$ s, red) and bottle-type measurements ($\bar{\tau}_{n,\mathrm{bottle}} = 879.4(6)\,\mathrm{s}$, red), with the values taken from Fig. 3.3. Data found in [Rob51, SSP$^+$56, SSP$^+$59, CNB$^+$72, BMS$^+$80, KKMT80, KMT86, Spi88].

A similar setup to the 1980 Byrne Penning trap beam experiment has been used in the 1996 and the 2013 measurements by Byrne [BDH$^+$96] ($\tau_n = 889.2(4.9)$ s) and Yue [YDG$^+$13]

(τ_n = 887.7(2.2) s, 'Sussex-ILL-NIST' experimental series [Wie18]). The current iteration, the BL2 experiment, is set up at the US National Institute of Standards and Technology (NIST [DGN+03]) and is briefly discussed in the following.

As Fig. 3.2 shows, the decay protons resulting from a passing cold neutron beam in the BL2 experiment are trapped 'in-beam' in a cylindrical Penning trap [BDH+96] and are directed onto a detector for counting after a certain trapping time. To investigate systematic effects, the decay volume length (L_{det}) is varied. The neutron lifetime τ_n can then be calculated according to [Wie18]

$$\tau_n = \frac{R_n}{R_p} \cdot \frac{\varepsilon_p L_{\mathrm{det}}}{\varepsilon_0 v_{\mathrm{th}}} \tag{3.2}$$

with neutron/proton decay rates R_n/R_p, and thermal neutron velocity $v_{\mathrm{th}} = 2200\,\mathrm{m\,s^{-1}}$[1]. The measurement requires a precise knowledge of the respective detection efficiencies ε_0 (detection efficiency for detecting a thermal neutron with velocity v_{th}) and ε_p. Especially the accurate determination of ε_0, which is based on a ^{6}LiF detector placed inside the cold neutron flux [NDG+05], is still a challenge. Since the BL2 experiment is the only beam-type experiment currently publishing data, the beam method can be criticised to lack additional 'independent' measurement methods.

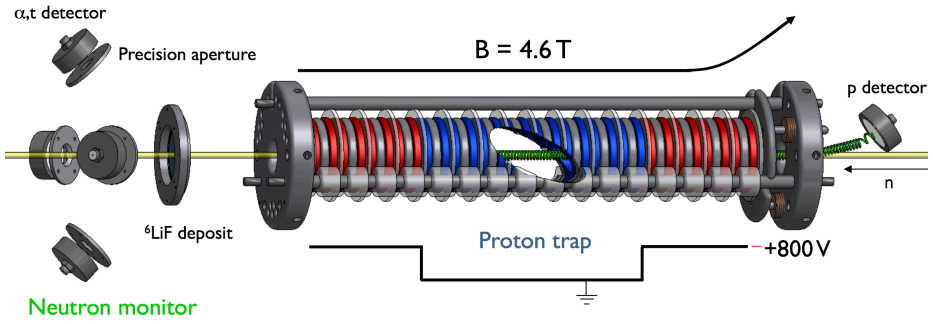

Figure 3.2: Measurement principle of the beam-type experiment BL2. The cold neutron beam enters the cylindrical Penning trap from the right, which leads to the production of decay protons inside the trap. The neutron beam is constantly monitored with a ^{6}LiF-based detector. After unloading the trap, the protons are counted. Rendering taken from [Sno17].

Bottle-type experiments

After the successful production of ultracold neutrons in 1969 by Steyerl [Ste69] and Luschikov [LPSS69], bottle-type measurements based on material confinement were possible. From the 1970s onwards, Kostvintsev stored UCN in an aluminium storage volume to extract τ_n. The 1980 [KKMT80] and 1986 publications [KMT86] yield τ_n = 875(95) s and τ_n = 903(13) s, respectively (cf. blue data points in Fig. 3.1).

As the name indicates, bottle-type measurements rely on filling a storage bottle with UCN. The storage principle can either be 'material', which implies that UCN are confined by a material-dependent Fermi potential V_{F}, or - in more recent experiments - 'magnetic', *i.e.,* the confinement results from the interaction of the neutron's magnetic moment with

[1] For a derivation of the equation and further details on the decay rates, refer to [Wie18].

a magnetic field[2]. After varying storage times, the storage bottle is emptied, with the detection of the 'surviving' (non-decayed) UCN. Measuring the number of 'surviving' UCN at different storage times ($C_{\mathrm{UCN}}(t_{\mathrm{s}})$) gives the storage curve, from which τ_n is extracted by an exponential fit [Byr11],

$$C_{\mathrm{UCN}}(t_{\mathrm{s}}) = C_{\mathrm{UCN}}(t_{\mathrm{s}} = 0) \exp\left(-t_{\mathrm{s}}/\tau_n\right) \ . \tag{3.3}$$

Consequently, bottle-type experiments are always relative measurements of τ_n and therefore - as opposed to beam-type experiments - independent on detection efficiencies.

The main challenge in bottle-type experiments is the determination of neutron losses, since the measured τ value is not only affected by the neutron lifetime τ_n, but also by loss terms [Wie18],

$$\frac{1}{\tau} = \frac{1}{\tau_n} + \frac{1}{\tau_{\mathrm{inelastic}}} + \frac{1}{\tau_{\mathrm{capture}}} + \frac{1}{\tau_{\mathrm{other}}} \ , \tag{3.4}$$

with losses due to inelastic scattering, $\tau_{\mathrm{inelastic}}$, neutron capture processes, τ_{capture}, and additional loss terms, τ_{other}, which *e.g.* comprises the probability of UCN escaping the storage volume or interacting with the residual gas. Experimentally, the loss terms could be successfully reduced by coating the walls with the fluorinated polymer Fomblin [SKF$^+$18], which exhibits a small neutron capture cross section. Cooled down to T$\sim$ 80 K, losses due to inelastic scattering are severely reduced. Furthermore, increasing the storage volume decreases the number of UCN wall collisions and therefore associated losses. A storage volume of infinite size would therefore imply an absence of wall collisions.

Recently, bottle-type experiments have become more precise than beam-type experiments (cf. Fig. 3.3). From 1993 until today, τ_n has also been more often inferred from bottle-type measurements than from beam-type experiments. Mampe first performed a τ_n measurement in 1989 using the MAMBO I setup at Institut Laue-Langevin (ILL), which was reanalysed in 1993 [MBM$^+$93] leading to τ_n = 882.6(2.7) s and again in 2012 by Steyerl [SPK$^+$12] (τ_n = 882.5(2.1) s). The updated 2010 MAMBO II experiment by Pichlmaier [PVS$^+$10] added the removal of high-energetic UCN in a prestorage volume (τ_n = 880.7(1.8) s).

A notably smaller and more precise value was measured by Serebrov [SVK$^+$05] in 2005 (τ_n = 878.50(76) s), which further challenged the UCN community and predominantly led to the formerly-mentioned recalculations of the MAMBO I measurement. The Gravitrap experiment used fluorinated polyether for coating the walls at T = 113 K. It was upgraded with a $\sim$ 5 times larger storage volume to measure τ_n = 881.50(92) s with higher statistics in 2018 [SKF$^+$18]. The given Arzumanov [ABC$^+$15] 2015 value (τ_n = 880.2(1.2) s) is extracted from a re-analysis of 2008-2010 measurements at ILL.

The 2018 Gravitrap measurement [SKF$^+$18] shows the limitations of material bottle-type experiments. Using a well-optimised setup based on fluorinated grease-coated copper walls cooled down to 80 K to reduce wall losses, a systematic error of 0.6 s was found. Significantly less systematic losses can be reached when confining UCN magnetically, which is possible due to the neutron's magnetic moment (cf. Ch. 3.2.1). Thus, wall interactions are absent. Already in its first 2017/18 production run, the magneto-gravitational UCNτ experiment [PCCW$^+$18] has yielded a systematic error of only $+0.4/-0.2$ s (τ_n = 877.70(76) s). As Fig. 3.4 demonstrates, this was achieved by storing UCN in a 'bath-tub' formed by permanent magnets at room temperature, with the vertical confinement caused by gravity

[2]The concept of material and magnetic UCN storage is discussed in Ch. 3.2.1.

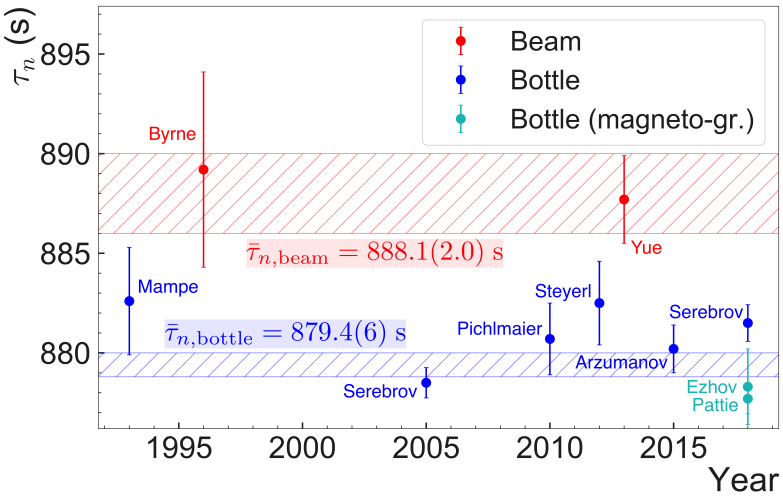

Figure 3.3: Most recent selected measurements of the neutron lifetime, τ_n. Taking the recent measurements into account, a deviation of $\sim 4.1\sigma$ is identified between the beam-type average ($\bar{\tau}_{n,\mathrm{beam}} = 888.1(2.0)$ s, red shaded area) and bottle-type mean ($\bar{\tau}_{n,\mathrm{bottle}} = 879.4(6)$ s, blue shaded area). Recent bottle-type measurements by Ezhov [EAB+18] and Pattie [PCCW+18] use a magneto-gravitational trap (cyan data points), while the blue data points indicate material bottle experiments. Both have been combined to give the bottle-type average, which has been scaled by a factor 1.5 according to PDG recommendations [THH+18, CMS18]. Data extracted from [MBM+93, BDH+96, SVK+05, PVS+10, SPK+12, YDG+13, ABC+15, EAB+18, SKF+18, PCCW+18].

(magneto-gravitational storage, cf. Ch. 3.2.1 for an overview on UCN storage methods). The UCN were detected by a 'dagger' moving from the top into the storage volume. Depolarisation losses due to zero points in the superimposed magnetic field have been estimated to have a $\Delta\tau_n = 0.07$ s contribution [Sau19], which is significantly less than uncertainties invoked by wall losses in material bottle-type experiments. In the same year, Ezhov [EAB+18] also measured τ_n magneto-gravitationally at ILL ($\tau_n = 878.3(1.9)$ s).

The 'neutron lifetime puzzle'

Taking recent τ_n measurements from the 1990s until today into account, Fig. 3.3 depicts a 4.1σ deviation between beam-type ($\bar{\tau}_{n,\mathrm{beam}} = 888.1(2.0)$ s) and bottle-type averages ($\bar{\tau}_{n,\mathrm{bottle}} = 879.4(6)$ s). Due to the conflicting τ_n values, the overall matter is often described as the 'neutron lifetime puzzle' [Pau09, Mum18, Ber19a] (resulting implications for BSM physics have been discussed in Ch. 2.2.3.3).

The reason for the 4.1σ deviation could not be found to date and has been debated thoroughly. Recently, it was postulated that the deviation stems from neutrons decaying into dark matter[3] [FG18]. The decay of the neutron into not yet discovered decay channels could explain the smaller neutron lifetime inferred from bottle-type experiments, $\tau_{\mathrm{n,\ bottle}}$, in comparison to $\tau_{\mathrm{n,\ beam}}$ determined from beam-type experiments. In beam-type experiments, the lifetime τ_β of ordinary neutron decay ($n \to p + e^- + \overline{\nu}_e$), is directly inferred from the

[3] Using the updated analysis in [CMS19], the associated branching ratio has been reduced from $\mathrm{BR_{n,\ exotic}} < 0.27\,\%$ to $< 0.16\,\%$.

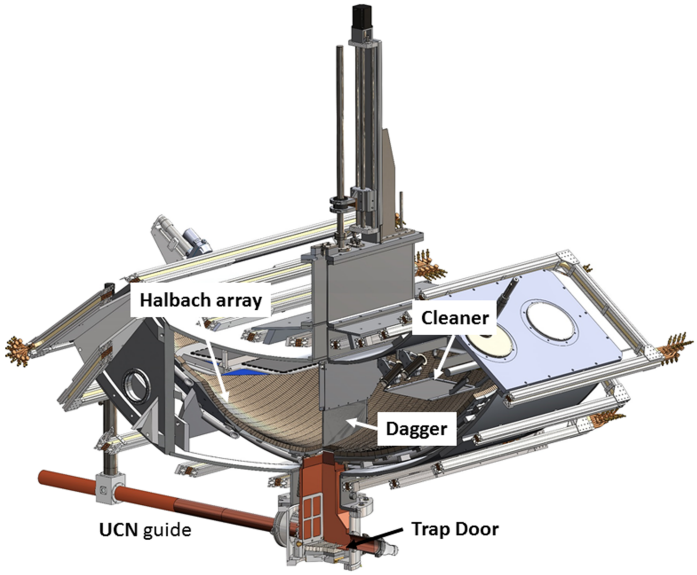

Figure 3.4: Setup of the magnetic storage in the UCNτ experiment. Following the UCN guide, the UCN pass the trap door to enter the magnetic storage volume formed by a NdFeB Halbach array configuration located in the lower half. In vertical direction, the UCN are confined by gravity (magneto-gravitational storage). After storage, they are counted by a dagger gradually moving downwards. Figure taken from [MAB+17].

rate of the electron/proton emission from the decay volume [Byr11],

$$\frac{dN_c(t)}{dt} = \frac{-N_n(t)}{\tau_\beta} \,, \tag{3.5}$$

while possible dark decays remain undetected. Therefore, the decay rate inferred from beam-type experiments equals the true partial β-decay rate,

$$1/\tau_{\mathrm{n,\ beam}} = 1/\tau_\beta \,. \tag{3.6}$$

In bottle-type experiments, the UCN trapped in the storage volume for storage time t_s could decay via both allowed and exotic channels, since

$$C_\mathrm{UCN}(t_\mathrm{s}) = C_\mathrm{UCN}(t_\mathrm{s}=0)\exp\left(-t_\mathrm{s}/\tau_{\mathrm{n,\ bottle}}\right) \,, \tag{3.7}$$

with

$$\frac{1}{\tau_{\mathrm{n,\ bottle}}} = \frac{1}{\tau_\beta} + \frac{1}{\tau_X} \tag{3.8}$$

also involving the partial decay rate into unknown channels X. Thus, the experimental observation of $\tau_{\mathrm{n,\ bottle}} < \tau_{\mathrm{n,\ beam}}$ could be explained by additional decay channels.

The postulated decay into dark matter could be ruled out by re-analysing PERKEO II data [KJM+19]. Another theoretical assumption is the oscillation between neutrons and mirror neutrons, which would cause the neutrons to disappear [Ber19a]. This claim was also declared as unlikely by citing experimental constraints [DSM+19].

3.1.2 Upcoming neutron lifetime data and new experiments

The beam-type BL2 experiment is currently taking data aiming at an accuracy of $\Delta\tau_n = 1\,\mathrm{s}$ and will soon be succeeded by the BL3 experiment with a 50 times larger trapping volume [Sau19]. In 2020, the bottle-type experiment UCNτ is expected to reduce the overall uncertainty to $\Delta\tau_n = 0.4\,\mathrm{s}$. Also, the Ezhov experiment is presently being upgraded to reach smaller uncertainties [Sau19].

The main criticism on the beam-type experiments is its lack in experimental variation (essentially performed by one group). This is about to change with the new experiments at J-PARC (Japan [NHI+17]) and UCN ProBe and Los Alamos National Laboratory (LANL, USA [Sau19]). The latter will be the first beam-type experiment to use a UCN beam instead of a cold neutron beam and therefore offers a completely new way to determine $\bar{\tau}_{n,\mathrm{beam}}$ [Sau19].

Several new magnetic bottle-type experiments are underway. The new magnetic bottle-type experiment HOPE at ILL [Zim14] has finished commissioning and has already taken first data with $\Delta\tau_n \sim 40\,\mathrm{s}$ [Sau19]. The Tau2 experiment at LANL is currently designed as an upgraded UCNτ version with superconducting coils replacing the permanent magnet array to achieve a higher maximum UCN storage energy [Sau19].

3.2 Ultracold neutrons - A tool for measuring the neutron lifetime

This chapter discusses the neutron interaction types which can be used for UCN storage (cf. Ch. 3.2.1) and motivates the requirement of high UCN densities for magnetic neutron lifetime experiments (cf. Ch. 3.2.2). In Ch. 3.2.3, the reader is concisely introduced to UCN production.

3.2.1 Interactions of ultracold neutrons

In general, UCN are defined as storable neutrons [GRL91]. As Fig. 3.5 shows, UCN are at the lowest end of the neutron energy spectrum, with typical energies $\lesssim 350\,\mathrm{neV}$. The exceptionally low energy of UCN allows for their storage and thus long observation times, which apart from measuring the neutron lifetime can be used to *e.g.* search for an electric dipole moment of the neutron [AAA+20]. To demonstrate the low energy, the temperature, velocity and the de Broglie wavelength of an UCN with an energy of $E_{\mathrm{UCN}} = 100\,\mathrm{neV}$ has been calculated in Tab. 3.1.

Table 3.1: Temperature, velocity, and de Broglie wavelength of a UCN with energy $E_{\mathrm{UCN}} = 100\,\mathrm{neV}$. The used constants are the Boltzmann constant ($k_{\mathrm{b}} = 1.380\,649 \times 10^{-23}\,\mathrm{J\,K^{-1}}$ [THH+18]), the neutron mass ($m_{\mathrm{n}} = 1.67492749804(95) \times 10^{-27}\mathrm{kg}$ [cod19a]), and the Planck constant ($h = 6.626\,070\,15 \times 10^{-34}\,\mathrm{J\,s}$ [THH+18]).

Property	Value
Energy	$E_{\mathrm{UCN}} = 100.00\,\mathrm{neV}$
Temperature	$T = E_{\mathrm{UCN}}/k_{\mathrm{B}} = 1.16\,\mathrm{mK}$
Velocity	$v = \sqrt{(2E_{\mathrm{UCN}})/m_{\mathrm{n}}} = 4.37\,\mathrm{m\,s^{-1}}$
De Broglie wavelength	$\lambda = \sqrt{h^2/(2m_{\mathrm{n}}E_{\mathrm{UCN}})} = 90.45\,\mathrm{nm}$

Since neutrons are sensitive to the weak, strong, magnetic and the gravitational interaction, four interaction types result, which are shortly summarised based on [GRL91] and graphically depicted in Fig. 3.5.

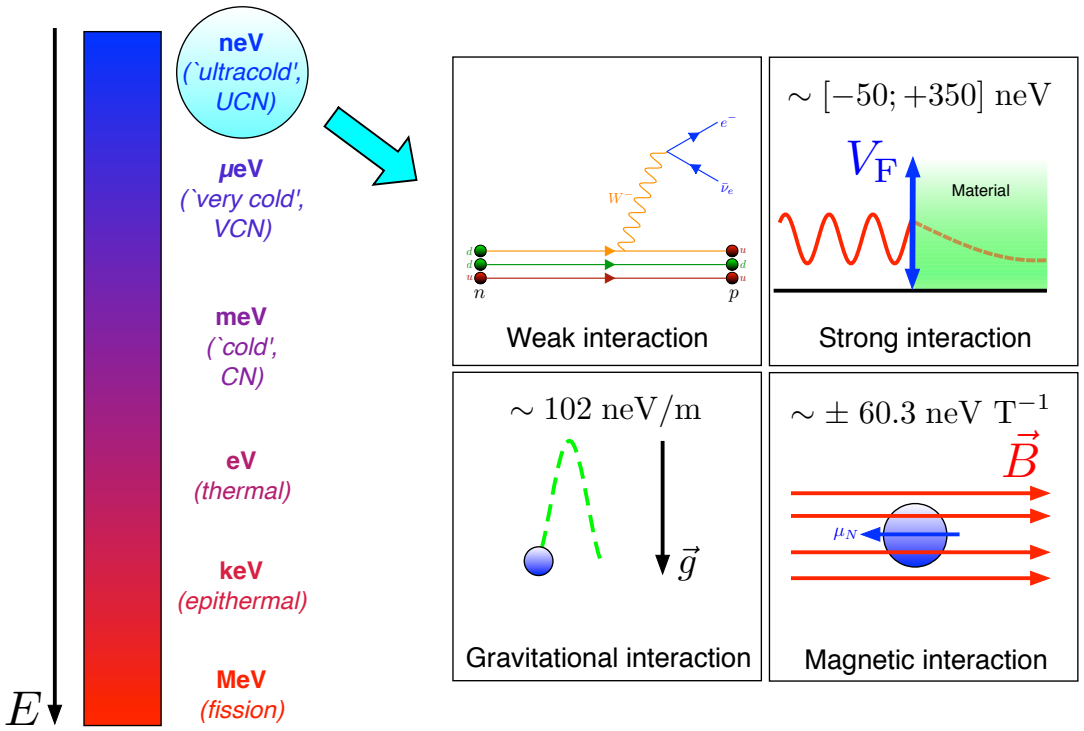

Figure 3.5: Energy scale of neutrons and overview over interactions. Neutrons can interact according to all given interaction types. The low UCN energy of $\lesssim 350\,\mathrm{neV}$ allows for using the strong, the gravitational, and the magnetic interaction for UCN manipulation and confinement. Details on the mentioned Fermi potential, V_F, the gravitational constant, $\vec{g}$, and the neutron magnetic moment, $\vec{\mu}_n$, are given in the following.

Weak and strong interaction

As discussed in Ch. 2.1, free neutrons decay by the weak interaction according to $n \rightarrow p + e^- + \overline{\nu}_e$ with a lifetime of $\tau_n \sim 15\,\mathrm{min}$.

The strong interaction is highly dependent on the neutron energy. If UCN impinge on matter (viewed as a collection of atomic nuclei), they experience an effective potential - just like the interaction of a material wave with a quantum mechanical potential well. This potential is the so-called effective Fermi potential [GRL91][4]

$$V_\mathrm{F} = \frac{2\pi\hbar^2}{m_n} N a \,, \tag{3.9}$$

which is proportional to the material's number density, N, and the coherent scattering length a of the material nuclei. UCN with energies $E_\mathrm{UCN} < V_\mathrm{F}$ are fully reflected. Typical values of V_F range up to 335 neV in case of nickel-58 [GRL91], further examples are given in Table A.1. In UCN experiments, V_F is typically used to confine UCN in material storage bottles and to guide UCN to the experiment using beam lines made of *e.g.* stainless steel or fused silica.

[4] For a detailed derivation, refer to [GRL91].

Magnetic interaction

Since neutrons exhibit a magnetic moment $\vec{\mu}_n$[5], the interaction potential with an external magnetic field $\vec{B}(\vec{r})$ can be written as [GRL91]

$$V_{\text{magn}} = -\vec{\mu}_n \cdot \vec{B}(\vec{r}) \sim \pm 60.3\,\text{neV}\,\text{T}^{-1} \cdot \left|\vec{B}\,(\vec{r})\right| \ . \tag{3.10}$$

Since the neutron's g-factor is negative, the neutron spin $\vec{S}_n$ is antiparallel to $\vec{\mu}_n$. For neutrons with $\vec{\mu}_n \parallel \vec{B}(\vec{r})$ ($\vec{S}_n \nparallel \vec{B}(\vec{r})$), the potential minimum lies in the magnetic field maximum ('high-field seekers', HFS [SKL+17]). If $\vec{\mu}_n \nparallel \vec{B}(\vec{r})$ and $\vec{S}_n \parallel \vec{B}(\vec{r})$, neutrons are termed 'low-field seekers' (LFS), since the magnetic field minimum corresponds to their potential minimum.

In case of a magnetic field gradient, $\vec{\nabla}\left|\vec{B}(\vec{r})\right|$, a Stern-Gerlach force $\vec{F}_{\text{SG}}$ [GS22] acts on the UCN,

$$\vec{F}_{\text{SG}} = -\vec{\nabla} V_{\text{magn}} = \pm\,|\vec{\mu}_n|\ \vec{\nabla}\left|\vec{B}(\vec{r})\right| \ . \tag{3.11}$$

Since $\vec{F}_{\text{SG}}$ is repulsive for UCN spin-prepared to the LFS state, it can be used for UCN storage in a magnetic field. Following Eq. (3.10), a magnetic field of 1 T allows for storing UCN up to an energy of 60.3 neV. During storage, the UCN must remain in the LFS state, which implies that a 'spin flip' to the HFS state must be prevented by ensuring adiabatic conditions. If adiabatic conditions are met, the direction of $\vec{S}_n$ relative to $\vec{B}(\vec{r})$ does not change while the UCN moves within the magnetic field. Furthermore, since $\vec{S}_n$ is always relative to $\vec{B}(\vec{r})$, $\left|\vec{B}(\vec{r})\right| \neq 0$ must be valid in the entire storage volume.

Further details on the spin flip are provided in Ch. 5.3.2. The usage of magnetic fields for the UCN storage in the neutron lifetime experiment τSPECT is detailed in Ch. 4.1 (prototype measurement without full-magnetic storage) and Ch. 5.1.2 (full-magnetic storage).

Gravitational interaction

The gravitational potential of a neutron is given by [GRL91]

$$V_{\text{grav}} = m_n g h \sim 102\,\text{neV}\,\text{m}^{-1} \cdot h_{\text{m}} \ , \tag{3.12}$$

with neutron mass m_n, gravitational constant g and height h (h_{m} gives the height in m). Consequently, if a UCN moves away from V_{grav} by $h = 1$ m, it loses 102 neV of energy. This principle is used to slow down UCN by guiding them from their production location to the storage volume through an elevated beam line ($h \gtrsim 1.4$ m, cf. Ch. 4.2.3). Since in the UCN energy range, the UCN density ϱ_{UCN} increases with the squared UCN velocity (v^2 [GRL91]), higher ϱ_{UCN} values are reached by decelerating the UCN prior to storage. The gravitational interaction is also used by magneto-gravitational storage experiments such as the UCNτ experiment in order to store UCN in vertical direction (cf. Fig. 3.4).

3.2.2 Motivation for high densities of ultracold neutrons for magnetic neutron lifetime experiments

From the short review on bottle-type lifetime experiments in Ch. 3.1.1, it becomes clear that determining τ_n with higher precision requires magnetic storage. The main advantage of magnetic storage compared to material storage is the presence of less systematic losses

[5] The value for $\mu_n = (e\hbar)\,/\,(2m_p)$ is $2.792\,847\,344\,6(8)\mu_N$, with Bohr magneton μ_N [THH+18].

due to the absence of wall interactions. Therefore, assuming ideal conditions, Eq. (3.4) can be simplified ($\tau_{\text{inelastic}} \to 0$, $\tau_{\text{capture}} \to 0$):

$$\frac{1}{\tau} = \frac{1}{\tau_n} + \frac{1}{\tau_{\text{other}}} \,. \tag{3.13}$$

Wall interactions are currently the main systematic effect of material storage experiments and will not allow for measuring τ_n with significantly better precision than $\Delta\tau_n \sim 1\,\%$ [SKF+18]. The main systematic loss in magnetic storage is the depolarisation of UCN. The depolarisation occurs whenever a stored UCN in low-field seeking (LFS) spin state is converted to the non-storable high-field seeking (HFS) state by reaching a zero point within the superimposed magnetic field (cf. Ch. 3.2.1). To estimate the impact on τ_n, the effect requires a precise measurement of the magnetic field map[6]. Besides its lower effect on the uncertainty of τ_n, another advantage of depolarisation effects is the ability of their detection[7], which is not possible in case of wall interaction losses.

A major drawback of current magnetic storage experiments, however, is the maximum storable UCN energy of $\lesssim 60\,\text{neV}$, which results from typical maximum magnetic fields of $\sim 1\,\text{T}$ [PCCW+18]. In the material bottle-type experiment with the currently highest precision, UCN with energies up to 106.5 neV are stored due to the Fermi potential of the Fomblin grease, $V_{\text{F}} = 106.5\,\text{neV}$ [Ste01]. Also beneficial for the UCN counting statistics is the much higher storage volume of material bottle-type experiments. The magnetic neutron lifetime experiment PENELOPE will exhibit the largest volume of $V \sim 0.7\,\text{m}^3$ after construction [MPA+09], which is more than a factor of 2 less than in case of the latest material bottle-type Gravitrap experiment ($V \sim 1.5\,\text{m}^3$ [SKF+18]).

Both the lower storage depth and the lower storage volume are a huge challenge for the UCN source development. Thus, neutron lifetime experiments based on magnetic storage call for even more powerful UCN sources, which has resulted in the upgrade of the Mainz UCN D source to run the full-magnetic τSPECT experiment (cf. Ch. 4.2).

3.2.3 Ultracold neutron production and the superthermal principle

Ultracold neutrons are produced by moderating neutrons from nuclear research reactors or spallation sources. Convential UCN production is based on the thermalisation of the UCN with the surrounding material. A method to increase the UCN density significantly is the superthermal principle. The basic concepts are presented in the following.

Thermalisation-based UCN production

For UCN production, a moderator downshifts the energies of incoming thermal neutrons. Assuming no absorption mechanisms and an infinite moderator volume, the moderated neutrons can be discribed by a Maxwellian spectrum after having reached thermal equilibrium with the moderator material. Thus, the following UCN density distribution is attained

[6] In the UCNτ experiment, which uses a permanent magnet array, depolarisation effects account for $\Delta\tau_n = 0.07\,\text{s}$ [Sau19].

[7] Monitoring of depolarisation effects, *i.e.,* the detection of non-storable UCN in HFS spin state, is possible by placing a detector behind a magnetic shutter. The magnetic shutter is transparent to UCN in HFS state, which are thus counted. The technique was pioneered by Ezhov [Ezh19]. For the τSPECT experiment, LFS converted to HFS could be detected by placing scintillators behind the magnetic wall in a future upgrade.

[GRL91],

$$\varrho(v)\, dv = \frac{2\Phi_0 v^2}{\alpha^3} \exp\left(\frac{-v^2}{\alpha^2}\right) \frac{dv}{\alpha} \,, \tag{3.14}$$

with the UCN density ϱ, the thermal neutron flux Φ_0, the UCN velocity v, and the factor $\alpha = \sqrt{2k_\mathrm{B}T/m}$ (with moderator temperature T). To find the maximum density of storable UCN (ϱ_UCN) in a material with Fermi potential V_F, such that $E_\mathrm{UCN} \leq V_\mathrm{F}$, Eq. (3.14) is integrated while neglecting v compared to α ($v \ll \alpha$) [GRL91],

$$\varrho_\mathrm{UCN} = \int_0^{V_\mathrm{F}} dv\ \varrho(v) = \frac{2}{3}\frac{\Phi_0}{\alpha}\left(\frac{V_\mathrm{F}}{k_\mathrm{B}T}\right)^{\frac{3}{2}} \,. \tag{3.15}$$

According to Golub, cooling the moderator to $T \sim 20\,\mathrm{K}$ would yield a maximum UCN density of $\varrho_{\mathrm{UCN,\,max}} = 2000\,\mathrm{cm}^{-3}$ storable in a Fermi potential of $V_\mathrm{F} = 250\,\mathrm{neV}$ at a powerful high-flux reactor providing a thermal flux $\Phi_0 = \mathcal{O}(10^{-15}\ \mathrm{n\ cm^{-2}s^{-1}})$ [GRL91]. For comparison, the world's highest continuous thermal flux of $\Phi_0 = 1.65 \times 10^{-15}\ \mathrm{n\ cm^{-2}s^{-1}}$ is reached at the Institut Laue-Langevin (ILL, [RFG+00]).

Golub [GRL91] gives several reasons for observing significantly lower UCN densities in experimental setups. Besides the UCN not reaching the moderator temperature due to absorption processes, low extraction efficiencies of UCN from the moderator to the experiment are severely limiting [GRL91]. Returning to the example of the maximum attainable UCN density of $\varrho_{\mathrm{UCN,\,max}} = 2000\,\mathrm{cm}^{-3}$, it has to be noted that $\varrho_{\mathrm{UCN,\,max}}$ only refers to the UCN stored in the moderator material with potential V_F. In order to use the UCN, they need to be extracted from the moderator material. In case of the PF2 source at ILL, neutrons of the VCN energy range ($v \sim 60\,\mathrm{m\,s}^{-1}$) are extracted from a deuterium (D_2) source and subsequently downscattered to the UCN energy range by colliding with a rotating turbine [SNS+86].

In general, the output of all 'conventional' UCN sources is limited by Liouville's theorem. The theorem states states that for conservative forces, the phase space density needs to be conserved at all times[8]. For UCN production, this implies that the maximum extractable UCN density equals the UCN density produced in the moderator. Despite the experimental technique employed at the PF2 source, only UCN densities of $\rho_\mathrm{UCN} \sim 20\,\mathrm{cm}^{-3}$ (stored in a stainless steel bottle with Fermi potential of $V_\mathrm{F} \sim 190\,\mathrm{neV}$ and volume of $V \sim 32\,\mathrm{l}$) are usable for performing experiments [BDK+17].

The superthermal principle

To overcome the limitations of Liouville's theorem, UCN sources based on the 'superthermal principle' [GP75, GP79, GRL91] were proposed. The main idea is to not let the UCN become in thermal equlibrium with the moderator. Thus, downscattering processes occur to decrease the neutron energy, while the rivaling upscattering rate becomes negligible [GRL91]. For an effective downscattering, neutrons hit the crystal lattice of condensed matter while causing a phonon excitation upon collision[9]. Before reaching thermal equlibrium with the moderator material, the UCN are extracted, whereby a higher UCN density than given by the Maxwell-Boltzmann distribution is attainable. Rivaling upscattering processes can be suppressed by keeping the moderator at low temperatures.

[8] For an overview on Liouville's theorem with classical mechanics in mind, refer to [Hen19].

[9] Consider [GRL91] and [Gol95] for a detailed discussion of the superthermal principle.

Superthermal UCN sources can use superfluid helium-4 (^{4}He) as a moderator, which needs to be kept at low temperatures of 0.5 K to strongly suppress upscattering [FSA$^+$07]. As a main advantage, the nuclear absorption in ^{4}He is negligible [BDK$^+$17]. Thus, the accumulation of UCN in the moderator material is predominantly limited by the neutron lifetime, τ_n. A first ^{4}He-based superthermal source was realised in 1978 [AMG$^+$78]). Current superthermal sources using ^{4}He moderators are in operation at ILL (SUN-2 [LIP$^+$16]) and at TRIUMF in Canada [AAA$^+$19].

Additionally, solid deuterium (sD_2) at liquid helium temperature ($T = 4.2\,\mathrm{K}$) can be used as the moderator material of a superthermal UCN source. Compared to ^{4}He, sD_2 offers a $\sim$ 30 times higher UCN production rate [GB83]. A major drawback is the presence of nuclear absorption in sD_2, which dominates UCN upscattering at $T < 5\,\mathrm{K}$ [YMG86, LYL00]. Due to the nuclear absorption processes, the UCN lifetime in sD_2 is $\tau_{D_2} \sim 70\,\mathrm{ms}$ [YMG86]. Since the short τ_{D_2} value does not permit an effective accumulation of UCN inside the moderator material, the UCN are quickly extracted. Examples for currently operational superthermal UCN sources with sD_2 converters are the UCN source at Paul-Scherrer-Institut (PSI, [Lau14]), the source at Los Alamos National Laboratory (LANL, [IAC$^+$18]), and the Mainz UCN D source [KRR$^+$17].

Despite notable advances over the recent years, the performance of superthermal UCN sources is still not considerably better compared to the 'conventional' PF2 UCN source. In recent comparison measurements, a UCN density of $\varrho_{\mathrm{UCN}} \sim 22\,\mathrm{cm}^{-3}$ was stored in a stainless steel storage bottle of $\sim 32\,\mathrm{l}$ volume at the sD_2-based PSI source. Using the same storage setup at the PF2 UCN source, a density of $\varrho_{\mathrm{UCN}} \sim 20\,\mathrm{cm}^{-3}$ was reached[10] [BDK$^+$17].

[10] An overview over the comparison measurements is provided in Ch. A.2.

4 Preparatory studies and developments at the research reactor TRIGA Mainz

Several preparatory studies leading to the setup of the τSPECT experiment have been performed, which are presented in this chapter. First, the results of the 2015 prototype measurement are reviewed to identify challenges for the implementation of full-magnetic storage (cf. Ch. 4.1).

An upgrade of the pulsed superthermal UCN D source at the research reactor TRIGA in Mainz has been completed to increase the number of storable UCN (cf. Ch. 4.2). Along with detailed measurements on the source performance, fluctuations of the UCN output have been identified. These fluctuations require normalisation methods, which have been experimentally investigated (cf. Ch. 4.3). Apart from optimising the UCN transport from the source to the experiment, measurements have been performed to emulate the full-magnetic storage conditions in τSPECT (cf. Ch. 4.4). Based on these measurements, the required measurement time to reach an accuracy of $\Delta\tau_n \lesssim 1\,\mathrm{s}$ has been calculated.

4.1 Prototype measurement with longitudinal magnetic storage

The τSPECT experiment represents a novel bottle-type neutron lifetime experiment, since it offers full-magnetic storage at a pulsed UCN source. After the successful completion of the aSPECT experiment [BGB$^+$19], the cryostat with superconducting coils[1] generating a strong longitudinal magnetic field over a distance of $\sim 3.5\,\mathrm{m}$ became available[2]. For τSPECT, it was decided to reuse the aSPECT cryostat with its characteristic double-hump structured longitudinal magnetic field configuration [GBB$^+$05, KGB$^+$14].

The prototype measurement, which had been performed by J. Karch in July 2015, successfully demonstrated the UCN storage using the cryostat's superconducting coils at current $I_{\mathrm{main}} = 56.7\,\mathrm{A}$ to generate the magnetic field in longitudinal direction ($\vec{B}$) and a fused silica tube for material confinement in radial direction [Kar17]. Fig. 4.1 shows the measurement setup, which is used to explain the measurement sequence in the following.

[1] The cryostat was manufactured by Cryogenics Ltd. (`http://www.cryogenic.co.uk`), for further details refer to [BGB$^+$08].

[2] In the following, the aSPECT coordinate system is used, which defines $z = 0\,\mathrm{mm}$ at the centre of the former cold neutron decay volume.

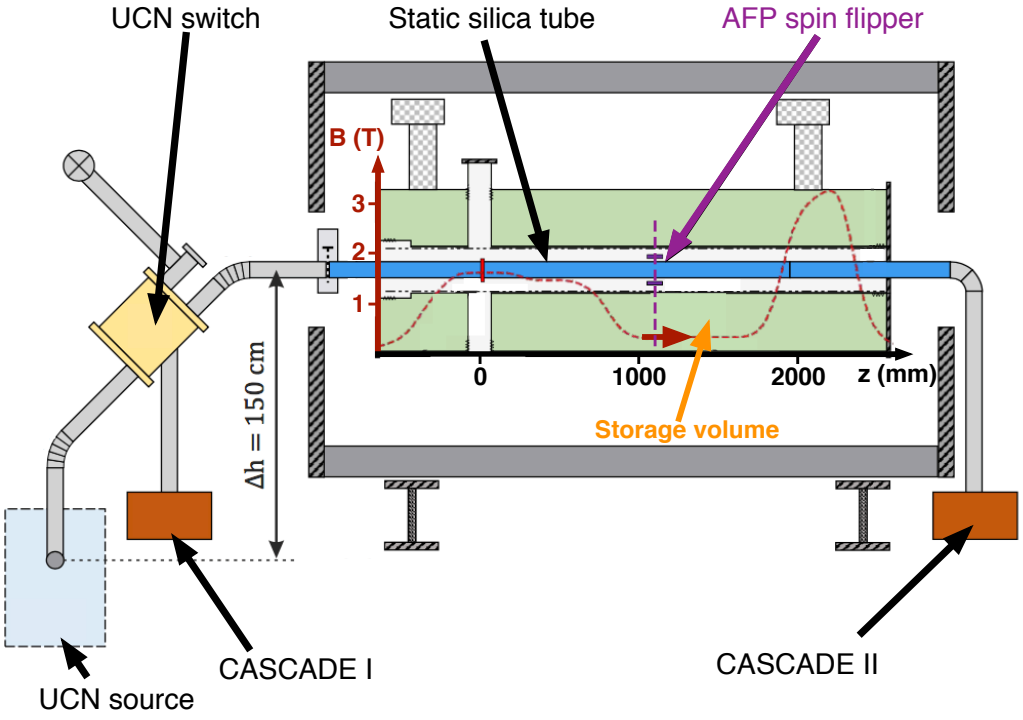

Figure 4.1: Setup used for the prototype measurement with longitudinal magnetic storage in July 2015. The UCN are guided from the UCN source to the storage volume inside the former *a*SPECT cryostat (green). The storage volume is formed by the magnetic flux density maxima in longitudinal direction (absolute magnetic flux density B given by red dashed line, field direction given by horizontal red arrow) and a fused silica tube (blue) in radial direction. The higher-energetic UCN spin component, *i.e.,* the high-field seekers (HFS, spin $\vec{S}_{\mathrm{UCN}}$ indicated by arrow), is able to pass the first maximum at $z \sim [-500, 950]$ mm. Using an adiabatic fast passage (AFP) spin flipper at $z \sim 1140$ mm (purple), the transmitted UCN are spin-flipped into their magnetically storable lower-energetic low-field seeker (LFS) spin state (details on the LFS/HFS transmission are provided in Fig. 4.2). After storage, the UCN are backextracted by activating the spin flipper again. After guidance to a commercial CASCADE detector (CASCADE I) by a UCN switch, they are counted. The second detector (CASCADE II) was used for evaluating the spin flip performance. For details, refer to the text. Figure adapted from [Kar17].

After being produced in the UCN source, the unpolarised UCN were guided to the entrance of the cryostat by a stainless steel beam line. Depending on their spin orientation $\vec{S}_{\mathrm{UCN}}$ relative to the magnetic field lines[3] ($\vec{B}$), the UCN have a 50 % probability to either belong to the 'high-field seeker' (HFS, energy $+60.3\,\mathrm{neV\,T^{-1}} \cdot B$ if $\vec{S}_{\mathrm{UCN}} \nparallel \vec{B}$) or the lower-energetic 'low-field seeker' spin state (LFS, energy $-60.3\,\mathrm{neV\,T^{-1}} \cdot B$ if $\vec{S}_{\mathrm{UCN}} \parallel \vec{B}$). As Fig. 4.2 depicts, the first magnetic flux density maximum at $z \in [-500, 950]$ mm is a po-

[3]The UCN interaction with magnetic fields due to the UCN magnetic moment μ_n is decribed in Ch. 3.2.1.

tential barrier for the LFS, which leads to the LFS with energies $< 60.3\,\text{neV}\,\text{T}^{-1} \cdot 1.7\,\text{T} = 102.5\,\text{neV}$ being reflected. HFS, on the other hand, are accelerated towards the magnetic flux density maximum, since it implies a potential minimum.

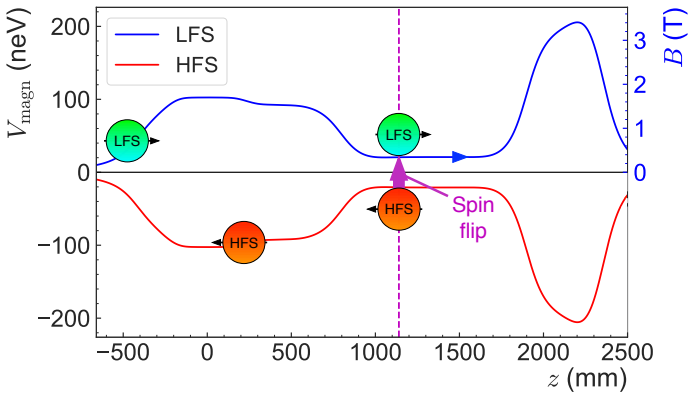

Figure 4.2: Magnetic field potential V_{magn} for UCN in low-field seeking (LFS, blue line) and high-field seeking spin state (HFS, red line) as a function of z-position. The right axis is valid for the blue line and gives the absolute magnetic flux density B applied during the prototype measurement. While LFS entering from the left side with $E_{\text{UCN}} \lesssim 102.5\,\text{neV}$ are reflected by the first magnetic field bump, HFS are accelerated towards it. The reason for this observation can be seen in V_{magn}. For LFS, the first magnetic field bump is a local potential maximum, whereas it constitutes a potential minimum for the HFS. At $z \sim 1140\,\text{mm}$ (indicated by the dashed vertical line), the transmitted HFS are spin-flipped to the LFS spin state and become thus longitudinally storable in the region between the two potential maxima ($z \sim [550, 1880]$ mm).

Thus, all HFS as well as LFS with $E_{\text{UCN}} > 102.5\,\text{neV}$ could reach the storage volume region ($z \sim [550, 1880]$ mm) after being guided by a fused silica (SiO_2) tube. To prevent the HFS from escaping the storage volume in longitudinal direction due to the acceleration towards the second magnetic flux density maximum at $z \gtrsim 1700\,\text{mm}$, they were spin-flipped to the LFS spin state using an adiabatic fast passage (AFP) spin flipper[4] at $z \sim 1140\,\text{mm}$ with added correction coils decreasing the longitudinal gradient[5] to $\nabla_z B \sim 1\,\text{G}\,\text{cm}^{-1}$. Although having passed the potential barrier formed by the first magnetic field bump, LFS with $E_{\text{UCN}} > 102.5\,\text{neV}$ are spin-flipped to the HFS spin state and thus escape the storage volume.

Stored are HFS which - considering their reference frame - are guided through the first magnetic potential minimum (cf. red line in Fig. 4.2) and are spin-flipped to LFS at the position of the spin flipper. Just before reaching the longitudinal magnetic field, incoming HFS have a potential energy of $E_{\text{pot}} = 0\,\text{neV}$. Resulting from the HFS interacting with the magnetic field ($B_{\text{sf}} = 0.342\,\text{T}$), a potential energy of $E_{\text{pot, mag}} = 60.3\,\text{neV}\,\text{T}^{-1} \cdot B_{\text{sf}} = -20.6\,\text{neV}$ results at the spin flip position. Since the energy is conserved, which implies

[4]The spin flipper parameters had been previously optimised by analysing the number of UCN reaching the second CASCADE detector (CASCADE II, cf. Fig. 4.1). The more non-converted HFS able to pass the second magnetic flux density maximum are detected in CASCADE II, the lower the spin flip efficiency. For more details on the CASCADE detector, refer to Ch. A.1.

[5]The spin flip efficiency ε_{AFP} improves with lower gradients in the spin flip region. For a longitudinal gradient of $0.6\,\text{G}\,\text{cm}^{-1}$, an efficiency of $\varepsilon_{\text{AFP}} = 99.9\,\%$ was reached in the UCNA experiment [HBD+12]. More details on the adiabatic fast passage spin flip are given Ch. 5.3.2.

$E_{\text{total}} = E_{\text{kin}} + E_{\text{pot, mag}}$, the HFS also have a kinetic energy of 20.6 neV. After conversion to a LFS due to the spin flip, the potential energy changes sign and is now given by $E_{\text{pot, mag}} = 20.6\,\text{neV}$, along with $E_{\text{kin}} = 20.6\,\text{neV}$.

Within the storage volume, energy conservation also holds. It shall now be considered up to which initial maximum kinetic energy $E_{\text{kin, max}}$, *i.e.,* the maximum kinetic energy before reaching the longitudinal magnetic field, UCN can be stored. Before reaching the first magnetic bump, the total energy equals $E_{\text{kin, max}}$. After the spin flip, the following condition holds, with the Fermi potential of the SiO_2 tube ($V_{\text{F, SiO}_2} = 90\,\text{neV}$, cf. Tab. A.1) determining the maximum potential energy in the trap:

$$E_{\text{total}} = \underbrace{E_{\text{pot, mag}}}_{=20.6\,\text{neV}} \underbrace{+E'_{\text{kin, max}}}_{=E_{\text{kin, max}}+20.6\,\text{neV}} = \underbrace{V_{\text{F, SiO}_2}}_{=90\,\text{neV}} . \tag{4.1}$$

Thus, the maximally storable kinetic energy is given by

$$E_{\text{kin, max}} = 90\,\text{neV} - 2 \cdot 20.6\,\text{neV} = 48.8\,\text{neV} := \Delta E_{\text{prototype}} \tag{4.2}$$

in a resulting effective storage volume of $V_{\text{prototype}} \sim 3.5\,\text{l}$. The value $\Delta E_{\text{prototype}} = 48.8\,\text{neV}$ implies that during the prototype measurements, τSPECT accepted UCN with energies in the range of $[0, 48.8]$neV for storage.

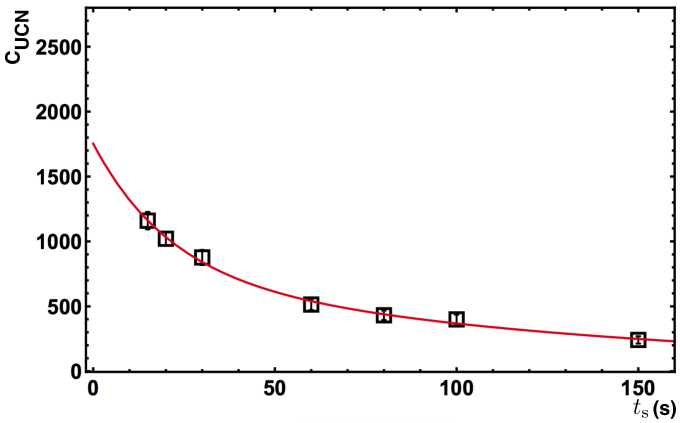

Figure 4.3: Storage curve measured in the prototype measurement using a fused silica tube for radial confinement. The number of detected UCN C_{UCN} is plotted against the storage time, t_{s}. In total, $\sim$ 1750 UCN were contained in the storage volume at $t_{\text{s}} = 0\,\text{s}$, with the decay constant $\tau = 134(57)\,\text{s}$ inferred from the exponential fit (red curve). Figure adapted from [Kar17].

After storing the UCN for variable storage times in the range $t_{\text{s}} = [15, 150]$ s, they were back-extracted in direction of the CASCADE I neutron detector by re-enabling the AFP spin flipper and activating the UCN switch[6].

The resulting storage curve, which is obtained from plotting the number of detected UCN C_{UCN} against storage time, is depicted in Fig. 4.3. In total, $\sim$ 1750 UCN were detected after interpolation to $t_{\text{s}} = 0\,\text{s}$. The decay constant extracted from the exponential fit was

[6] The activation of the UCN switch causes the back-extracted UCN to be guided onto the detector instead of returning to the source.

$\tau = 134(57)\,\mathrm{s}$ [Kar17]. A conservative estimate in [Kar17] approximates the measurement time $t_{\mathrm{meas,\ estimate}}$ needed to reach the desired accuracy of τSPECT for phase 1, *i.e.,* $\Delta\tau_n = 1\,\mathrm{s}$. To reach this accuracy, $t_{\mathrm{meas,\ estimate}}$ was calculated as

$$t_{\mathrm{meas,\ estimate}} = 630\,\mathrm{h}\ . \tag{4.3}$$

This would correspond to measuring for 42 days (with 15 h of data taking each day) to reach the desired accuracy of the neutron lifetime measurement for phase I, *i.e.,* $\Delta\tau_n = 1\,\mathrm{s}$.

Note that the prototype measurement has been performed using the UCN source at beamport D before its upgrade. To considerably increase the statistics for τSPECT, an upgrade of the UCN source at beamport D has been performed.

4.2 Upgrade of the superthermal ultracold neutron source at beamport D

For measuring the neutron lifetime with τSPECT and performing systematic checks, a UCN density as high as possible is required[7]. Thus, the UCN source at beamport D has been upgraded to achieve a 3.5 times higher UCN density, which has additionally led to a stable and reproducible source operation over measurement runs of several weeks. Since the UCN D source is a pulsed source, UCN are only produced shortly after the reactor pulse (thermal power peaking at $P_{\mathrm{th}} \sim 250\,\mathrm{MW}$ within pulse width of $\sim 30\,\mathrm{ms}$ [MTK75]) and are subsequently filled into the storage volume. After the pulse, the reactor is run in low-power mode ($P_{\mathrm{th}} = 50\,\mathrm{W}$), which leads to a low-background environment for the τ_n measurement regarding thermal neutrons and gamma radiation. The advantage of DC sources such as the PF2 source at ILL is a constant UCN flow at high-power reactor ($P_{\mathrm{th}} = 58\,\mathrm{MW}$ [RFG$^+$00]), which is however not required for neutron lifetime experiments based on UCN storage.

Details on the source are given in Ch. 4.2.1, with the upgrade steps discussed in Ch. 4.2.2. The resulting performance gains in comparison to the old source along with a discussion on the UCN yield stability are provided in Ch. 4.2.3. The upgrade steps and partial results on the performance found in these two sections were also published in November 2017 [KRR$^+$17].

4.2.1 Specifications of the UCN D source at TRIGA Mainz

The UCN source at radial beamport D (UCN D) of the research reactor TRIGA Mainz produces UCN according to the superthermal principle (cf. Ch. 3.2.3). It relies on solid deuterium (sD_2) as a converter material and currently uses a mixture of 95 % hydrogen (H_2) and 5 % D_2 for premoderation. The incoming neutrons are produced by the TRIGA reactor running in pulsed mode.

To be operated in pulse mode, the reactor is first run in steady state with low thermal power ($P_{\mathrm{th}} = 50\,\mathrm{W}$). Compressed air causes the pulse rod to be shot out of the reactor core after which the reactor remains critical for some milliseconds [MTK75]. At its maximum allowed criticality of 2 \$[8], the TRIGA Mainz produces ~ 5 pulses per hour[9] with

[7] For a detailed discussion on the statistics of τSPECT, refer to Ch. 4.4.

[8] The criticality β, given in \$ units, describes the ratio between produced and lost neutrons during fission. If $\beta > 1$, the system is critical, *i.e.,* the neutron production dominates over loss mechanisms - a chain reaction is induced.

[9] The decay time of fission products in the surrounding of the reactor core dictates the pulsed repetition rate. For pulses with lower criticality, an upper limit of 12 pulses per hour is officially prescribed by the authorities.

253.0(8.2) MW maximum thermal peak power and a pulse width of 29.4(4) ms [MTK75], resulting in a typical pulse energy of $9 - 10$ MW s. This translates into a typical thermal neutron flux of $\Phi_{\text{thermal}} \sim 4.5 \times 10^{11}$ n cm^{-2}s^{-1} at beamport D (measured at the moderator position in proximity to the reactor core [Kar17]).

The in-pile cryostat

As Fig. 4.4 demonstrates, the UCN D source is encapsulated in an in-pile aluminium cryostat of wall thickness 7.5 mm, which is inserted into the reactor's beamport D. The cryostat's front is in direct proximity to the reactor core, only separated by a graphite/bismuth stopper (cf. inset Fig. 4.4). The cryostat houses an advanced cooling system based on liquid helium (lHe) with temperature 4.2 K to allow for the freeze-out of solid hydrogen (sH_2, freeze-out at 13.96 K) and solid deuterium (sD_2, freeze-out at 18.73 K [Sou86]) from the gas phase. For reliable operation, a lHe buffer volume is included in the cryostat. Moreover, a Joule Thomson valve is used to accurately regulate the He flow. The UCN are produced inside the sD_2 crystal, which is frozen out at the very end of a stainless steel neutron guide with a total length of ~ 4.4 m and an inner diameter of $\varnothing_{\text{inner}} = 66$ mm. To reduce the heat flow from the neutron guide kept at room temperature to the sD_2 crystal, the neutron guide's wall thickness is reduced from 2 mm to 0.6 mm ('thermal bridge'). To provide clean vacuum conditions inside the neutron guide for sD_2 freeze-out, an AlMg3 separation foil with 100 μm thickness is included.

To vary the distance of the aluminium cryostat front to the graphite/bismuth stopper just before the reactor core, d_{core}, which allows for a variation of the thermal neutron flux Φ_{thermal}, the cryostat is mounted on a rail system (cf. Fig. 4.5). During the characterisation measurements of the upgraded UCN D source, the distance was decreased from $d_{\text{core, II}} \sim 30$ mm to $d_{\text{core, I}} \sim 0$ mm ($\sim 10\,\%$ gain in UCN yield proportional to the increased thermal fluence [KRR$^+$17]). The figure also depicts the thermal shield of the front part of the neutron guide[10]. Around the thermal bridge, a heating wire was installed which gives the opportunity for thermal conditioning of the sD_2 crystal, *i.e.,* to expose the sD_2 crystal to increased amounts of thermal energy.

Freeze-out of premoderator and converter

As the detailed view of the UCN D source front in Fig. 4.6 a) shows, ~ 620 cm^3 of solid hydrogen (sH_2) is first frozen out in the outer part of a double-walled cup. Inside the inner part, a typical lHe flow of ~ 8 l/h ensures appropriate temperature conditions. Using H_2 as premoderator optimises the UCN production rate in sD_2 by slowing down incoming neutrons in a way that the Maxwellian spectrum of the neutrons impinging on the sD_2 crystal is shifted towards the optimum temperature of ~ 30 K [YMG86]. This procedure is termed 'phonon matching', since neutrons impinging on the crystal lattice of the sD_2 crystal invoke a phonon excitation upon collision ('superthermal principle', cf. Ch. 3.2.3). As a primary effect, the premoderator was found to significantly reduce the thermal heat load on the sD_2 crystal[11] to prevent its degradation [KSB$^+$14].

At the inner part of the neutron guide surrounded by the 1.4 mm thin lHe line, the

[10] To prevent a direct heat flow from contacting the cryostat walls, the outside of the thermal shield is surrounded by PEEK distance holders.

[11] According to Monte Carlo (MC) simulations, the thermal heat is caused by 25 % γ radiation and 75 % neutrons [KSB$^+$14].

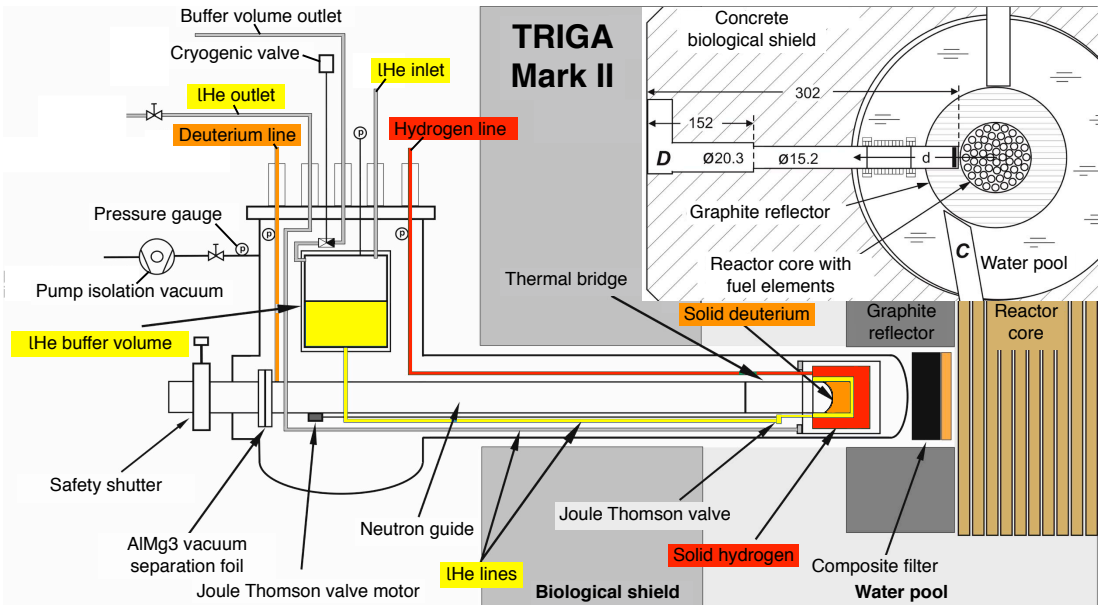

Figure 4.4: Cut view of the in-pile cryostat containing the UCN D source. The *l*He cooling system (yellow) including a buffer volume and a Joule Thomson valve for accurate flow control provides freeze-out conditions for the premoderator solid hydrogen (sH_2, red) and the converter solid deuterium (sD_2, orange). During operation, the UCN source encapsulated in a large aluminium cryostat is inserted into the beamport D (see inset), only separated from the reactor core by a graphite/bismuth stopper. Being encapsulated by the cup-shaped sH_2 crystal, the sD_2 crystal (8 mol $\sim$ 160 cm^3) is frozen out at the very end of a stainless steel neutron guide. In the front part, the guide diameter is reduced to decrease the heat flow ('thermal bridge'). The guide ends downstream in a 100 μm thin AlMg3 separation foil, which ensures necessary vacuum conditions for D_2 freeze-out. Left of the safety shutter, which is outside of the biological shield of the reactor, the experimental setup is connected. The graphic is based on [KSB+14].

sD_2 crystal (160 cm^3 $\sim$ 8 mol)[12] is frozen out in a second step[13]. Before freeze-out, the D_2 gas passes a cryogenic cell filled with Oxisorb®[14], which leads to an accelerated para-ortho conversion resulting in an ortho-D_2 concentration of $c_{o,\,D2} \geq 98\,\%$[15]. The high $c_{o,\,D2}$ concentration is beneficial, since the inelastic UCN upscattering cross-section mainly results from the induced para-ortho conversion in D_2,

$$\mathrm{UCN} + \text{para-}\mathrm{D_2} \rightarrow \mathrm{CN}(E_{\mathrm{CN}}) + \text{ortho-}\mathrm{D_2}\ , \tag{4.4}$$

with $E_{\mathrm{CN}} = 86\,\mathrm{K} = 7.4\,\mathrm{meV}$ [Sou86] denoting the energy of the cold neutron after the upscattering process. In the ortho-D_2 state, the cross-section is reduced by a factor of 150

[12] Official regulations prohibit freezing out more than 8 mol of sD_2, which was found as the optimum in a prototype source at beamport C [FSA+07].

[13] Typical freeze-out times for premoderator and converter are $\sim$ 16 h [KSB+14]. For more details on the freeze-out process, refer to [Lau10].

[14] Oxisorb® has originally been designed as a gas purification system by Messer Industriegase GmbH (`https://www.messer.de`) relying on silica gel and chromium oxide [mes18]. Due to its paramagnetism, it accelerates the D_2 conversion from its natural state (1/3 para-D_2 at $J = 1$, 2/3 ortho-D_2 at $J = 0$) to its converted state ($\geq$ 98 % ortho-D_2). J denotes the D_2 molecule's rotational quantum number (more details given in Ch. A.4).

[15] This value was confirmed by several Raman spectroscopy measurements, cf. Ch. A.4.

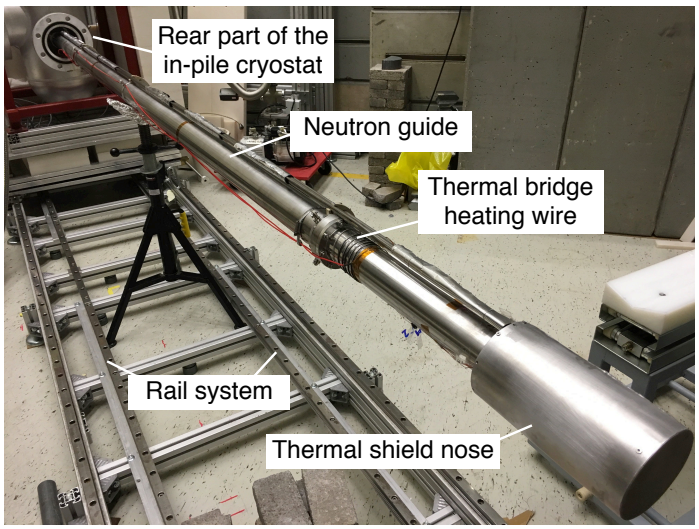

Figure 4.5: View on the UCN D source without installing the front part of the aluminium in-pile cryostat. The rails allow for changing the source's distance to the reactor core. A heating wire on the thermal bridge enables the experimentalist to locally heat the sD_2 crystal.

[FSA+07] (with data from [LYL00]), which is required for efficiently extracting the UCN from the sD_2 crystal. According to the local heat distribution, the sD_2 crystal is likely to form a concave meniscus shape with curvature radius $r_c = 3.5\,\text{cm}$ and length $L = 6.2\,\text{cm}$, which has been calculated in Monte Carlo (MC) simulations[16] by matching the simulated time-of-flight (TOF) spectrum to the measured spectrum. Inside the sD_2 crystal, the UCN loss is described by the mean free loss length, λ_{loss}, which was calculated as $4.6\,\text{cm} \leq \lambda_{\text{loss}} \leq 10.0\,\text{cm}$ at a temperature of 5 K [FSA+07].

The CAD rendering in Fig. 4.6 b) demonstrates the direction of the *l*He flow (yellow) and the H_2 flow (red) and gives the positions of installed Lake Shore Cernox® temperature sensors. Right after a reactor pulse, a strong heat load on the stainless steel nose[17] causes the sensors to increase the temperature reading for several seconds up to minutes, which masks the actual H_2 and D_2 temperatures.

After being produced in the sD_2 crystal, the UCN are extracted to the stainless steel guide, which is held in vacuum conditions. The UCN have a minimum energy of 105 neV [ADF+08], which corresponds to the Fermi potential of sD_2. Thus, they need to be gravitationally decelerated in a beam line of $\Delta h > 1\,\text{m} = 102\,\text{neV}$ height (cf. Ch. 3.2.1) before entering the experiment's storage volume.

4.2.2 Details on the upgrade procedure of the existing source

The source upgrade includes an addition of a helium (He) liquefier to the cooling system, a nickel molybdenum (^{58}NiMo) coating on the nose and the thermal bridge, as well as a neutron guide material with improved UCN transmission.

[16] The Monte Carlo simulation package used to model the UCN D source behaviour in this work was written by Y. Sobolev and iteratively improved by including the most recent measurement results.
[17] A calculation of the deposited thermal energy in the sD_2 crystal per reactor pulse is provided in [KSB+14].

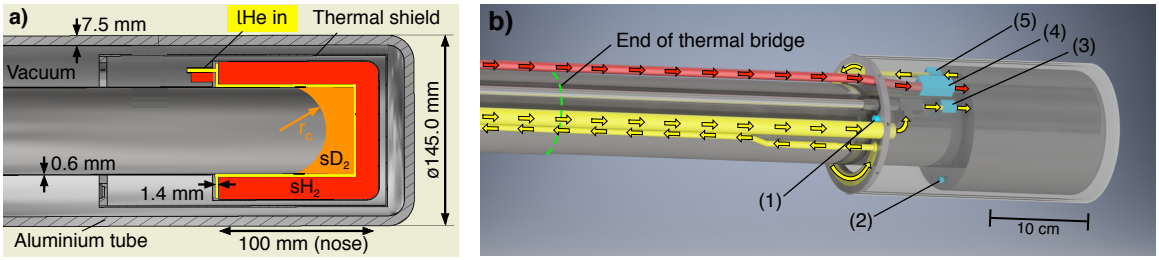

Figure 4.6: Inner and outer CAD view of the UCN source. (a) Front part of the neutron guide with nose, which is double-walled to permit *l*He flow (yellow) around the stainless steel cup, in which volume H_2 (red) is frozen out. In the inner part of the neutron guide, the sD_2 crystal (orange) is formed, which takes on a meniscus shape with curvature radius r_c. The nose is surrounded by a thermal shield, which is held in distance to the cryostat's aluminium tube. (b) The nose is cooled by a constant *l*He flow (yellow, arrows indicate flow direction). Before flowing back, the *l*He flow passes a stainless steel ring, to which the thermal shield (transparent) is attached for further cooling. The red arrows indicate the H_2 flow direction. The following temperature sensors are installed: (1) Thermal shield ($\sim 50\,\mathrm{K}$), (2) nose ($\sim 7\,\mathrm{K}$), (3) He inlet ($\sim 5\,\mathrm{K}$), (4) H_2 inlet ($\sim 8\,\mathrm{K}$), (5) He outlet ($\sim 6\,\mathrm{K}$). The adapted graphics were also published in [KRR+17].

Addition of a Helium liquefier

As a general upgrade of the cryogenic system, a He liquefier (Linde TCF10) with 1500 l He buffer volume was installed in the reactor hall, which provides a maximum *l*He flow of 14 l/h[18]. Thus, the UCN D source now works reliably over 3 weeks with 16 h of reactor pulses per day in two-shift operation. The improved cooling further allowed for decreasing the distance of the cryostat aluminium tube to the graphite/bismuth stopper to $d_{\mathrm{core,\,I}} = 0\,\mathrm{mm}$, whereby the thermal fluence and conclusively the UCN yield was increased by $\sim 10\,\%$ [KRR+17].

^{58}NiMo coating on nose and thermal bridge

For the upgrade of the source, the complete internal system contained in the aluminium cryostat was replaced by remodelled parts of the previous UCN D source. First, the inner surfaces of the nose in which the sD_2 crystal is frozen out and the subsequent thermal bridge were coated with ^{58}NiMo instead of natural NiMo. The ^{58}NiMo is composed of 85 % ^{58}Ni and 15 % Mo to prevent rest magnetism. Due to the higher Fermi potential of 311 neV instead of 225 neV [KRR+17], which implies that the effective Fermi potential for UCN inside the sD_2 crystal has increased from $V_{\mathrm{F}}(\mathrm{NiMo}) - V_{\mathrm{F}}(\mathrm{sD_2}) = (225 - 105)\mathrm{neV} = 120\,\mathrm{neV}$ to $V_{\mathrm{F}}(^{58}\mathrm{NiMo}) - V_{\mathrm{F}}(\mathrm{sD_2}) = (335 - 105)\mathrm{neV} = 230\,\mathrm{neV}$, the UCN phase space acceptance is improved. The improved nose coating implies an increased probability of UCN back-reflected at the inner wall of the nose reaching the UCN guide. The coating at the thermal bridge provides a better transmission for higher-energetic UCN.

Just from the ^{58}NiMo coating, Monte Carlo (MC) simulations have predicted an expectable gain factor of ~ 2.2 for the UCN yield compared to the non-upgraded source (cf. Fig. 9 in [KRR+17]). Taking a detailed look at these simulations, insights on the energy of the transmitted UCN depending on the coating can be gained. With a ^{58}NiMo coating, the maximum of the UCN energy distribution right behind the thermal bridge is at a velocity of $v_{\mathrm{UCN}} = 8.3\,\mathrm{m\,s^{-1}}$, which equals an UCN energy difference of $\Delta E_{\mathrm{UCN}} \sim 265\,\mathrm{neV}$ relative to

[18] The liquefier was financed by the PRISMA Cluster of Excellence.

the starting point in the sD_2 crystal ($V_F(sD_2)$= 105 neV). With a pure NiMo coating, this energy difference was simulated to be $\Delta E_{UCN} \sim 140$ neV and therefore ~ 125 neV lower. Due to the shift in the energy spectrum towards higher energies, the UCN need more gravitational deceleration, which implies that a stainless steel storage bottle, which due to its Fermi potential can store UCN of $\lesssim 200$ neV energy, must be mounted at a higher height. It should be noted, though, that placing the storage bottle higher also implies a longer UCN transmission path and therefore more losses. Thus, an UCN energy-dependent optimum between storage bottle height and beam line length must be found.

Vacuum separation foil and neutron guide material

Further investigations were made to find a more efficient replacement for the vacuum separation foil AlMg3 and for the neutron guide (before the upgrade, a stainless steel guide Nocado HE4 was used[19]). Fig. 4.7 illustrates the setup for the measurement of the foil transmission (a) and the tube transmission (b) at the UCN D source before the upgrade. In both cases, the beam line and the UCN source were at an equal gravitational level to model the conditions within the source. A 45° bend was added to avoid saturation effects of the CASCADE detector caused by *e.g.* thermal neutrons and gamma radiation (for a brief introduction to the CASCADE detection principle, cf. Ch. A.1.). The integral number of counts per pulse for different foil/tube configurations were measured in flow mode (C_{flow}), at a pulse energy of 1.25 \$ (number of measurements $N = 4$). Since no mechanical shutters were involved in the measurement process, the integral number of counts C_{flow} thus gives the transmission without differentiation between UCN and VCN energies[20].

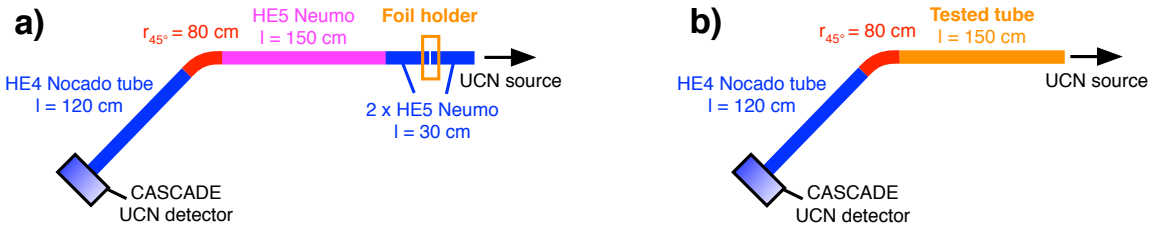

Figure 4.7: Measurement setup for foil and tube transmission measurement (top view). (a) The different vacuum separation foil samples are inserted into the foil holder, which is placed between two neutron guide tubes with $l = 30$ cm each. The following $l = 150$ cm tubes and bends guide the UCN to the CASCADE detector. The entire beam line is mounted at the same gravitational level. (b) For measuring the tube transmission, a similar setup is used. The neutron guide tube, which is directly connected to the UCN D source's neutron guide, is exchanged in-between measurements.

The transmission of several foils with 100 μm thickness was measured (cf. Fig. 4.8 a). Note that the data has been normalised to 10 MW s, which corresponds to the maximum pulse energy of the TRIGA reactor. Despite decreasing the transmission by only ~ 4 %, the

[19] Nocado GmbH (`https://www.nocado.com`) and Neumo GmbH (`https://www.neumo.de`) provide electropolished stainless steel tubes certified according to the HE4 and HE5 standard. The HE4 standard ensures a surface roughness of $R_a \leq 0.4\,\mu$m. The highest commercially available standard, HE5, provides $R_a \leq 0.25\,\mu$m.

[20] In the used beam line configuration, also very cold neutrons (VCN) with energies $\gtrsim 350$ neV reach the CASCADE detector and therefore contribute to C_{flow}. A comparison with regards to UCN transmission is still possible, since the VCN contribution in the different measurement configurations is approximately constant.

silicon (Si) wafer already broke after the second pumping and does therefore not provide the required stability. The zirconium (Zr) foil showed a worse performance than the two batches of the AlMg3 foil by manufacturer GoodFellow and by Paul Scherrer Institute (PSI). It was therefore decided to use the previously-used PSI AlMg3 separation foil, which decreases the total UCN transmission by $\sim 12\,\%$.

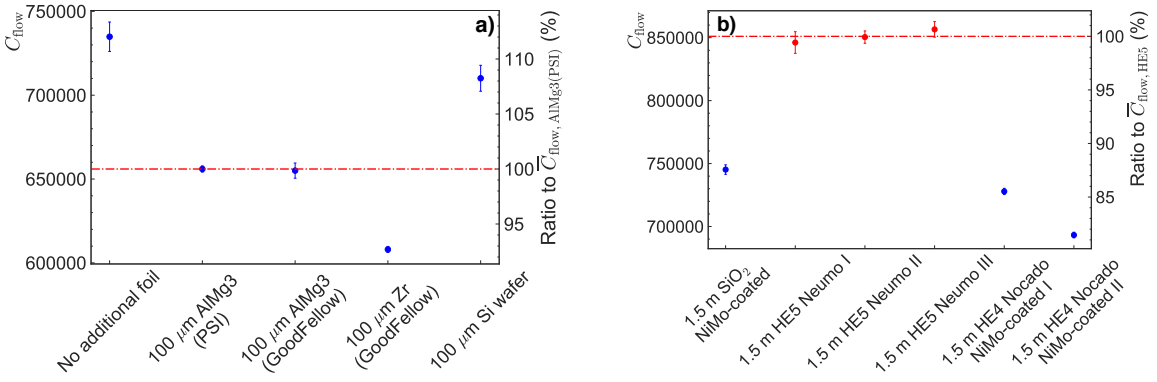

Figure 4.8: Comparison of foil and tube transmissions. Given are the counts in flow mode (C_{flow}), which were normalised to 10 MW s pulse energy for different configurations. (a) The silicon (Si) wafer performed best, but could not be used due to its fragility. Both AlMg3 foils show comparable performance, with only $\sim 12\,\%$ total transmission loss. The zirconium (Zr) foil exhibited the worst transmission. (b) The HE5 Neumo tubes, which were all cut from the same batch, performed significantly better ($C_{\mathrm{flow}} \geq +12\,\%$) than all remaining NiMo-coated HE4 stainless steel/fused silica (SiO_2) tubes.

In Fig. 4.8 b), the transmission of different tubes of length $l = 1.5\,\mathrm{m}$ is compared. In the former UCN source, HE4 Nocado tubes were used, which have been coated with NiMo in two different sputtering facilities (I: T. Lauer[21], II: C. Siemensen in Mainz[22]) to increase the Fermi potential. Former measurements have shown a comparable performance of the uncoated and the NiMo-coated HE4 tubes. The HE5 Neumo tubes were cut from one 6 m piece and therefore show a similar performance, with a more than 12 % better transmission than all other tubes. Due to the outstanding performance, the HE5 Neumo tubes were used as neutron guide for the source upgrade. Compared to the formely-used neutron guide, an improvement in the UCN transmission by $\sim 17\,\%$ across the total length of the neutron guide inside the source ($\sim 3.8\,\mathrm{m}$) was estimated [KRR+17].

Using a perthometer, the surface roughness R_{a} of the used tubes in 2-4 different tube sections were measured. The HE5 Neumo tubes provided an average value of $R_{\mathrm{a}} = 0.075(16)\,\mu\mathrm{m}$, which is notably worse than *e.g.* the NiMo-coated glass ($R_{\mathrm{a}} = 0.013(3)\,\mu\mathrm{m}$) and can therefore not explain the good transmission values. Further R_{a} values were measured for an uncoated HE4 tube ($0.312(45)\,\mu\mathrm{m}$), a NiMo-coated HE4 tube (II, $0.114(9)\,\mu\mathrm{m}$), and an uncoated fused silica (SiO_2) tube ($0.009(3)\,\mu\mathrm{m}$). As a result, the determined surface roughness is no accurate measure of a neutron guide's UCN transmission.

4.2.3 Performance of the upgraded source

The commissioning of the source had finished in August 2016. In September and November 2016, researchers of the Paul-Scherrer Institute (PSI) in Villigen, Switzerland were invited

[21] The coating was applied by T. Lauer (Movatec GmbH, `http://www.movatec.de`).
[22] C. Siemensen used the sputtering facility of Prof. Werner Heil at the Mainz Institute of Physics.

to measure the achievable UCN density in a standardised stainless steel bottle of $\sim 32\,\mathrm{l}$ volume (cf. Ch. 4.2.3). The same measurement has been performed in November 2015 with the UCN D source before its upgrade to compare its performance to the majority of UCN sources worldwide[23]. After the upgrade, a completely new behaviour of the UCN D source was identified: Instead of a constant UCN yield as observed before the upgrade, the yield now rises by $\sim 40\,\%$ until reaching saturation - a phenomenon which has been reproduced in subsequent beam times. The characterisation measurements prior to and after the upgrade have been published in academic journals [BDK+17, KRR+17].

In beam times from 2016 until 2018, additional source characterisation measurements have been performed using the versatile Mainz storage bottle with a volume of $\sim 10\,\mathrm{l}$ and an adaptable Fermi potential. The results of these measurements provide a detailed insight into the height dependency for different UCN storage energies (cf. Ch. A.5.1).

Measurements with the standardised PSI storage bottle

For the world-wide comparison of ultracold neutron sources (cf. Ch. A.2), a NiMo-coated stainless steel storage bottle with storage volume of $V_{\mathrm{storage,\ PSI}} = 32.044(164)\,\mathrm{l}$ and a Fermi potential of $V_{\mathrm{F}} = 220\,\mathrm{neV}$ was designed [BBD+16]. The setup was used in November 2015 by D. Ries to determine relevant properties for performing a world-wide comparison of UCN source performances.

Fig. 4.9 depicts the storage bottle connected to the 'standard' beam line, which has been used to guide the UCN from the source to the storage bottle[24]. It allowed for a quick adaption of the relative height of the storage bottle above beam exit (h) by exchanging the length l of the tilted UCN guide. For the beam line, neutron guides of type HE5 Neumo were used along with bends electropolished according to HE4 standard[25]. For UCN detection, the CASCADE detector[26] was set to an operating voltage of $1350\,\mathrm{V}$[27]. In all measurements, a counting time of $200\,\mathrm{s}$ was selected, which implies that after the emptying of the UCN contained in the storage bottle had started, the detector counted all events for $200\,\mathrm{s}$.

Various properties have been selected to compare the UCN source's performance[28]. As a first property, it was decided to compare the maximum UCN density, $\varrho_{\mathrm{UCN,\ 2\ s}}$. It is determined by counting the UCN stored inside the storage bottle for a storage time of $t_s = 2\,\mathrm{s}$. For this measurement, the CASCADE detector is mounted in vertical direction (cf. Fig. 4.9). Performing the same measurement in horizontal extraction mode, the source's horizontal to vertical (h/v) ratio can be calculated, which is thereby defined as

$$\mathrm{h/v} = \frac{\varrho_{\mathrm{UCN,\ 2\ s}}\,(\mathrm{h})}{\varrho_{\mathrm{UCN,\ 2\ s}}\,(\mathrm{v})}\,. \tag{4.5}$$

The determination of the h/v ratio allows for evaluating the 'hardness' of the spectrum, *i.e.,* the higher the proportion of lower-energetic UCN, the softer is the spectrum. This is also

[23] An overview over the results published in [BDK+17] is provided in Ch. A.2.

[24] The 'standard' beam line has been used throughout all UCN D characterisation measurements unlike otherwise noted, regardless of the installed storage bottle.

[25] Stainless steel surfaces polished according to HE5 standard exhibit a surface roughness of $R_{\mathrm{a}} \leq 0.25\,\mu\mathrm{m}$. The HE4 standard represents $R_{\mathrm{a}} \leq 0.4\,\mu\mathrm{m}$

[26] Details on the CASCADE detector are found in Ch. A.1.

[27] During all measurement, the values $V_{\mathrm{ref,\ 0}}$ and $V_{\mathrm{ref,\ 1}}$ were set to the integer value 108.

[28] For a more detailed explanation on the UCN density determination, the horizontal/vertical ratio and the properties extracted from fitting a storage curve, refer to Ch. A.1.

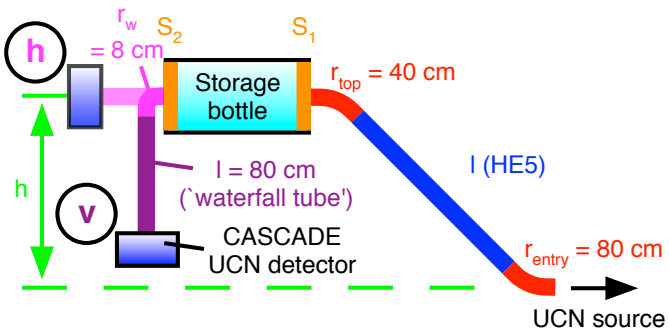

Figure 4.9: Measurement setup during UCN D characterisation measurements. The 'standard' beam line used throughout all UCN D characterisation measurements can be set up either in horizontal (h) or in vertical (v) extraction mode. After the upgrade, a tilted HE5 Neumo tube of $l = 150\,\mathrm{cm}$ was installed (before upgrade: HE4 Nocado $l = 120\,\mathrm{cm}$), resulting in a total height of $h = 142\,\mathrm{cm}$ (before upgrade: $h = 130\,\mathrm{cm}$). In horizontal extraction mode, the CASCADE detector is on the same gravitational level as the storage bottle. To ensure UCN penetration through the detector's aluminium entrance foil, a vertical tube of $l = 80\,\mathrm{cm}$ ('waterfall tube') is mounted before the detector in vertical extraction mode.

expressed by the proportion of low-energetic UCN in the spectrum,

$$E_{\mathrm{UCN,\,low}} = 1 - \left(\frac{\varrho_{\mathrm{UCN,\,2\,s}}\,(\mathrm{h})}{\varrho_{\mathrm{UCN,\,2\,s}}\,(\mathrm{v})} \right) \,. \tag{4.6}$$

The energy discrimination can be performed due to the AlMg3 entrance foil of the CASCADE detector, which implies that when mounted on the same gravitational level as the storage volume, the detector is only sensitive to UCN with energies $E_{\mathrm{UCN}} > V_{\mathrm{F}}(\mathrm{Al})$. A gravitational acceleration of UCN after storage before detection gives access to all formerly stored UCN, if the gravitational energy boost is $\geq V_{\mathrm{F}}(\mathrm{Al})$.

Measuring the UCN density for different storage times t_{s}, which is typically varied from $2 - 200\,\mathrm{s}$, allows for plotting the storage curve. In the storage curve, the UCN density $\varrho_{\mathrm{UCN}}\,(t_{\mathrm{s}})$ is plotted against t_{s} (an example can be found in Fig. 4.11). The data is fitted using a biexponential function [GRL91],

$$\varrho\mathrm{UCN}(t_{\mathrm{s}}) = A_1 \exp\left(t_{\mathrm{s}/\tau_1}\right) / A_2 \exp\left(t_{\mathrm{s}/\tau_2}\right) \,, \tag{4.7}$$

with coefficients A_1, A_2, τ_1, τ_2 extracted from the fit function. The first term accounts for UCN losses due to a non-cleaned spectrum, *i.e.,* during the time constant τ_1, non-storable UCN with energies $E_{\mathrm{UCN}} > (V_{\mathrm{F}} = 220\,\mathrm{neV})$ are contained in the storage bottle. As the second term refers to the stored UCN, the decay constant τ_2 was taken into account for the comparison of source performances.

Since the Mainz UCN D source is a pulsed source, fluctuations of the reactor pulse energy and thus of the neutron fluence are directly correlated to the UCN yield. As a standard approach, it was therefore agreed on normalising the measured UCN density ϱ_{UCN} to the average pulse energy of the respective beam time, $\overline{E}_{\mathrm{pulse}}$ (also used in [KRR+17]),

$$\varrho_{\mathrm{UCN,\,norm},\,i} = \frac{\varrho_{\mathrm{UCN},\,i}}{E_{\mathrm{pulse},\,i}} \cdot \overline{E}_{\mathrm{pulse}} \,. \tag{4.8}$$

All UCN densities measured at UCN D after the upgrade are therefore given in its normalised form, with $\overline{E}_{\mathrm{pulse}}$ determined for each individual beam time. In direct performance comparisons of the upgraded to the non-upgraded source, the formerly-used normalisation to $\overline{E}_{\mathrm{pulse}} = 10\,\mathrm{MW\,s}$ [KSB+14] is used. These cases are clearly indicated.

Prior to the measurements, the height as well as the filling time have been optimised. Exchanging the tilted tube length (cf. Fig. 4.9), the height is varied until the maximum $\varrho_{\mathrm{UCN,\,2\,s}}$ value is determined. For optimising the filling time, the shutter timing of the entry shutter S_1 (cf. Fig. 4.9) is varied until the density measured at a storage time of 5 s is maximised. The maximum $\varrho_{\mathrm{UCN,\,5\,s}}$ value refers to the optimum between the number of UCN entering the bottle and later exiting in direction of the source.

The gain factors caused by a characteristic development of the UCN yield are seen in all measurements with the upgraded source. Fig. 4.10 shows an exemplary yield development measured in the November 2016 beam time. The yield pattern starts with an initial dip, after which it starts to rise after ~ 40 reactor pulses (N_{pulse}). After $N_{\mathrm{pulse}} \sim 150$, saturation sets in, with the overall UCN density increased by $\sim 40\,\%$. This implies that the UCN yield is saturated after ~ 2 days of exposing the sD_2 crystal to reactor pulses[29]. A major factor leading to the observed yield pattern is the heat load on the sD_2 crystal invoked by the thermal impact of the reactor pulse. This heat load causes an evaporation of the crystal material, which is reflected by a pressure increase in the deuterium line (cf. Fig. A.5 b). According to our current hypothesis, the crystal consecutively changes its shape, which is over time beneficial to the number of UCN produced per pulse. For more details, refer to Ch. A.3.

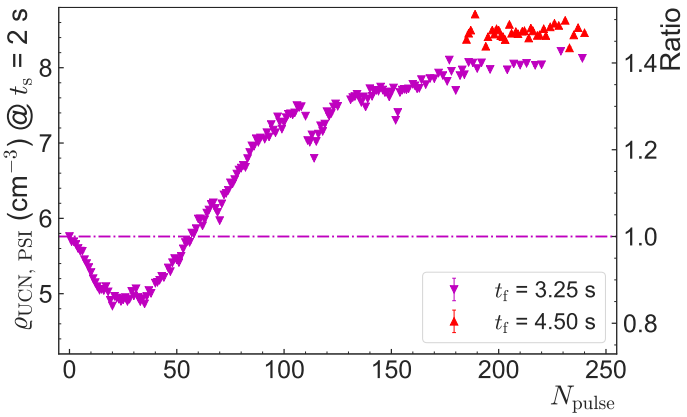

Figure 4.10: UCN density in PSI storage bottle ($\varrho_{\mathrm{UCN,\,PSI}}$ for a storage time of $t_s = 2\,\mathrm{s}$) as a function of reactor pulses (N_{pulse}) during the November 2016 beam time. The depicted data was taken during the second freeze-out, with the moderator in closest position to the reactor core ($d_{\mathrm{core,\,I}}$). Initially, a filling time of $t_f = 3.25\,\mathrm{s}$ was chosen, which was later changed to $t_f = 4.50\,\mathrm{s}$ after a further filling time optimisation. After an initial dip, $\varrho_{\mathrm{UCN,\,PSI}}$ increases, until it reaches a saturation after $N_{\mathrm{pulse}} \sim 150$. Compared to the initial value, $\varrho_{\mathrm{UCN,\,PSI}}$ has increased by $\sim 40\,\%$ when saturated (right axis).

The results of the source upgrade for different relevant properties are provided in Tab. 4.1. In summary, an improvement factor of 3.51(1) for UCN with maximum energy of 220 neV

[29] In a double shift, the TRIGA reactor manages 5 2 $ pulses per hour, which leads to 75 pulses per day when operating for 15 hours.

stored in a volume of $\sim 32\,\mathrm{l}$ is reached. This corresponds to a density of $\varrho_{\mathrm{UCN,\ PSI,\ 2\ s}}\ (\mathrm{v}) = 8.51(5)\,\mathrm{cm}^{-3}$, which was determined after optimising the filling time[30]. The comparison of the proportion of low-energetic UCN before and after the upgrade (cf. Eq. (4.6)) indicates that the hardness of the spectrum has remained unchanged[31]. Still, the τ_2 value, which represents the storage time of UCN stored in the bottle, has increased by $\sim 50\,\%$ due to the upgrade[32].

Table 4.1: Comparison of relevant properties measured with the PSI storage bottle ($V_{\mathrm{storage,\ PSI}} \sim 32\,\mathrm{l}$) before and after the UCN D source upgrade (saturated UCN yield). As properties, the UCN density after 2 s storage time in vertical (v) and horizontal (h) extraction mode are given by $\varrho_{\mathrm{UCN,\ PSI,\ 2\ s}}$ (normalised according to Eq. (4.8)). Determining $\varrho_{\mathrm{UCN,\ PSI,\ 2\ s}}$ after the short storage time was defined prior to the measurement run to allow for a worldwide comparison of UCN source performances [BBD+16]. The value in brackets after the densities gives the optimised filling time, t_{f}. The proportion $E_{\mathrm{UCN,\ low}}$ represents the number of UCN with energy $E_{\mathrm{UCN}} < 54\,\mathrm{neV}$ relative to the total number of UCN calculated according to $1-(\varrho_{\mathrm{UCN,\ PSI,\ 2\ s}}\ (\mathrm{h})/\varrho_{\mathrm{UCN,\ PSI,\ 2\ s}}\ (\mathrm{v}))$. Due to data availability, it was determined from measuring the densities in the $d_{\mathrm{core,\ II}}$ position, which is 30 mm further distanced from the reactor core than $d_{\mathrm{core,\ I}}$. τ_2 is the second decay constant of the biexponential fit. For comparsion of the values, the ratio is given in the rightmost column. If not noted otherwise, the values were determined at position $d_{\mathrm{core,\ II}}$. In case of the upgraded source, the measurements were taken after the UCN yield saturation (cf. Ch. A.3) had set in.

Property	Before upgrade	After upgrade	Ratio
$\varrho_{\mathrm{UCN,\ PSI,\ 2\ s}}$ (v)	$2.43(2)\,\mathrm{cm}^{-3}$ (4.0 s)	$7.81(10)\,\mathrm{cm}^{-3}$ (3.0 s)	3.21(2)
		$8.53(5)\,\mathrm{cm}^{-3}$ ($d_{\mathrm{core,\ I}}$, 4.5 s)	3.51(1)
$\varrho_{\mathrm{UCN,\ PSI,\ 2\ s}}$ (h)	$1.60(1)\,\mathrm{cm}^{-3}$ (3.0 s)	$4.98(10)\,\mathrm{cm}^{-3}$ (2.5 s)	3.32(2)
Proportion $E_{\mathrm{UCN,\ low}}$	0.34(1)	0.36(2)	1.06(6)
τ_2	63.56(84) s	93.56(2.25) s ($d_{\mathrm{core,\ I}}$)	1.47(3)

Fig. 4.11 compares the storage curves in the PSI storage bottle before and after the upgrade. An increase in UCN yield of factor 3.73(0.17) is seen averaged over all storage times. The parameters of the respective biexponential fits are given in the figure caption. Also, the UCN energy distribution was simulated by running a the Monte Carlo (MC) simulation written by Y. Sobolev (cf. Fig. 8 of [KRR+17]). After the upgrade, crucial parameters were re-evaluated by Y. Sobolev such that the simulated TOF spectrum matched the measured spectra.

Following the upgrade, the Mainz UCN D source could considerably improve its performance by a factor of 3.5. Compared to all UCN D sources worldwide, it is now ranked

[30] The maximum UCN density was inferred from considering the values for a filling time of 4.5 s (cf. red data points in Fig. 4.10) in vertical extraction (v). During these measurements, the source was shifted 30 mm closer to the reactor core (position $d_{\mathrm{core,\ I}}$).

[31] Note that unlike the optimum value of $\varrho_{\mathrm{UCN,\ PSI,\ 2\ s}}$ (v), the densities for determining $E_{\mathrm{UCN,\ low}}$ were measured in the $d_{\mathrm{core,\ II}}$ position, *i.e.,* with the moderator 30 mm further removed from the reactor core. In the $d_{\mathrm{core,\ I}}$ position, the thermal neutron flux is notably higher than at the $d_{\mathrm{core,\ II}}$ position. Thus, the values for determining $E_{\mathrm{UCN,\ low}}$ must be taken at the same position. This was due to the fact that the density in horizontal extraction mode had not been measured at the later $d_{\mathrm{core,\ I}}$ position.

[32] For an analysis of the time-development of the UCN proportion with $E_{\mathrm{UCN}} \lesssim 54\,\mathrm{neV}$ and a dependency on the storage volume, see Figs. A.14 a) and b).

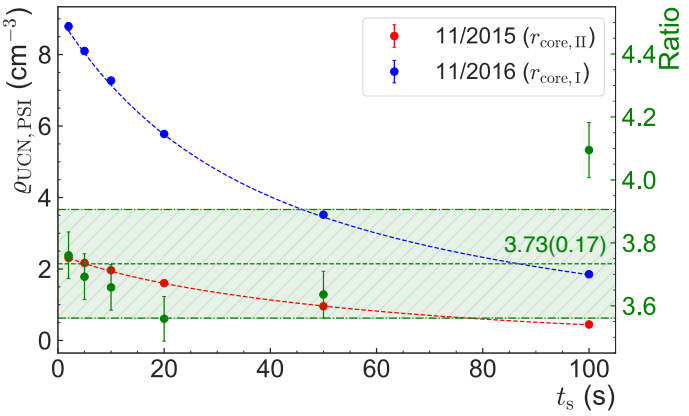

Figure 4.11: UCN storage curve measured with PSI storage bottle before and after upgrade. The UCN density in the $\sim 32\,\mathrm{l}$ storage volume, $\varrho_{\mathrm{UCN,\,PSI}}$, is plotted against the storage time t_{s}. The source performance before the upgrade is represented by the red data points ($d_{\mathrm{core,\,II}} = 30\,\mathrm{mm}$), while the blue data points refer to the upgraded source ($d_{\mathrm{core,\,I}} = 0\,\mathrm{mm}$). The dashed lines depict the respective biexponential fits (red: $\varrho_{\mathrm{UCN,\,0\,s}} \equiv A_1 + A_2 = 2.41(20)\,\mathrm{cm}^{-3}$, $\tau_1 = 12.42(3.88)$ s, $\tau_2 = 63.56(84)\,\mathrm{s}$; blue: $\varrho_{\mathrm{UCN,\,0\,s}} = 9.12(7)\,\mathrm{cm}^{-3}$, $\tau_1 = 21.45(2.06)$ s, $\tau_2 = 93.56(2.25)$ s). The right-hand axis shows the ratio between upgraded and non-upgraded source (green data points) as a function of t_{s}. Apart from one minor and one outlier at $t_{\mathrm{s}} = 100\,\mathrm{s}$, the ratios agree with each other fairly well (average of 3.73(0.17), green dashed line).

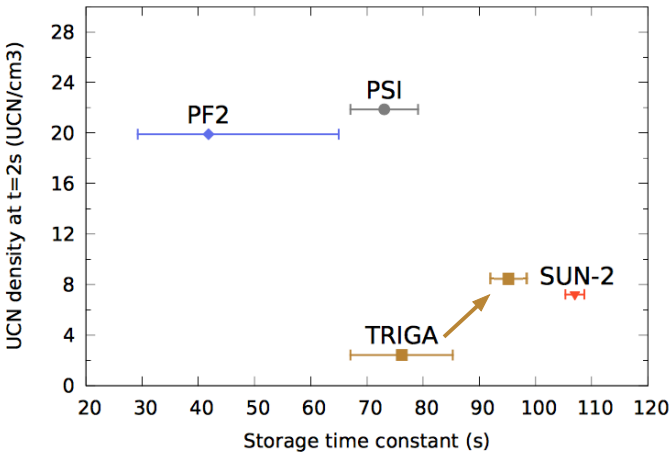

Figure 4.12: UCN density after 2 s storage time as a function of storage time constant for different UCN sources. The storage time constant refers to the τ_2 value, which has been extracted from performing a biexponential fit to the respective storage curve (cf. blue dashed line in Fig. 4.11). The effect of the UCN D upgrade on the performance regarding a higher UCN density and a longer τ_2 value is indicated by the brown arrow. A detailed description of the comparison measurement is found in Ch. A.2. Figure adapted from [BDK+17].

among the best within a factor < 3 in UCN yield (cf. Fig. 4.12). For a detailed description of the worldwide comparison measurements, refer to Ch. A.2.

Average reactor pulse energy during all beam times and pulsing stability

Since the UCN D source is a pulsed source, fluctuations in the reactor pulse energy translate into a varying thermal neutron flux to which the sD_2 crystal is exposed. Due to the proportionality of the UCN production to the neutron flux (cf. Eq. (3.14)), the standard normalisation method (cf. Eq. (4.8)) therefore assumes a direct correlation between pulse energy and UCN yield in flow and storage mode. The reactor pulse energy, E_{pulse}, is measured in an uncompensated ionisation chamber [MTK75], which is situated in proximity to the reactor reflector and is calibrated on a regular basis. After the signals have been analysed by an electronic circuit, the E_{pulse} value is read out by the responsible operator.

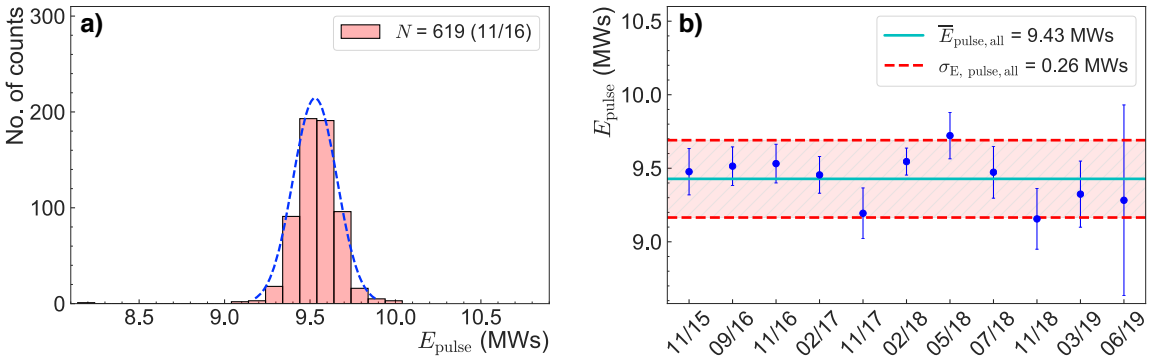

Figure 4.13: Reactor pulse energy over November 2016 beam time and average over all beam times. (a) The pulse energies E_{pulse} of the November 2016 beam time are Gaussian distributed (blue dashed line depicts Gaussian fit), with number of pulses $N = 619$, mean $\overline{E}_{\mathrm{pulse}} = 9.53\,\mathrm{MW\,s}$, and standard deviation $\sigma_{\mathrm{E,\ pulse}} = 0.13\,\mathrm{MW\,s}$. In general, all pulse energies were found to be Gaussian distributed. (b) Average pulse energies over all beam times, with $\overline{E}_{\mathrm{pulse}}$ plotted against the month/year of the respective beam time. The standard deviation of each beam time, $\sigma_{\mathrm{E,\ pulse}}$, is taken as error bars. Averaged over all beam times, the mean of all pulse energies, $\overline{E}_{\mathrm{pulse,\ all}} = 9.43(26)\,\mathrm{MW\,s}$ (cyan line) fluctuates on average by $\sigma_{\mathrm{E,\ pulse,\ all}} = 0.26\,\mathrm{MW\,s}$ (red dashed line).

As illustrated in Fig. 4.13 a), the reactor pulse energy during one beam time is Gaussian distributed. Therefore, the distribution's mean ($\overline{E}_{\mathrm{pulse}}$) and the standard deviation ($\sigma_{\mathrm{E,\ pulse}}$) can be taken as a measure to characterise the pulsing stability. Fig. 4.13 b) shows the $\overline{E}_{\mathrm{pulse}}$ values with $\sigma_{\mathrm{E,\ pulse}}$ as error bars for different beam times. Considering each individual beam time, the $\overline{E}_{\mathrm{pulse}}$ values fluctuate by $\sim 0.9 - 2.3\,\%$ (cf. Fig. A.21 b) and onwards). An exception is the June 2019 beam time, during which a fluctuation of $\sim 7.0\,\%$ was observed, which was caused by a defect in the reactor's pulse rod (cf. Fig. A.20). Averaged over all beam times (a histogram of the values is found in Fig. A.21 a), the reactor pulse energy fluctuates by $\sim 2.8\,\%$.

The fluctuation of the reactor pulse energy translates into a fluctuation of the integral thermal neutron flux impinging on the sD_2 converter ($\Phi_{\mathrm{n,\ thermal}}$), with $\Phi_{\mathrm{n,\ thermal}}$ being proportional to E_{pulse}. To account for this dependency, the measured UCN densities are normalised to the pulse energy (cf. Eq. (4.8)). If no further effects affecting the UCN yield would be present, this normalisation method would remove fluctuations in the observed UCN yield.

Stability of UCN yield

Besides a reliable source operation for multiple weeks, which could successfully be demonstrated, a high reproducibility of the UCN yield is essential to the τSPECT experiment. Variations in the UCN yield cause non-statistical fluctuations in the number of UCN being initially filled into the storage volume. If these effects are not met by a suitable normalisation method (cf. Ch. 4.3), the experiment's accuracy in the neutron lifetime determination is limited.

Further analyses have shown that the stability of the UCN yield is not only affected by fluctuations of the reactor's pulse energy, but also by temperature effects on the sD_2 crystal. The temperature influence on the UCN yield is due to the high sensitivity of UCN upscattering processes on temperature in the sD_2 crystal [LYL00]. Each reactor pulse causes a heat flux on the crystal, which changes its steady state temperature of $\sim 5\,\mathrm{K}$ to a maximum value of $\sim 25\,\mathrm{K}$ (cf. Fig. A.6) before returning to thermal equilibrium again[33]. This implies that during pulsing, the crystal is exposed to different thermal conditions each $\sim 12\,\mathrm{min}$. The associated increase in the D_2 pressure by $\Delta p_{\mathrm{D2}} \gtrsim 0.5\,\mathrm{mbar}$ (cf. Fig. A.5 b) points to evaporation effects caused by the local heating. With the evaporated D_2 molecules refreezing, the crystal shape is likely to change as a function of pulses, N_{pulse}. When saturation of the yield sets in after $N_{\mathrm{pulse}} \sim 150$ (cf. Fig. 4.10), D_2 is still evaporated at the surface ($\Delta p_{\mathrm{D2}} > 0$), but according to our current hypothesis, the crystal has reached its general final form.

When considering the $\varrho_{\mathrm{UCN,\,PSI}}$ values in Fig. 4.10 with the source in saturation, fluctuations in the yield (cf. red triangles) are still observed due to the heat affecting the sD_2 crystal. To quantify, the UCN yield still fluctuates by 0.6 %. Note that the yield has already been normalised to the reactor pulse energy according to Eq. (4.8), which implies that the observed fluctuation is only due to crystal effects.

Concerning its reproducibility, the saturated UCN yield has been observed for various beam times with the same setup (cf. Ch. A.5.3). Fluctuations of $\sim 10\,\%$ were identified between beam times. These fluctuations likely occur due to minor differences in the freeze-out procedure of both the sH_2 and the sD_2 crystal, which potentially affects the thermal properties of both crystals. Furthermore, a non-constant UCN transmission is present, which results from a complete re-assembly of the beam line connected to the storage bottle (cf. Fig. 4.9) during each beam time.

When performing measurement runs with τSPECT, the characteristic source behaviour concerning its increasing yield needs to be considered. Not only the strong yield increase within the first ~ 150 reactor pulses, but also the yield fluctuations after reaching saturation are of concern and require an additional normalisation method besides normalising to the reactor pulse energy.

4.3 Normalisation issue

In τSPECT, the neutron lifetime τ_n is always determined in a relative measurement. For its determination, the number of UCN counted in the storage volume (C_{UCN}) is plotted as a function of the storage time t_{s}, which gives the storage curve (an exemplary storage curve is depicted in Fig. 5.4). Assuming that only storable UCN are contained in the storage volume, τ_n is extracted as the decay constant from an exponential fit to the storage curve.

[33] Deuterium freezes out at a temperature of $T = 18.73\,\mathrm{K}$ [Sou86].

Only statistical fluctuations of C_{UCN} need to be considered if the same number of initial UCN is always filled into the storage volume at $t_{\mathrm{s}} = 0$. If this is not the case due to fluctuations of the UCN yield, additional non-statistical fluctuations are also observed at a given storage time. These additional fluctuations in turn lead to an increasing error in τ_n and must thus be accounted for to reach the desired accuracy of $\Delta\tau_n = 1\,\mathrm{s}$. Since the UCN yield was found to fluctuate $\mathcal{O}(1\,\%)$ after normalising to the effect of a non-constant reactor pulse energy due to thermal effects on the sD_2 crystal (cf. Ch. 4.2.3), an additional normalisation method is required for τSPECT.

4.3.1 Ultracold neutron normalisation methods and their implementation

Several possibilities for UCN normalisation exist and are based on:

(i) Pulse energy from TRIGA ionisation chamber (standard procedure, used throughout all UCN source characterisations and τSPECT preparatory studies),

(ii) higher-energetic UCN, which 'escape' from the storage region during filling,

(iii) UCN from storable region.

Option (i) is well-established but is not sufficing, since the method to normalise the UCN counts to the reactor pulse energy only takes the fluctuations of the thermal neutron flux into account. Since UCN production occurs within the sD_2 crystal, no 100 % proportionality to the thermal neutron flux is given. Option (ii), which implies going lower in the energy spectrum, *i.e.,* towards the energy range of non-storable UCN, could provide a more precise normalisation, since the energy ranges are closer to the maximum storable kinetic UCN energy of $\Delta E = 23\,\mathrm{neV}$ (cf. Ch. 4.4.2). Following the same argumentation, best normalisation results should be gained from UCN extracted from the storable region directly (option (iii)), which however has the drawback of decreasing the statistics, since less UCN remain for counting.

For τSPECT will full-magnetic storage implemented, all three options can be realised and were tested using a dedicated measurement setup[34] as laid out in Ch. 4.3.2.

4.3.2 Measurement setup for comparing normalisation methods

To emulate the normalisation methods (i) - (iii) listed above, a measurement setup was developed. The measurement setup comprised a modified stainless steel storage bottle with the second shutter's 2 mm thick stainless steel blade exchanged for a 500 nm thin nickel molybdenum (NiMo) foil embedded in a stainless steel frame. Modifying the shutter S_2 in direction of the CASCADE detector (cf. Fig. 4.9) was necessary since the shutter's original thickness would absorb all neutrons of the desired energy range. The inclusion of the NiMo foil with its Fermi potential $V_{\mathrm{F}}(\mathrm{NiMo})$ gives access to the non-storable UCN and very cold neutrons (VCN) of energies $E_{\mathrm{VCN}} \geq V_{\mathrm{F}}(\mathrm{NiMo}) = 220\,\mathrm{neV}$ (cf. Tab. A.1). These non-storable UCN, which are now referred to as VCN for simplicity, are close to the maximum storable energy in stainless steel (VA), *i.e.,* $E_{\mathrm{UCN,\,max}} = V_{\mathrm{F}}(\mathrm{VA}) = 190\,\mathrm{neV}$. Apart from the shutter modification, the standard beam line at $h = 1.35\,\mathrm{m}$ over beam exit was used, with the CASCADE detector installed for vertical extraction (cf. Fig. 4.9). The usage of a stainless steel bottle was required due to the inclusion of a NiMo foil, which leads to significantly higher storable UCN energies and therefore better statistics than the maximal UCN energy of $\sim 60\,\mathrm{neV}$ storable in τSPECT.

[34] A preliminary analysis of the measurement data is found in [Ros17].

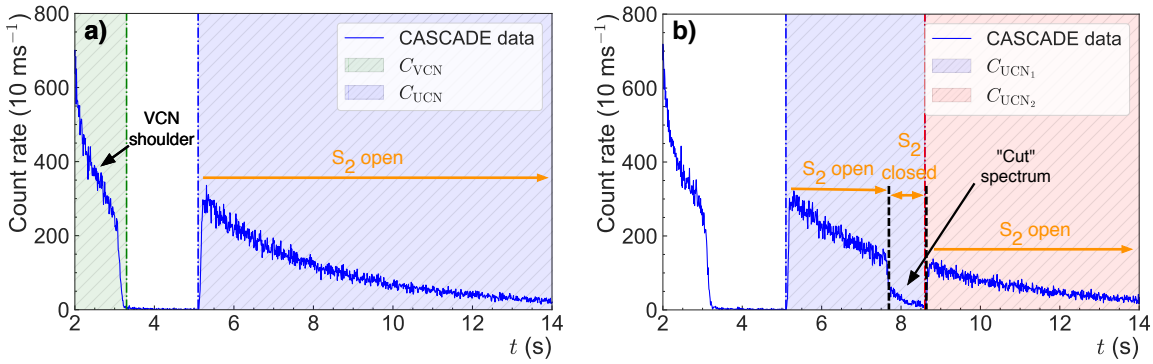

Figure 4.14: Measurement methods for comparing UCN normalisation, with filling time $t_f = 2.5\,s$, storage time $t_s = 2\,s$, and thermal peak at $t \sim 0.5\,s$. (a) CASCADE detector spectrum for normalisation method (ii), which implies normalisation to VCN. The VCN leaking through the NiMo foil of the closed shutter S_2 ('VCN shoulder') were counted, giving the integral counts C_{VCNs} (green region). When S_2 is open, the integral counts of the UCN (C_{UCN}, blue region) are determined. (b) A short closure and a re-opening of S_2 cuts the UCN spectrum, giving the two integral count regions C_{UCN_1} (blue region) and C_{UCN_2} (red region). For details, refer to the text.

The setup was used in two different configurations to emulate normalisation method (ii), *i.e.,* using VCN for normalisation, and method (iii) using an UCN fraction for normalisation. Normalisation method (i) comprising a normalisation to the reactor pulse energy was simultaneously accessible during both options (ii) and (iii). A preceding filling time optimisation measurement[35] has yielded an optimum filling time of $t_f = 2.5\,s$.

For realising option (ii), the UCN were stored in the storage bottle for a storage time of $t_s = 2\,s$, which implies that the shutter S_2, as depicted in Fig. 4.14 a), was opened after $t \sim 5\,s$, which corresponds to $\sim 4.5\,s$ after the reactor pulse. From the opening of S_2 onwards, the UCN were counted for a counting time of 200 s, yielding the integral counts C_{UCN} (blue region). According to the design of the modified S_2 shutter, the VCN could penetrate and could thus reach the detector ('VCN shoulder'). It was decided to count all VCN for $t = 0.8\,s$ from $t = 1.5\,s$ onwards, which corresponds to $t = 1.3\,s$ and $t = 2\,s$ in the time scale of the figure. In consequence, the integral counts C_{VCN} were determined.

To realise normalisation method (iii) The S_2 shutter movement was adapted. With no change in the storage and filling times, S_2 was again opened after $t \sim 5\,s$, *i.e.,* 4.5 s after the reactor pulse (cf. Fig. 4.14 b). Only 1.6 s after opening, S_2 was closed and opened again after another second, which has led to a 'cut' spectrum. Consequently, two regions for integral counts were existing, *i.e.,* C_{UCN_1} (blue area) and C_{UCN_2} (red area).

Both configurations were measured in two experimental runs, with $N_1 = 23$ measurements according to method (ii) and $N_2 = 11$ measurements according to (iii). For each measurement $i = 1, \ldots, N_1$ or $j = 1, \ldots, N_2$, respectively, the UCN integral counts were normalised to either the VCN (option (ii)) or the first fraction of UCN (option (iii)), which

[35] The filling time optimisation and the shutter movement during filling/storage processes are described in detail in Ch. A.1.

is expressed in the ratios

$$r_{\mathrm{UCN/VCN},\,i} = \frac{C_{\mathrm{UCN},\,i}}{C_{\mathrm{VCN},\,i}} \,, \tag{4.9}$$

$$r_{\mathrm{UCN_2/UCN_1},\,j} = \frac{C_{\mathrm{UCN_2},\,j}}{C_{\mathrm{UCN_1},\,j}} \,. \tag{4.10}$$

Also, each measurement was normalised to the pulse energy of each measurement, $E_{\mathrm{pulse},\,i}$ or $E_{\mathrm{pulse},\,j}$, with $\overline{E}_{\mathrm{pulse}}$ being the mean of all pulse energies during the measurements N_1 and N_2:

$$r_{\mathrm{UCN/E_{pulse}},\,i} = \frac{C_{\mathrm{UCN},\,i}}{E_{\mathrm{pulse},\,i}} \cdot \overline{E}_{\mathrm{pulse}} \,, \tag{4.11}$$

$$r_{\mathrm{UCN_2/E_{pulse}},\,j} = \frac{C_{\mathrm{UCN_2},\,j}}{E_{\mathrm{pulse},\,j}} \cdot \overline{E}_{\mathrm{pulse}} \,. \tag{4.12}$$

All errors were computed by Gaussian error propagation. For a better comparison to the VCN and UCN normalisation methods, the standard deviation of the pulse energy of the respective measurement sequence, $\sigma_{E_{\mathrm{pulse},\,n}}$, was taken as an additional error.

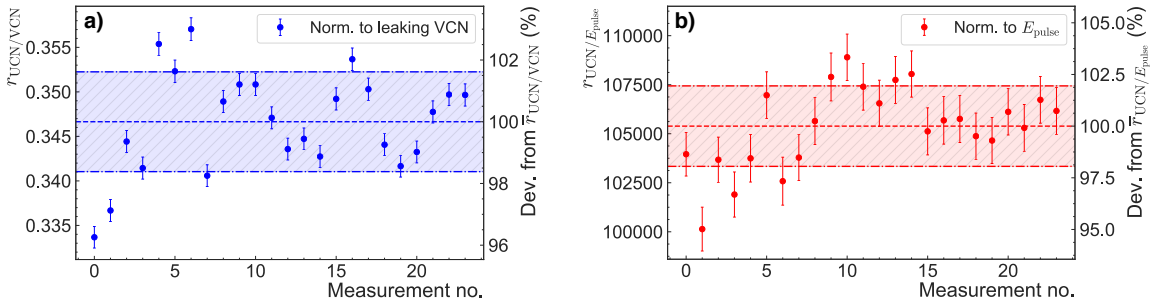

Figure 4.15: Evaluation of the normalisation to VCN (option (ii)) for $N_1 = 23$ measurements. (a) The mean (μ, dashed blue line) and the standard deviation (σ, dashed-dotted blue line) of the ratio of the integral counts $r_{\mathrm{UCN/VCN}}$ yield $\mu \pm \sigma = 0.3466(56)$ (mean and standard deviation, denoted by the dashed line and the dash-dotted line) and therefore fluctuates by 1.62 %. (b) For the normalisation to the pulse energy ($r_{\mathrm{UCN/E_{pulse}}}$, cf. Eq. (4.11)), an average deviation of 1.95 % around the mean ($\mu \pm \sigma = 105\,388(2052)$) is found. For (a) and (b), the fluctuations around the mean in % are provided on the right axis.

Fig. 4.15 shows the results of the normalisation to VCN (option (ii)), the normalisation to the primary UCN fraction (option (iii)) is depicted in Fig. 4.16. Both normalisation methods (a) were compared to the normalisation method considering the reactor pulse energy (b). To investigate the effectiveness of each normalisation method, the mean (μ) and the standard deviation (σ) of the measurement points was calculated. The fluctuation was then expressed as σ/μ and given in %. For the UCN being normalised to the pulse energy, both normalisation options yield a comparable fluctuation around the mean value, *i.e.,* 1.95 % (VCN, $N_1 = 23$) and 1.81 % (UCN, $N_2 = 11$). The normalisation to VCN is almost comparable to the normalisation to the pulse energy, with an average fluctuation of 1.62 %. A significantly smaller fluctuation of 0.74 % is found for the UCN normalisation method, which is therefore clearly superior and offers a ~ 2.5 times better normalisation than the pulse energy. Note

that the overall observed fluctuation after normalisation to the pulse energy is $\mathcal{O}(2\,\%)$ and therefore considerably larger than the fluctuation of 0.6 % discussed in Ch. 4.2.3.

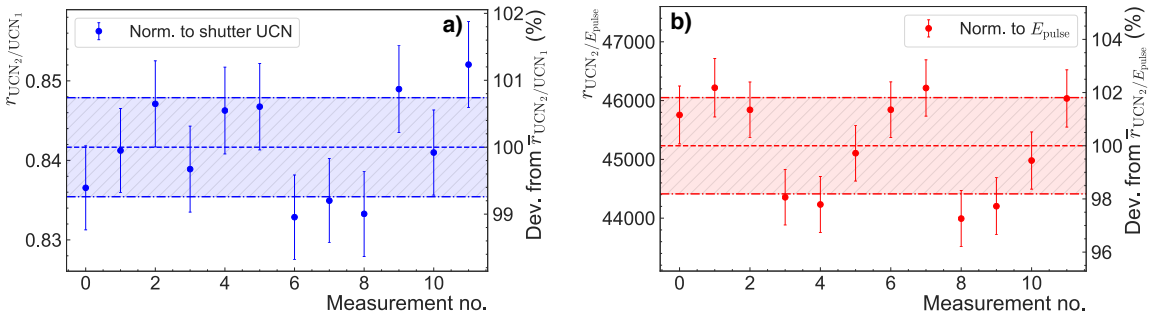

Figure 4.16: Evaluation of the normalisation to a UCN fraction (option (iii)) for $N_2 = 11$ measurements. (a) Calculating the mean (μ, dashed blue line) as well as the standard deviation (σ, dashed-dotted blue line) of the ratios r_{UCN_2/UCN_1} provides $\mu \pm \sigma = 0.8417(62)$. As a result, fluctuations of 0.74 % have been observed. (b) For comparison, the normalisation to the reactor pulse energy ($r_{UCN_2/E_{pulse}}$) gives a fluctuation of 1.81 % around the mean value of $\mu \pm \sigma = 45\,232(819)$. The right axis visualises the fluctuations around the mean in %.

For τSPECT, these measurement results clearly show that the UCN normalisation method according to option (iii) should be implemented. Due to the expected low number of UCN storable in τSPECT, the normalisation to stored UCN will remain a challenge. The previously-discussed approach to use $\sim 26\,\%$ of the UCN spectrum by driving the neutron detector into the storage volume right after the cleaning procedure should be most promising in the current state of the experiment.

4.4 Transmission and storage measurements approaching τSPECT conditions

An effective UCN guidance from the exit of the UCN D source to the full-magnetic storage volume, which is achieved by a UCN guide system ('beam line'), is crucial for the τSPECT experiment. To optimise the number of UCN guided to the τSPECT storage volume and therefore the number of storable UCN, the UCN guidance has been optimised using several experimental setups. First, an appropriate guide material for the neutron guide section leading to the storage volume (cf. Fig. 5.2) was selected by performing transmission measurements (cf. Ch. 4.4.1). Also, the detailed transmission properties of the assembled neutron guide section and its height over the UCN D source exit, which is another factor influencing the UCN yield, has been optimised by storing UCN in an material bottle.

The PSI storage bottle with a Fermi potential of $V_F(\mathrm{NiMo}) = 220\,\mathrm{neV}$ defining the maximum storable UCN energy and a volume of $V \sim 32\,\mathrm{l}$, which was formerly used to characterise the upgraded UCN source performance, was not suitable to emulate the conditions in τSPECT (maximum potential $\sim 47.0\,\mathrm{neV}$, maximally storable kinetic energy $\Delta E \sim 23.0\,\mathrm{neV}$, volume $V_{full} \sim 6.8\,\mathrm{l}$, cf. Ch. 4.4.2). Instead, the UCN were stored inside an aluminium bottle. Despite offering a larger volume of $9.67(2)\,\mathrm{l}$ (inner diameter of $\varnothing_{inner} = 150\,\mathrm{mm}$), its Fermi potential of $V_F(\mathrm{Al}) = 54\,\mathrm{neV}$ (cf. Tab. A.1) translates to a similar maximum storable UCN energy. Except for evaluating the neutron guide transmission, the aluminium storage bottle has been used for all measurements discussed in this section.

The measurement results of these preparatory studies yielded an estimate on the number of storable UCN in τSPECT (cf. Ch. 4.4.2). Based on these findings, a statistical consideration led to an estimate on the required run time of the experiment to reach an accuracy of $\Delta\tau_n \lesssim 1\,\mathrm{s}$.

4.4.1 Transmission properties of the neutron guide section

The neutron guide system inside τSPECT is composed of two neutron guide sections of lengths $\sim 174\,\mathrm{cm}$ (rear part) and $\sim 85\,\mathrm{cm}$ (front part, cf. Fig. 5.14). To find a suitable material, the transmission of the longer rear part ('long tube section') was evaluated for different tube materials and a fixed height using the 'standard' beam line, which had also been used for the UCN D characterisations (cf. Fig. 4.9). For the front part ('short tube section'), a narrowing of the UCN guide was required, which influence on the UCN transmission was also measured. Lastly, the UCN guidance of the entire neutron guide section, *i.e.,* the front part connected to the rear part, was optimised for different heights.

Material selection

First, an appropriate material for the neutron guides inside τSPECT had to be found, with the characterisation focusing on the rear part of the neutron guide ('long tube section'). Inside τSPECT, the neutron guide system is exposed to a maximum magnetic flux density of $\sim 1\,\mathrm{T}$ (cf. Fig. 5.2). The Neumo HE5 stainless steel tubes used for the source upgrade (cf. Ch. 4.2.2) offer the currently best transmission, but are not suitable since they are magnetised by the high magnetic field. The magnetisation of stainless steel leads to losses due to UCN depolarisation, as has been observed for materials such as different NiMo alloys in [BCD+17].

To prevent depolarisation losses, a copper-coated titanium tube was ordered[36]. Alternatively, a fused silica (SiO_2) tube was prepared as the guide material. For the final implementation in τSPECT, geometric constraints require an inner tube diameter of $\varnothing_{\mathrm{inner}} = 73\,\mathrm{mm}$ (cf. Ch. 5.4.1). This condition was met by both the titanium as well as the SiO_2 tube. Later in the ongoing construction process, the length of the neutron guide was defined as $l = 1.74\,\mathrm{m}$, which corresponds to the length of the custom-made SiO_2 tube[37]. The previously purchased titanium tube had a length of 1.5 m.

To compare the UCN transmission of the copper-coated titanium tube and the SiO_2 tube to the current optimum[38], the HE5 tube ($\varnothing_{\mathrm{inner}} = 70\,\mathrm{mm}$, surface roughness $R_{\mathrm{a}} \leq 0.25\,\mu\mathrm{m}$, $l = 1.5\,\mathrm{m}$), the setup depicted in Fig. 4.17 a) was constructed. The tube to be tested was inserted at the position of the orange tube in the figure. Additionally, a Nocado HE4 stainless steel tube with lower surface roughness ($R_{\mathrm{a}} \leq 0.4\,\mu\mathrm{m}$, $\varnothing_{\mathrm{inner}} = 70\,\mathrm{mm}$, $l = 1.5\,\mathrm{m}$) as well as a second SiO_2 tube with slightly too small inner diameter ($\varnothing_{\mathrm{inner}} = 72\,\mathrm{mm}$, $l = 1.8\,\mathrm{m}$) were included in the measurement. With the CASCADE neutron detector mounted in vertical extraction and no storage bottle installed, the transmission was defined as the number of

[36] The copper coating was applied by T. Lauer (Movatec GmbH, `http://www.movatec.de`).

[37] The SiO_2 tube intended to be installed in τSPECT was fabricated by TQS - Technical Quartz Solutions GmbH, `https://tqs-quartz.com`.

[38] A preliminary analysis of the tube transmission, with a smaller number of tubes included, is found in [Ros17].

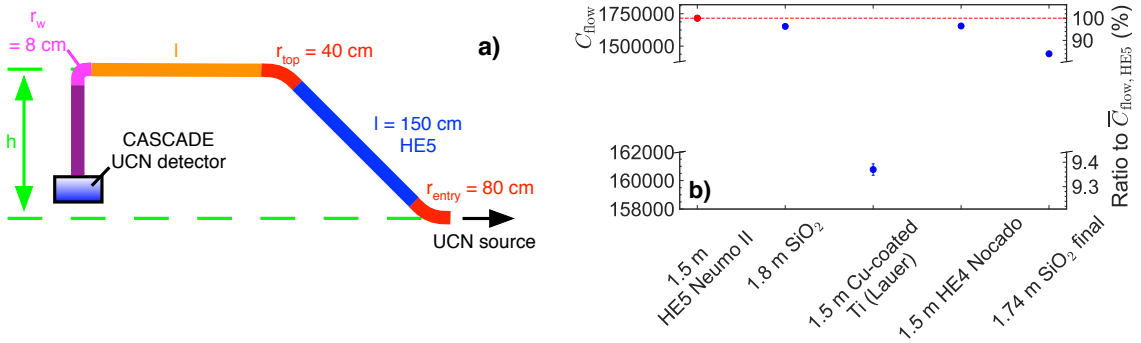

Figure 4.17: Comparison of rear part neutron guide UCN transmissions. (a) Flow mode measurement setup at 1.35 m height over source exit. For comparing the rear part ('long tube section') transmission, the horizontal section (orange) was exchanged. (b) Counts in flow mode (C_{flow}) for different horizontal tubes. The τSPECT-specific fused silica (SiO_2) tube shows a lower transmission than a 1.8 m SiO_2 tube with similar dimensions. The copper-coated titanium (Ti-Cu) tube coated by T. Lauer yielded a ten times worse transmission compared to the Neumo HE5 tube. The right axis gives the ratio to the transmission of the HE5 tube in percent.

UCN reaching the detector ('flow mode')[39]. The thermal neutrons originating from the thermal peak were subtracted from the data analysis. For a counting time of 200 s, the integral counts (C_{flow}) were evaluated.

The results of the flow mode measurements are shown in Fig. 4.17 b). In terms of transmission, the copper-coated titanium tube yielded a ten times worse result than the Neumo HE5 tube, which offered the best transmission. The exceptionally low transmission can be explained by a non-sufficient coating, leading to titanium being partly exposed to the tube's inner surface. Due to the negative Fermi potential of titanium ($V_{\mathrm{F}} = -48$ neV, cf. Tab. A.1) and its property to absorb neutrons, UCN hitting areas of exposed titanium on the surface are lost. Both the 1.8 m long SiO_2 tube with the non-fitting diameter as well as the HE4 Nocado tube offered a similar performance, yielding a $\sim 5\,\%$ worse transmission than the HE5 tube. The τSPECT-specific 1.74 m SiO_2 tube provided a $\sim 13\,\%$ lower transmission when compared to the $l = 1.8$ m SiO_2 tube. The difference likely originates from a worse surface quality of the custom-made τSPECT tube.

Impact of the narrowing on the UCN transmission

The implementation of full-magnetic storage requires adding a radial magnetic field to the longitudinal magnetic field created by the former aSPECT cryostat (cf. Fig. 4.1). In the depiction of the prototype measurement (cf. Ch. 4.1), it has been discussed that a spin flip is required for storing UCN magnetically. In order to reach a high spin flip efficiency, it has been stated that low magnetic field gradients need to be realised.

The adiabatic fast passage (AFP) spin flip efficiency[40], $\varepsilon_{\mathrm{AFP}}$, for a UCN passing the spin

[39] In flow mode, very cold neutrons (VCN) with energies higher than storable in an aluminium storage bottle ($E_{\mathrm{UCN}} > V_{\mathrm{F}}(\mathrm{Al}) = 54$ neV) are also contained in the spectrum, which are counted by the CASCADE detector and therefore contribute to C_{flow} (for an experimental proof, cf. Ch. A.5.6). Since the initial parts of the beam line were kept constant for all measurements, the VCN contribution is also constant. Therefore, a comparison of the C_{flow} values with sufficient statistics contains the information about the UCN transmission. The detection principle is presented in Ch. A.1.

[40] For a detailed explanation of the UCN spin flip mechanism, refer to Ch. 5.3.2.

flipper with velocity v, gyromagnetic ratio γ, and oscillating magnetic field amplitude B_1 is given by [HBD+12]

$$\varepsilon_{\mathrm{AFP}} > 1 - \frac{\left(\nabla_z B_0\right)^2 v^2}{\left(\nabla_z B_0\right)^2 v^2 + \gamma^2 B_1^4} \ . \tag{4.13}$$

Note that Eq. (4.13) is only valid for $\varepsilon_{\mathrm{AFP}} \gtrsim 0.9$. The equation demonstrates the dependency of $\varepsilon_{\mathrm{AFP}}$ on the gradients of the external magnetic field in the spin flip region, $\nabla_z B_0$, with values of $\nabla_z B_0 \sim 1\ \mathrm{G\,cm^{-1}}$ typically yielding a spin flip efficiency of $\gtrsim 99\,\%$, if the B_1 amplitude is sufficiently high[41].

Adding a radial magnetic field introduces additional magnetic field gradients, which need to be compensated in the spin flip region by a $\sim 15\,\mathrm{cm}$ long Halbach octupole array formed of Sm_2Co_{17} (for a detailed discussion, cf. Ch. 5.3.3). The addition of the compensating Halbach octupole, however, leads to spatial constraints in the design of the neutron guide's front part across a length of $\sim 32\,\mathrm{cm}$ (cf. Fig. 4.18), which, along with further reducing the radial gradients, causes the guide to be narrowed by somewhat more than 50 % in area (inner diameter reduced from $\varnothing_{\mathrm{inner}} = 73\,\mathrm{mm}$ to 50 mm, cf. Fig. 5.14).

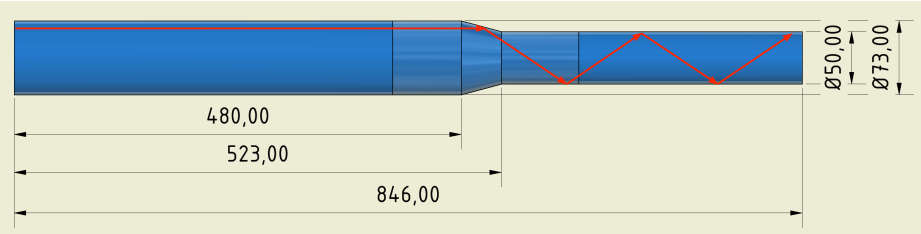

Figure 4.18: Narrowing of the neutron guide front part ('short tube section', with $l \sim 85\,\mathrm{cm}$). The SiO_2 tube's inner diameter decreases from $\varnothing_{\mathrm{inner}} = 73\,\mathrm{mm}$ to 50 mm. The red arrows indicate a UCN beam entering the neutron guide section parallel to the guide axis. Dimensions are given in units of millimetre.

For a UCN beam entering a neutron beam section with inner radius r_{full} under average emittance angle φ_{full}, the following condition holds after passing a narrowing with $r_{\mathrm{reduced}} < r_{\mathrm{full}}$:

$$r_{\mathrm{full}} \cdot \sin\left(\varphi_{\mathrm{full}}\right) = r_{\mathrm{reduced}} \cdot \sin\left(\varphi_{\mathrm{reduced}}\right) \ . \tag{4.14}$$

This condition is based on Liouville's theorem (conservation of phase space density, cf. Ch. 3.2.3) and implies that after passage of the narrowing, the average emittance angle has changed to $\varphi_{\mathrm{reduced}}$. If a beam enters the guide section with r_{full} parallel to the guide axis ($\sin\varphi_{\mathrm{full}} = 0$, cf. Fig. 4.18), no transmission losses occur upon passage of the narrowing, since Eq. (4.14) is valid. The equation is no more valid for a diffuse UCN beam with $\varphi_{\mathrm{full}} \gtrsim 45°$, since this would demand $\sin\left(\varphi_{\mathrm{reduced}}\right) > 1$. Therefore, for $\varphi_{\mathrm{full}} \gtrsim 45°$, the number of UCN after the narrowing is decreased. Thus, the transmission T is reduced by the squared ratio of the inner guide radii,

$$T \sim 1 - \left(\frac{r_{\mathrm{reduced}}}{r_{\mathrm{full}}}\right)^2 \ . \tag{4.15}$$

[41] In the UCNA experiment, $\varepsilon_{\mathrm{AFP}} = 99.9\,\%$ at $\nabla_z B_0 = 0.6\,\mathrm{G\,cm^{-1}}$ and $B_1 \sim 0.25\,\mathrm{mT}$ was reached [HBD+12].

For the neutron guide geometry with $r_{\text{reduced}} = 25\,\text{mm}$ and $r_{\text{full}} = 36.5\,\text{mm}$, a diffuse spectrum would yield a UCN of transmission loss of $\sim 50\,\%$. Apart from the discussed effect on the transmission in the direction 'left to right' (cf. Fig. 4.18), the narrowing also affects the UCN diffusion in the opposite direction during the filling of UCN into a storage bottle. The associated probability of back diffusion, which is > 0 due to the shutter S_1 (cf. Fig. 4.19) being open during filling, decreases with smaller inner tube radii since the resulting smaller area leads to a smaller probability for UCN to escape the storage volume. To conclude, the measurable effect of the narrowing on the UCN transmission is a superposition of both phenomena.

To measure the effect of the narrowing on the UCN transmission, the UCN were filled into an the aluminium storage bottle with a volume of 9.696(16) l at a fixed height of 1.35 m (cf. Fig. 4.19). The aluminium storage bottle was chosen since it emulates the full-magnetic storage conditions found in τSPECT. In the first measurement run, the short SiO_2 tube section with included narrowing (cf. Fig. 4.18) was added in front of the storage volume. The front of the SiO_2 section was placed immediately before the entry shutter S_1 using a custom adapter. In the second measurement run, the tube section shown in Fig. 4.18 was replaced by a SiO_2 tube with same length but constant inner diameter ($l = 85\,\text{cm}$, $\varnothing_{\text{inner}} = 73\,\text{mm}$). Thus, the influence of the narrowing on the UCN transmission could be investigated.

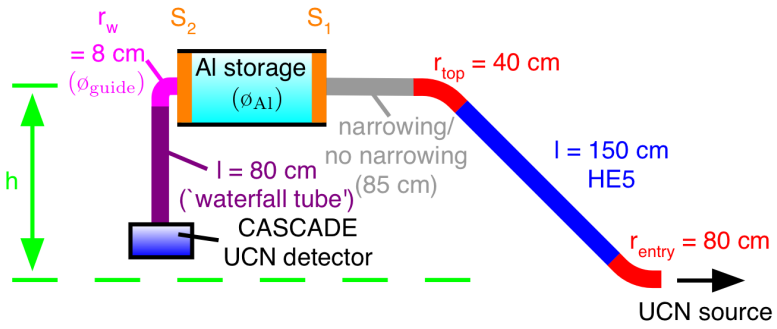

Figure 4.19: Setup to evaluate impact of the neutron guide narrowing on the UCN density after aluminium storage. The short tube section was installed just before the shutter S_1 and later exchanged with a straight fused silica tube of same length and inner guide dimension. The UCN were stored in an aluminium storage bottle (inner diameter $\varnothing_{\text{Al}} = 15\,\text{cm}$, with overall guide diameter of $\varnothing_{\text{guide}} = 6.6\,\text{cm}$) to emulate the energy spectrum later found in τSPECT. The setup was mounted at $h = 1.35\,\text{m}$ above source exit, which is the typical height reached with the 'standard' beam line.

As the storage curves in Fig. 4.20 illustrate, the narrowing has a small effect on the number of stored UCN in aluminium. At a storage time of 20 s, which limits the maximum stored UCN energies to V_{F}, the number of stored UCN after passing the narrowing is $\sim 10\,\%$ less than without the narrowing. In conclusion, the combined effect of the narrowing on the transmission as well as on the back diffusion has been measured to have a $\sim 10\,\%$ impact on the number of UCN storable in τSPECT.

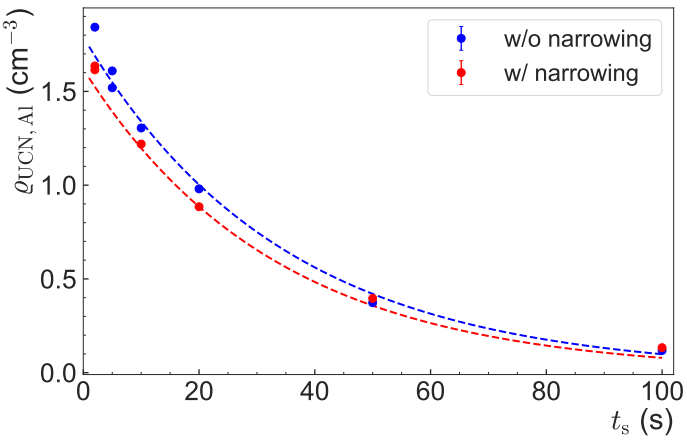

Figure 4.20: Storage curve for narrowed front tube part (red) compared to straight tube (blue) after UCN storage in the aluminium bottle, with the stored UCN density $\varrho_{\mathrm{UCN,\,Al}}$ plotted as a function of storage time, t_{s}. The dashed lines guide the eye and are no fit to the data. The error bars are smaller than the symbol size.

Height dependence of the neutron guide system

An effective guidance of UCN from the source to the experiment at optimal height is of high importance. The energy spectrum of the UCN exiting the source starts at the Fermi potential of the converter sD_2, *i.e.*, $E_{\mathrm{UCN,\,source}} \gtrsim V_{\mathrm{F}}(sD_2) = 105\,\mathrm{neV}$ [ADF$^+$08, KRR$^+$17]. Since UCN lose $\sim 102\,\mathrm{neV}$ per metre (cf. Ch. 3.2.1), they can be decelerated by being guided along beam lines leading to increasing heights. An optimal height needs to be considering both the efficiency of the deceleration and also the transmission loss which increases with beam line length. Previously, the transmission properties of the neutron guides within the experiment have been discussed in detail (cf. Ch. 4.4.1), but no height optimisations have been performed yet. Now, the findings on the total transmission after connecting the front part ('short tube section', $l = 85\,\mathrm{cm}$, cf. Fig. 4.18) and the rear part ('long tube section', $l = 174\,\mathrm{cm}$) of the neutron guide are presented, without evaluating the influence of the narrowing by comparison to a straight tube section.

As is known from previous characterisation measurements of the UCN D source (cf. Fig. A.11 a), the UCN density of UCN stored in an aluminium storage bottle increases with higher heights. To investigate the impact of the height over the source exit on the filling efficiency in τSPECT, the entire inner (fused silica) part of the neutron guide system was installed at varying heights over the source exit before final commissioning. To quickly adapt the height, a measurement setup with a vertical beam line section formed by a HE5 stainless steel tube[42] was chosen (cf. Fig. 4.21). Please note that the used beam line offered a notably better transmission than the later-used beam line for the first τSPECT measurements. As could be inferred from additional measurements, the τSPECT beam line offered only $\sim 40\,\%$ of the transmission compared to the 'standard' beam line (based on the density of UCN stored in an aluminium storage bottle for both beam lines, cf. Ch. A.5.4)[43].

Fig. 4.22 a) shows the result of the filling time optimisation, which implies measuring the

[42] Tubes electropolished according to HE5 standard have a low surface roughness of $R_{\mathrm{a}} \leq 0.25\,\mu\mathrm{m}$.

[43] Apart from a characterisation of the beam line used in the τSPECT measurements, Ch. A.5.4 contains detailed measurements on the influence of beam line radii on the UCN transmission.

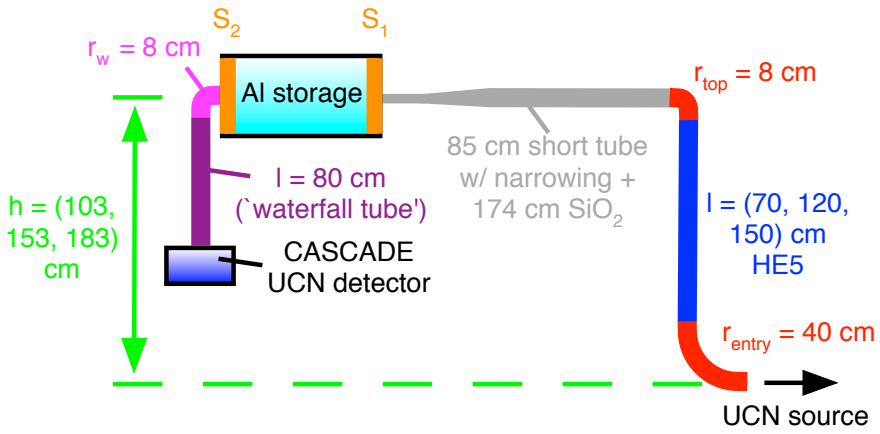

Figure 4.21: Setup to measure the height dependence of the τSPECT neutron guide. The beam line consisted of a vertical stainless steel HE5 tube (blue) in-between two 45° radii for easy height adaption. Horizontally, the whole inner part of the neutron guide section was installed (grey). The UCN were stored in an aluminium storage bottle to emulate the storage conditions in τSPECT.

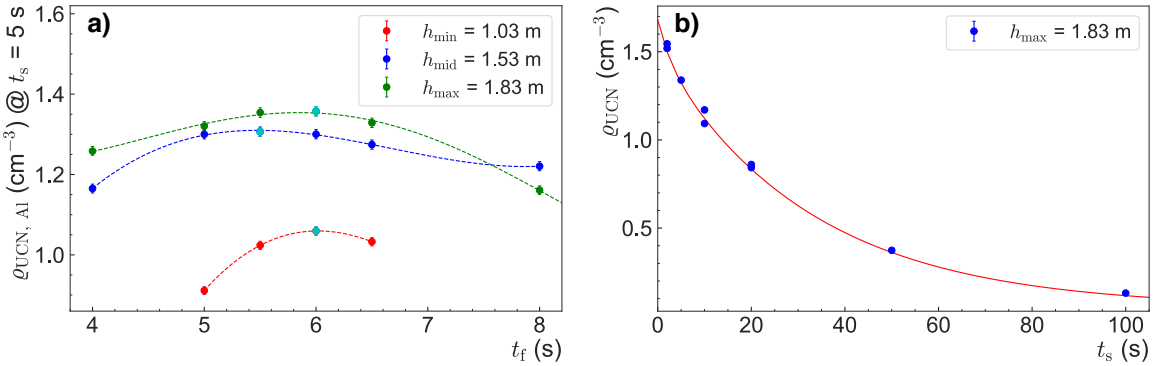

Figure 4.22: Height-dependence measurement of the τSPECT neutron guide. (a) UCN density $\varrho_{\mathrm{UCN,\,Al}}$ after storage time $t_s = 5\,s$ as a function of filling time, t_f for heights $h_{min} = 1.03\,m$ (red data points), $h_{mid} = 1.53\,m$ (blue data points), and $h_{max} = 1.83\,m$. The data points represent the actually measured density at $t_s = 5\,s$, with no further calculations involved. The filling time values yielding the highest density are depicted in cyan for all heights. The dashed lines guide the eye. (b) UCN density $\varrho_{\mathrm{UCN,\,Al}}$ as a function of t_s at h_{max}. A biexponential fit with parameters $A_1 = 0.18(1)\,cm^{-3}$, $A_2 = 1.45(6)\,cm^{-3}$, $\tau_1 = 2.74(49)\,s$, $\tau_2 = 32.55(3.36)s$ is depicted by the red line. The error bars are smaller than the symbol size.

UCN density after a storage time of $t_s = 5\,s$ for varying filling times[44], t_f. The difference between $h_{min} = 1.03\,m$ and $h_{mid} = 1.53\,m$ is striking, as $\sim 23\,\%$ more UCN are storable at h_{mid}. Only a minor difference of $\sim 4\,\%$ between the values of $h_{mid} = 1.53\,m$ and $h_{max} = 1.83\,m$ is found. Remarkable is the flatness of the filling optimisation curve at the optimal height of both h_{mid} and h_{max}, as the values in between $t_f = 5.0\,s$ and $6.5\,\%$ only fluctuate by $\lesssim 3\,\%$ percent. Even at $t_f = 4.0\,s$ and $8.0\,s$, the UCN density is only decreased by $11\,\%$ and $7\,\%$, respectively.

[44] After $t_s = 5\,s$, the spectrum is cleaned, *i.e.*, $E_{\mathrm{UCN,\,max}} = V_F(\mathrm{Al}) = 54\,neV$.

Fig. 4.22 b) depicts the storage curve at h_{max}, which results are used to estimate the number of UCN storable in τSPECT (cf. Ch. 4.4.2). The setup at the chosen height allows for reaching UCN densities similar to the results at $h = 1.35\,\mathrm{m}$ (cf. Fig. 4.20) using the 'standard' beam line (cf. Fig. 4.19). Due to the non-availability of longer neutron guide tubes, 1.59 m was chosen as the final height for the τSPECT experiment (cf. Ch. 6.2.1), which approximately equals h_{mid}.

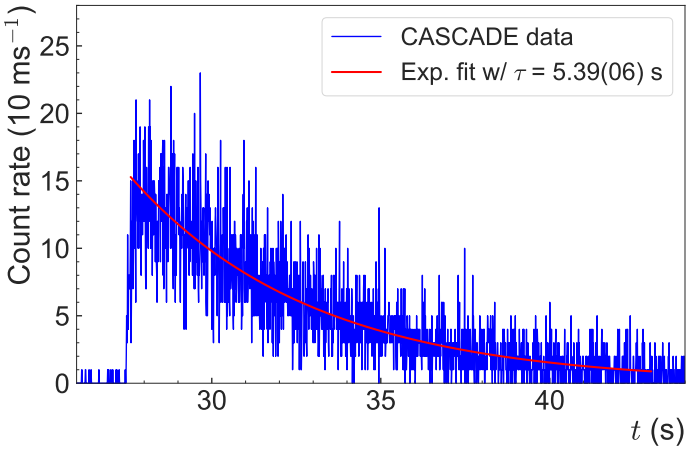

Figure 4.23: Emptying time constant observed with the aluminium storage bottle at $h_{\mathrm{max}} = 1.83\,\mathrm{m}$ (cf. Fig. 4.21). After a filling time of $t_{\mathrm{f}} = 6\,\mathrm{s}$ and a storage time of $t_{\mathrm{s}} = 20\,\mathrm{s}$, the UCN were reaching the detector when the shutter S_2 opened. For the emptying process, a time constant of $\tau = 4.91(6)\,\mathrm{s}$ was determined from an exponential fit to the data (red line).

From the measurements at $h_{\mathrm{max}} = 1.83\,\mathrm{m}$, the signal when 'emptying' the bottle, *i.e.,* the count rate measured in the CASCADE detector after the shutter S_2 is opened, has been fitted using an exponential function (cf. Fig. 4.23). The extracted time constant $\tau = 5.39(6)\,\mathrm{s}$ implies that 95 % of the UCN have escaped from the aluminium storage bottle after $3\tau \sim 16\,\mathrm{s}$. This analysis is relevant to systematic investigations in τSPECT, since it emulates the conditions when enabling the spin flipper while the neutron guide system is driven inside the full-magnetic storage volume (cf. Ch. 6)[45]. Considering the inner diameters of the storage volumes and the neutron guides, the conditions found in the discussed aluminium bottle measurement ($\varnothing_{\mathrm{Al}} = 15\,\mathrm{cm}$, guide with $\varnothing_{\mathrm{guide}} = 6.6\,\mathrm{cm}$ centred at end of storage volume, cf. Fig. 4.19) is similar to those in the full-magnetic storage volume ($\varnothing_{\mathrm{full}} = 10.8\,\mathrm{cm}$, narrowed guide with $\varnothing_{\mathrm{reduced}} = 5\,\mathrm{cm}$). Consequently, a similar time constant for emptying the storage volume by enabling the spin flipper inside the τSPECT cryostat can be assumed.

4.4.2 Estimation on the number of storable UCN in τSPECT and first statistical considerations

To estimate the number of fully-magnetically storable UCN in τSPECT, the maximally storable kinetic energy with the magnetic field configuration for full-magnetic storage needs to be computed first. Following the description in Ch. 4.1 and adapting it to the concept of

[45] In its final implementation in the τSPECT experiment, the neutron guide can be moved into the storage volume during the filling of UCN and retracted from it to prevent material wall interactions during the storage phase. For further details on the measurement sequence, refer to Ch. 5.1.2.

full-magnetic storage, the maximum kinetic energy of incoming UCN which can be stored (ΔE) is determined by the maximum magnetic potential in the trap and the magnetic potential at the spin flip position. With the Halbach octupole defining the maximum potential (47 neV, cf. Ch. 5.3.1), ΔE is highly sensitive to the spin flip position. At the τSPECT design spin flip position of $z_{\mathrm{sf}} \sim 1100\,\mathrm{mm}$ (cf. Ch. 5.3.3), a magnetic field of $B_{\mathrm{sf}} \sim 0.2\,\mathrm{T}$ gives a potential energy of $E_{\mathrm{pot,\,mag}} = 60.3\,\mathrm{neV\,T^{-1}} \cdot B_{\mathrm{sf}} = 12.0\,\mathrm{neV}$ for a HFS converted to a LFS after spin flip. Correspondingly, a kinetic energy of $E_{\mathrm{kin}} = 12.0\,\mathrm{neV}$ results (cf. Ch. 4.1 for a detailed discussion). From Eqs. (4.1) and (4.2), a maximally storable kinetic energy of

$$\Delta E \sim 47\,\mathrm{neV} - 2 \cdot 12\,\mathrm{neV} \sim 23\,\mathrm{neV} \tag{4.16}$$

follows, which implies that UCN with initial energies of $[0, 23]$neV are accepted for storage in the full-magnetic implementation of τSPECT. The high sensitivity on the spin flip position is especially striking when considering the conditions during the first storage measurements, during which a spin flip at a longitudinal field position of $B_{\mathrm{main}} \sim 0.338\,\mathrm{T}$ (cf. Ch. 6.2.2) led to $\Delta E \sim 6.2\,\mathrm{neV}$, significantly reducing the number of storable UCN.

Compared to the prototype measurements (cf. Ch. 4.1), the full-magnetic storage causes the maximum potential energy in the storage volume to be reduced from the fused silica tube's Fermi potential ($V_{\mathrm{F,\,SiO_2}} = 90\,\mathrm{neV}$) to 47 neV, which leads to a reduction in the number of storable UCN[46] by a factor of [GRL91]

$$\left(\frac{\Delta E_{\mathrm{prototype}}}{\Delta E}\right)^{\frac{3}{2}} \sim \left(\frac{48.8\,\mathrm{neV}}{23.0\,\mathrm{neV}}\right)^{\frac{3}{2}} \sim 3.1\ . \tag{4.17}$$

Moreover, the storage volume has increased from $V_{\mathrm{prototype}} \sim 3.5\,\mathrm{l}$ to $V_{\mathrm{full}} \sim 6.8\,\mathrm{l}$, which implies that a factor of $V_{\mathrm{full}}/V_{\mathrm{prototype}} \sim 1.9$ more UCN can be stored.

For the quantitative estimation on storable UCN in τSPECT, the measurements in which UCN were stored in the 9.696(16) l aluminium storage bottle after entering through the narrowed neutron guide section at $h_{\mathrm{max}} = 1.83\,\mathrm{m}$ were considered (cf. Fig. 4.21). Thus, conditions close to the full-magnetic storage in τSPECT were emulated. For this, it needs to be considered that in an aluminium storage bottle, UCN up to the Fermi potential of aluminium ($V_{\mathrm{F}}(\mathrm{Al}) = 54\,\mathrm{neV}$, cf. Tab. A.1) are stored, with the UCN density and thus the number of storable UCN being proportional to $(V_{\mathrm{F}}(\mathrm{Al}))^{3/2}$ (cf. Eq. 3.15). This number is compared to the ΔE value in Eq. (4.16), which implies that in τSPECT the number of storable UCN decreases by a factor of $(23\,\mathrm{neV}/54\,\mathrm{neV})^{3/2} \sim 0.28$.

The resulting estimation on the number of UCN, C_{UCN}, along with all decreasing effects, is provided in Tab. 4.2. The initial value of 14 050(650) stored UCN extrapolated to storage time $t_{\mathrm{s}} = 0\,\mathrm{s}$ was directly determined from the A_2 constant of the biexponential fit to the respective storage curve (cf. Fig. 4.22 b). First, the UCN spin polarisation (cf. Ch. 4.1) leads to a loss factor of 50 % if a spin flip efficiency $\varepsilon_{\mathrm{AFP}} = 100\,\%$ is assumed. As noted above, the difference in energy acceptance gives the reducing factor $(23\,\mathrm{neV}/54\,\mathrm{neV})^{3/2} \sim 0.28$, which must be applied to the data. Lastly, a volume scaling factor of $6.8\,\mathrm{l}/9.7\,\mathrm{l} \sim 0.70$ is introduced to account for the smaller τSPECT volume of $\sim 6.8\,\mathrm{l}$. The resulting estimate on the number of UCN storable in τSPECT depending on the storage time t_{s} is thus ~ 1370 ($t_{\mathrm{s}} = 0\,\mathrm{s}$).

[46] The storable density of UCN as a function of maximum potential is described in Eq. (3.15).

Table 4.2: Details on the estimate on storable UCN in τSPECT. Given are several effects decreasing the estimated number C_{UCN} extrapolated to the storage time $t_{\mathrm{s}} = 0\,\mathrm{s}$. The calculation is explained in the text.

Effect on number of storable UCN	$C_{\mathrm{UCN}}(t_{\mathrm{s}} = 0\,\mathrm{s})$
Extracted from biexponential fit (Al storage)	14 050(650)
Spin polarisation	~ 7020
Proportion storable UCN	~ 1960
Volume scaling factor	~ 1370

The expectable number of UCN in the storage volume can now be used to estimate the required measurement time to reach a neutron lifetime precision of $\Delta\tau_n \leq 1\,\mathrm{s}$. Note that the following analysis only considers the effect of statistical fluctuations, without taking currently unknown systematic effects into account. Based on the results in Tab. 4.2, 1370 initial UCN extrapolated to storage time $t_{\mathrm{s},\,0} = 0\,\mathrm{s}$ were considered ($C_{\mathrm{UCN}}(t_{\mathrm{s},\,0}) = 1370$). According to

$$C_{\mathrm{UCN,\,expect}}(t_{\mathrm{s}}) = C_{\mathrm{UCN}}(t_{\mathrm{s},\,0}) \cdot \exp\left(-t_{\mathrm{s}}/\tau_n\right) \tag{4.18}$$

with $\tau_n = 879.4\,\mathrm{s}$ (cf. Fig. 3.3), expectation values $C_{\mathrm{UCN,\,expect}}(t_{\mathrm{s}})$ were generated for the hypothetical measurement sequence

$$t_{\mathrm{s}} = (50, 200, 400, 800, 1000)\ \mathrm{s}\ . \tag{4.19}$$

For a complete measurement cycle, several additional time periods need to be taken into account (cf. Fig. 4.24, for a detailed description of the measurement cycle refer to Ch. 5.1.2). Considering all time periods involved in a measurement cycle and the fact that the reactor is ready for pulsing every $\sim 12\,\mathrm{min}$ implies that for measuring the storage time sequence in Eq. (4.19), a total time of $\sim 4200\,\mathrm{s}$ is needed.

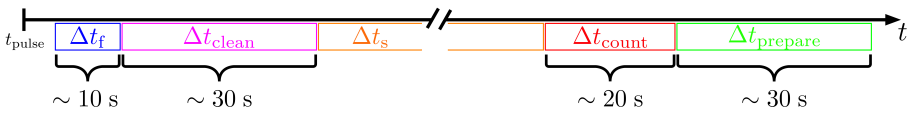

Figure 4.24: Schematic time line of the entire τSPECT measurement cycle, starting with the reactor pulse at t_{pulse}. Additional to the variable storage time Δt_{s}, which is given by Eq. (4.19), the measurement cycle consists of a filling time (Δt_{f}), a cleaning time ($\Delta t_{\mathrm{clean}}$), a counting period ($\Delta t_{\mathrm{count}}$), and a time to prepare the system for the upcoming reactor pulse (t_{prepare}).

Using a random number generator, Gaussian-distributed values fluctuating statistically around the expectation values were created, *i.e.*,

$$C_{\mathrm{UCN}}(t_{\mathrm{s}}) = C_{\mathrm{UCN,\,expect}}(t_{\mathrm{s}}) \pm \sqrt{C_{\mathrm{UCN,\,expect}}(t_{\mathrm{s}})}\ . \tag{4.20}$$

New values were generated N times (N refers to the number of measurement sequences in

Eq. (4.19)) until an optimisation routine implemented in Wolfram Mathematica[47] based on an exponential fit yielded an error $\Delta\tau_n \leq 1\,\mathrm{s}$. Fig. 4.25 a) shows an exemplary storage curve for $N = 100$ measurement sequences. After the optimisation routine had found $\Delta\tau_n$ values $\leq 1\,\mathrm{s}$, the routine was run again for five times to gain sufficient statistics.

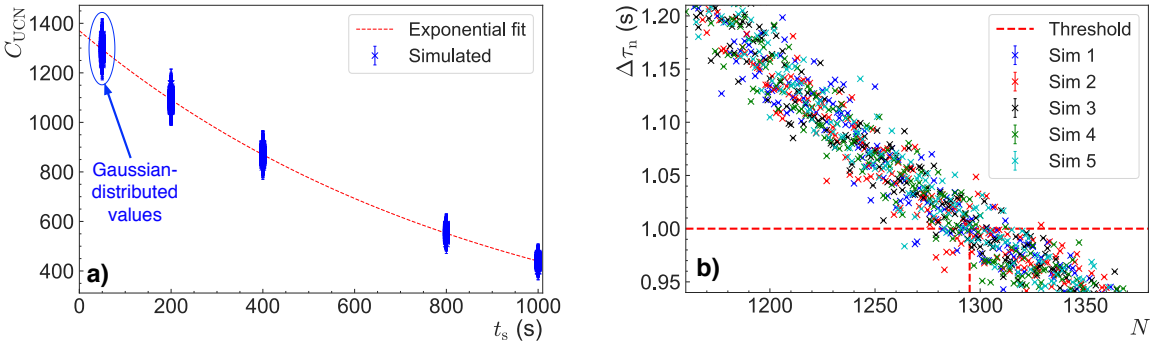

Figure 4.25: Statistical consideration for determining the measurement time required for a precision of $\Delta\tau_n = 1\,\mathrm{s}$. (a) Exemplary storage curve for $N = 100$ measurement sequences according to Eq. (4.19). Plotted are the Gaussian-distributed number of UCN counts ($C_{\mathrm{UCN}}(t_s) = C_{\mathrm{UCN,\,expect}}(t_s) \pm \sqrt{C_{\mathrm{UCN,\,expect}}(t_s)}$) against the storage times $t_s = (50, 200, 400, 800, 1000)$ s (blue data points). The red dashed line represents the exponential fit with $C_{\mathrm{UCN}}(t_{s,\,0}) = 1370$ and $\tau_n = 879.4\,\mathrm{s}$. (b) Accuracy $\Delta\tau_n$ as a function of measurement cycles, N. The data was obtained from running an optimisation routine (sim), which was repeated 5 times to increase statistics. The condition $\Delta\tau_n \leq 1\,\mathrm{s}$ (red dashed horizontal line) is fulfilled if $N \geq 1295$ (red dashed vertical line), which equals ~ 101 measurement days. On average, 68 pulses were considered per day.

As Fig. 4.25 b) shows, a total number of $N \geq 1295$ measurement sequences leads to $\Delta\tau_n \leq 1\,\mathrm{s}$. Considering a typical double-shift operation with 15 hours daily data taking, this corresponds to ~ 101 measurement days, with 68 daily pulses on average. Taking weekend breaks into account, ~ 4.6 months of total measurement time would be required to reach the aforementioned accuracy.

Since the estimation relies on a spin flip efficiency of 100 %, the expectable number of stored UCN in these early measurements should be lower. Due to the gradients in the spin flip region (cf. Ch. 4.4.1), achieving a high spin flip efficiency remains an experimental challenge and therefore strongly influences the number of storable UCN. The discussion also shows that in the present state, τSPECT is limited by its low acceptance to initial kinetic energies, which is due to its currently-implemented spin flip mechanism.

[47] For the calculation, Wolfram Mathematica 11.0.1.0 was used. The commercial software (`https://www.wolfram.com/mathematica/`) is widely used for technical computing.

5 Setup of the τSPECT experiment for full-magnetic storage (phase I)

The implementation of full-magnetic storage requires a complete re-design of the cryostat's internals and closer surroundings. Based on the shortcomings identified during the 2015 prototype measurement, the necessary modifications are discussed and, along with their function during the measurement sequence, presented to the reader in schematic form (cf. Ch. 5.1).

The remaining sections refer to the technical details of the central components and also cater to the physical requirements in detail. At first, the vacuum chamber system containing the translation stage for moving the spin flip unit inside the cryostat is discussed (cf. Ch. 5.2). Next, the physical consequences resulting from the installation of the Halbach octupole along with the challenges during the installation process are laid out (cf. Ch. 5.3). The movable neutron guide section with the installed spin flip unit is shown in Ch. 5.4. Being responsible for the efficient detection of ultracold neutrons (UCN), the movable custom UCN detector along with characterisation studies and its movement mechanics is presented (cf. Ch. 5.5). Finally, the data acquisition concept is demonstrated (cf. Ch. 5.6).

5.1 Towards full-magnetic storage - Necessary modifications

This section involves the technical modifications needed to prepare τSPECT for the first measurement phase, which aims to measure the neutron lifetime with an accuracy of $\Delta\tau_n = 1\,\mathrm{s}$. The modifications are motivated and summarised in Ch. 5.1.1. To prepare the reader with the necessary information to understand the involvement of the modified components in the τSPECT measurement sequence, Ch. 5.1.2 provides a series of schematic drawings.

5.1.1 From the prototype measurement to full-magnetic storage

The most important step towards full-magnetic storage was to provide radial magnetic storage. As shown in Fig. 5.1, the storage concept relies on the superposition of a longitudinal field (red) and a radial magnetic field (blue). The superimposed magnetic fields create a storage volume in the magnetic potential minimum, in which the UCN are fully-magnetically trapped (green). Since both longitudinal field and radial field can remain 'static' during measurement conditions, it was decided to use a Halbach octupole permanent magnet array to create the radial magnetic field.

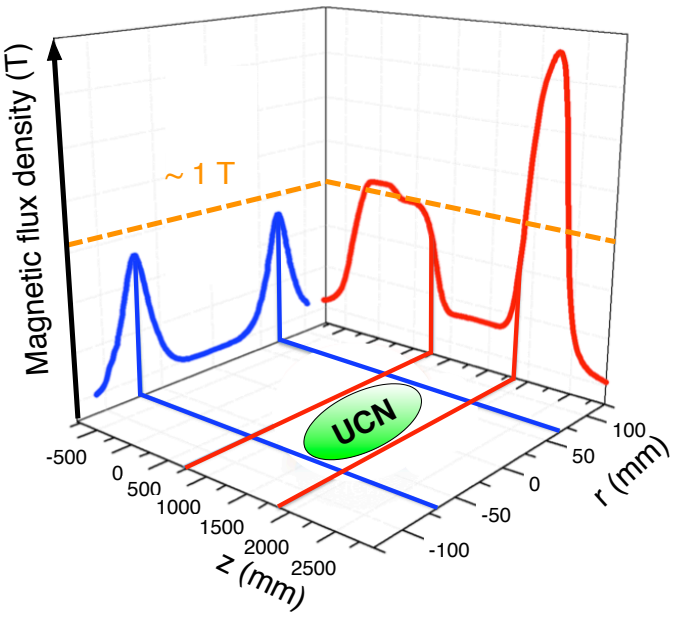

Figure 5.1: Concept of full-magnetic storage. The UCN are trapped in the magnetic field potential minimum (green), which is created by a superposition of the longitudinal (red, created by *a*SPECT superconducting coils) and radial (blue, invoked by permanent magnet array in Halbach octupole configuration) magnetic fields. Figure adapted from [Dra14].

The inclusion of the $\sim 150\,\mathrm{kg}$ Halbach octupole array into the former *a*SPECT cryostat has led to severe challenges in the design process. With regards to cryogenic conditions, the local temperatures required to operate the niobium-titanium superconducting coils[1] generating the longitudinal magnetic field had to be reached. For all components added at the outside of the cryostat, great care had to be taken to suppress the thermal flux into the inner of the cryostat by thermal insulation. Also, the inclusion of the Halbach octupole and further components affect the pressure conditions (degassing). The system therefore had to be designed to reach a vacuum of at least $\sim 10^{-7}\,\mathrm{mbar}$, which would reduce UCN losses due to upscattering by interactions with residual gas atoms. At the given pressure level, a contribution of $\Delta\tau_n \sim 0.2\,\mathrm{s}$ [Ezh19] would follow.

Due to its resulting magnetic field shape, another implication of the Halbach octupole is the introduction of strong radial gradients. At the inner surface of the Halbach octupole ($r \sim 50\,\mathrm{mm}$), the UCN are exposed to radial gradients up to $\nabla_r B \sim 5400\,\mathrm{G\,cm^{-1}}$. Since the UCN spin flip efficiency is highly dependent on the gradients within the spin flip volume (cf. Eq. (4.13)), which is determined by the volume covered by the radio frequency (RF) coil (V_{RF}), a compensation octupole was built to - assuming an idealised case - reduce the gradients in V_{RF} to $\nabla_r B \sim 0\,\mathrm{G\,cm^{-1}}$. Considering this idealised case, the spin flip efficiency would only be affected by the longitudinal field gradient, which is $\sim 3\,\mathrm{G\,cm^{-1}}$. This field gradient would correspond to the conditions during the prototype measurements, with no radial magnetic storage (cf. Ch. 4.1). The compensation octupole, which was designed and commissioned by K. Ross, offered no perfect compensation. Owing to geometrical constraints, slightly differing energy densities of the used Sm_2Co_{17} permanent magnets, non-

[1] Niobium-titanium (NbTi) reaches its superconducting transition temperature at $T_c = 9\,\mathrm{K}$ [SML04].

constant local temperatures after cooldown, and mechanical uncertainties, a maximum radial gradient of $\nabla_r B_{\text{radial}} \sim 215\,\text{G}\,\text{cm}^{-1}$ after narrowing the neutron guide to $r_{\text{inner}} = 25\,\text{mm}$ (cf. Ch. 5.3.3) was reached.

Since the spin flip occurs within the storage volume, the spin flip unit including the compensation octupole along with the non-magnetisable neutron guide[2] must be removed from the storage volume to prevent losses due to material interactions. To enable the maximum required movement range of $\Delta z \sim 730\,\text{mm}$, a differentially-pumped vacuum chamber system[3] has been added to the cryostat, which contains the translation stage to move the entire neutron guide section of $\sim 2.6\,\text{m}$ length.

To achieve a high UCN extraction efficiency, a boron-10-coated custom UCN detector has been designed which moves into the storage volume to absorb the UCN with high efficiency. Due to the cryogenic environment, the detector was designed to work in temperature conditions $\sim (150 - 200)\,\text{K}$ and at high magnetic fields up to $\sim 1.7\,\text{T}$. The associated movement mechanics could be placed in ambient conditions and permits a longitudinal movement by $\sim 266\,\text{mm}$.

All requirements which had to be fulfilled to convert the *a*SPECT cryostat into the full-magnetic storage experiment τSPECT are now summarised in order of appearance:

(i) Retract the neutron guide section from the storage volume after filling by a translational movement of $\leq 730\,\text{mm}$ such that no material wall interaction losses occur during storage (cf. Ch. 5.2),

(ii) install the Halbach octupole inside the cryostat with high precision to achieve radial storage (cf. Ch. 5.3),

(iii) use non-magnetisable neutron guides inside the cryostat to avoid depolarisation effects (cf. Ch. 5.4),

(iv) reduce the radial gradients caused by the Halbach octupole magnetic field in the spin flip region to achieve a higher spin flip efficiency using a compensation octupole (cf. Ch. 5.4),

(v) realise a custom neutron-absorbing detector operational in high longitudinal magnetic fields up to $\sim 1.7\,\text{T}$ and at low temperatures $\mathcal{O}(150 - 200)\,\text{K}$ which can be moved into the storage volume by $\sim 250\,\text{mm}$ for UCN counting (cf. Ch. 5.5 and for details on the detector electronics, cf. Ch. B.3),

(vi) provide modularity in the UCN detector mechanics to allow for a later replacement of the UCN detector by a proton detector (detection of decay protons, *e.g.* by a silicon drift detector as used in *a*SPECT [BGB+19]) to provide 4π proton detection with an added proton mirror electrode in phase II (cf. Ch. 5.5),

(vii) control the relevant components remotely and log the required data (cf. Ch. 5.6),

(viii) keep the vacuum at $\sim 10^{-7}\,\text{mbar}$ in the storage volume to reduce UCN upscattering due to interactions with residual gas atoms (considered in all technical modifications, cf. Ch. 6.1.1 for the resulting pressure values),

[2] Moving inside the cryostat, the neutron guide is exposed to magnetic fields of $\sim 1\,\text{T}$. To avoid UCN losses due to depolarisation, a non-magnetisable material must be selected.

[3] The differential pumping is required to separate the cryostat main vacuum from the vacuum of the attached beam line.

(ix) reduce the heat load from components with direct room temperature contact to the inside of the cryostat to guarantee the temperature conditions required for operating the longitudinal field-creating superconducting coils (relevant for all designed parts, cf. Ch. 6.1.1 for a summary of the final temperature readings).

As indicated above, a detailed depiction of the design process and the technical realisation of listed requirements is provided in the referenced sections. Requirement (vi) refers to phase II of τSPECT, which will focus on the in-situ detection of decay protons. This will be made possible by adding a mirror electrode and reusing the detector mechanics. Thus, an independent access to measuring the neutron lifetime is provided.

5.1.2 Introduction to relevant components and the measurement sequence

In Fig. 5.2, all relevant components are depicted. The *a*SPECT cryostat (light green) is surrounded by a magnetic shielding (dark grey) and provides the cryogenic conditions for the operation of the longitudinal magnetic field (dark blue, magnetic flux density shown on left axis). Furthermore, a scale is drawn, with the zero point $z = 0\,\mathrm{mm}$ defined by the former *a*SPECT decay volume. The Halbach octupole, which has been installed inside the cryostat, provides the magnetic field in radial direction (dark green, left axis gives magnetic flux density). The superposition of both fields leads to the storage volume (light orange, cf. top of Fig. 5.3).

The figure also shows the adiabatic fast passage (AFP) spin flipper moved inside the cryostat (orange), which marks its position during the filling process (orange line). Left of the spin flipper, the movable part of the neutron guide section is depicted (light blue), which is connected to the translation stage (red) within the vacuum chamber assembly. To carry the additional weight, the vacuum chamber is placed on a fixation platform (black). The movable part glides over the static neutron guide section (yellow), which provides the connection to the stainless steel beam line. On the right side of the storage volume, the movable neutron detector is shown, with its neutron-absorbing boron-10 layer marked in red (position given by red line).

To understand the physical function of the involved components, the measurement sequence for extracting the neutron lifetime is explained in the following, visualised by schematic drawings (cf. Figs. 5.2 and 5.3):

(i) **Filling process:** The UCN produced right after the reactor pulse (t_{pulse}) are guided from the source to the potential minimum of the magnetic flux density by driving the movable part of the neutron guide into the storage volume (cf. Fig. 4.2). 50 % of the UCN belong to the 'high-field-seeker' (HFS) spin state, while the remaining 50 % are termed 'low-field seekers' (LFS, cf. Ch. 3.2.1). By performing an AFP spin flip at $t_{\mathrm{AFP,\,start}}$, the UCN spin state is transformed from HFS to LFS ('low-field seeker') with a certain efficiency $\varepsilon_{\mathrm{AFP}}$. The remaining UCN with HFS spin state and the LFS with energies greater than the first magnetic bump ($E_{\mathrm{UCN}} \sim 1\,\mathrm{T} \cdot 60\,\mathrm{neV\,T^{-1}} \sim 60\,\mathrm{neV}$) reach the detector situated in the second magnetic bump for providing a normalisation method. Defining the maximum potential energy for full-magnetic UCN storage, the maximum field inside the Halbach octupole ($B_{\mathrm{octupole,\,max}}$) gives $E_{\mathrm{UCN,\,pot,\,max}} \sim B_{\mathrm{octupole,\,max}} \cdot 60\,\mathrm{neV\,T^{-1}} \sim 0.78\,\mathrm{T} \cdot 60\,\mathrm{neV\,T^{-1}} \sim 47\,\mathrm{neV}$. The minimum potential energy of UCN spin-flipped to the LFS state[4] depends on the magnetic field potential

[4] A more detailed explanation of the spin flip concept for UCN storage is provided in Ch. 4.1.

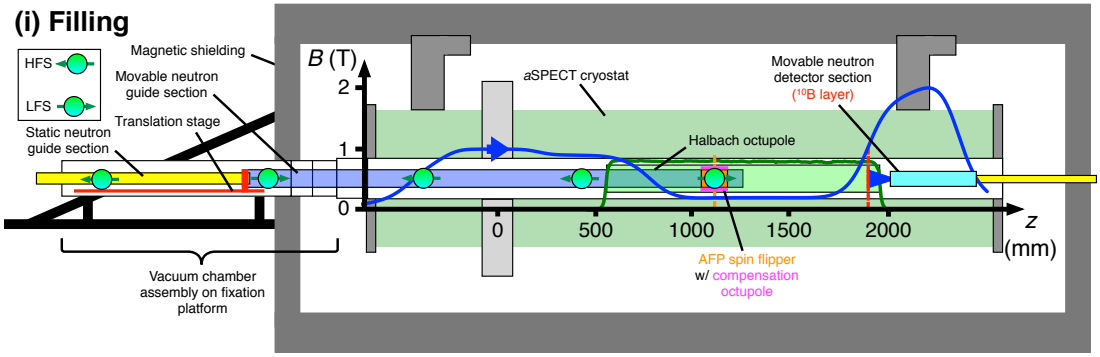

Figure 5.2: Overview over relevant components and depiction of the τSPECT filling sequence. The magnetic flux density B (longitudinal field, blue solid line, field direction depicted by arrow) as a function of z-position is plotted for the current $I_{\text{main}} = 33\,\text{A}$ generating the longitudinal field. Also, the respective radial magnetic field of the Halbach octupole field (green solid line) is shown, which along with the longitudinal field forms the 3D magnetic trap for low-field seekers (LFS) for $z \in [700, 1800]$ mm. The measurement sequence starts with the 'filling' process (i). During filling, a spin flip of 'high-field seeking' UCN (HFS, see legend) which have passed the first potential minimum to their lower energy LFS spin state is performed (LFS - not shown - are reflected at the correspondingly repulsive potential wall). For this, the movable neutron guide section is driven into the storage volume with the compensation octupole and the AFP spin flipper at its very end. On the right side, the movable neutron detector is situated, which, when driven into the 3D magnetic storage trap, collects UCN for counting.

in the spin flip position ($E_{\text{UCN, pot, min}} = 60.3\,\text{neV}\,\text{T}^{-1} \cdot B_{\text{main, sf}}$) and thus varies, with an acceptance to incoming UCN of $\Delta E \sim 23\,\text{neV}$ maximum energy for storage (cf. Ch. 4.4.2). The duration of the filling process needs to be optimised to increase the stored UCN yield, *i.e.,* determining the start time of the spin flip after the reactor pulse, $t_{\text{AFP, start}}$, and the time interval of operation, Δt_{AFP}. After completion of the filling process, the movable part of the neutron guide is retracted from the storage volume, as it would otherwise lead to losses due to material wall interactions.

(ii) **Cleaning process:** During the filling process, so-called 'marginally-trapped' UCN with energies higher than $E_{\text{UCN, max}}$ remain in the storage volume on 'quasi-bound orbits' [BP05, SAB+14], which implies that for the normal component of the UCN kinetic energy, the condition $E_{\text{UCN, kin,}\perp} < E_{\text{UCN, max}}$ is valid. Despite their higher energy, these UCN stay within the storage volume by being specularly reflected at the magnetic potential walls for times in the order of τ_n [IB06]. As a consequence, these 'marginally-trapped' UCN are counted, which leads to a distorted τ_n value. It is therefore a necessity to remove these UCN from the trap by a characteristic 'chaotic-cleaning' method [IB06]. To implement cleaning, the magnetic field can be slightly reduced by 3 % [BP05], which could be realised in τSPECT by decreasing the longitudinal field. In τSPECT, the asymmetric storage trap causes a conversion of quasi-bound to chaotic UCN trajectories. UCN on chaotic trajectories cannot be marginally trapped for energies $> E_{\text{UCN, max}}$ and therefore leave the trap. The process can be accelerated by inserting an UCN-absorbing cleaner into the trap at a position corresponding to

$E_{\text{cleaner}} < E_{\text{UCN, max}}$ for a short time and retracting it afterwards[5]. After the cleaning period, the condition $E_{\text{UCN, kin},\perp} = E_{\text{UCN, max}}$ should be reached, with no 'marginally-trapped' UCN left prior to the storage phase. To accomplish the primary cleaning method in τSPECT, the neutron detector with its neutron-absorbing boron-10 layer is driven into the storage volume to remove UCN with energies higher than $E_{\text{UCN, max}}$ (cf. Fig. 5.3 with cleaning position at $z \sim 1850\,\text{mm}$). The process starts shortly after the beginning of the filling process, leading to $t_{\text{clean, start}} \gtrsim t_{\text{AFP, start}} + \Delta t_{\text{AFP}}$. After the cleaning of duration Δt_{clean}, the detector returns back to its initial position.

(iii) **Storage process:** The UCN in LFS spin state remain trapped in $\pm z$ direction by the longitudinal field and in r direction by the magnetic field created by the Halbach octupole. Assuming an absence of material interactions and a perfect magnetic field configuration (no non-adiabatic spin flip in the entire trap volume leading to $\tau_{\text{loss}} \to 0$), τ_n is the only parameter affecting the number of stored neutrons over time. The storage time starts right after the cleaning has been performed ($t_{\text{s, start}} \gtrsim t_{\text{clean, start}} + \Delta t_{\text{clean}}$) and has a variable duration $\Delta t_{\text{s}} \equiv t_{\text{s}}$ depending on the selected storage time.

(iv) **Counting process:** After $t \gtrsim t_{\text{s}}$, the neutron-absorbing UCN detector is moved into the storage volume. Consequently, the detector remains in the storage volume until all 'surviving' UCN are detected with detection efficiency ε_{det}.

For the extraction of the neutron lifetime τ_n, the measurement sequence depicted in Figs. 5.2 and 5.3 is repeated for different t_{s} values. The resulting $C_{\text{UCN}}(t_{\text{s}})$ values are plotted against t_{s}, which gives the storage curve (for an example, cf. Fig. 5.4). An exponential fit directly determines τ_n, assuming the UCN spectrum has previously been cleaned, $\varepsilon_{\text{det}} = 1$ is valid for the detection efficiency, and no further loss mechanisms are present (idealised case):

$$C_{\text{UCN}}(t_{\text{s}}) = C_{\text{UCN}}(t_{\text{s}} = 0) \cdot \exp\left(-\frac{t_{\text{s}}}{\tau_n}\right) . \tag{5.1}$$

A non-cleaned spectrum would require a bi-exponential fit, in which the first component describes losses caused by marginally-trapped UCN. As indicated in (ii), an absence of cleaning implies that higher-energetic UCN might survive for times $\mathcal{O}(\tau_n)$. Since these UCN could not be separated from the actually-stored UCN in the data analysis, an accurate extraction of τ_n from the decay constant of the second exponential fit would no longer be possible. Furthermore, it has to be noted that in non-ideal conditions, several further systematic effects need to be considered for the determination of τ_n.

5.2 The vacuum chamber system

As discussed in Ch. 5.1.1, the storage of UCN in τSPECT requires reaching a vacuum of $\sim 10^{-7}\,\text{mbar}$. For technical reasons, only vacuum conditions $\mathcal{O}(10^{-5}\,\text{mbar})$ were feasible in the beam line connecting the UCN D source to τSPECT and in the first vacuum chamber, in which the translation stage of the movable neutron guide section was installed. To separate these regions from the cryostat vacuum in the storage volume, a differential pumping section had to be realised (cf. Ch. 5.2.1). Moreover, technical details on the translation stage (cf. Ch. 5.2.2), the associated vacuum feedthrough, and the electrical drive system responsible for the guide movement (cf. Ch. 5.2.3) are given.

[5] Moving an absorber into the storage volume to remove marginally-trapped UCN is a common cleaning technique and has *e.g.* been employed in the UCNτ experiment [PCCW+18].

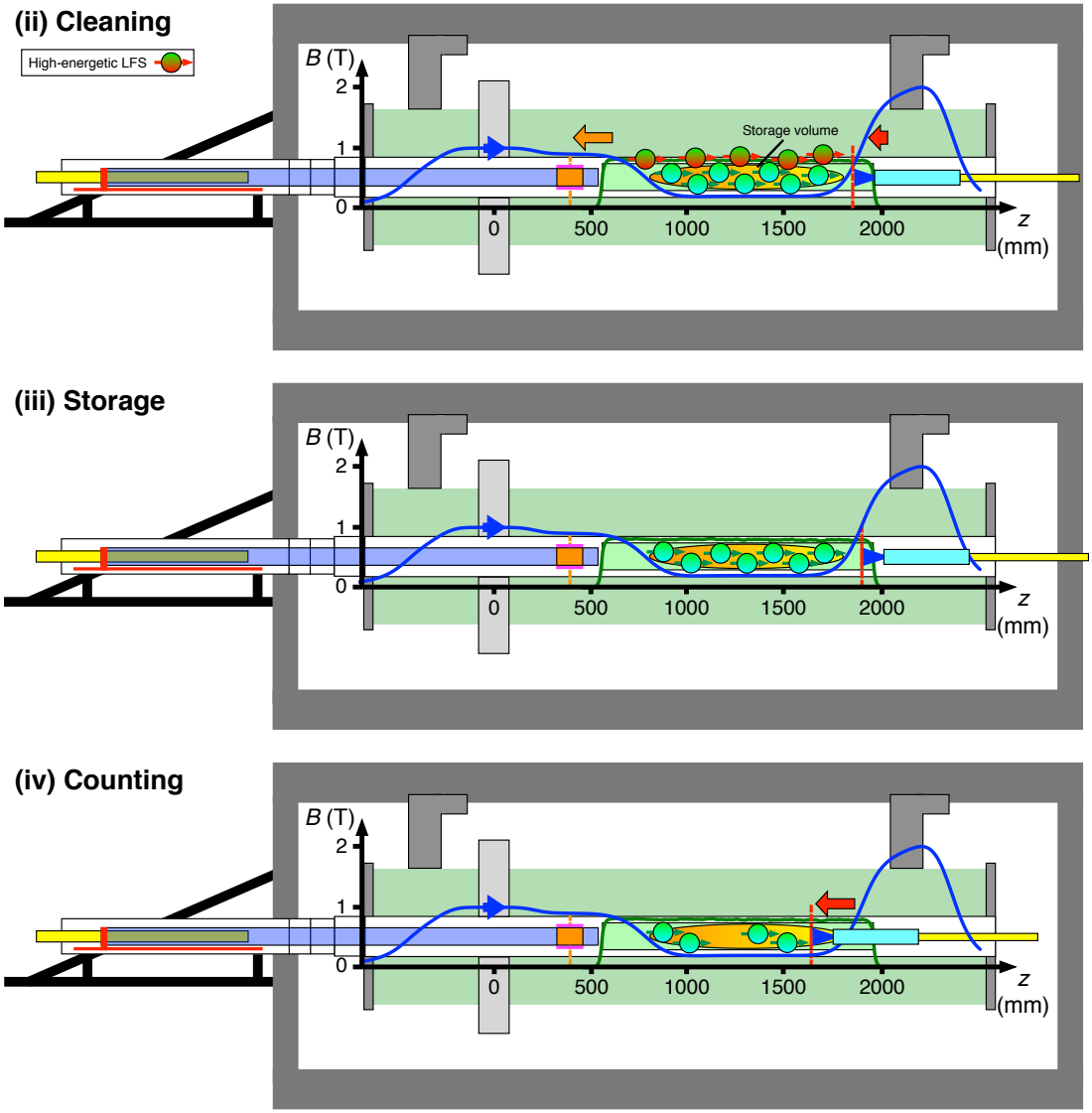

Figure 5.3: The cleaning, storage and counting sequences of τSPECT with the magnetic flux density B plotted against the z-position for the longitudinal magnetic field current $I_{\text{main}} = 33\,\text{A}$. Upon completion of the filling process, the neutron guide section is retracted (orange arrow). Next, the UCN detector is partly moved into the storage volume (red arrow) to absorb marginally-trapped UCN (reddish UCN, 'cleaning', (ii)). After the cleaning process, the UCN detector returns to its initial position. With the detector fully retracted, the storage process (iii) begins. During counting (iv), the detector is driven inside the magnetic potential minimum (red arrow) to count 'surviving' UCN after varying storage times.

5.2.1 Implementation of differential pumping

The primary goal of the vacuum chamber design was to provide differential pumping to suppress gas exchange between the first vacuum chamber containing the translation stage

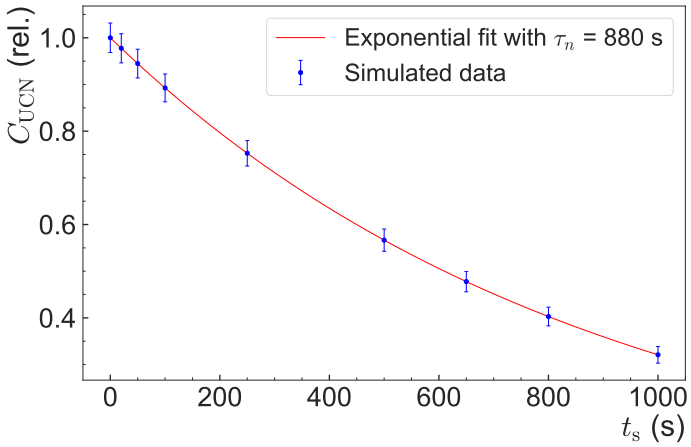

Figure 5.4: Extraction of τ_n from exponential fit, with the relative number of stored UCN (C_{UCN}) as a function of storage time, t_{s}. Counting 'surviving' UCN after several storage times gives an idealised storage curve, along with an exponential fit ($\tau_n = 880\,\mathrm{s}$, red line) for illustration purposes.

and the cryostat vacuum, which follows right after the bottom chamber[6]. In a design study, a differential pumping was regarded to be necessary due to the expectable end pressure of $\sim 10^{-3}\,\mathrm{mbar}$ in the first vacuum chamber[7] containing the translation stage. To ensure differential pumping, the outlets within the three sections of the vacuum chamber system were designed to be individually connected to a turbo pump (cf. Fig. 5.5). Furthermore, the slids between the moving neutron guide and the vacuum chamber sections were reduced to 1.1 mm, which was realised by pressing flexible PTFE (polytetrafluoroethylene) rings between a custom aperture. The design goal of final pressure of $\sim 10^{-7}\,\mathrm{mbar}$ is required to keep UCN losses due to residual gas collisions to a minimum. Throughout the design process, it was agreed to use CF200 (CF = ConFlat® flange) flanges as the common standard for the vacuum chambers, which were - apart from the bellow - tubes with $\varnothing_{\mathrm{inner}} = 200\,\mathrm{mm}$ ($\varnothing_{\mathrm{outer}} = 204\,\mathrm{mm}$) welded together with CF200 flanges.

The middle vacuum chamber section is formed by a bellow, which main purpose is to provide radial flexibility required for the mechanical alignment of the system. Moving the neutron guide section with length $l = 2598.4\,\mathrm{mm}$ by up to $\Delta z_{\mathrm{guide}} = 730\,\mathrm{mm}$ requires a high degree of mechanical precision. The bellow (wall thickness of $d = 1\,\mathrm{mm}$) provides a radial degree of freedom which otherwise would not be present in the entire vacuum chamber system and would not have permitted the longitudinal movement of the neutron guide.

To carry the weight of the vacuum chamber system, a fixation platform consisting of an aluminium sheet with 10 mm thickness and an array of ITEM profiles was built[8]. Both inner CF200 flanges of the first vacuum chamber are placed in half shell-shaped holders

[6] The bottom chamber provides 6 CF40 (CF = ConFlat® flange) and 2 CF16 connections and was used to mount electrical feedthroughs containing temperature sensor cables, spin flipper cables and Hall probe cables.

[7] Following further improvements, an end pressure $\mathcal{O}(10^{-5}\,\mathrm{mbar})$ could be reached (cf. Ch. 6.1.1).

[8] The fixation platform was designed to hold a static load of 150 kg, which was confirmed by a FEM simulation performed in Autodesk Inventor 2018. Considering safety margins, short-time loads of up to 250 kg are tolerable. It should be noted that these limitations mainly stem from the ITEM angles connecting the fixation platform to the magnetic shielding at the top side.

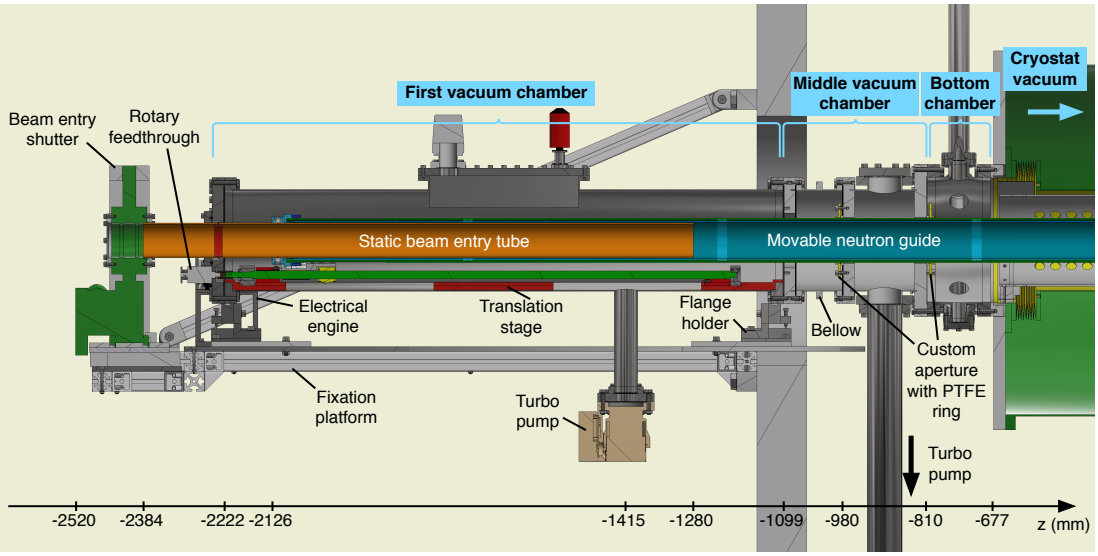

Figure 5.5: Overview of the vacuum chamber assembly, with the neutron guide section driven to the storage position (spin flipper position $z_{\mathrm{sf}} = 390\,\mathrm{mm}$). The first vacuum chamber contains the translation stage, which is required for moving the neutron guide through the custom aperture. It is connected to the bottom chamber and thus to the cryostat's main vacuum system by the middle vacuum chamber, which is designed to realise differential pumping. The position in z-direction relative to the cryostat coordinates is provided by the bottom axis. Further details are either given in the text or referred to in later sections in case of internal components.

which are screwed onto the fixation platform. The flange holders are capable of fine-tuning the position of the vacuum chamber system by $\Delta x = \pm 10\,\mathrm{mm}$ (perpendicular to chamber) and $\Delta z = \pm 10.5\,\mathrm{mm}$ (height of chamber) for ensuring the longitudinal movement of the neutron guide in the assembled system. Left of the first vacuum chamber, the fixation platform also provides the entry beam shutter position.

The first vacuum chamber ($l_{\mathrm{first\ vac\ cham}} = 1123\,\mathrm{mm}$) was designed to fit the double rail system of the translation stage ($l_{\mathrm{rail}} = 940\,\mathrm{mm}$). At the top of the first vacuum chamber, a O-ring sealed lid is placed which can be opened for connecting the translation stage to the neutron guide section and for various maintenance purposes. In closed state, it provides two CF16 connectors, which are used to connect two pressure gauges.

5.2.2 The vacuum translation stage

The basis of the translation stage (cf. Fig. 5.6), which is exposed to the vacuum conditions in the first vacuum chamber, forms a dual rail system onto which two wagons are moved by a nut connected to a shaft. The inclusion of two rails offers an optimised weight distribution along with improved stability due to a larger contact area. For being rotated, the shaft is coupled to a vacuum feedthrough, at which ambient side a gearwheel is positioned. The engine is placed off-axis with a distance of $\sim 230\,\mathrm{mm}$ (depending on roller chain tension) to prevent malfunctioning due to strong magnetic leakage fields[9] and drives the shaft with a roller chain (1:1 transmission).

[9] At the on-axis position left of the first vacuum chamber, a residual magnetic field of $\sim 0.1\,\mathrm{mT}$ was measured.

Since the rail system is situated within the vacuum, a system by THK[10] certified to be suitable for optimation in pre-vacuum conditions of 10^{-3} mbar was chosen. A private communication with a THK consulting engineer confirmed a suitability of the system in vacuum conditions better than 10^{-5} mbar. The large shaft pitch of 5 mm allowed for a fast retraction of the neutron guide section from the storage volume (theoretically, a retraction within 6 s is possible, cf. Ch. 5.4.2) to prevent UCN material interaction. Due to imperfections caused by the welding of the two CF 200 flanges of the first vacuum chamber, an accurate positioning and alignment of the rail system within the vacuum chamber became a challenge. In collaboration with the mechanical workshop of the Institute of Physics, it was agreed on installing the rails on top of custom holders which were oriented on the inner flanges of the vacuum chamber tube.

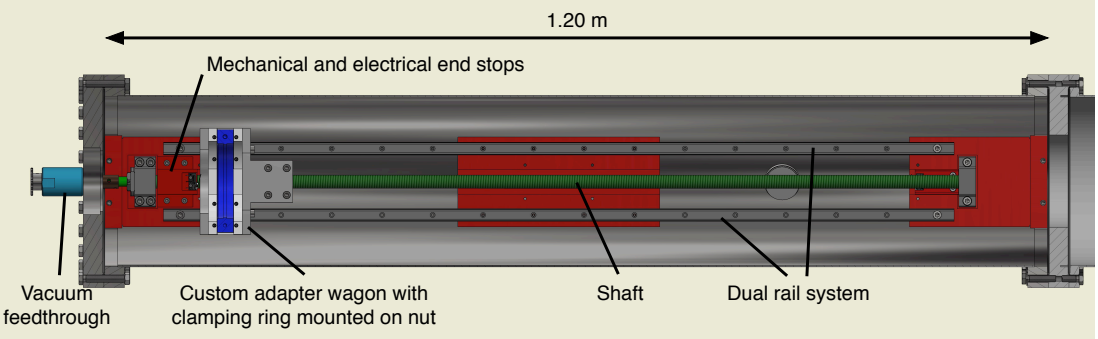

Figure 5.6: Overview translation stage for moving the neutron guide system. Details are given in the text.

The two rails and the nut[11] were connected by a custom adapter wagon onto which a clamping ring is fixated for connecting the neutron guide section. In the final assembly, the clamping ring sits in a groove with 0.1 mm precision in longitudinal direction which had been carved into the outer stainless steel tube of the double-tube neutron guide (cf. Ch. 5.4). To suppress the thermal flux from the first vacuum chamber to the cryostat, the clamping ring is not directly screwed into the stainless steel adapter, but is separated by a ≥ 5 mm PTFE inlay. A rotation of the shaft therefore leads to a longitudinal movement of the adapter wagon, which is transmitted to the neutron guide system by the clamping ring.

For safe operation of the experiment, mechanical and electrical end stops were included in the rail system. The electrical end stops[12] were mounted onto the mechanical end stops, which were screwed onto the holders of the double rail system. Just before the adapter wagon reaches the mechanical end stop (~ 1.3 mm), the activation of the electrical end stop leads to a current flowing to the engine's controller, which thereby sends an immediate stop signal. In case of a failure of the electrical end stop, the wagon would reach the mechanical end stop which forces the engine to stop its rotational movement since it could not deliver the required torque. A conforming safety protocol is already implemented in the engine controller by the manufacturer.

[10] THK K.K. (`https://www.thk.com`) is a manufacturer specialised in linear motion components.

[11] The used custom-adapted rails are of type THK SR15W1UU ($l_{\text{rail}} = 940$ mm) with included carriage wagons THK SR15WUUPB. The nut and the shaft are of type THK BNT1605-2_6 with a pitch of 5 mm. The left-hand side of the shaft has also been custom-made to fit the coupling requirements towards the direction of the rotary feedthrough. As bearings, THK BK12 and BF12 were used.

[12] Electrical end stops of type Cherry DC2C-L1LC were installed.

5.2.3 Rotary feedthrough and electrical engine

To connect the engine in ambient conditions to the translation stage, the shaft is coupled to a vacuum feedthrough on its left side. The gas leakage caused by the rotary movement of the engine should be minimised to prevent possible freeze-out processes inside the cryostat. The vacuum feedthrough has been co-engineered with the company VacSol to fit the needs of a small outer diameter ($o_{outer} = 34\,mm$) and compact length ($l = 79\,mm$) while still preserving its full functionality. According to specifications, the feedthrough remains vacuum-tight up to vacuum conditions of $10^{-6}\,mbar$[13], which is achieved by sealing a slid of width $\sim 10\,\mu m$ between the shaft and a permanent magnet array using a hydrocarbon-based magnetofluid. In the final experimental setup, a minor increase in pressure of $\lesssim 2 \times 10^{-7}\,mbar$ during rotation was found (cf. Fig. 6.4 a).

The engine of type Nanotec ST6018D4508-B[14] was installed $\sim 230\,mm$ off-axis (distance depending on the roller chain tension) for a reliable operation in the residual magnetic field of $\sim 0.5\,mT$. The 1:1 transmission is realised by mounting gear wheels on the shaft of the engine and the vacuum feedthrough and connecting them by a roller chain with sufficient chain tension[15]. The controller (Nanotec SMCI47-S-2 with RS485 connection) was chosen to drive the engine at 48 V operating voltage to guarantee a maximum torque. Combining the controller with a Mean Well DRP-480-48 power supply, a maximum torque of $\sim 2.7\,N\,m$ at a rotation speed of 450 rpm in the $48\,V/10\,A$ setting [nan10] was achieved. The current position of the engine is communicated to the controller by an optical encoder of type Nanotec WEDS5541-A06, which allows for a real-time position check. At the beginning of each measurement sequence, the engine was rotated until the left-hand electrical end stop is reached. Thus, a reliable starting position for each measurement sequence could be achieved.

5.3 Halbach octupole for radial storage

To provide radial magnetic storage, the Halbach octupole was installed into the cryostat. First, the reader is introduced to the principle of a Halbach octupole and the constraints resulting from the superposition with the longitudinal magnetic field (cf. Ch. 5.3.1). Next, the principle of the adiabatic fast passage spin flip is described (cf. Ch. 5.3.2). The resulting implications for the spin flip as well as measures to reduce the radial gradient using a second Halbach octupole in miniature format are explained in Ch. 5.3.3. Further on, the mechanical design of the octupole surroundings (cf. Ch. 5.3.4) are outlined.

5.3.1 Superposition of the Halbach octupole array and the longitudinal magnetic field

The radial magnetic field is provided by a Halbach octupole permanent magnet. Halbach octupole arrays rely on a special configuration of permanent magnets, which magnetic orientation is tilted by 45° relative to the preceding segment. The pattern of magnetic orientations is repeated each quarter, with a total of 32 permanent magnets in the array, resulting in a radial magnetic field with a maximum absolute flux density of $\sim 1\,T$ (cf. Fig. 5.7). The

[13] These values were guaranteed according to the delivered specification sheet by VacSol (`http://www.vacsol.com`), assuming a maximum transmitted torque of 3 N m, a rotary speed of 200 rpm and a radial load on the shaft end of 10 N caused by the 'pulling' of the roller chain on the gearwheel connected to the vacuum feedthrough. For a long lifetime of ~ 5 y, the upper duty cycle was given by $2\,h\,d^{-1}$ within $100\,dy^{-1}$.

[14] For more details on the used engine components, refer to `https://de.nanotec.com`.

[15] The used gear wheels and the roller chain were made by Holtech, `https://holtech-antriebstechnik.de`, with order numbers 601-061-0016, 700-061-0000 ($l_{chain} = 558\,mm$), respectively.

magnetic field flux density $\vec{B}_{\text{octupole}}(\vec{r})$ inside the octupole magnet with inner/outer radius r_i/r_a, remanence B_r, and unity vector $\vec{e}_r$ is given by [Hal80]:

$$\vec{B}_{\text{octupole}}(\vec{r}) = \left(\frac{r}{r_\text{i}}\right)^3 \cdot \frac{4B_r}{3} \cdot \left(1 - \left(\frac{r_\text{i}}{r_\text{a}}\right)^3\right) \cdot \vec{e}_r \ . \tag{5.2}$$

Due to its placement inside the cold bore of the cryostat, the main requirement for the permanent magnet material was to not reduce its inner coercivity at low temperatures ($\sim 150\,\text{K}$). After researching into this matter [Dra14] and considerations of technical feasibility, the material Sm_2Co_{17} with remanence $B_r \sim 1.1\,\text{T}$ [arn14] was selected, which has the advantage to increase its inner coercivity at low temperatures [arn03]. The required length which needed to be covered by the Halbach octupole was assessed by considering the longitudinal magnetic field distribution. Consequently, a Halbach octupole with a total length of 1380 mm made of 23 Halbach octupole segments with 60 mm thickness each, and inner/outer diameter[16] of $\varnothing_\text{in} = 108\,\text{mm}$, $\varnothing_\text{out} = 174\,\text{mm}$ was built by Arnold Magnetic Technologies[17].

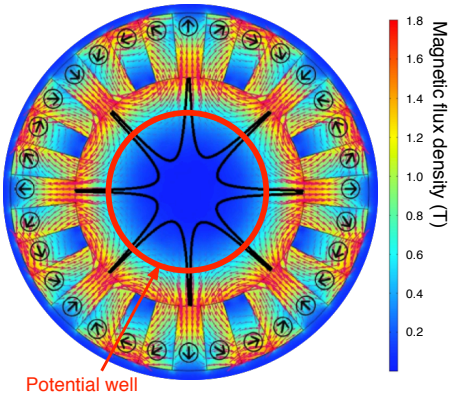

Figure 5.7: Simulated radial field created by the Halbach octupole. It can be seen that a rotation in every subsequent magnet's orientation by 45° results in a characteristic field distribution forming a magnetic potential well for UCN confinement (red circle). Figure adapted from [Dra14].

During the design process, the radial magnetic field of the Halbach octupole was measured with a 3-axis Hall probe at ambient conditions and at a mean distance of $\sim 2.5\,\text{mm}$ from the inner octupole surface ($r = 47\,\text{mm}$ [Haa16]). For the design of τSPECT, a conservative estimate was made, considering the radial flux density of $\sim 0.78\,\text{T}$ to define the maximum potential energy of $\sim 47\,\text{neV}$ in the storage volume.

The position of the Halbach octupole inside the cryostat is:

$$z_\text{Halbach} \in [570, 1950]\ \text{mm} \ . \tag{5.3}$$

[16] For design purposes, an inner diameter of $\varnothing_{\text{in, Halbach}} = 102\,\text{mm}$ should be assumed, due to irregularities and slight bends of the Halbach octupole.

[17] For the manufacturing of the Halbach octupole by Arnold Magnetic Technologies (`https://www.arnoldmagnetics.de`), the Sm_2Co_{17} material of type RECOMA 28HE with a magnetic remanence of $\sim 1.1\,\text{T}$ [arn14] was used. For further details on the selection process of the magnetic material, details on its assumed temperature behaviour, and magnetic field simulations, refer to [Dra14].

Since the longitudinal magnetic field is applied perpendicular to the permanent magnet's orientation, changes in the magnetisation might occur. The manufacturer Arnold Magnetics was therefore asked for recommendations, after which a custom experimental setup was installed at the manufacturer site, in which magnetic flux densities ranging from $0 - 1$ T were applied perpendicular to a Sm_2Co_{17} magnet with dimensions $50 \times 20 \times 5\text{mm}^3$. The measurements showed that up to a perpendicular magnetic flux density of ~ 1 T, no major changes in the magnet's magnetisation could be seen at room temperature[18]. For cryogenic environments, the manufacturer has therefore given the advice to operate the magnets below the remanence at room temperature, *i.e.*, < 1.1 T.

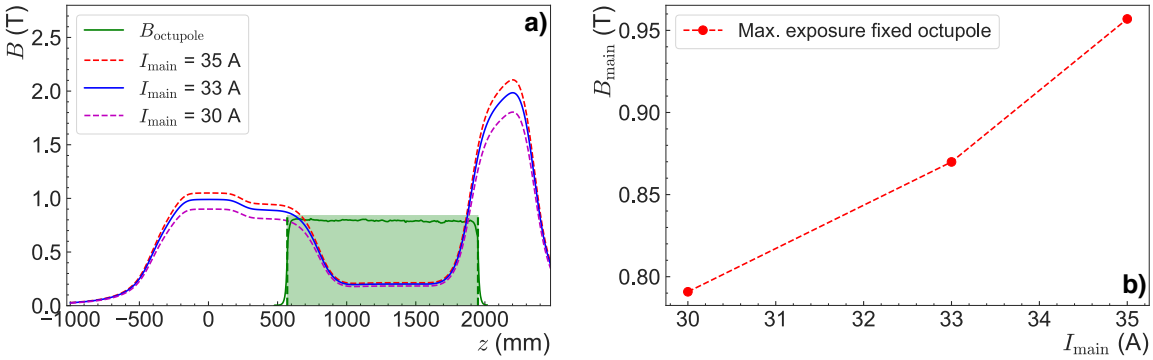

Figure 5.8: Superimposed magnetic fields in τSPECT and Halbach exposure to longitudinal magnetic fields. (a) Absolute magnetic flux density B of the octupole field (green) as a function of z-position, which was measured using a 3-axis Hall probe ($\left|\vec{B}_{\text{octupole}}\right| = \sqrt{B_x^2 + B_y^2 + B_z^2}$) at a medium distance of 2.5 mm from the octupole surface. The values for the resulting longitudinal magnetic flux densities B_{main} at the superconducting coil currents $I_{\text{main}} = (30, 33, 35)$A were simulated using the Kassiopeia package which was implemented by C. Schmidt for the *a*SPECT experiment [Sch19]. (b) Maximum exposure of the fixed Halbach octupole to the magnetic flux density created by the longitudinal field component (B_{main}) at different I_{main} values.

Considering safety margins, it was decided to limit the maximum magnetic flux density exposure of the Halbach octupole to $\sim 0.87\,\text{T} < 1\,\text{T}$ (cf. Fig. 5.8 b)[19], which is guaranteed using the selected current of $I_{\text{main}} = 33$ A for operating the superconducting coils (cf. Fig. 5.8 a).

5.3.2 The adiabatic fast passage spin flip

The 'spin flip' of nuclei, which leads to a π-flip of the spin $\vec{S}$ relative to magnetic field lines, is a well-established nuclear magnetic resonance (NMR) technique. It is based on polarising

[18] According to Arnold Magnetics, applying a magnetic flux density of 1 T in a direction perpendicular to the Sm_2Co_{17} magnetisation leads to irreproducible magnetisation losses $\mathcal{O}(1-2)$ % at room temperature. Repeatedly exposing a permanent magnet to the same magnetic field should not further weaken its magnetisation. The situation improves at the low temperatures in the τSPECT cryostat ($T \sim 200$ K) due to the increasing coercivity of Sm_2Co_{17} with lower T [arn03]. For a temperature change from room temperature (300 K) to 200 K, which is is the expectable temperature for the compensation octupole after cooldown, the inner coercivity of Sm_2Co_{17} increases by ~ 40 % [TG75].

[19] For reducing radial gradients caused by the Halbach octupole, a second smaller Halbach octupole was introduced to the experiment, which magnetic flux density exposure is also kept below 0.9 T at $I_{\text{main}} = 33$ A. Details on the radial gradient reduction will be discussed later in this section.

the nuclear magnetic moment by applying a homogeneous holding field $\left|\vec{B}_{\text{main}}\right| \equiv B_0$ and adding a second magnetic field $B_1 \ll B_0$ perpendicular to B_0 ($\vec{B}_1 \perp \vec{B}_0$), which oscillates with a frequency ω [HBD+12]. For a spin flip, ω must equal the local Larmor frequency ω_L (resonance), which is determined by B_0:

$$\omega_{\text{L}} = -\gamma B_0 \ . \tag{5.4}$$

The equation contains the gyromagnetic ratio $\gamma = \frac{g_n \mu_n}{\hbar} \sim -29.16\,\text{MHz}\,\text{T}^{-1}$ (with nuclear magneton $\mu_n = 3.152\,451\,258\,44(96) \times 10^{-14}\,\text{MeV}\,\text{T}^{-1}$ [THH+18] and the neutron g-factor ($g_n = -3.82608545(90)$ [cod19b]).

Let us now turn to the spin flip of UCN. Considering a frame of reference which is rotating around B_0 with the frequency ω of B_1, an effective time-dependent field acts on the UCN spin [LT84],

$$\vec{B}_e(t) = \left(B_0(t) - \frac{\omega}{\gamma}\right) \cdot \vec{k} + B_1 \cdot \vec{i}\,, \tag{5.5}$$

with unitary vectors $\vec{k}, \vec{i}$. The field B_1 is radiated circularly, with the direction corresponding to the rotation of the UCN spin. Thus, viewed in the rotating frame of reference, B_1 then becomes static.

In general, the frequency required for the spin flip, $\omega_e = \gamma B_e$, depends on the position in z-direction, since due to its time dependency, B_e changes along the flight path of the UCN. With the resonance condition $\omega = \omega_L$ fulfilled, the effective field B_e in Eq. (5.5) becomes equal to B_1. Therefore, the resonance condition for $B_e = B_1$ reads

$$\omega_e = \gamma B_1 \ . \tag{5.6}$$

After passage of this resonance region, the UCN spin is π-flipped, if adiabaticity is fulfilled ($\omega_{\text{UCN}}/\omega_e \ll 1$ [RRS54]). Considering the UCN moving with velocity v, a spin flip occurs within the time range $\Delta t = \Delta z / v$, which corresponds to a frequency of $\omega_{\text{UCN}} = \pi/\Delta t$. The distance in z-direction, during which a spin flip occurs (Δz), is affected by the local gradient in the resonance point, $\Delta z = B_1 / (\nabla_z B_z)$.

UCN spin flippers are based on the adiabatic fast passage (AFP) technique, which was adapted to UCN physics by V. Luschikov [LT84]. A magnetic field with a small but monotonic gradient in longitudinal direction leads to a holding field B_0 with a decreasing - and thus changing - ω_{L} value of the UCN along its flight path. To calculate the spin flip efficiency at the resonance point, Eq. (4.13) in [HBD+12] can be used as a first approximation. With more complex gradient fields, however, the differential equations in [LT84] allow for a better description of the spin flip motion[20], with the neutron spin $\vec{S}$:

$$\frac{dS_x}{dt} = -\gamma B_e(t) S_y - \Omega(t) S_z \ , \tag{5.7}$$

$$\frac{dS_y}{dt} = \gamma B_e(t) S_x \ , \tag{5.8}$$

$$\frac{dS_z}{dt} = \Omega(t) S_x \ . \tag{5.9}$$

The parameter $\Omega = (B_1 B_0) / B_e^2$ describes the angle velocity of the $\vec{B}_e$ rotation. Numerically solving these equations of motion leads to a precise calculation of the spin flip efficiency, ε_{AFP}.

[20] The expression of dS_x/dt has been corrected due to a calculation error in [LT84].

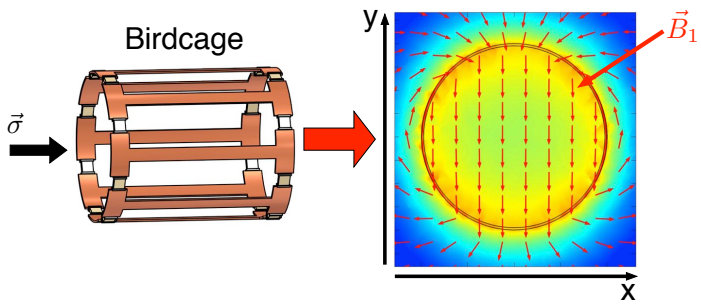

Figure 5.9: Birdcage resonator for UCN spin flip. The spin flip is technically realised by a birdcage coil, which divides the alternating current $\vec{\sigma}$ into individual 'rungs' around a cylindrical surface (depicted is a high-pass birdcage coil). The resulting $\vec{B}_1$ field is a transverse field similar to a cosine coil. For further details, refer to the text. Birdcage rendering and field distribution taken from [Kar17]. The birdcage has been constructed by K. Ross.

A typical approach for a technical realisation of a UCN spin flipper is a birdcage coil design, which has been developed by Hayes *et al.* in 1985 for magnetic resonance imaging (MRI) applications. Its principle is based on the application of a sinusoidal current [HES+69]

$$\vec{\sigma}\,(\phi, z) = \sigma_0 \cdot \sin(\phi) \cdot \hat{\vec{z}} \tag{5.10}$$

with frequency $\omega = \omega_{\mathrm{L}}(z_{\mathrm{resonance}})$ on a cylinder surface, which causes a B_1 field perpendicular to the surface. The birdcage coil design approximates the required sinusoidial current $\vec{\sigma}\,(\phi, z)$ over the whole cylinder surface by splitting the current onto the conductors ('rungs') with even spacing relative to the surface (cf. Fig. 5.9) [HBD+12]. The prototype measurement in July 2015 relied on a high-pass birdcage design, in which the rungs were capacitively coupled [Kar17]. In the September 2019 beam time, during which the first full-magnetic UCN storage has been performed, a low-pass birdcage design implemented by K. Ross has been used (capacitors were placed on the longitudinally-pointing rungs on the cylinder surface).

5.3.3 Compensation issue of radial gradients and implications for the adiabatic fast passage spin flip

Implementing full-magnetic storage in τSPECT implies that the absolute magnetic flux density (B) is a superposition of the absolute longitudinal (B_{main}) and the radial magnetic flux density (B_{radial}),

$$B = \sqrt{B_{\mathrm{main}}^2 + B_{\mathrm{radial}}^2}\,. \tag{5.11}$$

After measuring the magnetic flux density created by the Halbach octupole, the radial gradients in the spin flip region could be determined by additionally using COMSOL Multiphysics[21] finite element method (FEM) simulations. Taking the inner diameter of a typical neutron guide into account ($\varnothing_{\mathrm{inner}} = 66\,\mathrm{mm}$, $r_{\mathrm{guide}} = 33\,\mathrm{mm}$), the simulations showed that the UCN are exposed to a maximum radial field gradient of $\nabla_r B_{\mathrm{radial}} \sim 2035\,\mathrm{G\,cm^{-1}}$ in

[21] COMSOL Multiphysics is a simulation tool based on finite element method (FEM), `https://www.comsol.de`.

the spin flip region[22] [Ros17]. For comparison, the AFP spin flipper in the prototype measurement was placed in the longitudinal gradient of $\nabla_z B_{\text{main}} \sim 1\,\text{G}\,\text{cm}^{-1}$ (cf. Ch. 4.1) due to the absence of radial gradients ($\nabla_r B_{\text{radial}} \sim 0\,\text{G}\,\text{cm}^{-1}$) and the usage of correction coils (without the correction coils, a longitudinal gradient of $\sim 3\,\text{G}\,\text{cm}^{-1}$ is reached). Due to the dependency of the spin flip efficiency ε_{AFP} on the gradient in the spin flip volume (cf. Eq. (4.13)), a lower ε_{AFP} value results with the addition of radial magnetic storage. Also, as can be inferred from Eq. (5.11), the contribution of $B_{\text{radial}}(r)$ to B increases with radial distance, r (in the spin flip volume, with $B_{\text{main}} \sim 0.2\,\text{T}$, $B_{\text{radial}}(r)$ is the dominating contribution for $r \gtrsim 32\,\text{mm}$). The strong contribution of $B_{\text{radial}}(r)$ decreases the spin flip efficiency in regions where the B_1 field (cf. Ch. 5.3.2) is not perpendicular to B. This is due to the fact that in these regions, the component $B_1 \sin\alpha$ acts on the neutron, with α defined as the angle between B_1 and B.

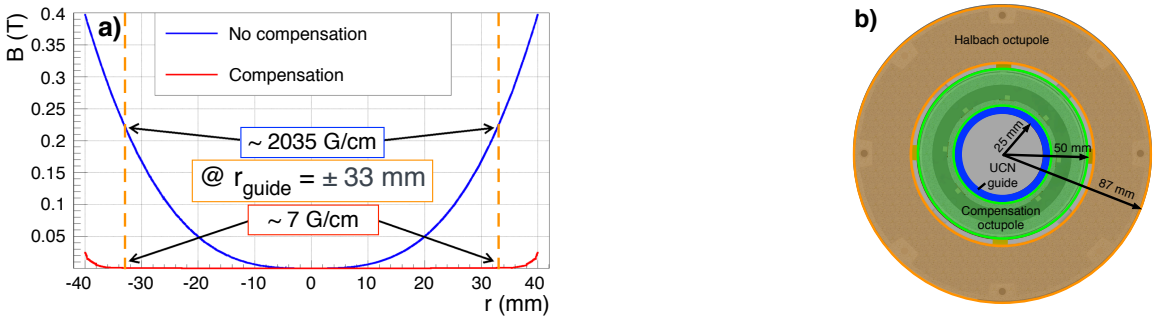

Figure 5.10: Compensation of the radial magnetic field. (a) The non-compensated absolute magnetic flux density of the Halbach octupole (B) plotted against radius r (blue line, cf. Eq. (5.2)) shows a radial gradient of $\nabla_r B_{\text{radial}} \sim 2035\,\text{G}\,\text{cm}^{-1}$ at $r_{\text{guide}} = 33\,\text{mm}$. Assuming perfect conditions, the simulated compensation octupole would decrease $\nabla_r B_{\text{radial}}$ to $\sim 7\,\text{G}\,\text{cm}^{-1}$ (red line). In reality, a radial gradient of $\sim 215\,\text{G}\,\text{cm}^{-1}$ was measured. Figure adapted from [Ros17]. (b) Cut through the xy plane of the Halbach octupole array (orange area, outer radius 87 mm) surrounding the compensation octupole (green area, outer radius 50 mm). The neutron guide with inner radius 25 mm is depicted in blue.

To reduce the radial gradients in the spin flip volume, a second Halbach octupole in miniature format ('compensation octupole') was built by K. Ross. Again, the octupole was composed of Sm_2Co_{17} permanent magnets. First FEM simulations assuming perfect conditions have yielded a radial gradient of $\sim 7\,\text{G}\,\text{cm}^{-1}$ at the typical inner UCN guide radius of $r_{\text{guide}} = 33\,\text{mm}$ [Ros17]. Fig. 5.10 a) shows the field distribution resulting with no compensation ($\nabla_r B_{\text{radial}} \sim 2035\,\text{G}\,\text{cm}^{-1}$, blue line) and perfect conditions ($\nabla_r B_{\text{radial}} \sim 7\,\text{G}\,\text{cm}^{-1}$, red line). In real conditions, systematic uncertainties such as the geometrical alignment relative to the Halbach octupole and differences in the magnetisation of the individual permanent magnets yield a higher $\nabla_r B_{\text{radial}}$ value. To further reduce the radial gradient in the spin flip volume by $\sim 50\,\%$ [Ros17], it was decided to narrow the inner guide radius to $r_{\text{guide, narrowed}} \sim 25\,\text{mm}$. First measurements at room temperature and $r_{\text{guide, narrowed}}$ by K. Ross have shown a compensated radial gradient of $\nabla_r B_{\text{radial}} \sim 215\,\text{G}\,\text{cm}^{-1}$ ($B_{\text{radial}}(r_{\text{guide, narrowed}}) = 16.2\,\text{mT}$). Considering the superposition of the longi-

[22] Note that for the efficiency of the UCN spin flipper, the gradients with respect to the superimposed magnetic field according to Eq. (5.11) are relevant, which are $\nabla_r B$ and $\nabla_z B$.

tudinal and the radial field, the total radial gradient, $\nabla_r B = B_{\text{radial}}/B \cdot \nabla_r B_{\text{radial}}$, equates to $\sim 17\,\text{G}\,\text{cm}^{-1}$ in the spin flip position ($B_{\text{main}}(z_{\text{sf}}) \sim 0.2\,\text{T}$ for $z_{\text{SF}} \sim 1100\,\text{mm}$). From measurements of the compensated magnetic field distribution (offset $\Delta B_{\text{main}} = 0.004\,\text{T}$) within the spin flip volume, the total magnetic field is calculated according to

$$B = \sqrt{\underbrace{B_x^2}_{=(0.0162\,\text{T})^2} + \underbrace{B_y^2}_{=(0.0160\,\text{T})^2} + (B_{\text{main}} + \Delta B_{\text{main}})^2} \sim 0.205\,\text{T}\,, \tag{5.12}$$

For determining the accurate τSPECT conditions in the spin flip volume, the superimposed longitudinal and radial field must be measured after a cooldown of the cryostat.

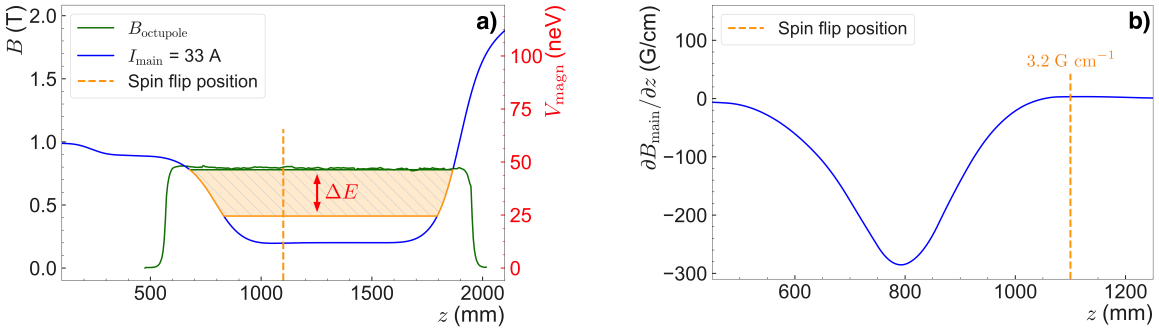

Figure 5.11: Storage volume and gradient for $I_{\text{main}} = 33\,\text{A}$. (a) Resulting storage volume with magnetic flux density B as a function of the z-position when performing the spin flip at $z \sim 1100\,\text{mm}$, accepting incoming UCN of $\Delta E \sim 23\,\text{neV}$ maximum energy for storage (light orange shaded area). (b) Associated longitudinal gradient ($\nabla_z B_{\text{main}}$) at $z \sim 1100\,\text{mm}$.

For the optimal spin flip position, $z_{\text{SF}} \sim 1100\,\text{mm}$ was chosen (cf. Fig. 5.11 a). Since the spin flipper's radio frequency ω_{RF} needs to be matched to the Larmor frequency, which is defined by the superimposed magnetic field ($\omega_{\text{L}} = -\gamma \left|\vec{B}\right|$, cf. Eq. (5.12)), ω_{RF} is $\sim 6\,\text{MHz}$. As Fig. 5.11 b) shows, a longitudinal gradient of $\nabla_z B_{\text{main}} \sim 3\,\text{G}\,\text{cm}^{-1}$ is present at z_{SF}, which leads to the radial contribution dominating the total gradient in the spin flip volume.

As depicted in Fig. 5.11 a) depicts, the selected spin flip position defines the maximum energy of incoming UCN which can be stored, $\Delta E \sim 23\,\text{neV}$ (cf. Ch. 4.4.2). Figure 5.12 shows the dependence of ΔE on the current causing the longitudinal magnetic field, I_{main}. It can be seen that for increasing I_{main}, ΔE decreases. Higher values than $I_{\text{main}} = 33\,\text{A}$ lead to a lower ΔE and should therefore be avoided.

The storage volume is obtained from computing the integral below the shaded area in Fig. 5.11 a), with $r_{\text{storage}} = 47\,\text{mm}$ given by the Halbach octupole measurement radius used for defining the maximum magnetic potential in the storage volume:

$$V_{\text{full}} \sim 6.81\,. \tag{5.13}$$

Note that the slight distortion of the storage volume caused by the gravitational interaction is a higher-order effect which has been neglected.

5.3.4 Design of the Halbach octupole surroundings

For fixating the $\sim 150\,\text{kg}$ heavy Halbach octupole inside the cryostat's cold bore (inner diameter $\varnothing_{\text{in, bore}} = 200\,\text{mm}$), a separate stainless steel tube (referred to as 'outer tube', cf.

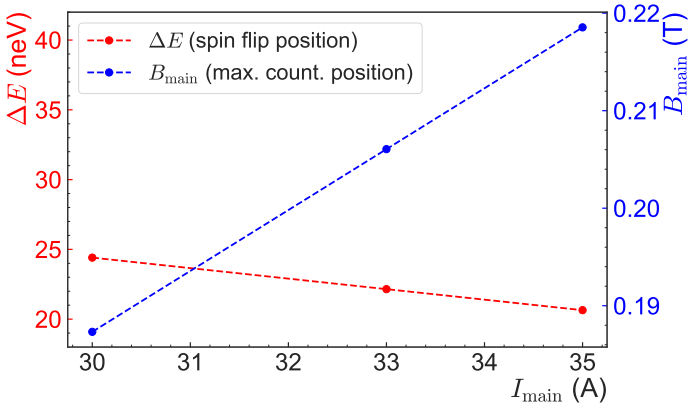

Figure 5.12: Effect of the longitudinal magnetic field current, I_{main}, on the maximum storable energy of incoming UCN, ΔE (red dashed line). The value of ΔE decreases with I_{main}, which is caused by the increasing magnetic field (given in the maximum counting position of the detector's UCN-absorbing layer, blue dashed line). The dashed lines represent a linear fit to the data.

Fig. 5.13) with outer diameter $\varnothing_{\text{out, outer tube}} = 184.0\,\text{mm}$ and $d = 3\,\text{mm}$ wall thickness was used. The outer tube was placed on the outer flanges of the cryostat. In order to reduce the heat flow from the flanges to the cryostat's interior, the outer tube was thermally insulated from the outer flanges by a PEEK layer.

Table 5.1: Placement of temperature sensors on outer tube, with the longitudinal z-position for each sensor number. The sensors were installed with an accuracy of $\Delta z = 5\,\text{mm}$.

Sensor number	z (mm)
S1	94
S2	630
S3	1122
S4	1485
S5	1895

Before installing the outer tube, 5 standard Pt1000 temperature sensors were glued onto it to cover a wide range of $z \in [94, 1895]$ mm and thus provide a sensitivity to possible temperature gradients caused by the Halbach octupole (cf. Tab. 5.1). For a later fixation of the Halbach octupole, the central fixation ring was installed in the outer tube. The detailed installation process has been documented as part of this work and is accessible on the group directory of AG Heil.

Left of the Halbach octupole, a stainless steel tube with outer diameter $\varnothing_{\text{out, stabilisation tube}} = 168.3\,\text{mm}$, wall thickness 2.6 mm, and length 898 mm ('stabilisation tube', cf. Fig. 5.13) is installed. It contains four stabilisation rails, displaced by 90°, in which the guiding flange of the movable neutron guide moves (cf. Ch. 5.4.1). In-between the Halbach octupole and the stabilisation tube, a stainless steel adapter cylinder ($\varnothing_{\text{inner, adapter cylinder}} = 108\,\text{mm}$) is attached. The adapter cylinder allows the neutron guide section with rolls attached to its very front to be further retracted. For the movement of the custom UCN detector,

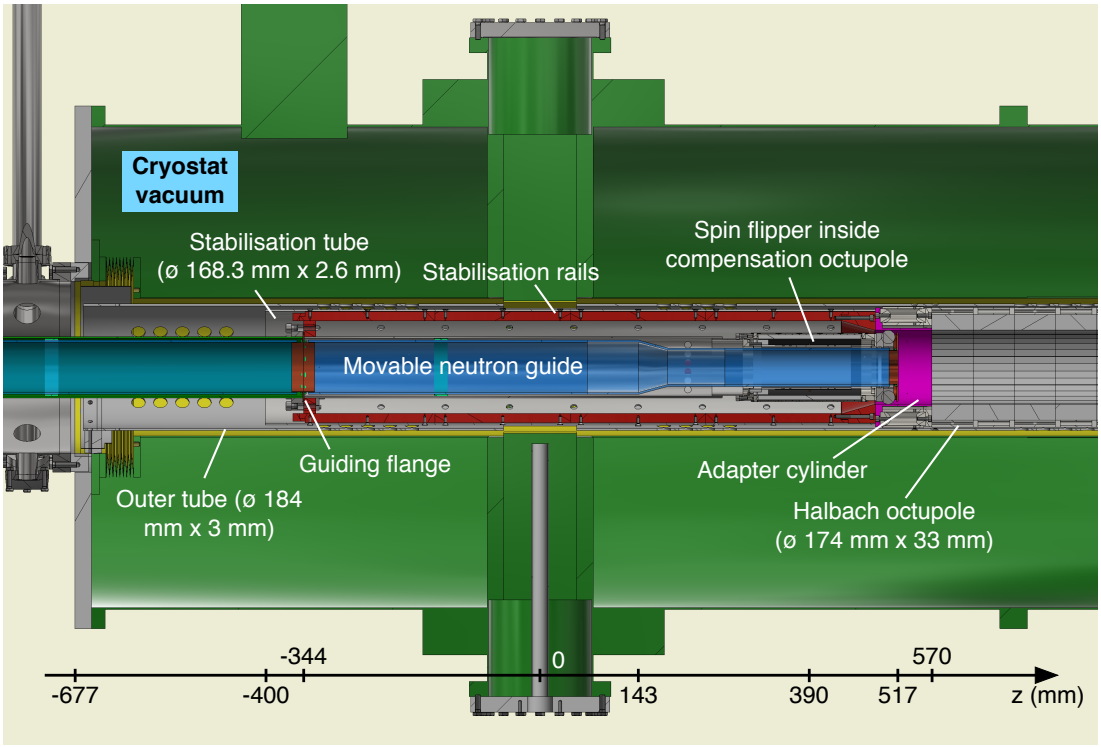

Figure 5.13: Design of the Halbach octupole surroundings with the neutron guide section in storage position (spin flip position $z_{\mathrm{sf}} = 390\,\mathrm{mm}$). The Halbach octupole is placed within a stainless steel tube ('outer tube'), which sits inside the cryostat's cold bore and is placed on the cryostat's outer flanges. Left of the Halbach octupole, the stabilisation tube is attached, which provides stabilisation rails through which the guiding flange glides (cf. Ch. 5.4.1). The adapter cylinder extends the travelling distance for the spin flipper inside the compensation octupole reaching the storage position. Given dimensions refer to the outer diameter and the wall thickness of the respective component. The position relative to the cryostat coordinates in z-direction is provided by the bottom axis.

a stabilisation tube has also been attached to the right side of the Halbach octupole. A detailed description along with the mechanical components required for the movement of the detector follows in Ch. 5.5.3.

5.4 The movable neutron guide section

According to the preparatory studies, fused silica was chosen as the neutron guide material, since it cannot be magnetised when exposed to local magnetic fields $\sim 1\,\mathrm{T}$ inside the cryostat (cf. Ch. 4.4.1). To provide the mechanical stability which is required for the movement of the neutron guide section, the fused silica tubes are surrounded by stainless steel tubes (cf. Ch. 5.4.1). The interplay of the $\sim 2.6\,\mathrm{m}$ long neutron guide section and the translation stage in the first vacuum chamber, which has been discussed in Ch. 5.2.2, leads to constraints on the possible position of the adiabatic fast passage spin flipper (cf. Ch. 5.4.2).

5.4.1 Design of the neutron guide section

As shown in Fig. 5.14, the neutron guide section comprises a long tube section (length $l_{\mathrm{long}} = 1736\,\mathrm{mm}$, outer diameter and wall thickness $79 \times 3\,\mathrm{mm}$) and a short tube section

($l_{\text{short}} = 846\,\text{mm}$, $79\times3\,\text{mm}$ with narrowing to $56\times3\,\text{mm}$, detailed dimensions in Fig. 4.18)[23]. In total, the neutron guide section has a length of $l_{\text{guide}} \sim 2600\,\text{mm}$.

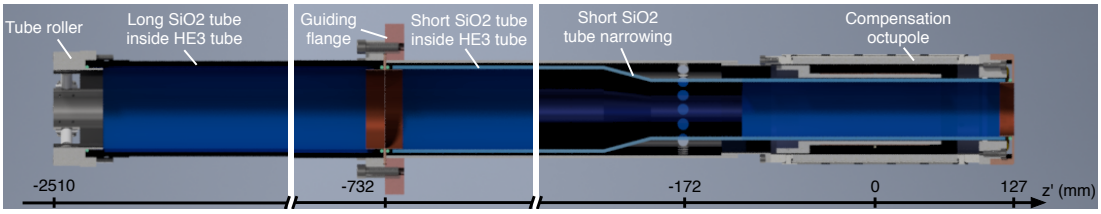

Figure 5.14: Overview over the neutron guide system. Both fused silica (SiO_2) tubes are surrounded by HE3-grade stainless steel tubes. The stainless steel tubes are each welded to one side of a guiding flange, which provides mechanical stability. On the left, the neutron guide system ends in the tube roller, while the compensation octupole assembly (detailed view in Fig. 5.18) marks its right end. The position in terms of the neutron guide length in z-direction is given by the bottom axis.

During the measurement, the neutron guide section must be first moved into the cryostat for filling the storage volume with spin-flipped UCN. Next, it must be retracted to avoid material interactions during the UCN storage time. Since pulling a SiO_2 tube would put the material under high mechanical stress eventually leading to its breaking, the SiO_2 tubes are surrounded by HE3 Neumo[24] stainless steel tubes ($\varnothing_{\text{outer, tube}} = 88.9\,\text{mm}$, wall thickness[25] 2.3 mm, lengths 1750 mm for left and 608 mm for right tube). On their outer edges, both the long and the short SiO_2 tubes are attached to the respective HE3 tubes in only two attachment points. In case of the long SiO_2 tube, these attachment points are formed by the copper T piece found in the guiding flange (cf. Fig. 5.16) and the tube roller assembly (cf. Fig. 5.15). Likewise, the short SiO_2 tube is attached to the copper T piece in the guiding flange and additionally to the copper shield following the tube roller at the guide's right end (cf. Fig. 5.16). To avoid direct contact between the SiO_2 tubes and the stainless steel and copper components, PTFE rings are inserted. Furthermore, the PTFE rings on both sides compensate for the different thermal expansion coefficients of stainless steel and SiO_2, which leads to a different contraction during cooldown.

Fig. 5.15 shows the left part of the fully-installed multi-layered neutron guide, which rolls over a flexible stationary beam entry tube ($\varnothing_{\text{outer, tube}} = 70\,\text{mm}$, 2 mm wall thickness, length 952 mm). The outside of the stainless steel beam entry tube (Neumo HE5 grade[26]) is coated with PTFE[27] to prevent scratching or breaking of the SiO_2 tube, which moves over it. Also, it facilitates the gliding of the tube roller's rolls, which are made of POM (polyoxymethylene). In order to prevent the neutron guide getting stuck during movement, the beam entry tube was mounted flexibly to allow a slight radial freedom of $\sim 5°$. At the intersection between the coated tube and the outer CF flange, a T piece electropolished

[23] The fused silica guides were ordered from TQS (`https://tqs-quartz.com`).
[24] The hygienic class HE3 refers to a surface roughness of $R_a \leq 0.6\,\mu\text{m}$. Neumo is a manufacturer for pharmaceutical-grade stainless steel tubes (`https://www.neumo.de`).
[25] To decrease the heat flux from the left vacuum chamber into the cryostat, the diameter of the left stainless steel tube has been partially reduced to 1.4 mm.
[26] Electropolished stainless steel tubes of hygienic class HE5 exhibit a low surface roughness of $R_a \leq 0.25\,\mu\text{m}$.
[27] The coating (PTFE, 20 µm thickness) was carried out by Kersten Kunstoffcoating GmbH, `https://www.kersten-gmbh.de`.

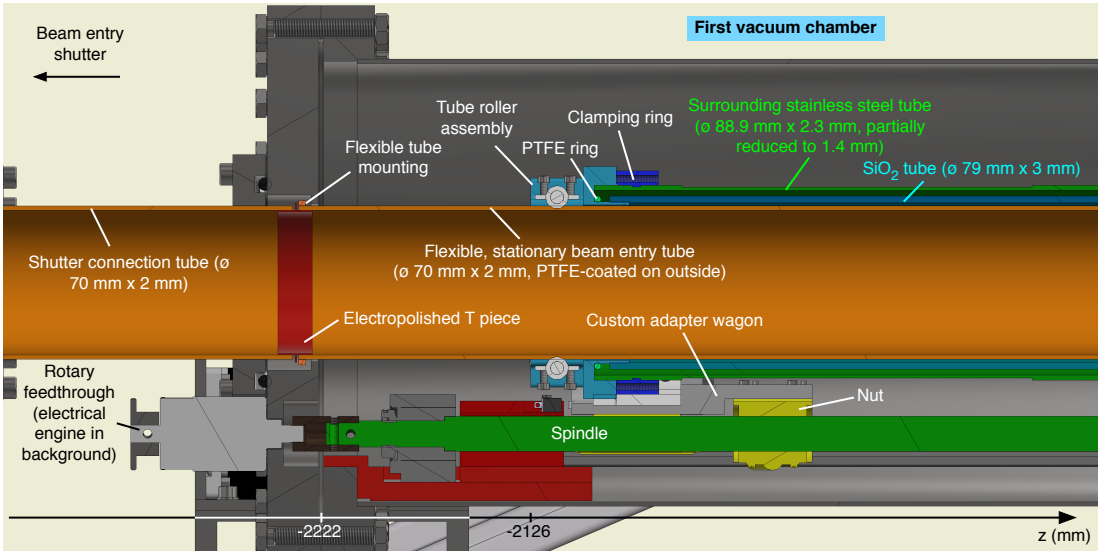

Figure 5.15: Tube-over-tube system on the left side of the neutron guide, with the neutron guide retracted to the storage position (spin flip position $z_{\mathrm{sf}} = 390\,\mathrm{mm}$, cf. Fig. 5.5 for a zoomed-out overview). After passing the beam entry shutter and the shutter connection tube, the UCN enter the stationary beam entry tube. The multi-layered movable neutron guide section rolls over the PTFE-coated beam entry tube in longitudinal direction, with stainless steel as the outer and fused silica (SiO_2) as the inner material. Upon rotation of the spindle by an electrical engine in ambient conditions, the nut moves the custom adapter wagon, which in turn pushes or pulls the entire movable neutron guide section. The z-position relative to the cryostat coordinates is provided by the scale at the bottom. The dimensions refer to the outer diameter and the wall thickness, respectively. Further details are given in the text.

according to HE4 standard[28] is included to prevent UCN losses. Left of the beam entry tube, the HE5 shutter connection tube ($\varnothing_{\mathrm{outer,\,tube}} = 70\,\mathrm{mm}$, 2 mm wall thickness, length 150 mm) guides the UCN from the shutter to the flexible tube.

Following the depiction in Fig. 5.15, the movable neutron guide is connected to a custom adapter wagon installed on the translation stage (for a top view on the translation stage, cf. Fig. 5.6). The connection is realised by tightening a clamping ring, which is screwed to the custom adapter wagon with a 5 mm thick PTFE layer in-between for thermal insulation. Attached to a nut, the adapter wagon and thus the entire movable neutron guide section moves in longitudinal direction upon rotation of the spindle. The necessary torque is provided by an electrical engine in ambient condition, which is coupled to a rotary feedthrough using a roller chain (cf. Ch. 5.2.3 for a more detailed description).

The guiding flange, which moves inside the stabilisation rails of the stabilisation tube (cf. Ch. 5.3.4), marks the transition of the long to the short SiO_2 tube (cf. Fig. 5.16). Additional to providing mechanical stability, the guiding flange with insets made of POM (cf. Fig. 5.17 a) prevents a rotation of the neutron guide system, which would otherwise occur due to the magnetic forces between the Halbach octupole and the compensation octupole. The possibility of a rotating guide system needs to be prevented, since it would introduce a

[28] Stainless steel tubes electropolished according to the HE4 standard are characterised by a surface roughness of $R_{\mathrm{a}} \leq 0.4\,\mu\mathrm{m}$.

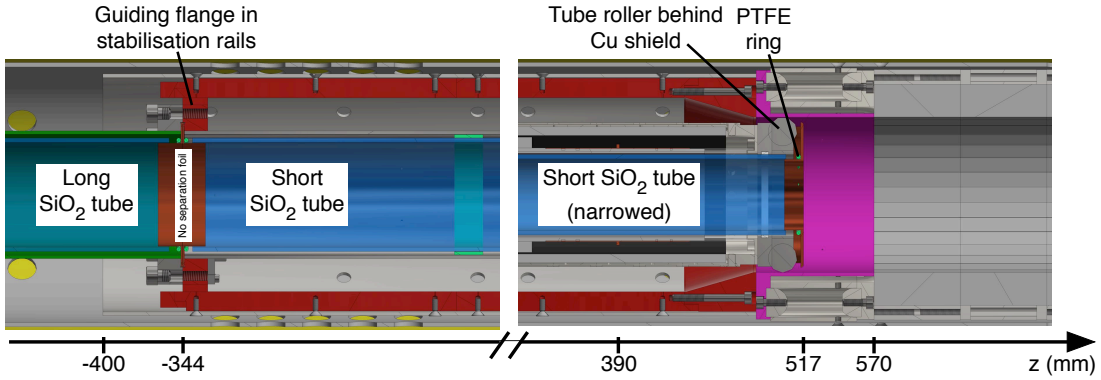

Figure 5.16: Depiction of the guiding flange and the tube roller of the movable neutron guide section (cf. Fig. 5.13 for an overview of the position inside the cryostat). The neutron guide section is retracted to its storage position (spin flip position $z_{\mathrm{sf}} = 390\,\mathrm{mm}$), with the guiding flange dividing the long and the short fused silica (SiO_2) tubes. The separation foil, which was relevant according to the original design, has been removed to increase the UCN transmission. At its very right end, the movable neutron guide contains a tube roller with PEEK rolls to move on the Halbach octupole surface. To inhibit breaking of the SiO_2 tube, a PTFE ring prevents the direct contact to the copper (Cu) shield. The bottom axis provides the guide position relative to the cryostat coordinates in z-direction. A detailed depiction of the spin flip unit is given in Fig. 5.18.

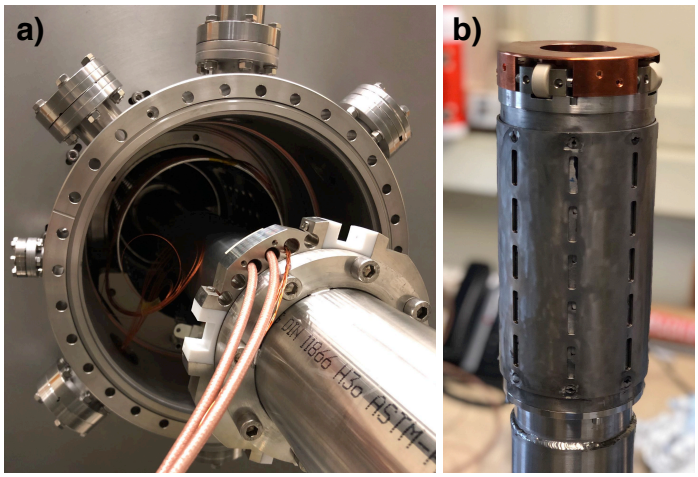

Figure 5.17: Photograph of the guiding flange and the compensation octupole assembly. (a) Insertion of the guiding flange into the stabilisation tube, which is already installed inside the cryostat. The POM insets which correspond to the stabilisation rail positions can be clearly identified. (b) Right end of the movable neutron guide section, with the titanium surrounding of the compensation octupole (dark grey), the PEEK rolls of the tube roller (beige-coloured), and the copper shield (dark orange).

variation in the compensated magnetic field distribution in the spin flip region. According to the original design, a vacuum separation foil should be installed at the intersection between the long and the short tube section, which is marked by two custom CF flanges with a custom Cu sealing (cf. Fig. 5.14). Since the vacuum conditions in the first vacuum chamber were notably better than assumed, it was decided to remove the separation foil. As a result, the

transmission of low-energetic UCN could be expected to increase by $\sim 20-30\,\%$ (analytical calculation taking the neutron attenuation into account). At its very right, the neutron guide section comprises a tube roller flange to enter the Halbach octupole (cf. Fig. 5.16). The tube roller flange contains four PEEK rolls displaced by 90° (for a photograph, cf. Fig. 5.17 b) to roll on the inner surface of the Halbach octupole.

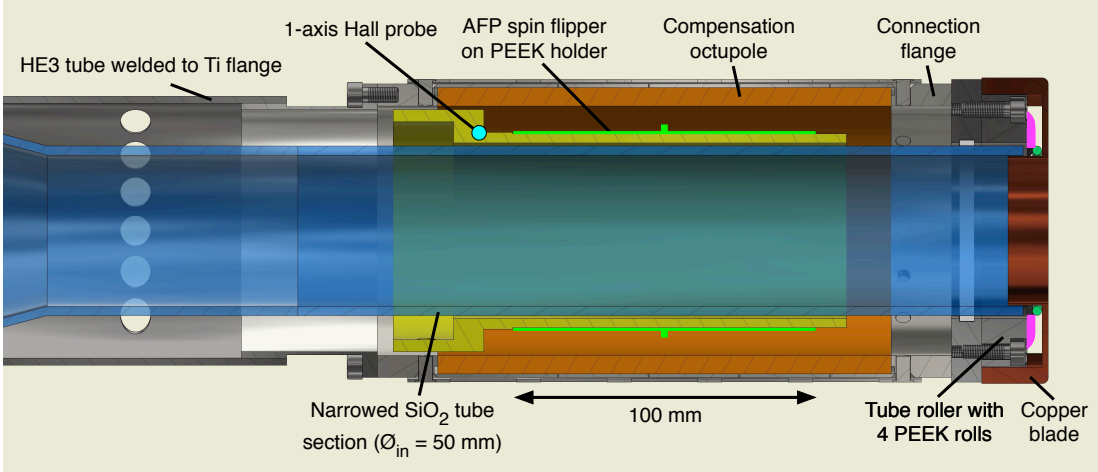

Figure 5.18: Detailed view of the spin flip unit at the right end of the movable neutron guide section. To the right side of the surrounding HE3 stainless steel tube, a titanium flange is welded providing the connection to the compensation octupole. A titanium connection flange attaches the tube roller to the compensation octupole, which contains 4 PEEK rolls to allow for moving on the Halbach octupole surface (cf. Fig. 5.16). At the very end, a copper blade ensures that no UCN is exposed to UCN-absorbing titanium surfaces. Inside the compensation octupole, the adiabatic fast passage (AFP) spin flipper is positioned on a PEEK holder, which is slid over the narrowed part of the short SiO_2 section. For monitoring the longitudinal magnetic field, a 1-axis Hall probe is installed. More details are found in the text.

Fig. 5.18 shows a detailed view of the spin flip unit. The tube roller is connected to the compensation octupole, which compensates the magnetic field gradients inside the spin flip region (cf. Ch. 5.3.3). In order to avoid magnetisation effects, the tube roller and the connection flange in direction of the compensation octupole were built from titanium. Also, the compensation octupole is surrounded by a titanium cylinder (cf. Fig. 5.17). Since titanium has a negative Fermi potential (cf. Table A.1), it acts as a neutron absorber, which would result in UCN losses. Therefore, a copper shield was designed which prevents the UCN from contacting the titanium. Due to its comparably high Fermi potential of 168 neV (cf. Tab. A.1), it furthermore has the function to reflect the UCN after the filling phase, when the neutron guide is not yet fully retracted from the storage volume. To improve the shield's reflectivity, it was electropolished to meet the HE4 standard[29]. On the narrowed SiO_2 section, the adiabatic fast passage (AFP) spin flipper in low-pass birdcage design is positioned[30] (green). The spin flipper is positioned on a PEEK holder, which is slid over the tube. At a distance of $\Delta z \sim -61$ mm from the middle of the spin flipper, a 1-axis Hall

[29]The copper shield was polished by Metano (`http://www.metano.de`).
[30]The AFP spin flipper was designed and commissioned by K. Ross.

probe[31] (cyan) has been installed at $r \sim 33\,\mathrm{mm}$. It can be used to measure the longitudinal magnetic field near the spin flip region.

5.4.2 Mechanical constraints on the spin flip position

The dimensioning of the translation stage gives constraints on the movement of the neutron guide section (cf. Ch. 5.4) and therefore on the spin flip position. Overall, the mechanics was designed to provide a free movement across a wide range of $\Delta z = 729.2\,\mathrm{mm}$. Thereby, as Fig. 5.19 illustrates, it enables a hypothetical spin flip position between the minimum and maximum,

$$\begin{aligned} z_{\mathrm{sf,\,min}} &= 390.0\,\mathrm{mm}\ , \\ z_{\mathrm{sf,\,max}} &= 1119.2\,\mathrm{mm}\ . \end{aligned} \tag{5.14}$$

Note that the spin flip position is defined by the middle of the spin flip unit of 100 mm length. Fig. 5.19 also shows the position of the UCN-reflecting copper (Cu) blade, which is installed at the front of the neutron guide section (cf. Fig. 5.18). Its position is always $\Delta z = +127.0\,\mathrm{mm}$ right of the middle of the spin flipper ($z_{\mathrm{Cu,\,max}} = 1246.2\,\mathrm{mm}$).

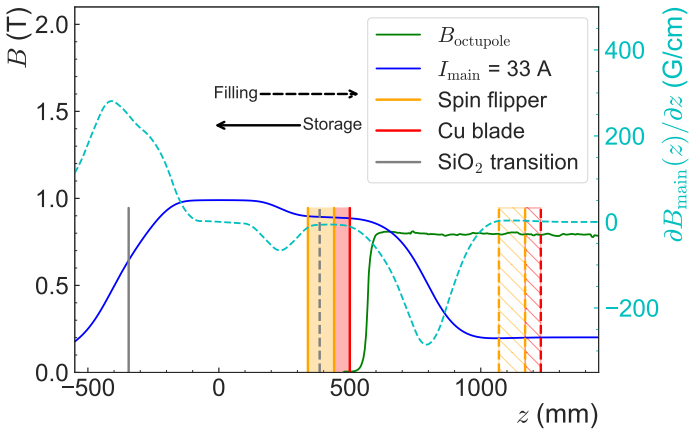

Figure 5.19: Movement ranges of the neutron guide system for the superconducting coil current $I_{\mathrm{main}} = 33\,\mathrm{A}$. Positions of the spin flipper (yellow area), the copper (Cu) blade front (red line), and the SiO_2 tube transition (grey line) are given relative to the longitudinal magnetic field (blue line) and the Halbach octupole magnetic field (green line). The dashed spin flip area represents the furthest-in filling position, while the filled area caters to the fully-retracted storage position. Also, the filling positions of the Cu blade and the transition are denoted by dashed lines. The cyan dashed line depicts the gradient of the longitudinal magnetic field, $\nabla_z B_{\mathrm{main}}$ (right axis).

The Nanotec engine divides one rotation into 160 steps and is typically set to a maximum velocity of 3840 steps per second, which equals 24 rotations per second. Theoretically, taking the 5 mm pitch and the 1:1 transmission into account, the total distance could be travelled in $\sim 6\,\mathrm{s}$. Variations in the rotational speed due to a rising edge and a falling edge just after starting/before stopping the engine results in lower absolute velocities, which implies that $\Delta z = 730\,\mathrm{mm}$ is travelled within $\sim 26\,\mathrm{s}$. The final optimum is still being determined. The overall precision of the movement is in the sub-millimetre range (the engine

[31] The AREPOC (`http://www.arepoc.sk`) Hall probe (type HHP-NA) can be used in cryogenic environments.

step resolution implies a translational movement of 31.25 μm). The maximum movement ranges are limited by electrical end stops, which cause the engine to stop rotating upon contact (cf. Ch. 5.6). Mechanically, an additional distance of $\Delta z \sim 1.3\,\text{mm}$ would be possible. It should be kept in mind, however, that the positions in this section refer to the computer aided design (CAD) model, which is an optimal case. After the final assembly, Hall probe measurements were carried out to check to what extent the actual position deviates from the CAD position (cf. Ch. B.1). After analysing the measured magnetic field gradient in the Halbach octupole region, a dip in the gradient was identified, which according to previous dedicated measurements of the octupole field gave the position of the Halbach octupole within the cryostat. Taking the determined Halbach octupole position as a reference point, it turned out that the neutron guide positions needed to be corrected by the offset $\Delta z_{\text{corr, spin flipper}} \sim -16\,\text{mm}$ after the final implementation.

5.5 Development and characterisation of a movable custom UCN detector

The following section provides the reader with relevant information on the custom UCN detector, starting with the detection principle and the steps leading to the final technical implementation of the detector unit (cf. Ch. 5.5.1). Performing characterisation measurements using a calibrated americium-241 source and ultracold neutrons, the event reconstruction has been optimised, with the custom UCN detector reaching a performance similar to a commercial neutron detector (cf. Ch. 5.5.2). Moreover, the radial dependency of the neutron detector was tested and later modelled by ray-tracing simulations. Chapter 5.5.3 presents the mechanics which moves the detector inside the cryostat. Further information on physical, electrical, and mechanical details on the detector are found in Ch. B.2.

5.5.1 The neutron detector unit

For a brief introduction into the neutron detector assembly, its detection principle and important considerations during the design process are laid out. Afterwards, technical details on the final implementation are provided.

Details on the detection principle

As Fig. 5.20 illustrates, the general detection principle is based on a neutron-capturing boron-10 (^{10}B) layer directly coupled to a silver-doped zinc sulfide (ZnS:Ag) inorganic scintillator. The UCN capture in the circular ^{10}B layer with diameter ø= 99 mm leads to the production of a lithium-7 (^{7}Li)/α pair. The decay products are emitted in opposite direction and cause the scintillator (thickness[32] $t = 22.6\,\mu\text{m}$) to emit photons, which are guided towards the rectangular detection area.

The scintillator properties and the photon detection are thoroughly discussed in Ch. B.2.1. Despite being comparably slow with a decay constant of $\tau_{\text{decay, ZnS:Ag}} = 200\,\text{ns}$ [Kno89], ZnS:Ag has a high light output of $\sim$ 49000 photons/MeV and emits photons in the UV range with the peak intensity at $\lambda_{\text{peak}} = 450\,\text{nm}$ (cf. Fig. B.2 a). Combined with a UCN-absorbing ^{10}B layer, it has proven to be well-suited for UCN detection in the UCNτ experiment [WHM$^+$15]. Due to the exposure of high magnetic fields ranging up to 1.7 T (cf. Fig. 5.32 a), conventional photomultiplier tubes could not be used for photon detection. Instead, the 16-channel 4 x 4 SiPM array Hamamatsu S13361-6050AE-04 matched to λ_{peak}

[32] The scintillator thickness has been calculated from the density of $\varrho_{\text{ZnS:Ag}} = 3.25\,\text{mg}^2\,\text{cm}^{-1}$ and the given thickness of the underlying polyethylene (PE) layer, $t_{\text{PE}} = 0.25\,\text{mm}$ [elj16].

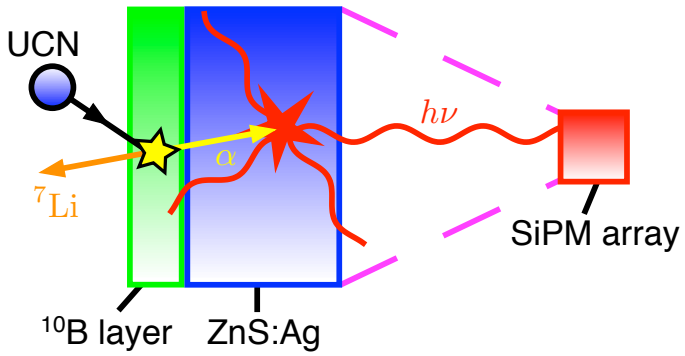

Figure 5.20: Detection principle of the custom ultracold neutron detector. The UCN is captured in the ^{10}B layer, whereby a ^{7}Li nucleus and an α particle are emitted in opposite direction. This implies that in any case, either a ^{7}Li nucleus or an α particle reach the ZnS:Ag scintillator, in which the decay products induce the generation of photons with energy $h\nu$ (red curly lines). For detection, the photons are guided onto a rectangular detection area.

with an effective detection area of $(25 \times 25)\text{mm}^2$ is used (more characteristics are found in Tab. B.1).

After the production in the scintillator, the photons need to be effectively guided from their origin on the circular ZnS:Ag scintillator surface with ø= 99 mm to the rectangular $(25\times25)\text{mm}^2$ detection area of the SiPM array (cf. Fig. B.3 b). For this, a light cone made of PMMA (cf. Fig. 5.21 and Fig. B.4 for detailed dimensions) has been built. To understand the light guidance, laser transmission measurements as well as ray-tracing simulations have been performed in great detail (cf. Ch. B.2.2.1). During the measurements, a radial dependence of the transmission was found for a laser shone perpendicular onto the circular PMMA surface. In order to quantify the photon transmission, ray-tracing simulations have confirmed the dependency of the photon transmission from the radial photon origin. The dependency was evaluated by simulating the photon transmission (T), *i.e.,* the number of photons being transmitted from the circular light cone front onto the detector area. Since the highest T value was found for a photon origin in the centre of the light cone (T_{centre} measured at $d_{\text{centre}} = 0\,\text{mm}$), the transmission for different radial distances $d_{\text{centre}} > 0\,\text{mm}$ is expressed relative to T_{centre}. It was found that T slightly decreases from 30 mm off-centre onwards, but does not decrease more than $\sim 20\,\%$ until $d_{\text{centre}} = 49\,\text{mm}$. Only close to the edge ($49\,\text{mm} < d_{\text{centre}} \leq 49.5\,\text{mm}$), the transmission drops to $\lesssim 50\,\%$ of T_{centre} (cf. Fig. B.8 a)[33].

Taking the photon transmission averaged over different values of d_{centre} and incident photon angles on the light cone's PMMA surface ($\overline{T} = 7.56\,\%$) into account, the expectable number of photons hitting the detector per neutron capture event can be calculated. Also, the calculation considers the ZnS:Ag light output and the photon detection efficiency (PDE) of the used SiPM array. Consequently, $\sim$ 1250 photons induced by the two possible ^{7}Li energies and $\sim$ 2200 for photons resulting from an α excitation can be expected to be counted on average per event (cf. Tab. B.2[34]).

[33] When considering Fig. B.8 a), the given numbers refer to the most general case, with the radial distance being increased in direction parallel to the light cone cutout ($\beta = 0°$, yellow dashed line).
[34] The respective α and ^{7}Li energies are provided in Eqs. (B.5)-(B.6).

Further considerations on the detector design

During the design phase, several physical and technical aspects leading to a functioning UCN detector were considered, which are summarised in the following. For further details, consider the provided sections in the appendix.

First, after the manufacturer Hamamatsu has guaranteed the SiPM to work down to liquid nitrogen temperature[35] ($T = 77\,\mathrm{K}$, cf. Ch. B.2.2.2), beneficial effects with regard to the dark count rate and thus the signal to noise ratio can be expected at lower temperatures, despite a significant decrease in the intrinsic SiPM gain factor. To account for the temperature-dependence of the detector bias voltage, a linear extrapolation of the SiPM array's bias voltage has been implemented according to the data sheet recommendations [ham16b]. Down to $T = 140\,\mathrm{K}$, the linear approximation was found to describe the temperature-related change in the bias voltage well [CBM$^+$11, ZHJGF$^+$12].

Second, an analytical calculation on the UCN conversion efficiency as a function of the ^{10}B layer thickness was performed (cf. Ch. B.2.2.3), which describes the efficiency of the ^{10}B to capture UCN and 'convert' them into a $\alpha/^7$Li pair. The simulations have yielded an optimum layer thickness of 80 nm for UCN with maximum energies of 47 neV in the trap (cf. Fig. B.11 a). During the initial design process, a ZnS:Ag scintillator sheet coated with a 20 nm ^{10}B layer was purchased. In characterisation measurements with UCN stored in an aluminium bottle, the detection efficiency using a 20 nm layer was experimentally compared to using a newly-purchased 80 nm layer. Due to time limitations, other layer thicknesses have not been tested. Since using the 80 nm led to a ~ 3.5 higher detection efficiency (cf. Ch. 5.5.2), a ^{10}B thickness of 80 nm was chosen for the final detector implementation.

Third, although the ^{10}B layer absorbs UCN due to the imaginary part of its complex Fermi potential, it also has a certain probability to reflect UCN from its surface according to its real part (cf. Ch. B.2.2.4). The reflectivity is highly dependent on the angle and the kinetic energy of the UCN impinging on the ^{10}B surface. Especially for low-energetic UCN, this is a quite substantial effect (cf. Tab. B.3). Since a reflected UCN in the storage volume has a high probability to be absorbed and thus counted when impinging on the surface at a later point it time, this property should not inhibit the overall UCN detection.

Finding an appropriate optical glue

The used ZnS:Ag scintillator[36] is applied to a PE layer of thickness $t = 0.25\,\mathrm{mm}$. From the given density of $\rho_{\mathrm{ZnS:Ag}} = 3.25\,\mathrm{mg\,cm^{-2}}$ [elj16], a thickness of $t_{\mathrm{ZnS:Ag}} = 22.6\,\mu\mathrm{m}$ is calculated. The scintillator is coated with a 80 nm layer of highly-enriched ^{10}B ($\gtrsim 96\,\%$)[37].

Experimental tests had to be performed to find an appropriate glue for attaching the PE substrate of the ZnS:Ag scintillator sheet to the front of the PMMA light cone. The glue selection was limited due to the involved requirements. First, the glue had to be optically transparent after drying. Second, the glue had to be flexible enough when cooling down to low temperatures to account for the different thermal expansion coefficients of PMMA and PE. The experimental tests involved the application of the glue at room temperature to attach test sheets of PE to a piece of PMMA. After having dried for 24 h, the glued samples were put inside a fused silica cold finger which was slowly brought into a bath of liquid nitrogen with $T_{\mathrm{lN2}} = 77\,\mathrm{K}$. The end temperature at the neutron detector surface was unknown, with T_{lN2} considered as the worst case. After $\sim 3\,\mathrm{min}$, T_{lN2} according to a

[35] The manufacturer Hamamatsu has made this claim in a private communication.
[36] The scintillator of type EJ-440 was fabricated by Eljen Technology, `https://eljentechnology.com`.
[37] The coating was done by CDT CASCADE Detector Technologies GmbH, `http://n-cdt.com`.

temperature reading inside the cold finger could be reached. After $\sim 6\,\mathrm{h}$ exposure to T_{lN2}, the sample was slowly extracted. After waiting another day, the sample was put under minor mechanical stress to check the adhesive bond. Meeting all requirements, the two-component adhesive Acrifix® 2R 0190 was chosen, which is based on PMMA and polymerises the surface to achieve a strong bond[38].

To provide a secure fixation at the large PE surface of the scintillator sheet, the experimental tests had shown that the surface had to be roughened by using very fine sandpaper of grade 600. While glueing the scintillator sheet to the PMMA surface, air gaps were attempted to, but could not completely be avoided. After drying, $\sim 30\,\%$ of the ^{10}B surface area were covered with air bubbles. According to ray-tracing simulations, the transmission is decreased by $\sim 50\,\%$ if air gaps of size $0.1 - 1\,\mathrm{mm}$ are present (cf. Fig. B.7). Despite being a local effect, it should also be taken into account for a later detector efficiency evaluation.

Implications of the combined SiPM array channels

In the original detector design, it was planned to read out all 16 channels of the 4 x 4 SiPM array individually. This is also reflected by the number of input channels of the shaper box (cf. Fig. B.17 b). The readout of all channels would have had the advantage to infer the approximate neutron capture position on the detector's ^{10}B layer from the photon intensity distribution in the SiPM array. Due to the radial magnetic field shape of the trap, stored UCN with higher energies can reach positions with more radial distance to the light cone centre - how this is reflected in the detected photon intensity distribution was not known. Analysing the distribution could give an information on the average energy distribution of the stored UCN, which would allow for investigating systematic effects. With a large number of stored UCN, an important systematic effect would be an energy-dependent analysis of the neutron lifetime.

To investigate a possible reconstruction method, *i.e.,* inferring the photon origin caused by the neutron capture position from the photon intensity distribution on the 4 x 4 SiPM array, ray-tracing simulations were run (cf. Ch. B.3.2). During the simulations, the detector area was divided into 16 evenly-spaced squares to emulate the 4 x 4 SiPM array. The photon origin was shifted in increasing distances from the light cone centre, taking different angles relative to the rectangular light cone cutout into account. For analysing the energy distribution of a detected UCN, not the accurate position but the radial distance from the light cone centre (d_{centre}) is relevant. In the simulations, a possible reconstruction of d_{centre} from the maximum intensity in any SiPM channel was found (cf. Fig. B.23 a). It has to be noted, that this reconstruction method is only working if the photon origin is shifted parallel to the light cutout ($\beta = 0°$) - for the worst case of $\beta = 45°$, the reconstruction leads to wrong conclusions. Other reconstruction methods were not successful, 2D maps of the photon intensity distributions at different d_{centre} values and different angles with respect to the light cone cutout are found in Figs. B.23 a) - B.24 b).

In the final detector design, spatial constraints only allowed for the installation of a 15 pin feedthrough, which in turn required an electrical combination the 16 SiPM array channels into one single output channel before entering the preamplification stage (cf. Ch. B.3.2). Since the SiPM array along with the preamplification stage sits in the main vacuum of the cryostat, it needs to be separated from the pre-vacuum found in the detector tube (cf. Fig. 5.21). Thus, the 16 $51\,\Omega$ resistors of the SiPM array channels were connected,

[38] The glue Master Bond EP30-2 was also tested, which remained optically transparent but could not provide the bond under mechanical stress.

which increases the capacity of 1.3 nF [ham16b] to 20.8 nF. Thus, the SiPM array count rate capability is reduced to ~ 0.2 MHz, since the recharging of the individual SiPM cells after photon detection now takes longer due to the increased capacity. Along with this assumption, a failure of the detector electronics at count rates $\gtrsim 0.1$ MHz (cf. Ch. 5.5.2) after exposure to thermal neutrons has been experimentally determined. This should have no consequences for the UCN count rates, which are typically one magnitude smaller.

The detector front assembly

A schematic drawing of the detector front assembly is depicted in Fig. 5.21 (a realistic CAD rendering with further details is given in Fig. 5.22 a). To improve the internal photon reflectivity, the light cone was loosely wrapped by a 30 μm thick metallised Mylar foil, which is the standard for high-energy detectors at the Mainz Institute of Physics. The light cone assembly is held in place by a PMMA clamping ring[39], which provides the mechanical connection to the bottom flange by a PMMA cylinder. Furthermore, the printed circuit board (PCB) to which top the SiPM array is connected is fixated on the clamping ring. By tightening tiny PEEK screws, the SiPM array top is optically coupled to the right side of the light cone[40].

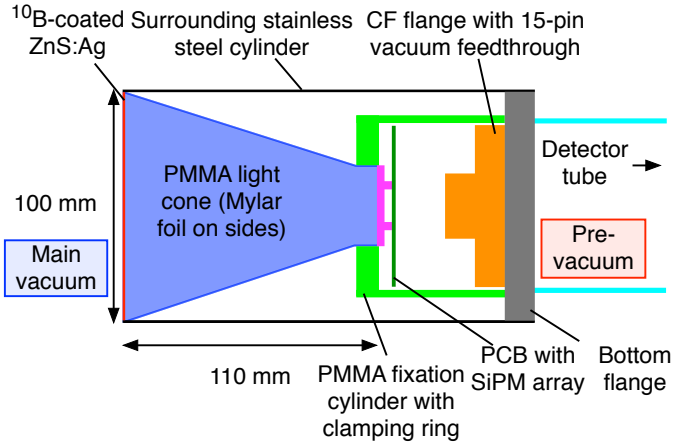

Figure 5.21: Schematic drawing of the neutron detector assembly. The ^{10}B-coated ZnS:Ag scintillator is glued onto the front of the PMMA light cone. The light cone, which is wrapped by a Mylar foil on its sides, is optically coupled to the 4 x 4 SiPM array sitting on a PCB. A PMMA cylinder fixates named components on a stainless steel bottom flange, which is welded to the stainless steel tube. A 15-pin vacuum feedthrough separates the cryostat's main vacuum to which all components left of the bottom flange are exposed to from the pre-vacuum inside the detector tube and ensures that the detector signals are sent to ambient conditions. Providing thermal shielding and mechanical protection, the detector front is surrounded by a stainless steel cylinder of 0.9 mm thickness. The entire assembly can be moved by ~ 267 mm in z-direction.

The PCB contains a SS4-40-3.00-L-D-K-TR Samtec connection for the Hamamatsu S13361-6050AE-04 SiPM array. Also, the pre-amplification electronics (cf. Ch. B.3) as well as a

[39] Since the light cone is made of PMMA, the material was also selected for the mechanically-coupled surroundings. Thereby, an equal thermal contraction of all relevant components during cooldown is guaranteed.

[40] To maintain repairability, the SiPM array was not glued to the light cone. Instead, the optical grease Saint-Gobain BC-630 was used for coupling.

Pt1000 temperature sensor for adjusting the bias voltage according to the temperature is included. In general, the functioning of the electrical components mounted on the PCB at low temperatures was unknown except for the SiPM array, which was specified to be working down to 77 K. Furthermore, the end temperature of the relevant electrical components after a complete cooldown of the cryostat could not be estimated beforehand. To account for possible temperature-related component failures, a thermal wire of 20 cm length was stretched across the rear side of the PCB. For currents of $I_{\text{heat}} = 0.1\,\text{A}, 0.5\,\text{A}, 1.0\,\text{A}$, thermal powers of $P_{\text{thermal}} = 0.13\,\text{W}, 3.2\,\text{W}, 12.6\,\text{W}$[41] are generated, which can provide a local heating of the electrical components on the PCB if needed.

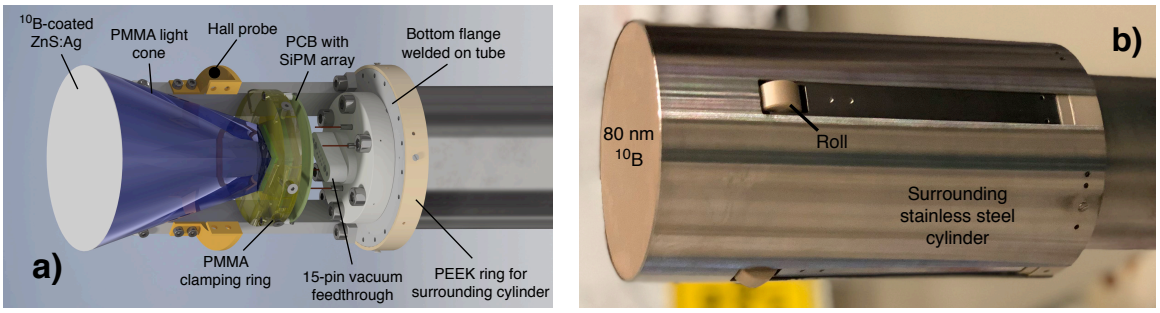

Figure 5.22: The finally-assembled neutron detector without and with installation of the surrounding stainless steel cylinder. (a) CAD rendering of the inner components of the neutron detector assembly. The assembly ends in the bottom flange, which is welded onto a detector tube. For monitoring the longitudinal magnetic field in the detector region, a Hall probe was included. All remaining components are described in Fig. 5.21. (b) Before insertion into the cryostat, the detector assembly is covered by a surrounding stainless steel cylinder, which functions as a mechanical protection of the ^{10}B layer and a thermal shield. The PEEK rolls for moving the detector inside the Halbach octupole are clearly visible.

The electronic signals are sent outside of the cryostat after passing the 15-pin SUB-D vacuum feedthrough CF40 flange[42], which is screwed on the bottom flange to separate the cryostat's main vacuum from the pre-vacuum inside the neutron detector tube assembly. After passing the tube, the signals are sent to ambient conditons by a MIL-DTL-26482 plug (cf. Ch. 5.5). The connection schemes are found in the appendix (cf. Fig. B.26 and Tab. B.4).

The neutron detector assembly was surrounded by a stainless steel cylinder with a thickness of $d = 0.9\,\text{mm}$ (cf. Fig. 5.21), which for the mechanical protection of the ^{10}B layer protrudes slightly over the detector front by 0.5 mm in radial direction. With the cylinder functioning as a thermal shield, the detector could be operated in a temperature not influenced by the surrounding Halbach octupole. Also, after activation of the thermal wire on the PCB, the shield made it possible to warm the detector electronics locally, reducing the impact on other sections of the cryostat. The thermal shield is also decoupled from the neutron detector assembly by insertion of a PEEK ring.

[41] The ISOTAN® (CuNi) thermal wire provides a resistance of $R = 63\,\Omega\,\text{m}^{-1}$.
[42] The flange of type 210-D15-C40 was ordered at Allectra GmbH (`https://www.allectra.com`).

On the bottom flange welded on the tube, four PEEK rolls[43] displaced by 90° were positioned (cf. Fig. 5.22 a) and b). The PEEK rolls have direct contact to the Halbach octupole surface and enable the detector to be moved inside the octupole. Selecting PEEK as material additionally ensures the detector assembly to be thermally decoupled from the octupole. To monitor the local magnetic field in longitudinal direction, a Hall probe[44] (cf. Fig. 5.22 a) is installed at $r \sim 45\,\text{mm}$ and a distance of $\Delta z \sim +75.9\,\text{mm}$ with respect to the ^{10}B layer.

5.5.2 Characterisation measurements using a calibrated americium-241 source and ultracold neutrons

After the final commissioning of the front neutron detector assembly, it was installed in a test chamber (cf. Ch. B.4.1). In the meantime, the shaper electronics were finalised (cf. Ch. B.3.2) and the readout system based on an analogue-digital converter (ADC) continuously streaming data with a time resolution of $\Delta t = 100\,\text{ns}$ was implemented (cf. Ch. B.4.1). This allowed for performing first test measurements using a calibrated americium-241 (^{241}Am) source with an activity[45] of 68(7) Bq. Additional to the influence of the bias voltage on the counting efficiency, the radial dependence could be experimentally determined and compared to the transmission values inferred from ray-tracing simulations (cf. Ch. B.4.3). Furthermore, due to the usage of a calibrated source, these measurements provided an excellent opportunity to test and develop an algorithm for event counting (cf. Ch. B.4.2). The algorithm was used for all subsequent analyses regarding the custom ultracold neutron detector.

A later measurement run at the UCN C source, which is unlike its counterpart at beamport D a continuously-running UCN source, has proven successful neutron detection at an optimised bias voltage of 57.2 V at room temperature[46] (cf. Ch. B.4.4). In order to get a quantitative comparison to the detector efficiency of the commercial CASCADE neutron detector (UCN detection efficiency $\sim 85\,\%$ [KS11]), a test setup at the pulsed source UCN D was constructed in a separate beam time. A storage of UCN in an aluminium storage bottle ensured a defined UCN energy and thus allowed for a comparison of both detectors.

Determination of the influence of the detector efficiency on the bias voltage using a calibrated americium-241 source

To determine the optimum bias voltage[47] for signal detection, the neutron detector assembly was placed in a light-proof test chamber at ambient conditions (cf. Fig. 5.23). The ZnS:Ag scintillator segment, of which a diameter of $\sim 5\,\text{mm}$ was covered with ^{241}Am (brown colour on scintillator sheet) after the corresponding solution had dried, was optically coupled to

[43] The PEEK rolls were designed to provide mechanical properties similar to the rolls of the guide section tube roller. Despite spatial limitations, this could be achieved by creating a force opposite to the direction of load using stainless steel blades with a thickness of $d = 0.4\,\text{mm}$.

[44] The Hall probe (type HHP-NP) by AREPOC (`http://www.arepoc.sk`) is certified for cryogenic operation.

[45] The activity of the ^{241}Am source was determined in a standard procedure by D. Renisch of the Mainz Institute of Nuclear Chemistry using a γ detector.

[46] The optimum bias voltage value decreases with temperature (cf. Ch. B.2.2.2) and is important to approach the breakdown voltage of the SiPM array for an efficient photon detection. Since the manufacturer gives an uncertainty of $\pm 5\,\text{V}$ [ham16b], the optimum bias voltage needs to be experimentally determined. The experimental determination was required due to the lack of measuring the individual breakdown voltages of the APD cells beforehand (cf. Ch. B.4.1).

[47] The bias voltage is automatically regulated according to the temperature reading on the detector PCB (cf. Ch. 5.5.1). During the ^{241}Am measurements in ambient conditions, the voltage was not fluctuating due to a constant temperature.

the centre of the light cone ($d_{\text{centre}} = 0\,\text{mm}$) using the optical grease Saint-Gobain BC-630. Therefore, α particles from the ^{241}Am decay were hitting the ZnS:Ag scintillator for photon generation - the α source therefore emulated the α particles emitted after a neutron is captured by the ^{10}B layer. Since the activity of the ^{241}Am was determined as 68(7) Bq for α particles being emitted in 4π direction, the expectable count rate of the detector reduces to $34(3.5)\text{s}^{-1}$ due to the 2π acceptance of the light cone.

With the CF100 flange closed, the system was lightproof. During the measurement, the ADC recorded the detector signal for a duration of 11(3) s[48] (for an electrical circuit scheme, cf. Fig. B.27 a) and was compatible with a maximum input voltage of ±2.5 V (cf. Ch. B.4.1). The bias voltage was successively increased by 0.5 V to cover the range from 55.2 V to 57.7 V. Changing the bias voltage was possible by turning a knob on the front side of the shaper box (cf. Fig. B.17 b).

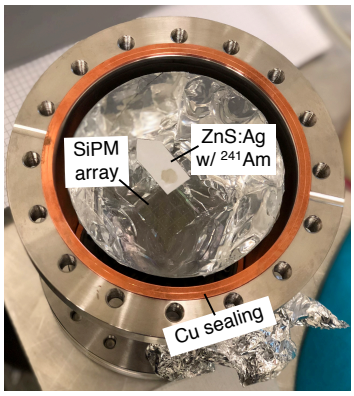

Figure 5.23: Test chamber for the ^{241}Am detector characterisation measurements. The light cone is optically coupled to the SiPM array and wrapped by a Mylar foil to improve the internal light reflection. ^{241}Am was applied to the ZnS:Ag scintillator sheet in liquid form. After drying, the ^{241}Am source formed a circular shape on the scintillator sheet with diameter ø∼ 5 mm. Before starting the measurement, the scintillator sheet was optically coupled to the light cone front using optical grease. To offer lightproof conditions, a CF100 blind flange is screwed to the top of the chamber, while pressing against a copper (Cu) sealing.

A typical signal shape after pulse shaping[49] with a distinctive peak signature is shown in Fig. 5.24 a), with the detector voltage[50], V_{det}, set to 57.2 V. The zoom into an event (cf. Fig. 5.24 b) provides a view on a typical zoomed-in signal shape to give an insight on the functioning of the algorithm for event identification (further details are given in Ch. B.4.2). Based on the voltage mean and a multiple of the standard deviation ($\overline{V}_{\text{det}} + k \cdot \sigma_{\text{det}}$), the algorithm iterates in negative V_{det} direction across the entire measurement file, until no more noise events are identified. This gives the threshold value $\widetilde{V}_{\text{thr}}$. Taking $\overline{V}_{\text{det}}$ as the mirror axis, this value is 'mirrored' in positive direction to set the threshold for peak identification,

[48] The uncertainty in the measurement timing stems from manually triggering the system, along with non-constant delays caused by the communication between the ADC and the connected PC.

[49] All detector signals which were used for event identification have always been preamplified and pulse-shaped by the detector electronics.

[50] During the ^{241}Am calibration measurements, the shaper gain was set to $G_{\text{shape}} = 9$.

i.e.,

$$V_{\mathrm{thr}} = \overline{V}_{\mathrm{det}} + |\widetilde{V}_{\mathrm{thr}}| \,. \tag{5.15}$$

Since setting only a peak threshold might also introduce false events to be counted, a second time-based threshold is also included. The time over threshold value (Δt_{thr}) equals the time during which the signal fulfils the condition $V_{\mathrm{det}} > V_{\mathrm{thr}}$.

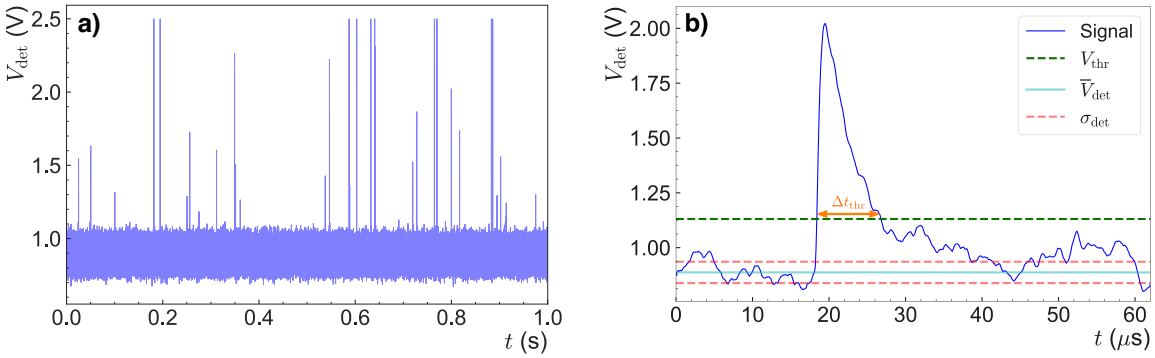

Figure 5.24: Detector signals during the ^{241}Am characterisation measurements after pulse shaping, for a bias voltage of 57.2 V and a shaper gain factor $G_{\mathrm{shape}} = 9$. (a) Detector voltage V_{det} during $t = 1$ s with distinctive peak shapes. Plotted is the raw signal data as measured by the analogue-digital converter (ADC). (b) Zoom into a signal peak with mean signal level $\overline{V}_{\mathrm{det}}$ and standard deviation, σ_{det}. The signal has overcome the peak threshold (V_{thr}), which was set by the peak finding algorithm. For event identification, the time over threshold (Δt_{thr}) is also used, which represents the time during which $V_{\mathrm{det}} > V_{\mathrm{thr}}$.

As depicted in Fig. 5.25, the count rate determined from the detector signal without any time thresholding to the data was too high taking the calibrated ^{241}Am source into account. The higher value was due to the probability of the detector voltage V_{det} being higher than the peak threshold V_{thr} outside of actual counting events. Applying a time threshold of $\Delta t_{\mathrm{thr}} = 1\,\mu$s, which was experimentally compared to other Δt_{thr} values, provided the best matching of the expectable to the measured count rate. The best matching count rate was reached for a bias voltage of 57.2 V.

Next, the dependence of the noise on the bias voltage was tested. For this, the detector assembly was mounted in the light-proof test chamber, with no ^{241}Am source installed. A broadening of the signal, which is described by its standard deviation (σ_{det}), and thus an increasing noise level was detected with increasing bias voltage (cf. Fig. 5.26 a). Interestingly, the average detector voltage ($\overline{V}_{\mathrm{det}}$) increases with increasing voltage (cf. Fig. 5.26 b), which is due to $\overline{V}_{\mathrm{det}}$ being shifted towards higher values. While the increasing noise level can be explained by the presence of more charge carriers released by higher local electric fields in the SiPM, $\overline{V}_{\mathrm{det}}$ growing with higher voltages might be due to the shaper electronics reacting to the increasing noise.

The radial dependence of the counting efficiency has also been evaluated by placing the scintillator at different radial distances from the centre (cf. Ch. B.4.3). It was found that from a centre distance of 30 mm onwards, the counting efficiency slightly decreases by $\sim 15\,\%$.

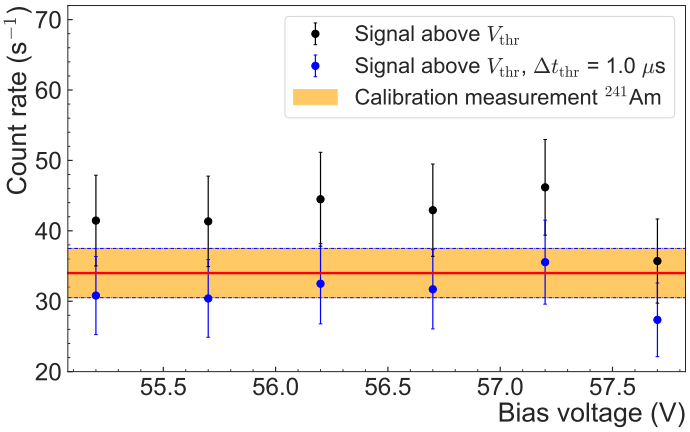

Figure 5.25: Detector count rate as a function of bias voltage during the ^{241}Am calibration measurements. The count rate determined by the peak finding algorithm without any time thresholding (black) is compared to the source activity of the ^{241}Am source in 2π direction, 34(3.5)Bq (yellow band with red line denoting the mean value). Due to the absence of a time threshold, false events are counted, which leads to a too high count rate. After applying a time threshold of $\Delta t_{\mathrm{thr}} = 1\,\mu$s (blue data points), the best fit to the calibration measurement was found. The highest count rate was achieved at 57.2 V bias voltage. The error in the count rate corresponds to the standard deviation.

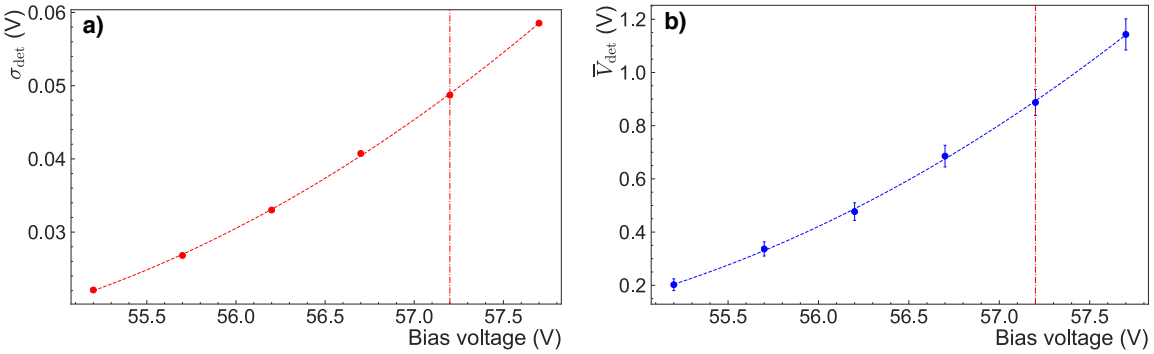

Figure 5.26: Rise of noise and voltage level with increasing bias voltage at room temperature. (a) The standard deviation of the signal (σ_{det}), which is a measure for the signal noise, doubles at a bias voltage of +57.2 V. Setting the bias voltage to 57.2 V (vertical red dash-dotted lines) has been determined as the optimum. (b) From 55.2 V to 57.2 V bias voltage, the average detector voltage $\overline{V}_{\mathrm{det}}$ rises by more than a factor of 4. The error bars denote σ_{det}.

Comparison to the CASCADE performance using stored UCN at the UCN D source

To estimate the detection efficiency of the custom UCN detector for UCN, it was compared to the performance of a commercial CASCADE detector, which offers a UCN detection efficiency $\sim$ 85 % [KS11]. The main difference in detecting UCN when compared to the ^{241}Am measurements is the energy of the decay products, which in case of the α particles emitted by ^{241}Am is $\sim 3-7$ times higher than the $\alpha/^{7}$Li energy released in the UCN-induced ^{10}B(n, $\alpha/^{7}$Li) reaction (cf. Ch. B.2.2.2). In a dedicated beam time, the UCN were stored for a storage time of $t_s = 20$ s in aluminium, such that only UCN with $E_{\mathrm{UCN}} \leq V_{\mathrm{F}}(\mathrm{Al}) = 54$ neV were present in the storage bottle after t_s. Furthermore, the formerly-used 20 nm

thin ^{10}B layer was compared to a 80 nm layer, which marked the optimum according to calculations on the UCN conversion efficiency (cf. Fig. B.11 a).

A photo of the setup is shown in Fig. 5.27 a), the beam line is depicted in b). For the neutron detector set to 57.0 V bias voltage, a vertical tube of 28 cm length was installed, which has led to UCN with energies $E_{\mathrm{UCN}} \sim [30, 84]$ neV impinging on the custom UCN detector. In this energy range, UCN close to the maximum potential energy in τSPECT ($E_{\mathrm{UCN,\,pot,\,max}} \sim 47$ neV) are also counted. To overcome the potential barrier of the CASCADE aluminium separation foil and make the detected energies comparable, the vertical tube after the 90° bend was exchanged by a 80 cm long tube when using the CASCADE detector. For both detection methods, the UCN density was determined by counting the number of UCN right after opening the second shutter (S_2) for a total time of $t_{\mathrm{count}} = 100$ s (for a depiction of the data, cf. Fig. 5.28 a). All given values for the custom UCN detector were background-subtracted[51].

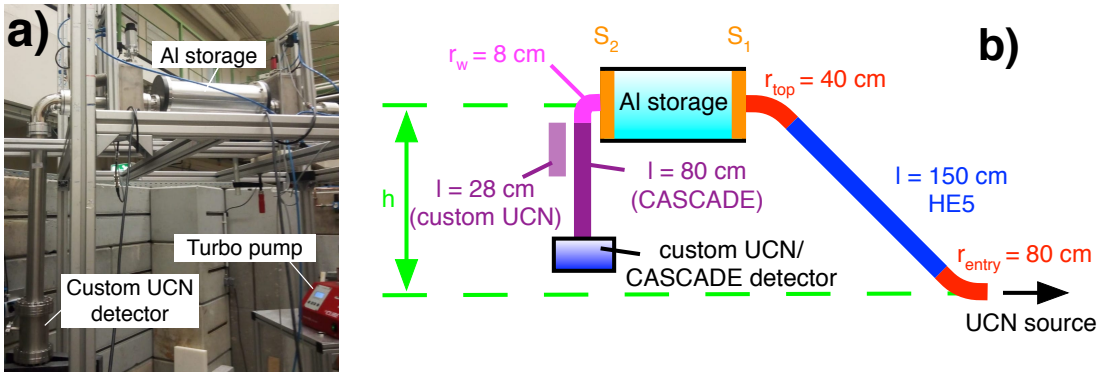

Figure 5.27: Setup for the detector comparison measurements using stored UCN. (a) Before being counted, the UCN were stored in aluminium. The custom UCN detector and the CASCADE detector were mounted at a vertical tube with lengths 28 cm and 80 cm, respectively (the photo shows a 80 cm vertical tube, which was used for additional test measurements). (b) Graphical depiction of the 'standard' beam line with the vertical tube being adapted to the detector type.

Along with the already purchased ZnS:Ag foil with 20 nm ^{10}B layer thickness, a second foil of the same batch was coated with 80 nm ^{10}B at the same coating facility[52]. In the first measurement run, both scintillator foils with different ^{10}B layer thicknesses were optically coupled using the optical grease Saint Gobain BC-630. As shown in Fig. 5.28 b), the neutron detector with optically-coupled 80 nm ^{10}B coating (non-glued) performed a factor of ~ 3.5 better than with the 20 nm ^{10}B coating and even provided a $\sim 15\,\%$ better detection efficiency compared to the CASCADE detector. The difference becomes apparent when comparing the calculated UCN conversion efficiency ε_c, *i.e.*, the ^{10}B layer's probability to convert a UCN into a ^{7}Li/α pair, of the 20 nm to the 80 nm layer (cf. Fig. B.11 a). According to the calculations, the 20 nm layer only reaches $\varepsilon_c \sim 68\,\%$ for a UCN energy of 26 neV, with ε_c decreasing for higher UCN energies. When taking the average UCN energy during the measurement into account ($\overline{E}_{\mathrm{UCN}} \sim 64$ neV assuming a $E^{3/2}$ dependency [GRL91]), the low

[51] At the selected bias voltage of 57.0 V, the background of the UCN detector was measured with closed (1.00(13) Hz) and open safety shutter (1.76(16) Hz). The closed safety shutter measurement was taken into account for background subtraction.

[52] The coating was applied by CDT CASCADE Detector Technologies GmbH, `http://n-cdt.com`.

detection efficiency of the thinner layer can be qualitatively comprehended. In quantitative terms, the experimental results clearly indicate a $\sim$ 3.5 times higher detection efficiency when using the 80 nm layer.

Following the measurement results, the 80 nm ^{10}B-coated scintillator foil was thus glued to the light cone in-between two beam time days using Acrifix® 2R 0190. Having dried overnight, the custom UCN detector was installed in the setup again. Measurements have shown a decrease in the detection efficiency of $\sim$ 15 %, which might be explained by the fact that the scintillator backside was roughened for glueing, which leads to a worse photon back-reflection probability. Repeated measurements with the CASCADE detector on the second beam time day confirm a stable UCN yield and are therefore not the cause for the decreased detection efficiency.

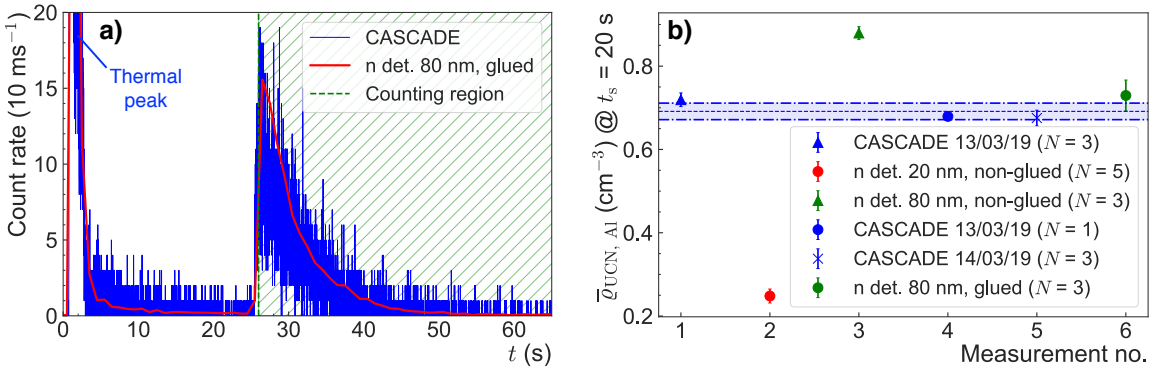

Figure 5.28: Comparison of the custom UCN detector performance to a commercial CASCADE detector using UCN stored in aluminium. For analysing the UCN detector data, a time threshold of $\Delta t_{\mathrm{thr}} = 1\,\mu$s was used. During all measurements, the custom detector's SiPM array was optically coupled to the light cone cutout using the optical grease Saint Gobain BC-630. (a) Count rate of the custom UCN detector with glued 80 nm ^{10}B layer after pulse shaping (red line) and the CASCADE detector (blue line) as a function of time. Both detectors measure the typical time-of-flight (TOF) spectrum with its thermal peak and the onset of UCN counts after opening the shutter S_2 in direction of the detector after storage. The shutter opening marks the beginning of the counting region for both detectors (green shaded area). In case of the custom UCN detector, a time binning of 1 s has been used, while the CASCADE data is plotted using time bins of 10 ms. (b) Average UCN density after 20 s storage in an aluminium bottle, $\bar{\varrho}_{\mathrm{UCN,\,Al}}$, for different measurement configurations of the CASCADE and the custom UCN detector. In case of the 80 nm layer (non-glued), the detection efficiency increased by $\sim$ 3.5 times when compared to the 20 nm layer (non-glued). After glueing, the custom detector's performance was comparable to the average CASCADE performance (blue area with mean and standard deviation of all CASCADE measurements during both measurement days). N given in the legend denotes the number of measurements per data point.

Despite the decreased detection efficiency, the measured UCN density by the custom UCN detector ($\bar{\varrho}_{\mathrm{UCN,\,n\,det}} = 0.73(4)\,\mathrm{cm}^{-3}$) was now in line with the average UCN density measured by the CASCADE detector over both days ($\bar{\varrho}_{\mathrm{UCN,\,CASCADE}} = 0.69(2)\,\mathrm{cm}^{-3}$, cf. Fig. 5.28 b).

Count rate limitations

During the measurements comparing the custom UCN detector performance to the CASCADE detector, saturation effects of the detector electronics became apparent. In the thermal peak region, count rates $\gtrsim 10^5\,\mathrm{s}^{-1}$, were identified, which could not be processed by the detector. This is represented by a 'gap' in the data (cf. Fig. 5.29). Such count rates are already close to the estimated count rate capability of the SiPM array ($\sim 0.2\,\mathrm{MHz}$, cf. Ch. B.3.2), which has been decreased by combining the capacitances of all individual APD cells. Also, a saturation of the shaping electronic is possible. This property has no consequences for τSPECT, since the thermal peak count rates measured inside the cryostat were significantly lower due to the larger distance to the reactor core.

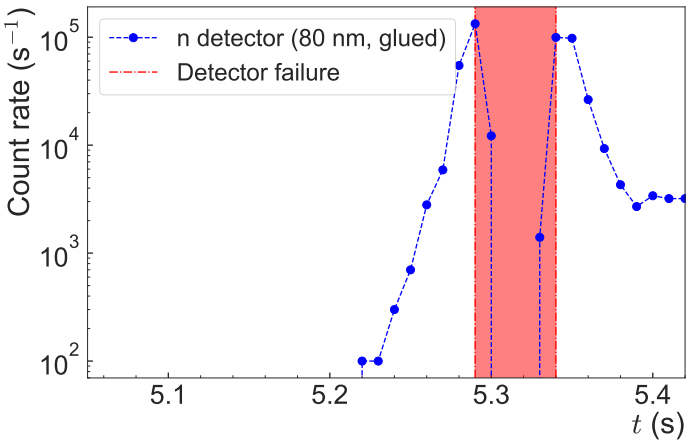

Figure 5.29: Ultracold neutron detector saturation at high count rates ($\gtrsim 10^5\,\mathrm{s}^{-1}$). The detector failure ('gap') is indicated by the red area, with the peak representing the characteristic thermal neutron peak of the TRIGA Mainz reactor after a pulse.

5.5.3 The movable UCN detector section

As discussed in Ch. 5.1, the UCN detector is moved into the storage volume for collecting the UCN after storage[53], whereby it travels a distance of $\Delta z = 266.6\,\mathrm{mm}$. In the following, the realised vacuum concept, which allows for sending the detector signals to ambient conditions, is presented. Furthermore, the electrical engine for the movement of the detector section and the resulting mechanical constraints on the neutron detector position are laid out. To conclude, the modularity for implementing a future decay proton detection is discussed.

The vacuum-separated tube and bellow system

As Fig. 5.30 shows, the front of the neutron detector is always inside the Halbach octupole, even if fully retracted. PEEK rolls close to the detector front (cf. Fig. 5.22 b) allow for moving the detector on the Halbach octupole surface. The stainless steel flange onto which the neutron detector assembly is mounted (for a detailed depiction of the neutron detector assembly, cf. Fig. 5.22 a) separates the high vacuum inside the cryostat ($p \sim 10^{-7}\,\mathrm{mbar}$) from the pre-vacuum ($p \sim 10^{-2}\,\mathrm{mbar}$) inside the moving tube system. For transferring the neutron detector signals, it contains a CF40 flange ('vacuum feedthrough flange') with

[53] A first prototype of the detector section has been designed by J. Karch. Shortcomings with regard to vacuum separation, heat transfer and the need for a pre-vacuum, however, required a complete re-engineering of the relevant components.

a welded-in 15 pin Sub-D feedthrough[54]. Inside the moving tube system, a pre-vacuum is needed to prevent H_2O freeze-out inside the contractable bellow, which could otherwise occur during cooldown and would prevent the movement of the entire system.

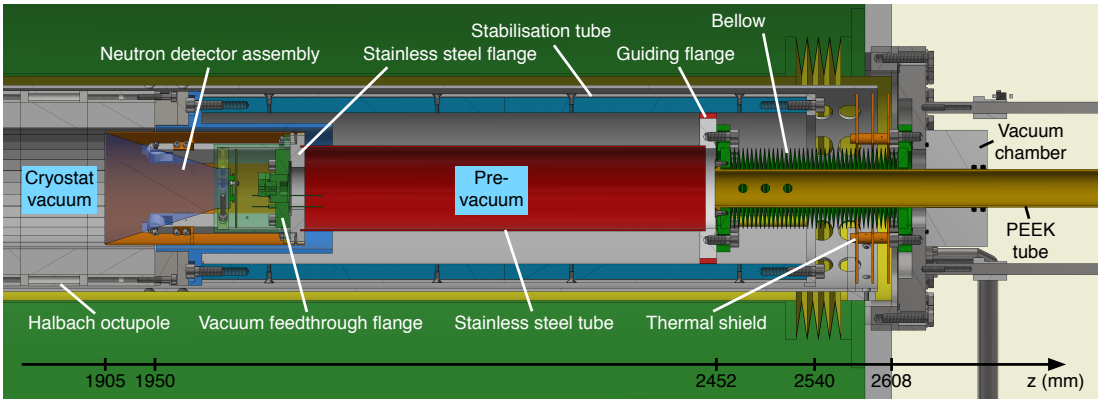

Figure 5.30: Overview over the left side of the neutron detector section, with the neutron detector being retracted to a typical non-counting position ($z_{\mathrm{det}} = 1905\,\mathrm{mm}$). When moved forward to detect stored UCN, the 4 PEEK rolls of the neutron detector assembly roll on the Halbach octupole surface. While the neutron detector assembly is exposed to the cryostat's main vacuum ($p \sim 10^{-7}\,\mathrm{mbar}$), a vacuum feedthrough flange separates it from the pre-vacuum inside the remaining neutron detector section ($p \sim 10^{-2}\,\mathrm{mbar}$). The stainless steel tube right of the neutron detector assembly ends in the guiding flange, which moves inside stabilisation rails to prevent the rotation of the neutron detector during movement. Ending in a CF63 flange, the stainless steel tube is connected to a bellow, which extends or compresses across the entire detector movement range. A PEEK tube connected to the bellow pushes or pulls the neutron detector section left of the bellow in longitudinal direction. Dividing ambient conditions from the pre-vacuum, the PEEK tube moves through a vacuum chamber containing two O-rings. To reduce the heat radiation from the outer cryostat flange, a three-layered thermal shield is included. The z-position relative to the cryostat coordinates is provided by the scale at the bottom.

The stainless steel flange is welded onto a stainless steel tube ($\varnothing_{\mathrm{outer,\ tube}} = 76.1\,\mathrm{mm}$, wall thickness 2.6 mm, length 361.8 mm) with integrated guiding flange. Similar to the movable neutron guide section (cf. Ch. 5.4.1), the POM inlays of the guiding flange glide through the rails of the detector stabilisation tube ($\varnothing_{\mathrm{outer,\ stabilisation\ tube}} = 168.3\,\mathrm{mm}$, wall thickness $d = 2.6\,\mathrm{mm}$, length 551.5 mm) to limit the total radial movement to $\pm 0.5\,\mathrm{mm}$. Using a CF63 connection, the guiding flange is connected to a bellow[55]. On its right side, the bellow is screwed to a CF200 flange, which separates the cryostat vacuum from ambient conditions. Reducing the heat impact on the inner of the cryostat has been a major design goal for the neutron guide section to guarantee the operation of the superconducting coils. Owing to

[54] The flange was purchased at Allectra, `https://www.allectra.com`, with order number 210-D15-C40.

[55] The stainless steel bellow (316L) was custom-made by MEWASA (`http://www.mewasa.com`), with outer/inner diameter $\varnothing_{\mathrm{out}} = 72.0\,\mathrm{mm}$ / $\varnothing_{\mathrm{in}} = 36.8\,\mathrm{mm}$, wall thickness $d = 0.15\,\mathrm{mm}$, and two CF63 flanges at each end. According to the specification sheet, the total length in rest position including flanges is $l_{\mathrm{bellow,\ rest}} = 378.0\,\mathrm{mm}$, with a maximum/minimum elongation to lengths $l_{\mathrm{bellow,\ max}} = 493.7\,\mathrm{mm}$ / $l_{\mathrm{bellow,\ min}} = 91.1\,\mathrm{mm}$. The elongation and contraction is needed to move the detector assembly in or out of the storage volume. Extended from minimum to maximum position, the manufacturer guarantees a lifetime of 10000 cycles.

the bellow's thin wall thickness of $d = 0.15\,\mathrm{mm}$, the thermal flux from the CF200 at room temperature is negligible. To further reduce thermal radiation from the CF200 flange to surrounding components, a three-layered thermal shield with electropolished stainless steel blades ($\varnothing_{\mathrm{outer}} = 170\,\mathrm{mm}$, $d = 2\,\mathrm{mm}$) separated by PEEK distance holders was built.

The longitudinal movement caused by the rotary movement of the shaft is transmitted from the nut in ambient condition to a PEEK tube screwed onto the left-hand side of the bellow. The inner PEEK tube ($l = 584\,\mathrm{mm}$, $\varnothing_{\mathrm{outer,\,tube}} = 50\,\mathrm{mm}$, wall thickness 10 mm) was designed to transmit the required force for the movement of the detector assembly. Since the tube is exposed to room temperature at its right side, the material PEEK was selected to suppress the resulting heat flux. Furthermore, the tube functions as a cable channel for the neutron detector cables and contains ventilation holes to permit pumping the space between the tube system and the inner side of the bellow.

For separating the pre-vacuum needed to prevent H_2O freeze-out on the inner surface of the bellow from ambient conditions, the PEEK tube is moved through two FKM O-rings contained in a small vacuum chamber. The vacuum chamber is screwed onto the outside of the CF200 flange and has a KF16 outlet to connect a scroll pump for pumping the pre-vacuum. For monitoring the cryostat vacuum, the CF200 flange provides a CF16 connection to which a pressure gauge installed at the end of a thin stainless steel tube is connected. The thin tube is needed to increase the radial distance of the pressure gauge to the cryostat to reduce its magnetic field exposure.

Detector engine assembly

As depicted in Fig. 5.31, the PEEK tube ends in a custom flange assembly on the ambient side, which has several functions. First, it contains a MIL-DTL-26482 vacuum feedthrough for the neutron detector cables (for pin connections, cf. Tab. B.4). Second, it transfers the momentum from the nut to the PEEK tube. For this, a ring is screwed onto the PEEK tube which is pushed and pulled by a large disk connected to the nut moving longitudinally upon spindle rotation[56]. To prevent dynamic misalignment of the entire system, the disk glides through three additional stainless steel rails[57] of length 477 mm.

On the top and bottom rail, mechanical end stops are installed to ensure that the system moves in the specified movement range (cf. Eq. (5.16)). Moving further in than allowed by the movement range would cause an overstretching and therefore breaking of the bellow, while exceeding the range in the opposite direction would cause the detector assembly to drop out of the Halbach octupole. Additionally, electrical end stops are installed onto the mechanical end stops to send a stop signal to the engine controller $\sim 1.3\,\mathrm{mm}$ before the mechanical end stop is reached.

At the end of the shaft sits a gear wheel which is connected to the electrical engine's gear wheel using a roller chain. The Nanotec ST5909L3008 engine is positioned with a radial distance of $\sim 245\,\mathrm{mm}$ (depending on the roller chain tension) to the middle of the cryostat, which limits its magnetic field exposure to $\sim 0.5\,\mathrm{mT}$. Due to the comparably low torque of the engine of $\sim 0.5\,\mathrm{N\,m}$ at 200 rpm at 24 V [nan13], which suffices to travel the distance of $\Delta z \sim 250\,\mathrm{mm}$ within $\sim 10\,\mathrm{s}$, an adaptable 2:1 transmission was chosen.

[56] A flanged ball screw nut made by Mädler (`https://www.maedler.de`) with 4 mm pitch (order number 64012045) was used.

[57] For improved gliding, slide bearings by igus (`https://www.igus.de`) of type iglidur J 10 were installed.

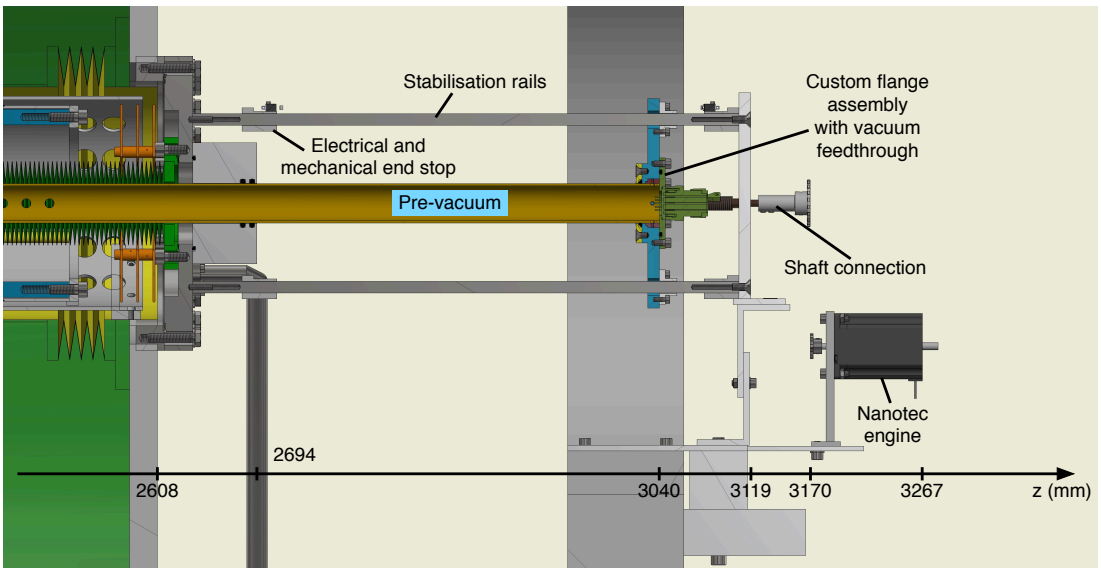

Figure 5.31: Overview over the right side of the neutron detector section, with the detector positioned at the non-counting position ($z_{\mathrm{det}} = 1905\,\mathrm{mm}$). For moving the neutron detector, the custom flange assembly contains a nut connected to a spindle, which is in turn rotated by an electrical engine ('Nanotec engine'). The engine and the spindle are connected by a roller chain, which is attached to the gear wheels of the engine and the shaft connection. Transferring the longitudinal movement to the PEEK tube and thus causing the movement of the neutron detector assembly in the cryostat (cf. Fig. 5.30), the custom flange assembly moves within stabilisation rods. Electrical and mechanical end stops ensure the detector moving within its constraints. The bottom scale provides the z-position relative to the cryostat coordinates.

Mechanical constraints on the neutron detector position and modularity for proton detection

The detector section has been designed to move the neutron-absorbing ^{10}B layer inside the storage volume to collect UCN during counting. Also, the absorbing ^{10}B layer can be fully retracted from the storage volume during the storage process. These conditions have determined the movement range of $\Delta z = 266.6\,\mathrm{mm}$, with the following minimum and maximum values in the τSPECT coordinate system (cf. Fig. 5.32 a):

$$\begin{aligned} z_{\mathrm{det,\,min}} &= 1899.5\,\mathrm{mm}\ , \\ z_{\mathrm{det,\,max}} &= 1632.9\,\mathrm{mm}\ . \end{aligned} \tag{5.16}$$

The detector energy sensitivity is shown in Fig. 5.32 b). For cleaning, all positions in-between the minimum and maximum positions (cf. Eq. (5.16)) are available. The detector electronics, in this case the middle of the detector PCB, is always $\Delta z = +117.3\,\mathrm{mm}$ right of the ^{10}B layer and exposed to magnetic flux densities up to $\sim 1.7\,\mathrm{T}$ (cf. Fig. 5.32 a). Within the provided movement range, the bellow is operated according to its specifications:

$$\begin{aligned} l_{\mathrm{bellow,\,max}} &= 434.0\,\mathrm{mm} < l_{\mathrm{bellow,\,max,\,spec}} = 493.7\,\mathrm{mm} \\ l_{\mathrm{bellow,\,min}} &= 167.4\,\mathrm{mm} > l_{\mathrm{bellow,\,min,\,spec}} = 91.1\,\mathrm{mm}\ . \end{aligned} \tag{5.17}$$

To further increase the bellow's lifetime, it is kept in its rest position ($l_{\mathrm{bellow,\,rest}} = 378.0\,\mathrm{mm}$) when the experiment is not running.

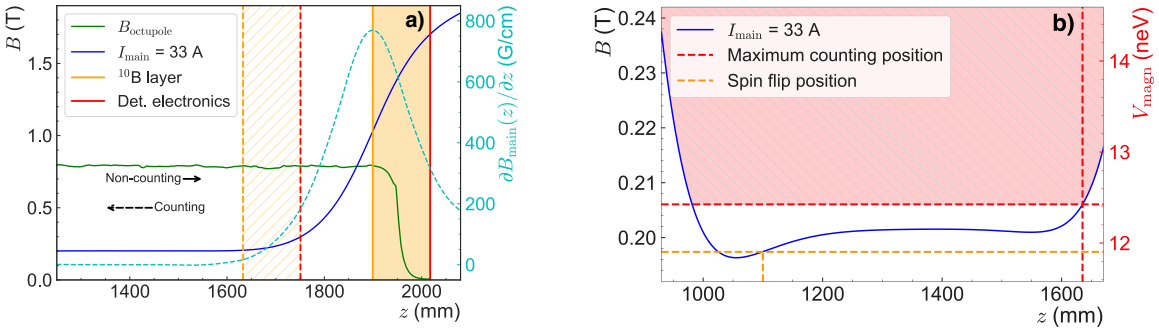

Figure 5.32: Movement ranges of the detector mechanics and sensitivity limitation. (a) Movement ranges of the detector mechanics for the superconducting coil current $I_{\text{main}} = 33\,\text{A}$. The positions of the ^{10}B layer (yellow line) and the detector electronics (red line) are given relative to the longitudinal (blue line) and the octupole magnetic field (green line). Also, the gradient of the longitudinal magnetic field, $\nabla_z B_{\text{main}}$, is depicted by the cyan dashed line (right axis). The respective minimum positions are given by the straight lines, while the dashed lines give the maximum positions. (b) Neutron detector energy sensitivity. In its maximum driven-in position, the detector can reach a position corresponding to 12.4 neV (red dashed lines), which is $\sim 0.5\,\text{neV}$ above the V_{magn} value corresponding to the spin flip at $z_{\text{sf}} \sim 1100\,\text{neV}$ (yellow dashed lines). The effect is negligible.

A combination of electrical and mechanical end stops mounted on the outer stabilisation rails (cf. Fig. 5.31) ensure a movement within the constraints. Relative to the CF200 flange, the ends of the mechanical end stops facing the flange are positioned in distances 42.3 mm and 440.1 mm. If the custom flange assembly contacts the electrical end stops $\Delta z \sim 1.3\,\text{mm}$ before reaching the mechanical end stops, the engine is immediately stopped (cf. Ch. 5.6).

The Nanotec engine driving the shaft rotates with 8000 steps s^{-1}. Since a 360° rotation equals 800 steps, 10 rotations per second are translated into a longitudinal velocity of $20\,\text{mm}\,\text{s}^{-1}$ (note the 2:1 transmission). Taking the rising edge of the engine rotation speed at startup and the falling edge just before reaching the end position into account, the total distance of $\Delta z_{\text{detector}} \sim 250\,\text{mm}$[58] can be traveled in $\sim 16\,\text{s}$. Along with the 4 mm pitch of the shaft, the system is engineered to reach a positioning precision well below 1 mm (the engine step resolution translates into 5 μm longitudinal movement). Given positions in this section are based on the computer aided design (CAD) model. The assembly process has introduced slight deviations from the positions, which is the reason why the magnetic field measured by the Hall probe in the detector region has been used to determine the deviation between the CAD and the actual position. The analysis is based on comparing the measured position-dependent magnetic field with the simulated field based on the CAD coordinates (cf. Ch. B.1). The analysis has shown that the actual position is offset by $\Delta z_{\text{corr, detector}} \sim +8\,\text{mm}$. This offset needs to be considered for the final position determination of the detector.

The whole system has been designed with modularity in mind. In phase II of τSPECT, the neutron detector assembly shall be exchanged for a proton detector. For this, only the parts left of the bellow need to be exchanged, while all other components can be reused.

[58] The total distance depends on the selected counting position, which can be varied in-between measurements.

Including a mirror electrode as well as acceleration electrodes, the detection of decay protons will thus be possible.

5.6 Data acquisition concept

All relevant measurement data is continuously logged. For logging pressure and temperature data, listed devices send data to a PC via serial connection[59]:

- Pfeiffer MaxiGauge®: Pressure logging of up to 6 pressure gauges (cf. Ch. 6.1.1).
- Keithley 2700: Temperature logging of 15 cryostat temperature sensors (cf. Ch. 6.1.1).
- LakeShore 218: Temperature logging of 5 temperature sensors on outer stainless steel tube (cf. Ch. 5.3).
- Arduino: Temperature logging of neutron detector temperature sensor (cf. Ch. 5.5).

The measurement cycle from a data acquisition perspective is shown in Fig. 5.33. The measurement cycle is controlled by an Arduino-based delay box, which offers 24 BNC outputs with TTL or +24 V logic. The graphical user interface has recently been rewritten by A. Tsvetkov to provide 'queues' of measurement cycles with different parameters. This becomes handy when measuring storage curves, since several measurement sets with varying storage times can be executed automatically.

The start of the measurement, t_0, is defined by the reactor sending a +24 V signal to the delay box. The delay box then returns the signal to the reactor which leads to the pulse rod quickly rising (initiation of the reactor pulse). Repeated measurements have shown that t_0 fluctuates by up to 1 s[60]. To date, it could not be determined whether this fluctuation stems from uncertainties in the reactor pulsing or from the delay box electronics. Apart from setting parameters for the filling and storage times, the positions of the neutron guide and the detector are configured prior to the measurement cycle.

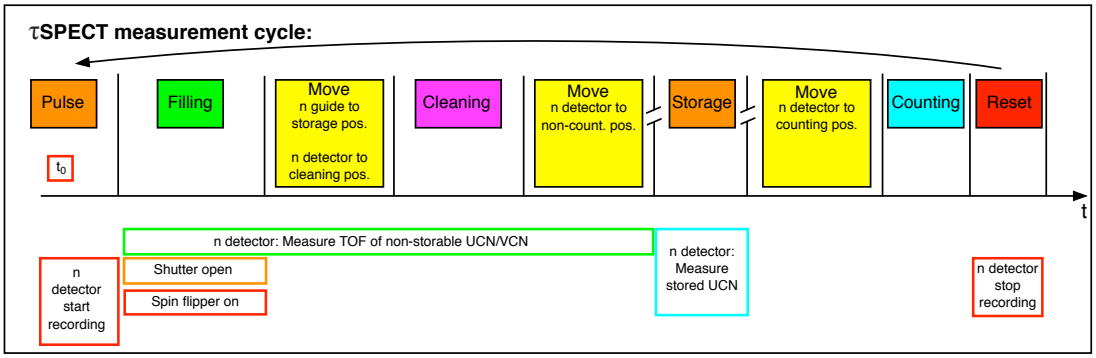

Figure 5.33: Data acquisition components during the simplified measurement cycle, which undergoes several sequences from 'pulse' to 'reset'. The depiction is limited to movement processes of the guide and the detector sections and the operation of the beam entry shutter and the detector. Neutron is abbreviated by 'n'. For details, refer to the text.

The return of the signal to the reactor simultaneously triggers the opening of the beam entry shutter right in front of the first τSPECT vacuum chamber[61]. Also, the data streamed

[59] The serial communication was implemented using the Python libraries pySerial/pyVISA.

[60] A t_0 peak-to-peak fluctuation of 1 s was found for data taken on 27/06/2019. The analysis is based on the thermal peak detection in the spectrum measured by the neutron detector. On average, t_0 deviated by $\sigma = 0.35$ s ($N = 20$ pulses).

[61] The used VAT shutter has an opening time of 1.5 s [vat17]. The timing is therefore adjusted to ensure the shutter being open before the first UCN passage.

from the neutron detector analogue-to-digital converter (ADC) is now written to disk by executing the Linux netcat (nc) command which is initiated by sending a TTL signal to a GPIO bridge[62]. From the detected thermal peak directly following the reactor pulse, a time stamp is extracted for timing analyses. Afterwards, the spin flipper is activated by sending a TTL signal to the Rigol DG1032Z frequency generator which produces the high frequency field for the spin flip coils at $t_{\text{fill, start}}$. The frequency generator and thus the spin flipper remains active for Δt_{fill}[63].

The deactivation of the spin flipper marks the end of the filling process, which is followed by the neutron guide section with the spin flipper and the compensation octupole at its very end being retracted from the magnetic trap. For this, a TTL signal is sent to the Nanotec SMCI 47-S-2 controller. Upon receiving the signal, the controller executes pre-configured sets to initiate the retraction of the neutron guide section[64]. After $\sim 26\,\text{s}$, the neutron guide section has reached its initial position. During the retraction of the neutron guide (quasi simultaneously in time), the neutron detector moves from its non-counting position to the cleaning position to count marginally-trapped UCN just before the onset of the 'storage' phase[65].

The 'storage' starts when the detector has returned from the cleaning position to the non-counting position. After a variable storage time, the detector moves from the non-counting to the counting position, which happens within $\Delta t_{\text{move, count}} \sim 19\,\text{s}$ and marks the beginning of the 'counting' phase. After reaching its counting position, the detector typically remains within the storage volume for $\sim 50\,\text{s}$. At the end of the measurement cycle, the neutron guide section moves to its initial filling position, while the neutron detector also returns to its initial position. To save disk storage, the recording of neutron detector data is stopped until a new measurement cycle is initiated.

[62] Implementation by D. Ries.

[63] Both $t_{\text{fill, start}}$ and Δt_{fill} are potentially sensitive to the UCN spectrum passing the spin flipper section in given time and must therefore be optimised.

[64] The electrical engine Nanotec ST6018D4508-B includes an optical encoder of type Nanotec WEDS5541-A06, which allows for a real-time position check feedback loop. Electrical end stops wired to the controller prevent the engine from moving outside mechanical constraints.

[65] A Nanotec SMCI 33-1 controller connected to the Nanotec ST5909L3008 engine drives the movement, with the engine being coupled to the optical encoder Nanotec WEDS5541-A06 for real-time position checks. If an electrical end stop is contacted during movement, a stopping of the engine is initiated.

6 First measurements with τSPECT

After the complete setup of τSPECT, first experiences regarding the pressure and temperature conditions and the detection of UCN inside the cryostat were made (cf. Ch. 6.1). In the September 2019 beam time, a storage curve demonstrating the first successful full-magnetic storage could be measured (cf. Ch. 6.2). Providing an outlook on the future of τSPECT, the measurement results are analysed and discussed taking theoretical considerations into account.

6.1 First experiences

The first evacuation of the entire system after the commissioning was crucial for the operation of τSPECT, since the vacuum conditions could not be estimated beforehand (cf. Ch. 6.1.1). Additionally, it was unclear whether the required temperature conditions to operate the superconducting coils generating the longitudinal field could be reached after cooldown. Furthermore, the performance of the ultracold neutron detector in the low-temperature environment and with exposure to magnetic fields up to $\sim 1.7\,\mathrm{T}$ was investigated (cf. Ch. 6.1.2).

6.1.1 Pressure and temperature conditions

In the following, the achieved pressure and the temperature conditions after the final setup of the τSPECT experiment are outlined.

Achieving high-vacuum conditions

The requirement for a successful run of τSPECT is a vacuum $\sim 10^{-7}\,\mathrm{mbar}$ in the storage volume, which would be sufficient for a τ_n measurement with an accuracy of $\Delta\tau_n = 0.2\,\mathrm{s}$[1]. Apart from an appropriate material selection, various iterative vacuum improvements could be made by optimising the rotary feedthrough connecting the engine in ambient conditions to the spindle contained in the first vacuum chamber (cf. Fig. 5.15). Also, the addition of a beam entry vacuum shutter (cf. Fig. 5.5) allowed for a separation of the experiment vacuum from the beam line vacuum. Furthermore, several weld seams in the region of the vacuum chamber assembly were not vacuum-tight and had to be provisionally covered

[1] According to calculations by Ezhov, a residual gas with pressure $10^{-7}\,\mathrm{torr} \sim 1.3 \times 10^{-7}\,\mathrm{mbar}$ corresponds to $\Delta\tau_n = 0.2\,\mathrm{s}$ [Ezh19].

with the sealant VacSeal[2]. All these measures were performed prior to the evacuation and cooldown discussed in the following.

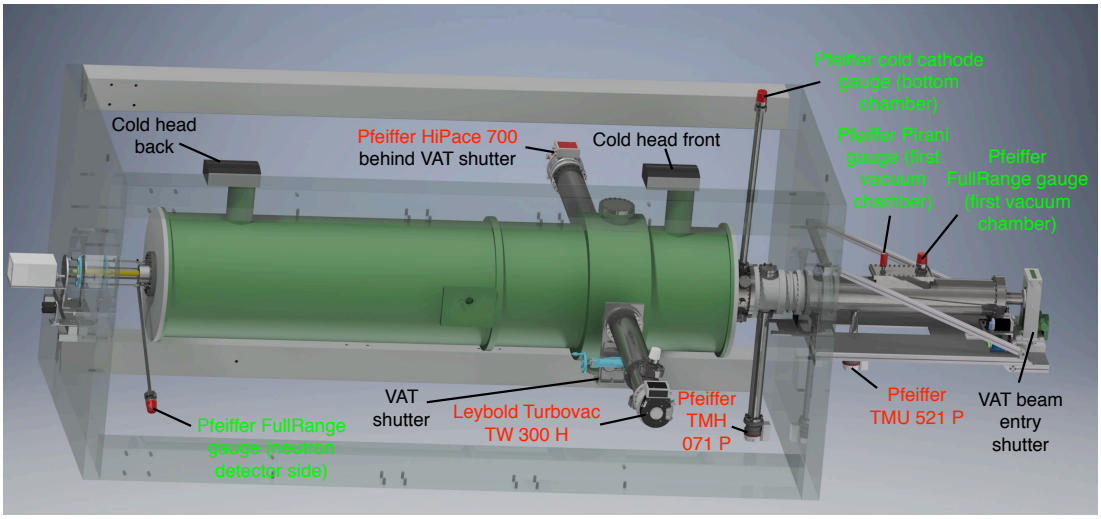

Figure 6.1: 3D rendering of turbo pumps and pressure gauges connected to τSPECT. With the UCN beam line connected on the right hand side, the beam entry shutter separates the experiment from the beam line vacuum. Turbo pumps are depicted in red letters, while pressure gauges are indicated by bright green letters. The two main turbo pumps of the main vacuum, Pfeiffer HiPace 700 and Leybold Turbovac TW 300 H, are placed behind shutters. The cold heads on top of the cryostat are required for cooling the cryostat. For a schematic drawing of the differential pump system including scroll pumps, cf. Fig. 6.2.

For reaching the end pressure, a suitable pump concept based on the differential pumping of the vacuum chamber assembly was implemented (cf. Fig. 6.1 for a rendering of the cryostat with all pumps and sensors, cf. Fig. 6.2 for a schematic depiction of the pump concept). The first vacuum chamber and the bottom chamber are pumped separately using a turbomolecular pump with CF40 (first vacuum chamber) and CF63 connection (bottom chamber). Two further turbomolecular pumps are connected to the cryostat (CF160 for large pump cross section) and can be exchanged during τSPECT operation due to shutters mounted between the main vacuum and the pumps. All mentioned turbomolecular pumps are connected to a Leybold SC 30D scroll pump. To prevent freeze-out of H_2O in the bellow of the neutron detector assembly which could lead to a non-mobility of the neutron detector (cf. Ch. 5.5), the scroll pump Leybold SC 15D is used for providing a pre-vacuum.

Great care had to be taken to ensure a good beam line vacuum. Since the beam entry shutter separating the main vacuum from the beam line vacuum (cf. Fig. 6.1) needs to be open for $\sim 15\,\mathrm{s}$ during UCN passage, a beam line vacuum of $\sim 10^{-5}\,\mathrm{mbar}$ with a leakage rate of $\sim 5 \times 10^{-8}\,\mathrm{mbar} \times \mathrm{l/s}$ was important to reach. For pumping, two turbomolecular pumps were added at the beginning (Pfeiffer HiCube 80 Eco, just after the UCN source exit) and at the end of the beam line (Leybold Turbovac SL 80, before the shutter). Both were connected to a Leybold SC 15D scroll pump.

The main vacuum is measured using a Pfeiffer cold cathode gauge connected to the bottom chamber and a Pfeiffer FullRange® gauge close to the neutron detector engine

[2]VacSeal is a silicone-based high-vacuum sealant for sealing leaks by Space Environment Laboratories, `http://www.vacseal.net`.

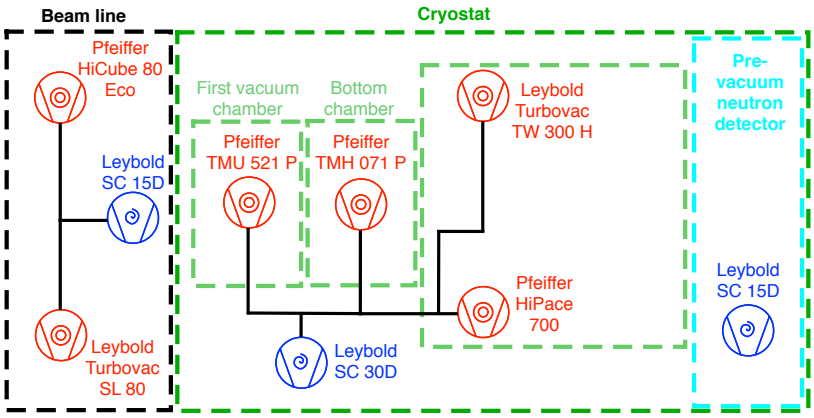

Figure 6.2: Pump concept of τSPECT. The beam line, parts of the cryostat and the neutron detector pre-vacuum are pumped individually. Turbomolecular pumps are represented by red symbols, while scroll pumps are shown in blue. For details, refer to the text.

assembly. Due to the gauges' sensitivity to external magnetic fields, they could not be directly mounted onto the respective cryostat ports. To keep their magnetic field exposure to $\lesssim 0.5\,\mathrm{mT}$, they were installed with a radial distance of $\gtrsim 1.1\,\mathrm{m}$ to the central cryostat axis. Additionally, the pressure is monitored in the first vacuum chamber containing the translation stage for the neutron guide system using a Pfeiffer FullRange® next to a Pfeiffer Pirani gauge.

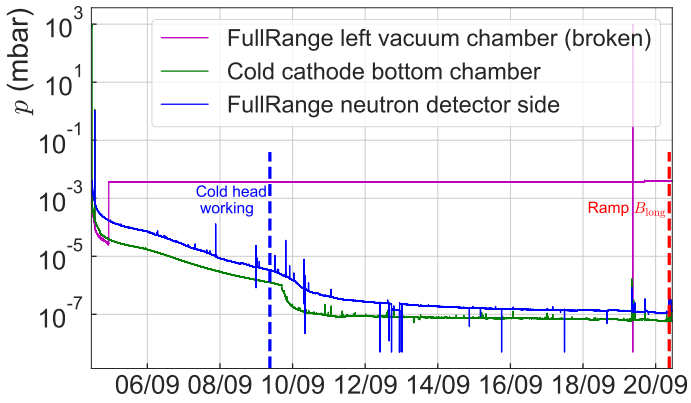

Figure 6.3: Pressure development during τSPECT cooldown in static conditions, *i.e.,* with closed beam entry shutter and no movement of the neutron guide section. Evacuating from 04/09 until measurement-ready state on 22/09, the final pressure $\sim 10^{-7}\,\mathrm{mbar}$ in the storage volume was reached (red dashed line). The pressure decrease after the activation of both cold heads (blue dashed line) can be clearly seen. The cold cathode part of the FullRange® gauge attached to the first vacuum chamber (magenta) broke shortly after cooldown, leading to a pressure reading saturating at $p = 3.9 \times 10^{-3}\,\mathrm{mbar}$ due to the technical limitation of its Pirani part.

The pressure development from 04/09 until 22/09 in static conditions, *i.e.,* without any movement of the neutron guide section and with the beam entry shutter closed, is shown in Fig. 6.3. Final pressures in the storage volume of $\sim 10^{-7}\,\mathrm{mbar}$ ($\sim 6.5 \times 10^{-8}\,\mathrm{mbar}$, measured at the bottom chamber and $1.3 \times 10^{-7}\,\mathrm{mbar}$, measured at the neutron detector

side) were reached after 18 days of pumping prior to the September 2019 beam time, with a delayed cooldown effectively starting after 5 days (cf. Fig. 6.3)[3]. A leakage rate of $\sim 3 \times 10^{-9}\,\mathrm{mbar} \times \mathrm{l/s}$ was measured at the position of the first vacuum chamber[4]. The final pressure values in the first vacuum chamber could not be reliably obtained due to a failure of the FullRange® gauge[5], but should be $\lesssim 10^{-5}\,\mathrm{mbar}$ due to the measured value of $1.6 \times 10^{-6}\,\mathrm{mbar}$ after a previous cooldown in June. The finally-reached pressure values in static conditions underline that the segmented pumping system with the different vacuum chambers functions as intended.

A crucial part of the τSPECT measurement cycle is the movement of the neutron guide section. For filling the UCN into the storage volume, the neutron guide is moved forward, while it is retracted afterwards (cf. Ch. 5.1.2). The neutron guide movement affects the main vacuum, since a rotary feedthrough had to be included, which transfers the engine movement from ambient conditions onto a spindle for moving the neutron guide system in longitudinal direction (cf. Fig. 5.6). To investigate the effect with the beam entry shutter closed, the neutron guide was moved from the storage to the filling position (neutron guide in) and back (neutron guide out) on 20/09, *i.e.,* just before reaching the measurement-ready state on 22/09. The resulting pressure curves were compared to data taken during the previous June cooldown, with the non-optimised version of the vacuum feedthrough installed. As Fig. 6.4 a) shows, the effect on the vacuum conditions in the pressure regions closest to the storage volume (pressure gauges at bottom chamber and neutron detector side, cf. Fig. 6.1) could be improved by installing the re-engineered vacuum feedthrough. The upgraded feedthrough has led to the pressure increase upon rotation being suppressed by approximately one order of magnitude. Furthermore, the time until the pressure value prior to the rotation is reached could be reduced by a factor of 2.

After evaluating the improved conditions owing to the upgraded feedthrough, the resulting effect of the moving neutron guide section on the vacuum conditions along with the necessary opening of the beam entry shutter is depicted in Fig. 6.4 b). The figure shows a complete measurement sequence of the September beam time for a storage time of 50 s, with the beam line attached to the beam entry shutter (during the beam time, a beam line vacuum of $\sim 10^{-5}\,\mathrm{mbar}$ was measured). Compared to Fig. 6.4 a), the final pressure conditions have been reached. At the beginning of the sequence, the beam entry shutter is opened for 15 s to allow for the passage of UCN. Right afterwards, the neutron guide is retracted from the filling to the storage position. At the end of the cycle, the guide returns to the storage position. With the effect of the shutter opening combined, the pressure maximally increases by $\Delta p \sim 1.6 \times 10^{-8}\,\mathrm{mbar}$ (measured at the bottom chamber) and $\Delta p \sim 0.5 \times 10^{-7}\,\mathrm{mbar}$ (measured at the neutron detector side). After $\Delta t < 40\,\mathrm{s}$, the initial pressure level prior to the movement are reached.

To conclude, the design goal of a final pressure of $\sim 10^{-7}\,\mathrm{mbar}$ in the storage volume

[3] Due to consistent failures of both cold heads, the effective beginning of the cooldown was delayed. The cooldown began 5 days after the evacuation had been initiated.

[4] The leakage rate was measured using a helium-sensitive vacuum leak detector of type Pfeiffer ASM340DRY.

[5] During the cooldown prior to the September 2019 beam time, the cold cathode part of the FullRange® gauge connected to the first vacuum chamber failed. In normal conditions, the Pirani part reads the pressure p until $p < 10^{-2}\,\mathrm{mbar}$ is reached. For a reliable pressure reading, the cold cathode part is activated if the pressure falls below the given threshold [pfe19]. A failure of the cold cathode part leads to a saturated pressure reading, since the Pirani part on its own cannot detect pressure levels $p < 5 \times 10^{-4}\,\mathrm{mbar}$ [pfe20]. In its implementation in the FullRange® gauge, saturation set in at $p = 3.9 \times 10^{-3}\,\mathrm{mbar}$.

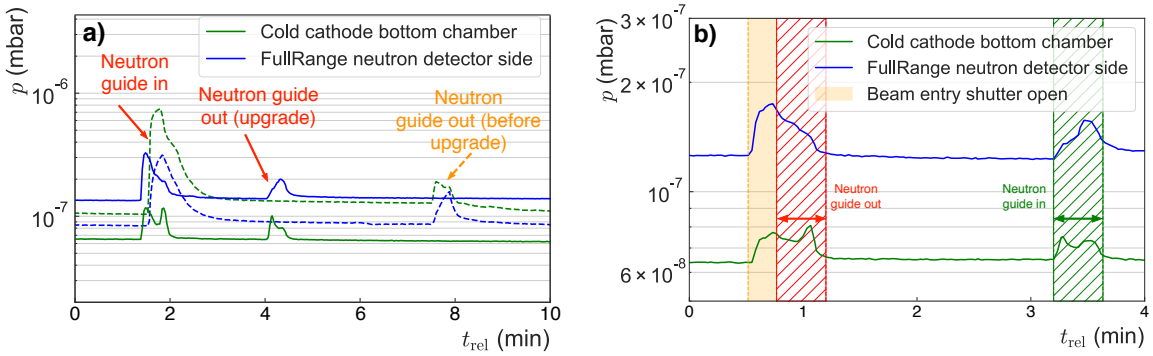

Figure 6.4: Effect of neutron guide movement on the vacuum conditions in proximity of the storage volume with closed and open beam entry shutter. The pressure p is plotted as a function of relative time, t_{rel}. (a) Effect of moving the neutron guide from filling to storage (out) and from storage to filling position (in) before upgrade of the rotary vacuum feedthrough (dashed lines) and after (full lines), with closed beam entry shutter. The pressure has been measured by the gauges installed at the bottom chamber (green lines) and the neutron detector side (blue lines). After the upgrade, the pressure changes by $\Delta p \lesssim 5 \times 10^{-8}$ mbar (measured at the bottom chamber) and by $\Delta p \lesssim 2 \times 10^{-7}$ mbar (measured at the neutron detector side), respectively. Measured at the bottom chamber, the upgraded feedthrough achieves Δp values which are approximately one magnitude smaller. Also, the initial pressure values before movement are now reached after $\sim$ 1 min, which is a factor 2 improvement. (b) During a typical measurement cycle of the September beam time, the beam entry shutter remained open for 15 s (light orange area) to ensure the passage of UCN. Consequently, the pressure increases by $\Delta p \sim 1.6 \times 10^{-8}$ mbar (bottom chamber) and by $\Delta p \sim 0.5 \times 10^{-7}$ mbar (neutron detector side). Note that the pressure values are now saturated, unlike the depiction in (a), which accounts for even shorter recovery times of the pressure conditions after movement. Immediately after closing the shutter, the neutron guide is retracted from the storage volume (red shaded area), which has a slight effect on the pressure reading in the bottom chamber, but no effect on the pressure at the neutron detector side. For both regions, the pressure returns to its initial value after $\Delta t < 40$ s. Towards the end of the measurement cycle with a storage time of 50 s, the neutron guide returns to the filling position (green shaded area), which impacts the pressure in both discussed regions even less ($\Delta p \sim 0.8 \times 10^{-8}$ mbar and $\Delta p \sim 0.4 \times 10^{-7}$ mbar, respectively). The initial value in the bottom chamber is reached after < 30 s, while the pressure level measured at the neutron detector side remains at a slightly increased value ($p = 1.3 \times 10^{-7}$ mbar instead of 1.2×10^{-7} mbar) after the movement.

could be reached, which provides the desired vacuum conditions for a first measurement of the neutron lifetime. In real measurement conditions, a final pressure $\lesssim 1.3 \times 10^{-7}$ mbar was realised, with a maximum increase to $\lesssim 1.6 \times 10^{-7}$ mbar during the opening of the beam entry shutter and the movement of the neutron guide section. A further improvement of the vacuum conditions would be reached by improving the beam line vacuum (currently $\sim 10^{-5}$ mbar), which would be possible by installing an optimised beam line with better vacuum sealings. This can be realised after the optimal height of the τSPECT relative to the source exit is determined, with a static beam line installed.

Cooldown to cryogenic temperatures

During the first cooldown after the installation of all components required for full-magnetic storage, it was not clear whether the temperature conditions necessary for the operation of the superconducting coils[6] could be reached. As discussed in Ch. 5, several measures were undertaken to reach this temperature design goal. Most importantly, the neutron guide section and the neutron detector mechanics were thermally isolated to decrease the heat flux from their outer parts at ambient temperature to the inner of the cryostat (details are given in Ch. 5.4 and 5.5). Furthermore, the thermal contact of the Halbach octupole to the cryostat was increased by inserting copper wool in-between the octupole and the cold bore tube which is at $\sim 100\,\mathrm{K}$.

To monitor the temperature, several temperature sensors are pre-installed inside the *a*SPECT cryostat (cf. Fig. C.1 for positions[7]). For temperature monitoring of the Halbach octupole region, 5 additional temperature sensors with different longitudinal position were installed on the outer stainless steel tube (cf. Ch. 5.3), into which the Halbach octupole is mounted. Furthermore, a temperature sensor was integrated into the neutron detector's PCB (cf. Ch. 5.5) to monitor and locally increase the temperature, if the detector components would show signs of malfunction due to low temperature.

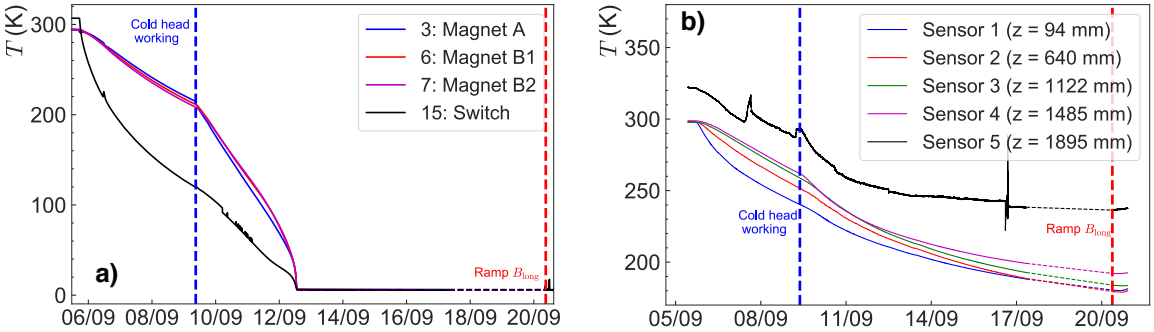

Figure 6.5: Temperature development after cooldown inside τSPECT. (a) Local temperatures relevant for the operating of superconducting coils. After 14 d, the relevant temperatures were reached to operate the coils (ramp B_{long}). (b) Local temperatures measured at the outer stainless steel tube containing the Halbach octupole, with a non-working temperature reading of sensor 5. According to measurements after the ramping of the coils, local temperatures were between $\sim 180\,\mathrm{K}$ and 200 K, with higher temperatures reached towards the detector side of the cryostat. Dotted lines indicate interpolation due to missing data. As previously mentioned, the cold heads started working at its full capability with a delay of $\sim 5\,\mathrm{d}$.

Fig. 6.5 shows the temperatures during the cooldown measured by the most relevant temperature sensors within the cryostat (a) and by the sensors across the outer stainless steel tube (b). After 14 days of cooling, the cryostat temperatures for turning on the superconducting coils were reached. The temperatures relevant for the operation of the superconducting coils were at $\leq 6\,\mathrm{K}$ on average[8], which is $\sim 3\,\mathrm{K}$ below the superconducting

[6] For operating the niobium-titanium coils, reaching the superconducting transition temperature of $T_{\mathrm{c}} = 9\,\mathrm{K}$ [SML04] is essential.

[7] Within the former *a*SPECT cryostat, the sensors with numbers 8, 9, 11, 14, and 19 are broken.

[8] The superconducting coils were operated after reaching the following local relevant temperatures: $\leq 7.2\,\mathrm{K}$ (temperature sensor 3, 'magnet A'), $\leq 6.2\,\mathrm{K}$ (6, 'magnet B1'), $\leq 5.9\,\mathrm{K}$ (7, 'magnet B2'), $\leq 5.5\,\mathrm{K}$ (15, 'switch'). More detailed temperature curves are found in Ch. C.1.2.

transition temperature of niobium-titanium (NbTi, $T_c = 9\,\mathrm{K}$ [SML04]. At the beginning of the September 2019 beam time, the temperatures across the outer stainless steel tube were around $\sim 180 - 200\,\mathrm{K}$ (cf. Fig. C.3 b). The temperature of the neutron detector was $\sim 180\,\mathrm{K}$, which allowed for operating the detector without increasing the temperature locally using the thermal wire (cf. Ch. 5.5.1).

Fig. 6.6 depicts the difference of the reached temperatures inside the cryostat to its design temperatures according to the manufacturer [cry04]. It is distinguished between two temperature measurements. The first measurement was performed in 12/2017 after 14 days of cooling with no installed mechanical additions except for the outer stainless steel tube later used for the fixation of the Halbach octupole. During the second (05/2019, 19 days of cooling) and third measurement (09/2019, 14 days of cooling), the temperature was measured after the complete installation of all required τSPECT components. Overall, typical differences to the design temperature are in the range of $< 5\,\mathrm{K}$, with the exception of sensor numbers 12, 13 and 20. Most importantly, the relevant temperatures for operating the superconducting coils (sensor numbers 3, 6, 7, and 15) did not increase by installing all τSPECT components. The readings of the temperature sensors 12, 13, and 20 imply that in proximity to the cold bore, temperatures are between $\sim 30\,\mathrm{K}$ and $\sim 50\,\mathrm{K}$ higher. Since similar differences to the design temperatures in these regions already occurred prior to the installation of the Halbach octupole, the outer stainless steel tube already installed in 12/2017 leads to a warming of the bore tube. This warming is possibly caused by the heat radiation of the cryostat's CF flanges, which are at ambient temperature and thus increase the temperature of the outer stainless steel tube. In these regions, thermal shields reflecting the heat radiation were not installed.

The design goal with regards to the final temperature within the cryostat could be met, since the superconducting coils could be activated and run in stable conditions during the entire beam time. Also, the temperature conditions at the position of the neutron detector allow for a reliable operation (cf. Ch. 6.1.2) without the need to exchange electronic components. Thus, further measures to reduce the temperature for a successful measurement of the neutron lifetime are not needed.

6.1.2 UCN detection in low temperature conditions

The successful operation of the custom UCN detector in low temperature conditions relied on theoretical assumptions (cf. Ch. B.2.2). Thus, a reliable functioning of the individual detector components had to be demonstrated. This includes a measurement of the noise level and a demonstration of the temperature effect on the pulse height.

Noise scan at low temperature

After installing the neutron detector in the τSPECT cryostat, a noise scan was performed at $T = 300\,\mathrm{K}$. The scan was repeated after the first successful cooldown of the cryostat, during which the temperature reading on the detector PCB (cf. Ch. 5.5.1) yielded $T = 180\,\mathrm{K}$. To make the data taken at both temperatures comparable, the bias voltage was set to the lowest possible value. At room temperature, this lowest bias voltage corresponded to 54.0 V, while it was decreased to 47.5 V at 180 K. The decrease was due to the temperature-dependent regulation of the bias voltage (cf. Ch. B.3.2), which down to the measured temperature of 180 K was assumed to behave linearly with T (cf. Ch. B.2.2.2). Therefore, the linear interpolation of the detector voltage with decreasing temperature ($54\,\mathrm{mV\,K^{-1}}$, which results in a voltage offset of $\sim 6.5\,\mathrm{V}$, cf. Ch. B.2.2.2) was successfully applied by the electronics. During these noise measurements, the reactor was shut down to provide

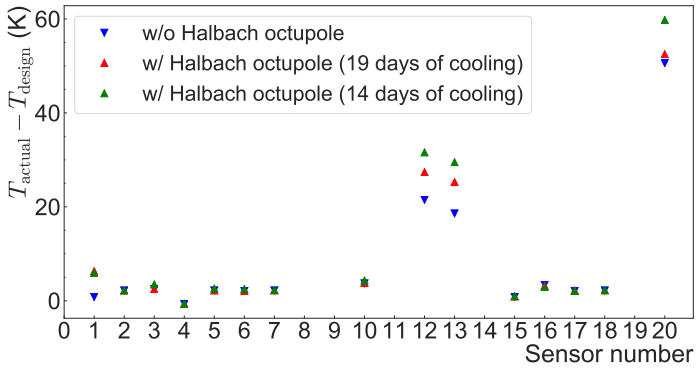

Figure 6.6: Effect of τSPECT components on the cryostat temperature. Plotted is the difference between the measured temperature and the cryostat design temperature by the manufacturer ($T_{\mathrm{actual}} - T_{\mathrm{design}}$) for different temperature sensors after 14 days (green markers, 09/2019) and 19 days of cooling (red markers, 05/2019), with all mechanical components required for full-magnetic storage installed. For comparison, the $T_{\mathrm{actual}} - T_{\mathrm{design}}$ values before the installation of the Halbach octupole are included (blue markers, 14 days of cooling in 12/2017). Already without additional mechanical components except for the outer stainless steel tube later used for the fixation of the Halbach octupole (12/2017), deviations from the design temperature by up to $\sim 50\,\mathrm{K}$ in the region of the cold bore (temperature sensors 12, 13, and 20) were observed. These differences therefore likely result from the installed outer stainless steel tube. Even after the full installation of the mechanical components (05 and 09/2019), the difference to the design temperature in the remaining regions was $< 5\,\mathrm{K}$. The high temperature in the cold bore region has no effect on the temperature relevant for operating the superconducting coils (sensors 3, 6, 7, and 15). Note that sensors 8, 9, 11, 14, and 19 are not working. The relation between sensor number and position is given in Fig. C.1.

reliable measurement conditions. From its lowest level at both temperatures, the bias voltage was increased by up to 4 V. The discussed data were determined from running the peak finding algorithm (cf. Ch. 5.5.2) over the respective measurement files, with the time over threshold value set to $\Delta t_{\mathrm{thr}} = 1\,\mu\mathrm{s}$. The Δt_{thr} value did not have to be adapted for the low-temperature measurements, since the timing behaviour of the signal was not observed to change (cf. Figs. 5.24 b) and 6.11 b) for typical pulse shapes measured at room temperature and 180 K).

With the gain setting in the second amplification stage reduced to $G_{\mathrm{shape}} = 3$, the formerly-observed shift of the average detector voltage[9], $\overline{V}_{\mathrm{det}}$, with increasing bias voltage was again present at room temperature (cf. red data point in Fig. 6.7 a). Also, the corresponding standard deviation of the detector voltage, σ_{det}, which is indicative of the detector noise, increased by almost a factor 3 going from 54.0 V to +58.0 V bias voltage (cf. Fig. 6.7 b). As Fig. 6.7 a) and b) show, no more $\overline{V}_{\mathrm{det}}$ shifts with rising bias voltage were observed at $T = 180\,\mathrm{K}$, with the noise remaining at a constant low level. Even more, the noise was $\gtrsim 6$ times less in the highest bias voltage setting compared to ambient conditions. The noise reduction at lower temperature can be explained by the lower dark count rate, which was expected to decrease by at least 2 orders of magnitude at the lower temperature due to reduced thermal noise (cf. Ch. B.2.2.2). The rising average detector voltage with increasing

[9]The average detector voltage, $\overline{V}_{\mathrm{det}}$, and the related standard deviation, σ_{det}, was computed by the algorithm described in Ch. 5.5.2 running over the entire measurement file.

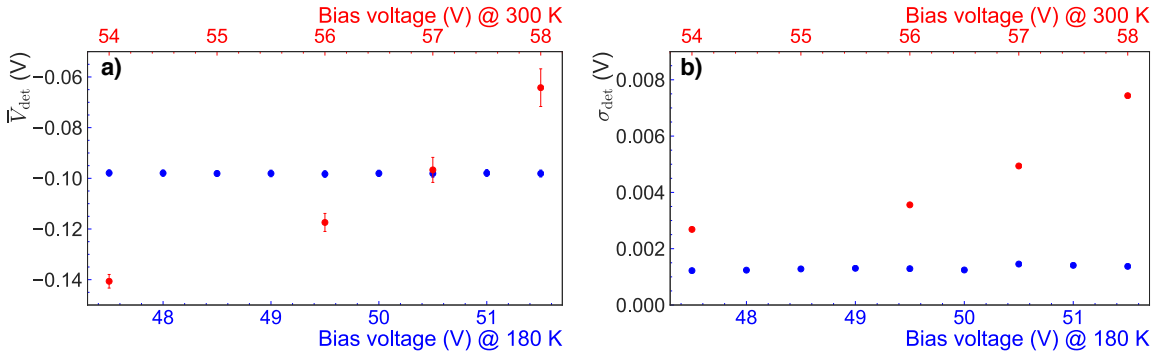

Figure 6.7: Temperature dependence of the detector voltage and the related noise. (a) The shift of the average detector voltage ($\overline{V}_{\mathrm{det}}$) with rising bias voltage at room temperature (red data points) can be seen. The shift vanishes after cooling the detector to 180 K (blue data points). The respective standard deviation, σ_{det}, is plotted as error bars. In case of $T = 180\,\mathrm{K}$, the error bars are smaller than the symbol size. (b) Accurate depiction of the standard deviation of the detector voltage, σ_{det}, which is indicative of the noise. The low temperature prevents the noise from increasing with higher bias voltage levels, since the thermal noise contribution to the dark count rate is suppressed. The time threshold was set to $\Delta t_{\mathrm{thr}} = 1\,\mu\mathrm{s}$.

voltage observed at room temperature can be explained by the integration stage of the pulse shaping electronics reacting to the increasing thermal noise. At $T = 180\,\mathrm{K}$, the noise does not increase with bias voltage, which implies that the integration stage responds with a constant detector voltage level.

UCN time-of-flight spectrum in τSPECT

During the first τSPECT beam time in June and July 2019, first detector response tests with the final detector electronics[10] were performed. At the time of the June and July measurements, the spin flipper was not yet operational. UCN passing the first field maximum, which can be both high field seekers (HFS) as well as low-field seekers (LFS) with $E_{\mathrm{UCN}} > 60\,\mathrm{neV}$ (cf. Ch. 5.1.2), exit the end of the movable neutron guide. Depending on their emission angle with respect to the guide axis they will either hit the inner Halbach octupole surface with a high absorption probability or reach the detector further downstream. These neutrons are of interest for τSPECT, since following the pre-characterisation measurements in Ch. 4.3, they are valuable for developing a normalisation method.

The corresponding time-of-flight (TOF) spectrum is shown in Fig. 6.8), which has been determined after running the peak finding algorithm over the raw detector measurement file (cf. Ch. 5.5.2 for a concise and Ch. B.4.2 for a detailed explanation of the peak finding algorithm). Shortly after the thermal peak, the first UCN are detected by the detector. Integrating the depicted spectrum in the time interval between 0.4 s and 8.0 s after the thermal peak (wide integration window) gives a total number of 14290(119) UCN (the error denotes the statistical error). First empirical tests on finding an appropriate normalisation after measuring the first storage curve (cf. Fig. 6.13) have led to the conclusion that

[10] During the June and July measurements, a 1.5 m long cable between shaper box and MIL-DTL-26482 plug of the detector vacuum feedthrough was used, which was exchanged for a cable of 7.0 m length prior to the September beam time. Comparison measurements have shown no additional noise introduction due to the 7 m long cable.

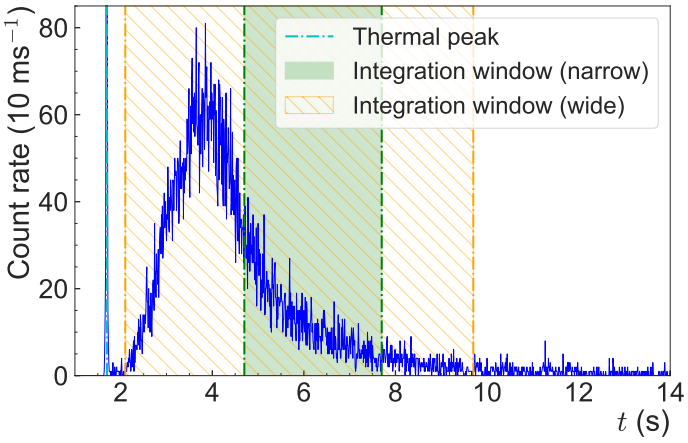

Figure 6.8: UCN time-of-flight (TOF, 'UCN flow') spectrum of non-stored UCN detected shortly after the reactor pulse in τSPECT based on the output of the peak finding algorithm ($\Delta t_{\mathrm{thr}} = 1\,\mu$s). During the measurement of the spectrum, the bias voltage was set to $V_{\mathrm{bias}} = 52.0\,$V, and the detector position to $z_{\mathrm{det}} = 1898\,$mm. The cyan dashed line indicates the position of the thermal peak caused by the reactor pulse. In the wide integration window between 0.4 s and 8.0 s after the thermal peak ($t_{\mathrm{pulse}} = 1.68\,$s, cyan dashed line, integration window represented by yellow shaded area), 14290(119) counts with the respective statistical error are contained. Due to the identification of non-linear effects, the narrow integration window in the time interval between 3.0 s and 6.0 s after t_{pulse} (green area, integral counts $C_{\mathrm{UCN,\,flow}} = 3914(62)$) was taken for normalisation.

normalising the data to the wide integration window leads to non-linear effects. After empirically evaluating different integration windows, it was therefore decided to use the narrow integration window, which implies that all counts in the time interval between 3 s and 6 s after the thermal peak are integrated. This integration window is likely to function better for a normalisation, since it contains lower-energetic UCN, which energies are closer to the energy of the stored UCN. In the given example, the wide integration window yields the integral counts $C_{\mathrm{UCN,\,flow}} = 3914(62)$, which is from now on taken for the normalisation of the September 2019 beam time data (cf. Fig. 6.14 for a depiction of the $C_{\mathrm{UCN,\,flow}}$ values).

With higher statistics in terms of stored UCN, which can be expected for future beam times, the normalisation method needs to be evaluated in detail. Setting integration windows differing from the selected values might lead to better results.

Temperature dependence of the pulse height

Unlike the September beam time, the detector data taken in June and July did not exhibit any noise signatures when the detector remained in a fixed position, which was the case when detecting the non-stored UCN as shown in Fig. 6.8. The 'clean' data taken at a temperature of $T = 180\,$K could therefore be used to analyse the pulse height spectrum resulting from the UCN detection. For evaluating the influence of the lower temperature on the pulse height, a comparison was made to the pulse height spectrum determined from the CASCADE comparison measurements at $T = 300\,$K, during which UCN pre-stored in an aluminium storage bottle were counted (cf. Ch. 5.5.2).

For the analysis, the raw detector signal after the pulse shaping stage was taken into account as recorded by the analogue-digital converter (ADC, cf. Fig. B.27 b). Therefore, no further processing of the data was performed. Fig. 6.9 a) depicts the detector signals recorded

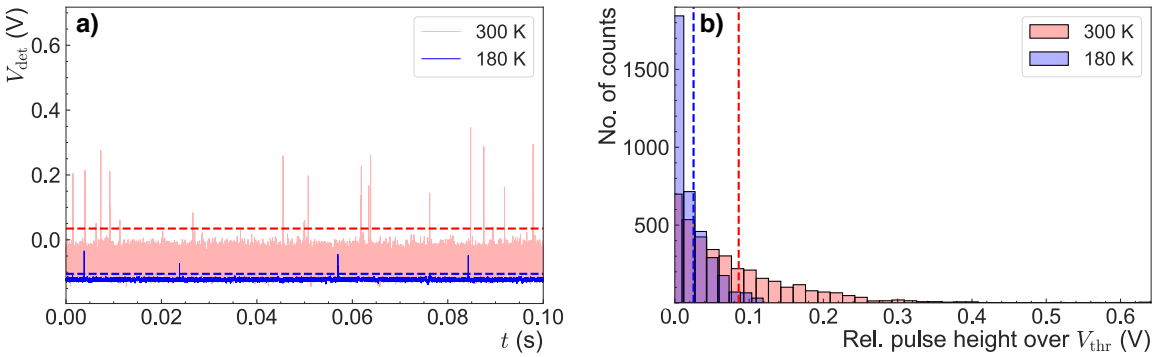

Figure 6.9: Temperature dependence on UCN event pulse height after pulse shaping. At both temperatures, the gain of the pulse shaping stage was set to $G_{\text{shape}} = 3$. The bias voltage was set to 52.0 V ($T = 180$ K) and 57.0 V ($T = 300$ K). (a) Raw detector voltage (V_{det}) plotted against time. The spectra contain UCN events at room temperature (red) and at $T = 180$ K (blue). The dashed lines represent the respective peak thresholds V_{thr} applied by the peak finding algorithm. (b) Histogram of the resulting relative pulse heights over V_{thr}, without any time thresholding applied. Their average is denoted by the dashed vertical lines (0.025 V for 180 K, 0.086 V for 300 K). At 180 K, the pulse height average is therefore ~ 3.4 times lower than at 300 K.

within a time span of 100 ms for $T = 180$ K (blue) and $T = 300$ K (red). The data for the measurement at 300 K was taken shortly after opening the shutter from the aluminium storage bottle to the detector (cf. Fig. 5.28 a) for the corresponding TOF spectrum, with the shutter opening at $t \sim 26$ s). In the case of $T = 180$ K, the depicted data is derived from the $C_{\text{UCN, flow}}$ region (cf. green area in Fig. 6.8). From the raw detector data, it can be concluded that despite the pulse heights decrease with lower temperature, the peaks representing the UCN events are still clearly above noise and can thus be identified by the peak finding algorithm (the corresponding thresholds are indicated by the dashed lines).

Taking the same data into account, the relative height of the pulses relative to the respective peak thresholds V_{thr} (represented by the dashed lines in Fig. 6.9 a) has been evaluated in more detail (cf. Fig. 6.9 b). To get a comparable amount of counts in the histogram, the pulse heights for $T = 300$ K were determined for a time span of $\Delta t = 0.32$ s, while the data for $T = 180$ K was considered for $\Delta t = 1.00$ s. The higher pulse heights at room temperature are clearly seen. On average, a ~ 3.4 times higher pulse height is inferred in ambient conditions, which can be explained by a lower intrinsic gain of the used SiPM array at low temperatures. Interestingly, the pulse height spectra do not show any double peak structure, which could be expected due to the different energies of the decay products α and ^{7}Li. As detailed in Eqs. (B.5) and (B.6), the α energy is $\sim 75\,\%$ higher than the ^{7}Li energy, which in turn leads to more photons generated in the scintillation process and therefore a higher pulse height in the detector signal. The strong fluctuations of the peak heights, however, which were also already present during the pre-characterisation measurements using an α source (cf. Fig. 5.24 a), prevent a further differentiation.

6.2 First storage measurements

After revealing the measurement conditions (cf. Ch. 6.2.1) and data analysis principles (cf. Ch. 6.2.2) in the September 2019 beam time, a first storage curve is presented (cf. Ch. 6.2.3). Finally, a first attempt to clean the stored UCN spectrum is laid out (cf. Ch. 6.2.4), along

with an explanation of the lower-than-expected number of stored UCN (cf. Ch. 6.2.5). The last section gives an outlook on recent measurement results (cf. Ch. 6.2.6).

6.2.1 General measurement conditions

In September 2019, first UCN were full-magnetically stored in τSPECT. The aim of the beam time was a first measurement of a storage curve to extract a characteristic storage time.

The final experimental setup is depicted in Fig. 6.10 a)[11]. The τSPECT full-magnetic storage volume is contained inside the green cryostat which is surrounded by magnetic shielding. A current of $I_{\mathrm{main}} = 33\,\mathrm{A}$ was used for the superconducting coils to produce the longitudinal magnetic field (for a plot of the longitudinal magnetic field and the resulting storage volume, cf. Fig. 5.8 a). The used beam line is shown in Fig. 6.10 b) and differs in the geometric shape from previously-used beam lines. Due to limitations in the available stainless steel beam line components, a combination of bends with 45° and 90° radii and straight Neumo HE5 tube parts formed the beam line. The limited component availability led to the final height of $h = 1.59\,\mathrm{m}$ over the UCN D source exit, which is below the optimum of $h = 1.83\,\mathrm{m}$ identified in the pre-characterisation measurements (cf. Fig. 4.22 a). Using the higher height, a $\sim 4\,\%$ increase in UCN yield would have been expectable.

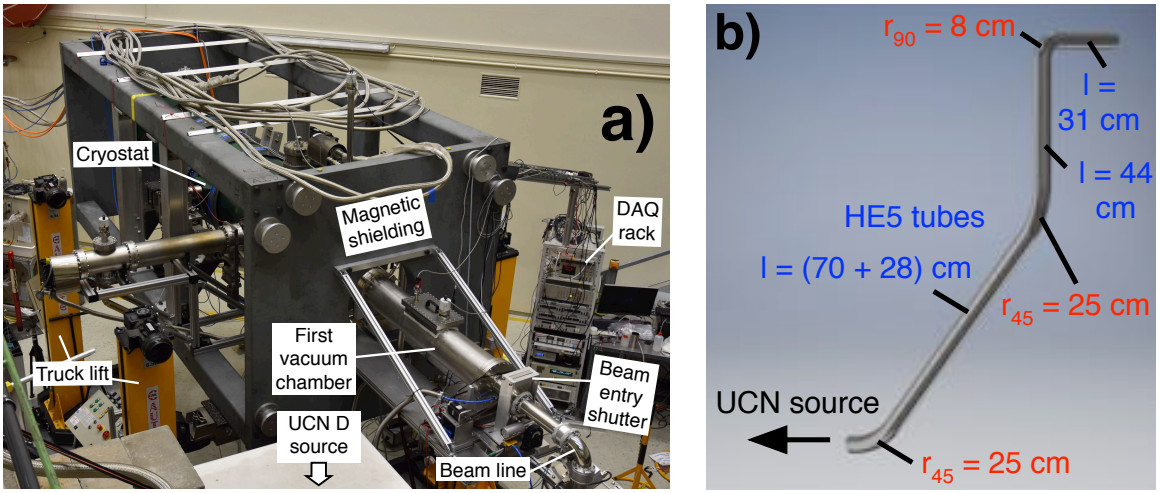

Figure 6.10: Setup of τSPECT in the TRIGA Mainz research reactor hall, viewed from the reactor platform above the UCN D source, and a detailed view of the beam line. (a) The τSPECT cryostat within its magnetic shielding is mounted onto a four-column truck lift. The truck lift allows for changing the height relative to the UCN source exit, h. During the first storage measurements, h was set to 159 cm. Also visible is the end part of the beam line, which is connected to τSPECT via a beam entry shutter. Next follows the first vacuum chamber, which contains the mechanical components for moving the neutron guide in and out of the storage volume. The data acquisition (DAQ) rack is depicted in the background. (b) The used stainless steel beam line in detail, with straight Neumo HE5 tube parts of length l (blue) and 45° and 90° radii (red).

Exiting the upgraded UCN D source, the UCN reach the movable neutron guide system in the first vacuum chamber, at which end an adiabatic fast passage (AFP) spin flip

[11] For a detailed description of the experimental setup, cf. Ch. 5.

is performed[12]. The characteristic frequency matching of the AFP spin flipper in low-pass birdcage design[13] yielded a fixed frequency of 10.315 MHz after cooldown. During the measurements, the fixed frequency required the spin flipper to be operated at a position of $z_{\mathrm{sf,\,corr}} = 863\,\mathrm{mm}$ in a longitudinal magnetic field of $B_{\mathrm{sf}} = 0.338\,\mathrm{T}$, corresponding to a magnetic potential of 20.4 neV (cf. Ch. 6.2.2). To reach a frequency of $\sim 6\,\mathrm{MHz}$, which would have allowed for performing the spin flip at the design position of $z_{\mathrm{sf}} \sim 1100\,\mathrm{mm}$ ($B_{\mathrm{sf}} \sim 0.2\,\mathrm{T}$, $\nabla_z B_{\mathrm{main}} \sim 3\,\mathrm{G\,cm^{-1}}$, cf. Ch. 5.3.3), the capacitors would have had to be increased, which would have resulted in dielectric losses and therefore a high dissipative power loss. Therefore, the used spin flipper design with a frequency of 10.315 MHz offered a compromise between low power loss and optimal spin flip position. The changed spin flip position reduces the acceptance to incoming UCN energies from $\Delta E = 23.0\,\mathrm{neV}$ to[14]:

$$\Delta E \sim 47\,\mathrm{neV} - 2 \cdot 20.4\,\mathrm{neV} \sim 6.2\,\mathrm{neV}\,, \tag{6.1}$$

which implies that only incoming UCN with energies $[0, 6.2]$neV can be stored. During the filling of UCN into the storage volume, the spin flipper was activated $\sim 3\,\mathrm{s}$ after the reactor pulse for a time span of $\Delta t = 4\,\mathrm{s}$. The spin flipper timing was determined after theoretical considerations at the beginning of the September beam time, without further experimental checks due to time constraints. When enabled, the spin flipper was excited by a frequency generator with quadrature pulses of amplitude 140 mV, which translates into a power of 109 W fed into the birdcage. Additional measurements following the first storage measurements have demonstrated that increasing the power to 362 W did not provide a higher number of stored UCN. An effect, however, was seen when adapting the spin flip position (cf. Ch. 6.2.2).

The beam line shutter closed after the spin flipper was turned off to separate the beam line vacuum ($\sim 10^{-5}\,\mathrm{mbar}$) from the cryostat vacuum ($\sim 10^{-7}\,\mathrm{mbar}$). After the filling process, the neutron guide section was retracted from the storage volume. As depicted in Fig. 6.8, the detector ($T \sim 180\,\mathrm{K}$) remained in the position $z_{\mathrm{det}} = 1898\,\mathrm{mm}$ for monitoring the UCN flow during the filling process. After storing the UCN for a specific storage time t_{s}, the neutron detector was moved into the storage volume to count the surviving UCN at the counting position $z_{\mathrm{det}} = 1772\,\mathrm{mm}$.

Timing fluctuations $\mathcal{O}(1\,\mathrm{s})$ of unknown origin were present in the data acquisition system, which led to an average uncertainty of the spin flipper timing of $1.41(22)\,\mathrm{s}$ (minimum and maximum values were 0.68 s apart). The unreliable timing has led to an uncertainty in the filling procedure, which should however be of no concern due to the relative insensitivity of the UCN yield on the filling time as measured with the final neutron guide section (cf. Fig. 4.22 b). Also, the movement of the neutron guide section and the detector is affected by these fluctuations. To improve the accuracy of the overall timing of the experiment, the thermal peak as recorded by the UCN detector should be taken as a reference point in future implementations.

6.2.2 Principles of the data analysis and optimisation of the spin flip position

Additional to the integration window for detecting non-stored UCN for normalisation (cf. Fig. 6.8 for a zoomed-in plot), Fig. 6.11 a) highlights the integral windows used for the determination of the number of stored UCN (light orange) and the background (red) in

[12] More details on the adiabatic fast passage spin flip are given in Ch. 5.3.2.
[13] The AFP spin flipper was constructed and implemented by K. Ross.
[14] For a detailed explanation, refer to Ch. 4.4.2. The equation is based on Eq. (4.16).

case of a storage time of $t_s = 50\,s$. Also, the detector count rate determined by the peak finding algorithm (cf. Chs. 5.5.2 for a concise and B.4.2 for a detailed explanation) is shown. Directly following the selected storage time, the UCN are counted for a time span of $\Delta t = 34\,s$ with the detector fully moved into the storage volume $\sim 10\,s$ after the counting period has begun. A typical stored UCN signal is depicted in Fig. 6.11 b). During all measurements, the detector bias voltage was set to 52.0 V.

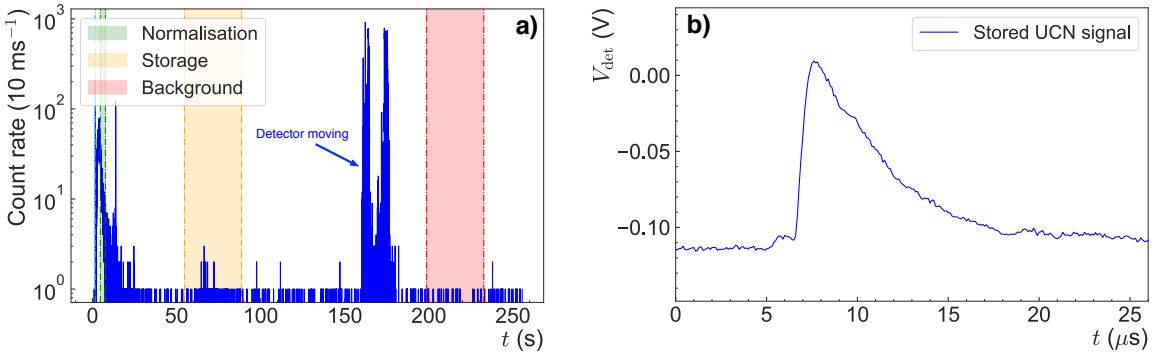

Figure 6.11: Detector count rate during a measurement cycle (storage time $t_s = 50\,s$) and typical stored UCN signal. (a) Right after the thermal peak ($t_{pulse} = 1.67\,s$), the normalisation counting interval follows (time interval $[t_{pulse} + 3\ s, t_{pulse} + 6\ s]$, green area). For the determination of the stored UCN, the integral counts are counted for $\Delta t = 34\,s$ (time interval $[t_{pulse} + t_s + 3\ s, t_{pulse} + t_s + 37\ s]$, orange area). To determine the background within the same time span Δt, the counts within the interval $[t_{pulse} + t_s + 147\ s, t_{pulse} + t_s + 181\ s]$ (red area) are integrated. (b) Typical UCN signal from the storage region after pulse shaping shaping, with the detector voltage V_{det} as a function of time.

Limiting the counting position to $z_{det} = 1772\,mm$, no more additional noise resulting from the detector movement was identified when moving inside the storage volume. The movement-dependent noise, however, repeatedly occurred when retracting the detector from the storage volume (indicated by the peak structures in Fig. 6.11 a). After the detector had returned to its retracted position, the detector background was determined by integrating over the same time span as during the storage integration window, *i.e.*, $\Delta t = 34\,s$. Thus, the resulting counts from the background could be directly subtracted from the detected UCN counts in the data analysis. The background contained various contributions resulting from the reactor running in low-power mode ($P = 50\,W$), cosmic rays, and detector noise as identified by the peak finding algorithm. On the second measurement day, the background (1.58(92) Hz) was on average slightly higher than on the first day (1.27(11) Hz). The determined background agrees within errors with the background measured at room temperature (1.00(13) Hz in CASCADE comparison measurement, cf. Ch. 5.5.2).

Event reconstruction based on the peak finding algorithm was a challenge in the September beam time, since 50 Hz noise caused a temporary shift of the average detector voltage ('baseline', cf. Fig. 6.12 a). While the formerly-optimised time over threshold value of $\Delta t_{thr} = 1\,\mu s$ was used (cf. Ch. 6.1.2), the algorithm selected a higher peak threshold than usual, since the fluctuation shown in Fig. 6.12 a) oscillated in both $+V_{det}$ and $-V_{det}$ direction. The selection of a higher peak threshold was due to the fact that the algorithm first iterates in $-V_{det}$ direction to determine the threshold until no more noise events are detected (cf. Chs. 5.5.2 and B.4.2 for a detailed discussion). Taking the mean value of V_{det} as the

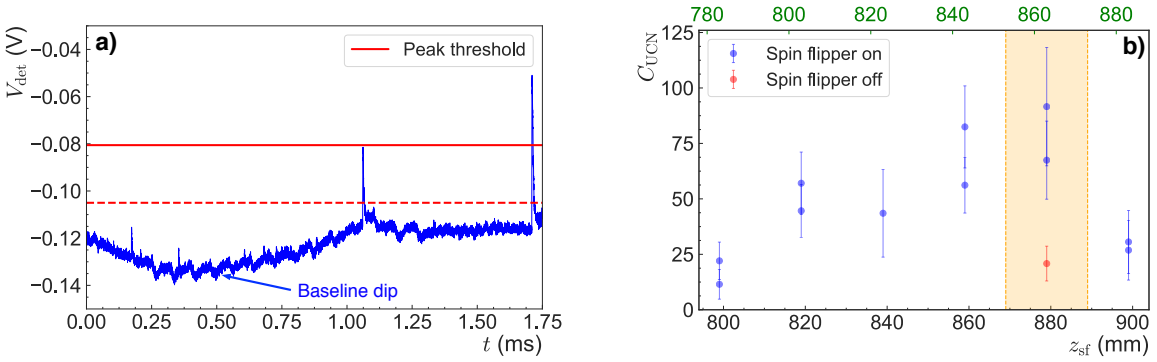

Figure 6.12: Fluctuations in the average detector voltage and number of stored UCN as a function of the spin flip position, z_{sf}. (a) Fluctuations of the average detector voltage ('baseline dip') due to noise with a frequency of 50 Hz occurred after pulse shaping. The fluctuating average detector voltage affects the peak identification algorithm, since it causes a higher peak threshold to be set (red line). In case of an absence of detector voltage fluctuations, the peak threshold would have been set to the value represented by the dashed red line. Note that the fluctuations occur similarly in both $+V_{det}$ and $-V_{det}$ direction. (b) The data has been normalised to the UCN flow in the time interval between 3.0 s and 6.0 s after t_{pulse}. Most UCN were stored for a storage time of $t_s = 50$ s at a position of $z_{sf} = 879$ mm (light orange area), with the number of UCN fluctuating within the error bars. After correction due to deviations between the CAD design and the actual position, this corresponds to a corrected spin flip position of $z_{sf,\,corr} = 863$ mm (the corrected positions are indicated by the top x-axis). The detection of UCN at this position during the spin flipper off measurement (red data point) indicates marginally-trapped UCN. All given data points depict measured data, with no subtraction of marginally-stored UCN.

mirror axis, the threshold is then applied in $+V_{det}$ direction for setting the peak threshold. The higher peak threshold (red line, cf. Fig. 6.12) than usual (indicated by the red dashed line) led to a non-identification of several events. Overall, the effect on the number of detected UCN can be approximated by $\lesssim 20\,\%$. In the mean time, the noise issue could be resolved by separating the shaper box power line from other electrical consumers.

Prior to measuring the first storage curve from the 27th September onwards, the spin flip position was optimised on the 26th September by counting UCN which had been fully-magnetically stored for a storage time of $t_s = 50$ s (cf. Fig. 6.12 b), the corresponding integral window in which the number of stored UCN has been determined is shown in the light orange area of Fig. 6.11 a). The measurements clearly demonstrate that the spin flip works and reaches the highest efficiency, *i.e.,* the highest number of stored UCN, at the position of $z_{sf} = 879$ mm. After correcting the position according to the findings in Ch. B.1, an offset of -16 mm was applied to z_{sf}, resulting in a corrected spin flip position[15] of $z_{sf,\,corr} = 863$ mm. At this position, a longitudinal magnetic flux density of $B_{sf} = 0.338$ T and a longitudinal gradient of $\nabla_z B_{main} \sim 210\,\mathrm{G\,cm^{-1}}$ are given. Considering the total field $B = 0.343$ T at the spin flip position (cf. Eq. (5.12)), the corresponding Larmor frequency ($\omega_L = 10.002$ MHz) is close to the frequency of the birdcage ($\omega_{sf} = 10.315$ MHz). The determined UCN spin

[15] The corrected spin flip position needs to be determined after each assembly process of the neutron guide section and the surrounding components. Thus, the calculated offset might differ for measurements in subsequent beam times.

flip position at $z_{\mathrm{sf,\,corr}} = 863\,\mathrm{mm}$ thus implies a low acceptance to incoming energies in the range of $[0, 6.2]\mathrm{neV}$ ($\Delta E \sim 6.2\,\mathrm{neV}$, cf. Ch. 6.2.1). The low acceptance therefore leads to the relatively low number of ~ 80 stored UCN at $t_\mathrm{s} = 50\,\mathrm{s}$ during the spin flipper position measurements. At the same storage time and with no adaptions to the measurement conditions, higher values were reached when measuring the storage curve one and two days later (cf. Fig. 6.15). The higher number of UCN can only be explained by a corresponding gain of the UCN yield in the low energy range, which has not been investigated yet.

Moreover, ~ 20 UCN were detected with the spin flipper turned off and an otherwise identical measurement sequence (typical count rate shown in Fig. 6.11 a), which corresponds to marginally-trapped UCN. Marginally-trapped UCN have larger-than-storable energies and remain on trajectories within the storage volume (cf. Ch. 6.2.4). With the spin flipper turned off and for the observed storage time of 50 s, they comprise low-field seekers (LFS, cf. Ch. 4.1 for a detailed explanation) which have overcome the first longitudinal magnetic field maximum of $B_\mathrm{main} \sim 1\,\mathrm{T}$ (cf. Fig. 5.8 a). The absolute magnetic flux density corresponds to a high energy of the LFS of $\sim 60\,\mathrm{neV}$ (cf. Ch. 3.2.1), which is notably larger than the magnetic potential maximum ($\sim 47\,\mathrm{neV}$) created by the Halbach octupole. With the spin flip activated, high-field seekers (HFS) are converted to LFS, which implies that additional non-storable LFS with initial energies $\gtrsim 6.2\,\mathrm{neV}$ reach the storage volume, corresponding to an energy $\gtrsim 47\,\mathrm{neV}$ in the storage volume. Since now the energy range between 47 neV and 60 neV is also populated with UCN, a larger number of marginally-stored UCN is expected when enabling the spin flipper. Due to the asymmetric trap potential (cf. Ch. 6.2.4), the number of marginally-stored UCN decreases over time. The marginally-stored UCN are counted by the detector and can be removed by cleaning the stored UCN spectrum (cf. Ch. 6.2.4). Note that the number of marginally-trapped UCN might fluctuate considerably, with the fluctuation not determined due to the low measurement statistics.

6.2.3 Measurement of a first storage curve

The data for the storage curve was taken on the 27$^{\mathrm{th}}$ and the 30$^{\mathrm{th}}$ September, at relative pulse numbers 33 to 61. Due to time constraints, the UCN yield was therefore not yet fully saturated. As discussed in Ch. 4.2.3, the UCN yield of the UCN D source changes as a function of the number of pulses due to crystal reformation effects, until it reaches a saturated maximum. The changing yield was also found when measuring the yield development of lower-energetic UCN with energies $E_\mathrm{UCN} \lesssim 54\,\mathrm{neV}$ (cf. Fig. A.18), which are of relevance for full-magnetic storage. According to these measurements, a gain in the UCN yield of $\sim 6 - 8\,\%$ would have been possible, if saturation would have set in.

Measuring the storage curve, storage times of $(20, 50, 250, 500, 650, 800)$ s were selected. To account for fluctuations of the UCN D source, the stored UCN counts were normalised to the UCN flow within 3 s and 6 s after the thermal peak, t_pulse (cf. Fig. 6.8 for an exemplary TOF spectrum). All depicted data has been analysed according to the discussion in Ch. 6.2.2. The fit to the data has been performed using the data analysis framework CERN ROOT v5.34/37[16].

Fig. 6.13 shows the resulting storage curve and gives the fit parameters of the biexponential fit $C_\mathrm{UCN}(t_\mathrm{s}) = A_1 \exp(-t_\mathrm{s}/\tau_1) + A_2 \exp(-t_\mathrm{s}/\tau_2)$. Taking the second exponential of the fit function into account, which corresponds to the 'cleaned' part of the UCN spectrum,

[16] The CERN ROOT framework (`https://root.cern.ch`) is written in C++ and provides the Minuit2 package, which is a standard minimization tool for fitting data in particle physics.

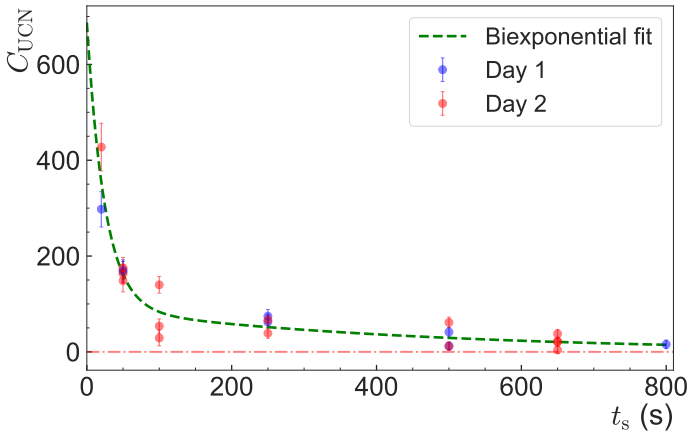

Figure 6.13: First storage curve. The number of stored UCN (C_{UCN}) after background subtraction and normalisation to the UCN flow in the time interval between 3.0 s and 6.0 s after the thermal peak is plotted as a function of storage time, t_s. Strong fluctuations in C_{UCN} were observed for constant t_s values, which is especially striking at $t_s = 100$ s ($C_{UCN}(100\,s) = 74.3(47.5)$). The biexponential fit to the data yields the parameters $A_1 = 571.3(72.6)$, $\tau_1 = 29.1(4.6)$ s, $A_2 = 67.4(20.2)$, and $\tau_2 = 537.6(165.5)$ s ($\chi^2/\mathrm{dof} = 3.7$).

a number of $A_2 = 67.4(20.2)$ stored UCN is derived. The data demonstrate a successful first full-magnetic storage, characterised by the storage constant $\tau_2 = 537.6(165.5)$ s. Compared to the spin flipper position measurements (cf. Ch. 6.2.2) performed one day earlier, a significantly higher number of stored UCN was detected. The most probable explanation is a gain of the source performance in the low energy range of $[0, 6.2]$neV, which could not be experimentally investigated[17]. Also, Fig. 6.13 demonstrates the high number of marginally-stored UCN with the spin flipper activated, which are characterised by a short decay constant $\tau_1 = 29.1(4.6)$ s due to the asymmetric trap potential (cf. Ch. 6.2.4). The loss of marginally-stored UCN therefore mainly accounts for the observed difference in the UCN counts at $t_s = 20$ s compared to $t_s = 50$ s.

Moreover, the stored UCN for constant storage times in Fig. 6.13 are strongly fluctuating, with maximum fluctuations $\sim 64\,\%$ at $t_s = 100$ s, which explains the bad quality of the fit function ($\chi^2/\mathrm{dof} = 3.7$). Averaging over all t_s values, fluctuations $\sim 35\,\%$ were determined. In order to rule out the UCN D source as the reason for the fluctuations, the $C_{UCN,\,flow}$ values determined from the integral counts[18] within 3 s and 6 s after the thermal peak were plotted against the number of pulses (cf. Fig. 6.14). For $C_{UCN,\,flow}$, an average fluctuation of $\sim 5\,\%$ was determined, which is slightly higher than the usual fluctuations ($\mathcal{O}(1\,\%)$) but 7 times less than the observed C_{UCN} fluctuations. These fluctuations can be explained by the acceptance to UCN with low initial energies of $[0, 6.2]$neV. Since these low energies refer to UCN which could just reach the horizontal neutron guide of τSPECT, the measurement is very sensitive to fluctuations of the source performance and the guiding mechanism.

[17] The lowest measurable energy range was investigated using an aluminium storage bottle, which due to its Fermi potential of $V_F(\mathrm{Al}) = 54$ neV provides a sensitivity to UCN energies between 0 neV and 54 neV (cf. Fig. A.18).

[18] An exemplary time-of-flight (TOF) spectrum measured in the earlier June beam time is depicted in Fig. 6.8. The integration window used for the C_{UCN} determination is also shown.

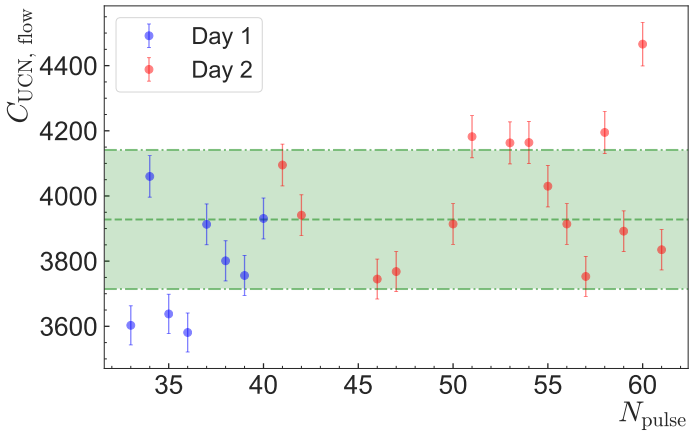

Figure 6.14: Stability of the UCN flow used for normalising the stored UCN counts. The number of the UCN measured in flow mode ($C_{\mathrm{UCN,\,flow}}$) in the time interval between 3.0 s and 6.0 s after the thermal peak (t_{pulse}) is depicted as a function of reactor pulses (N_{pulse}). The statistical error was taken as error bars. To determine the fluctuations in $C_{\mathrm{UCN,\,flow}}$, the mean ($\overline{C}_{\mathrm{UCN,\,flow}}$) and the standard deviation ($\sigma_{\mathrm{UCN,\,flow}}$) were computed. These values are represented by the green area, with the middle line denoting $\overline{C}_{\mathrm{UCN,\,flow}} = 3927.8$ and the outer lines $\sigma_{\mathrm{UCN,\,flow}} = 213.5$. This results in an average fluctuation of $\sim 5.4\,\%$, which is larger than typical fluctuations of the UCN yield ($\mathcal{O}(1\,\%)$).

6.2.4 First cleaning of the stored UCN spectrum

The cleaning process is required for removing 'marginally-trapped' UCN with energies $> E_{\mathrm{UCN,\,max}}$ from the storage volume. Since these UCN potentially remain in trajectories with low angles θ and energy $E_{\mathrm{UCN}} = E_{\perp}\sin^2\theta \leq V$ [GRL91] (cf. Fig. 6.15 a) for long times, their presence in the storage volume blurs the number of storable UCN, which is a strong systematic effect on the τ_n determination. As already discussed, these higher-energetic UCN need to be therefore removed by moving the neutron detector with the neutron-absorbing front into the storage volume.

In a first cleaning attempt, the detector was moved to the position[19] $z \sim 1865\,\mathrm{mm}$ (cf. red dashed line on the right in Fig. 6.15 b), which implies that UCN with storage energies of $\gtrsim 47\,\mathrm{neV}$ are absorbed at the intersection of the longitudinal and the Halbach octupole magnetic fields (cf. Fig. 6.15 b). Any other cleaning positions down to the magnetic potential minimum of 12.4 neV can be selected with a precision better than $1\,\mathrm{neV\,mm^{-1}}$. Note that this energy only refers to the longitudinal energy component, which implies that UCN with large transversal energy components moving on trajectories as shown in Fig. 6.15 a) can survive in the storage volume with total energies $> 47\,\mathrm{neV}$. Therefore, a mechanism to convert UCN with large transversal energy components to longitudinal components by 'disturbing' the UCN trajectories is needed before driving the detector to the cleaning position. This 'conversion' is realised by the asymmetric trap potential (cf. Ch. 5.1.2).

The number of stored UCN as a function of the storage times $t_{\mathrm{s}} = (50, 250, 500, 800)$ s after cleaning is shown in Fig. 6.16. The detector was driven to the cleaning position 25 s after the reactor pulse and returned to its non-counting position 10 s later. The 'cleaned' storage curve with normalisation to the UCN flow in the time interval $[t_{\mathrm{pulse}}+3, t_{\mathrm{pulse}}+6]$ s is shown in Fig. 6.16. The data has been analysed according to the principles laid out in

[19] The detector position was corrected according to the findings in Ch. B.1.

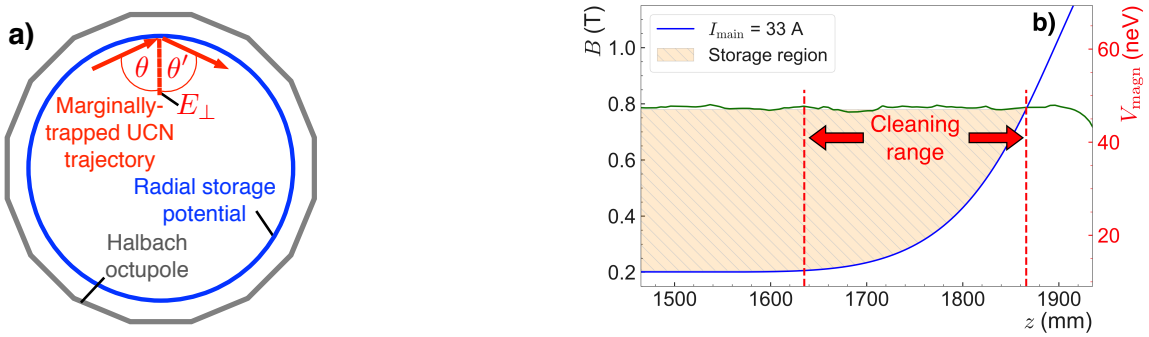

Figure 6.15: Marginally-trapped UCN trajectory and cleaning positions. (a) Marginally-trapped UCN inside the storage volume (radial potential caused by the Halbach octupole magnetic flux density, blue) follow trajectories with high angles θ perpendicular to the octupole surface component, $E_\perp$. Thus, their kinetic energy $E_{\mathrm{UCN}} = E_\perp \sin^2\theta$ might be notably higher than the otherwise storable energy. (b) Longitudinal magnetic flux density B for $I_{\mathrm{main}} = 33\,\mathrm{A}$ as a function of z position, and magnetic potential V_{magn} (right axis). The movable detector with its UCN-absorbing front can be positioned at any position corresponding to V_{magn} values between 47.0 neV and 12.4 neV (red dashed lines).

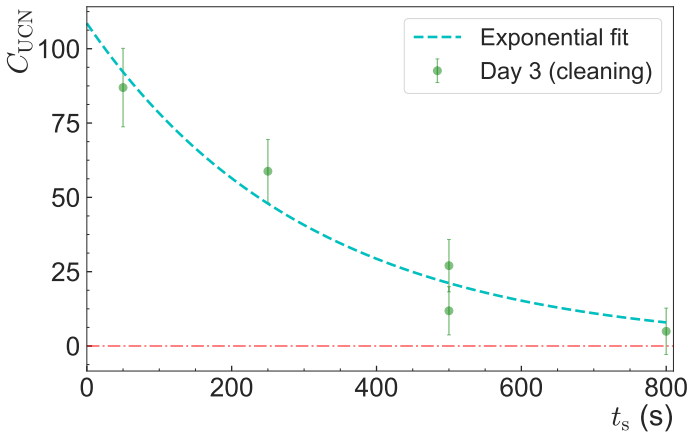

Figure 6.16: Storage curve after cleaning with number of stored UCN (C_{UCN}) as a function of storage time, t_{s}. C_{UCN} has been normalised to the UCN flow in the time interval between 3 s and 6 s after the thermal peak, t_{pulse}. The background-subtracted data were fitted using an exponential fit with parameters $A = 108.6(13.9)$ and $\tau = 305.7(46.7)$ s ($\chi^2/\mathrm{dof} = 1.4$).

Ch. 6.2.2, with the fit being computed by the framework CERN ROOT v5.34/37. After an exponential fit, which underlies the efficiency of the cleaning method, a number of 108.6(13.9) stored UCN was determined, which is slightly higher than the results derived from the second fit component of the non-cleaned storage curve ($A_2 = 67.4(20.2)$, cf. Fig. 6.13). For more insights into the cleaning efficiency, more measurement statistics would have been required, which was not possible due to time constraints.

6.2.5 Explanation of the measurement results

In the following, potential factors are identified to explain why the number of stored UCN in the September beam time turned out to be significantly less than the predicted number

of ~ 1370 UCN based on pre-characterisation measurements (cf. Ch. 4.4.2). The number of stored UCN is from now on indicated as $C_{\mathrm{UCN}}(t_{\mathrm{s}} = 0\,\mathrm{s})$ with extrapolation to a storage time of $t_{\mathrm{s}} = 0\,\mathrm{s}$. Based on the calculations in Ch. 4.4.2, a number of $C_{\mathrm{UCN}}(t_{\mathrm{s}} = 0\,\mathrm{s}) = 4925(230)$ results when taking the spin polarisation and the volume scaling factor into account. This number is the starting point for the following consideration, with all remaining factors summarised in Tab. 6.1.

Table 6.1: Identification of potential factors decreasing the number of stored UCN. Provided are the contribution(s) along with the corresponding factor and the number of UCN extrapolated to a storage time of $t_{\mathrm{s}} = 0\,\mathrm{s}$, $C_{\mathrm{UCN}}(t_{\mathrm{s}} = 0\,\mathrm{s})$. The data is based on Tab. 4.2, with initially $C_{\mathrm{UCN}}(t_{\mathrm{s}} = 0\,\mathrm{s}) = 14050(650)$ according to aluminium storage bottle measurements. Details on the factors are given in the text. Note that the C_{UCN} values have been rounded.

Contribution(s)	Decreasing factor	$C_{\mathrm{UCN}}(t_{\mathrm{s}} = 0\,\mathrm{s})$
Spin polarisation, volume scaling factor	~ 0.35	4925(230)
Spin flip efficiency	$\varepsilon_{\mathrm{AFP}} \sim 0.59(20)$	2905(995)
Acceptance to energies of incoming UCN	$\varepsilon_{\mathrm{storage}} \sim 0.04$	116(40)

As a further contributing factor, the spin flip efficiency ($\varepsilon_{\mathrm{AFP}}$) has been calculated. Numerically solving the differential equations[20] in [LT84] (cf. Eqs. (5.7)-(5.9)) for a spin flip position[21] of $z_{\mathrm{sf}} = 859\,\mathrm{mm}$ close to the September beam time ($z_{\mathrm{sf,\,corr}} = 863\,\mathrm{mm}$, cf. Ch. 6.2.2), $\varepsilon_{\mathrm{AFP}}$ values for B_1 amplitudes in the range of $[0.05, 0.20]$ mT were calculated (for an explanation of B_1, cf. Ch. 5.3.2). The selected range reflects the uncertainty in the measurement of the B_1 amplitude[22], which was inferred from the signal in a pick up coil close to the spin flipper. A second order polynomial fit to the calculated $\varepsilon_{\mathrm{AFP}}$ data is depicted in Fig. 6.17 (blue line). Including the uncertainty of the B_1 measurement, an efficiency of $\varepsilon_{\mathrm{AFP}} \sim 0.59(20)$ results.

The major limitation on the number of stored UCN in the September beam time stems from the acceptance to low energies of the incoming UCN in the range of $[0, 6.2]$neV ($\Delta E \sim 6.2\,\mathrm{neV}$, cf. Ch. 6.2.1). According to the relation of maximum storage potential and the number of storable UCN density (cf. Eq. (3.15)),

$$\varepsilon_{\mathrm{storage}} = \left(\frac{\Delta E}{V_{\mathrm{F}}(\mathrm{Al})}\right)^{\frac{3}{2}} = \left(\frac{6.2\,\mathrm{neV}}{54\,\mathrm{neV}}\right)^{\frac{3}{2}} , \tag{6.2}$$

with $V_{\mathrm{F}}(\mathrm{Al}) = 54\,\mathrm{neV}$ (cf. Tab. A.1) denoting the Fermi potential of the aluminium storage bottle, a decreasing factor of $\varepsilon_{\mathrm{storage}} \sim 0.04$ is calculated. Consequently, the number of $C_{\mathrm{UCN}}(t_{\mathrm{s}} = 0\,\mathrm{s})$ decreases to 116(40), which within errors agrees with the value extracted from the cleaned storage curve (108.6(13.9), cf. Fig. 6.16). Further potentially contributing factors, which have not been considered in the calculation, are due to the event identification ($\lesssim 0.8$), and the non-saturated UCN yield (~ 0.94). The worse beam line transmission compared to the 'standard' beam line used in the UCN D source characterisation measurements (cf. Ch. A.5.4) has also not been taken into account.

[20] The calculation is based on an idea of Prof. W. Heil. For solving Eqs. (5.7)-(5.9), the commercial software Wolfram Mathematica 11.0.1.0 (`https://www.wolfram.com/mathematica/`) was used.

[21] The deviation in the spin flip positions is negligible for the calculation of $\varepsilon_{\mathrm{AFP}}$.

[22] The estimated value of the B_1 amplitude was inferred by K. Ross.

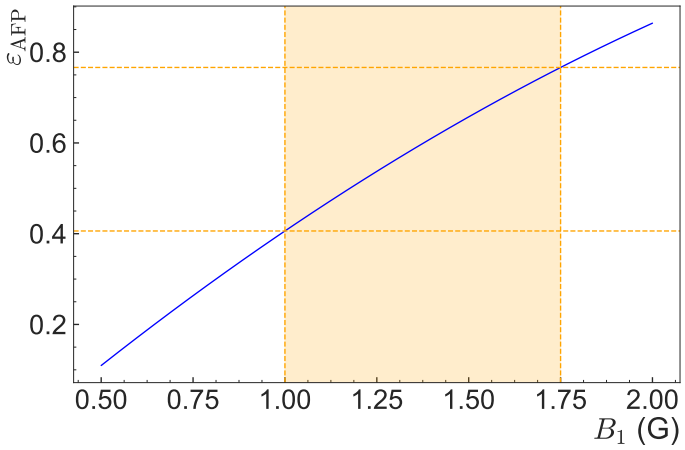

Figure 6.17: Spin flip efficiency $\varepsilon_{\mathrm{AFP}}$ as a function of B_1 amplitude, for a B_1 range of 0.5 G to 2 G. At an amplitude of $B_1 = 1.5\,\mathrm{G} = 0.15\,\mathrm{mT}$, an efficiency of $\varepsilon_{\mathrm{AFP}} = 0.59(20)$ is achieved, which was considered in Tab. 6.1. The blue line depicts a second order polynomial fit to data based on numerically solving the differential equations in [LT84] (cf. Eqs. (5.7)-(5.9)). A spin flip position of $z_{\mathrm{sf}} = 859\,\mathrm{mm}$ was assumed, leading to a magnetic flux density of $B_{\mathrm{sf}} = 0.346\,\mathrm{T}$ and a longitudinal gradient of $\nabla_z B \sim 220\,\mathrm{G\,cm^{-1}}$.

The ΔE value also explains the observed fluctuations while measuring the storage curve. These fluctuations $\sim 35\,\%$ were notably larger than statistical effects (cf. Fig. 6.13), clearly indicating a systematic effect. Also, it has to be noted that these fluctuations were observed after normalising the data to the flow of non-stored UCN, with the UCN flow showing a 7 times smaller fluctuation on average ($\sim 5\,\%$, cf. Fig. 6.14). Investigating potential systematics, fluctuations of the pulse energy ($\mathcal{O}(1\,\%)$) can be ruled out. For UCN with maximum energies of $E_{\mathrm{UCN,\,max}} = 190\,\mathrm{neV}$ and the UCN source in saturation, the UCN yield fluctuates by $\mathcal{O}(1\,\%)$ (cf. Ch. 4.3).

Larger fluctuations were identified for UCN stored in an aluminium bottle, which limits ΔE to 54 neV (cf. Fig. A.18). Within the relative pulse numbers corresponding to those during the measurement of the non-cleaned storage curve (33 - 61, cf. Ch. 6.2.3), peak-to-peak fluctuations of 5 % were found. Note that due to a shutter malfunction, the relative pulse numbers 33 - 43 in the aluminium storage measurement could not be included in the analysis. Due to the rising UCN yield, which can be clearly seen in Fig. A.18, the fluctuation could have been even larger. According to these results, larger fluctuations are expectable in the low-energetic UCN region corresponding to the accepted energies in the range of $[0, 6.2]$neV, which might correspond to the observed $\sim 35\,\%$ deviation. The reason why the UCN flow has shown fluctuations $\mathcal{O}(5\,\%)$ instead can be explained due to their higher maximum energies.

6.2.6 Outlook on improved results

In the February 2020 beam time, significantly better results were obtained, which have yielded a non-cleaned storage curve with $A_2 \sim 740$ stored UCN extrapolated to a storage time of $t_{\mathrm{s}} = 0\,\mathrm{s}$ for a duration of $\tau_2 \sim 713\,\mathrm{s}$ according to the fit parameters in Fig. 6.18. With a number of ~ 740 stored UCN, a total measurement time of ~ 8.5 months would be required for reaching a statistical accuracy of $\Delta\tau_n = 1\,\mathrm{s}$ (comparison to expected value in Ch. 4.4.2). The improved results mainly stem from a newly-constructed spin flipper

allowing for positioning the spin flipper close to its design position ($z_{\mathrm{det}} \sim 1100\,\mathrm{mm}$), which due to the lower magnetic potential in the spin flip region leads to an improved acceptance to the energies of incoming UCN. Thus, incoming UCN with initial energies in the range of $[0, 23]$neV could be stored ($\Delta E \sim 23.0\,\mathrm{neV}$ instead of $\Delta E \sim 6.2\,\mathrm{neV}$ in September beam time, cf. Ch. 4.4.2 for an explanation). Although the new spin flip position could have been reached using a birdcage spin flip design (cf. Fig. 5.9), it was decided to perform the spin flip using two saddle coil pairs, which provide a circularly-polarised field and allow for an in-situ matching of the spin flipper's Larmor frequency. Therefore, a fixed frequency matching prior to the beam time was not required anymore.

Taking the improved ΔE value into account, a factor of $(6.2\,\mathrm{neV}/23.0\,\mathrm{neV})\,3/2 \sim 6.8$ (cf. Eq. (6.2)) is calculated. Applying this factor to the number of stored UCN after cleaning ($\sim 109(14)$, cf. Fig. 6.16) while assuming a spin flip efficiency of $\varepsilon_{\mathrm{AFP}} = 1$ due to the lower gradients in the design spin flip position gives 741(95), which matches with the corresponding value extracted from the measured storage curve ($A_2 = 739.8(51.2)$, cf. Fig. 6.18). As a secondary effect of the increased ΔE value, the fluctuations in C_{UCN} were significantly reduced, which underlines the hypothesis of increasing fluctuations with decreasing ΔE in Ch. 6.2.5.

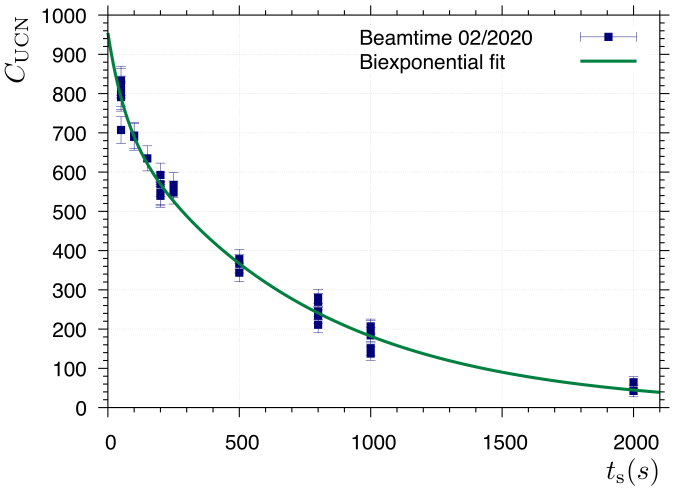

Figure 6.18: Outlook on the storage curve measured in the February 2020 beam time. The number of stored UCN (C_{UCN}) normalised to the reactor pulse energy is plotted as a function of storage time, t_{s}. A biexponential fit to the data has given the parameters $A_1 = 214.6(106.3)$, $\tau_1 = 65.9(65.1)$ s, $A_2 = 739.8(51.2)$, and $\tau_2 = 712.9(47.1)$ s ($\chi^2/\mathrm{dof} = 1.5$). The plot is property of the τSPECT collaboration, with the analysis being part of the PhD work of K. Ross. It has been submitted in a private communication.

As previously mentioned, the higher energy acceptance to incoming UCN could be reached by performing the spin flip at a longitudinal field of $\sim 0.2\,\mathrm{T}$, which corresponds to the design concept of τSPECT (cf. Ch. 5.3.3). Moreover, additional improvements were realised. Being able to match the spin flipper's Larmor frequency in-situ, a more detailed systematic investigation of the spin flip efficiency as a function of the position was furthermore possible. The absence of the 50 Hz noise allowed for an improved event identification. Due to time constraints, no further investigation has been made regarding the UCN normalisation method. For this reason, the stored UCN have been normalised to the reactor

pulse energy. Further details on the steps leading to the improved results are part of the PhD work by K. Ross.

With the recent improvements of the February beam time, the storage time is now close to the neutron lifetime, with an already promising statistics close to the estimation of ~ 1370 UCN at $\Delta E \sim 23\,\mathrm{neV}$ (cf. Ch. 4.4.2). Consequently, τSPECT is now ready for data taking in phase I. Significantly higher numbers of stored UCN can be expected if the acceptance to incoming UCN energies could be increased further. A possibility to increase the energy acceptance is to perform a primary spin flip in the high field region of the first magnetic field bump ($z_{\mathrm{sf,\ primary}} \sim 0\,\mathrm{mm}$, cf. Fig. 5.8) to convert low-field seekers (LFS, cf. Ch. 4.1) of energies $\gtrsim 60\,\mathrm{neV}$ to high-field seekers (HFS) and subsequently back to the storable LFS by performing a second spin flip. The higher initial LFS energies lead to a higher number of storable UCN, since more higher-energetic UCN are contained in the spectrum (the storable UCN density scales with $E^{3/2}$, cf. Eq. (3.15)). With the magnetic potentials of the spin flippers at $B_{\mathrm{sf,\ primary}} \sim 1\,\mathrm{T} \sim 60\,\mathrm{neV}$ and $B_{\mathrm{sf,\ secondary}} \sim 0.2\,\mathrm{T} \sim 12\,\mathrm{neV}$ (cf. Ch. 3.2.1), respectively, first estimations give a factor 5 increase in the number of storable UCN according to theoretical considerations of the UCN energy distribution. The actual gain factor needs to be determined experimentally, taking effects such as the influence of the higher initial UCN energy on the transmission within the neutron guide into account. The double spin flip mechanism will be implemented during the PhD work of K. Ross. With the improved statistics, a detailed study of the systematic effects will be possible.

7 Conclusion and outlook

This work has demonstrated how the τSPECT experiment was prepared for the first phase of data taking with full-magnetic storage, which aims at measuring the neutron lifetime with a precision of $\Delta\tau_n = 1\,\mathrm{s}$. First measurements could demonstrate the full-magnetic storage of ultracold neutrons (UCN), which was realised by a complex array of technical developments characterised and implemented throughout the past four years.

Being a high-precision UCN experiment, τSPECT is statistically limited by the number of storable UCN. In order to improve statistics, the UCN source at beamport D was successfully upgraded. Simultaneously to the advancement of the τSPECT experiment, the performance of the UCN D source was thoroughly characterised. Overall, a UCN density of $8.53(5)\,\mathrm{cm}^{-3}$ at a storage time of 2 s was determined using the nickel molybenum (NiMo)-coated stainless steel standardised storage bottle developed by the Paul Scherrer Institute to conduct world-wide comparison measurements of UCN sources. This 3.5 times gain in UCN density when compared to the non-upgraded source was achieved by coating the inside of the solid deuterium (sD_2) converter volume and the thermal bridge using ^{58}NiMo instead of natural NiMo to improve the UCN phase-space acceptance. Additionally, the neutron guides were replaced to improve the UCN transmission by $\sim 35\,\%$. A newly-installed helium liquefier system provided continuous operability of the source for three weeks, while further measures in the source cooling system improved the overall cooling of the converter. Moreover, a development of the UCN yield, which after an initial drop rises by $\sim 40\,\%$ until reaching its saturation after ~ 150 pulses, was measured. Additional measurements comprising the para- and ortho-concentration of the sH_2/sD_2 premoderator and converter, respectively, as well as the monitoring of the converter pressure point to the conclusion that the repeatedly reproduced phenomenon is likely due to reformation processes of the solid deuterium crystal caused by the heat impact of the reactor pulses. After reaching saturation, a fluctuation of the UCN yield $\mathcal{O}(1\,\%)$ was found, with a general reproducibility between beam times $\mathcal{O}(10\,\%)$.

The upgraded UCN D source was furthermore used for extensive preparatory studies to emulate the conditions found in the full-magnetic implementation of τSPECT. The UCN transmission of the neutron guide section was measured to select a proper guide material. Also, the $\sim 20\,\%$ impact of the guide narrowing in the front part of the guide system on the transmission has been evaluated, which is required to suppress the radial gradients

for a higher spin flip efficiency. Based on the experimental findings, a multi-layered non-magnetisable neutron guide comprising a fused silica tube on the inside and a stainless steel tube on the outside was realised, with its optimum height found at 1.83 m over the source exit.

To account for the fluctuations of the UCN D source's yield, the number of stored UCN in τSPECT has to be normalised to a suitable reference. In a dedicated measurement setup, different methods to evaluate the efficiency of the respetive normalisation method based on the reactor pulse energy, non-storable neutrons, and UCN have been compared. The highest precision (0.7 %) was found when normalising the data using UCN of a similar energy range. Based on the results of the pre-characterisation measurements, a number of ~ 1370 storable UCN in the τSPECT storage volume was predicted. For reaching a statistical accuracy of $\Delta\tau_n = 1\,\mathrm{s}$, which is the goal for the first measurement phase (phase I), a total measurement time of ~ 4.6 months at the UCN D source of TRIGA Mainz will be required.

For the implementation of full-magnetic storage, the Halbach octupole, an array of Sm_2Co_{17} permanent magnets, was successfully installed inside the cryostat of the former *a*SPECT experiment. The superposition of the magnetic fields caused by the Halbach octupole in radial direction and by the superconducting fields inside the cryostat in longitudinal direction creates a 3D magnetic storage volume of $\sim 6.8\,\mathrm{l}$ with a maximum potential energy of 47 neV. To convert the UCN into their storable low-energy state, a movable neutron guide section containing an adiabatic fast passage spin flipper was implemented. After filling the UCN into the storage volume, the guide section of $\sim 2.6\,\mathrm{m}$ length is retracted from the storage volume by 0.75 m to prevent material interaction. Additionally, a movable detector section was designed for moving the neutron detector 0.25 m into the storage volume to collect 'surviving', *i.e.,* not-yet-decayed UCN. The detector unit was designed modularly, which permits the installation of a silicon drift detector for decay proton detection in phase II. Regarding the technical implementation, a high movement precision and reliability could be established for both the movable neutron guide section and the detector section.

A crucial part of the τSPECT experiment in phase I is an efficient UCN detection in high magnetic fields up to $\sim 1.7\,\mathrm{T}$ and at low temperatures of $\sim 180\,\mathrm{K}$. To meet these requirements, a custom UCN detector based on a 80 nm thin boron-10 layer for neutron capture, a silver-doped zinc sulfide scintillator for photon generation, and a silicon photomultiplier array for photon detection was successfully implemented. Prior to its final assembly, the neutron detector was characterised to fine-tune the pulse shaping electronics and understand the peak height distributions for signal/noise discrimination, which was supported by ray-tracing simulations to infer the photon transmission. Using a calibrated low-activity americium-241 source, a working algorithm for event reconstruction was established. The algorithm was later used for test measurements with UCN at room temperature. In these measurements, the SiPM array's optimal bias voltage setting was experimentally determined by testing the event reconstruction for UCN signals. Furthermore, a performance similar to a commercial CASCADE detector was reached for UCN stored in a $\sim 10\,\mathrm{l}$ aluminium volume.

In a first beam time, all components of the τSPECT experiment were successfully tested. Undertaking several thermal-insulating measures, the low temperatures required for the operation of the superconducting coils within the cryostat were achieved. Also, by careful selection of materials and by including efficient vacuum feedthroughs, a final pressure of $\sim 10^{-7}\,\mathrm{mbar}$ could be realised in the storage volume. Installed into the cryostat at a temperature of 180 K, the detector signal pulse height was found to be reduced by a factor

3.4 on average compared to previous room temperature measurements, while typical noise levels determined by the algorithm remained at $\sim 1\,\mathrm{Hz}$. Despite the reduced peak height, event reconstruction was nevertheless possible.

In the September beam time, a preliminary full-magnetic storage curve was measured, which yielded 67.4(20.2) stored UCN with a storage constant of 537.6(165.5)s. Also, the cleaning of the UCN spectrum, which implies the removal of non-storable UCN by moving the UCN detector slightly into the storage volume, was proven to be working effectively and yielded a similar number of stored UCN (108.6(13.9)). The birdcage design of the used spin flipper yielded a static frequency of $\sim 10\,\mathrm{MHz}$, preventing from performing the spin flip at its design position offering at a lower magnetic field potential. The specific spin position led to an acceptance to incoming UCN in the energy range $[0, 6.2]$neV, which implies that only UCN with given initial energies before reaching the first magnetic field bump of τSPECT can be stored. As could be demonstrated in later calculations, the reduced energy acceptance accounted for not reaching the predicted value of ~ 1370 storable UCN. Moreover, the low energy acceptance explains the observed strong fluctuations of the number of stored UCN during the measurements.

Outlook

Performing a spin flip at the design position with a frequency of $\sim 6\,\mathrm{MHz}$ increased the acceptance to incoming UCN to energies within $[0, 23]$neV in the February 2020 beam time. With the energy acceptance improved by a factor ~ 6.8 compared to September, a number of ~ 740 UCN was stored. Thus, τSPECT is now ready to take data, with a required measurement time of ~ 8.5 months for reaching a statistical accuracy of $\Delta\tau_n = 1\,\mathrm{s}$. The improved statistics allows for performing systematic investigations, with further expectable statistical improvements due to the implementation of the double spin flip mechanism. Most importantly, an efficient cleaning method as well as a functioning normalisation method must be found. Further investigations should also be performed to fully understand the event reconstruction based on the neutron detector data. To quantify UCN depolarisation losses, a 3D field map of the superimposed magnetic field should be measured. Along with updated measurement results, conclusive Monte Carlo simulations to determine the energy distribution of the stored UCN are needed. This would allow for an investigation of energy-dependent effects regarding UCN detection and loss mechanisms.

After the completion of the first phase, phase II will deal with the in-situ detection of decay protons to demonstrate the independence of the τ_n measurement from the detection method. Afterwards, a UCN detection-based measurement with $\Delta\tau_n = 0.2\,\mathrm{s}$ calls for an increased UCN yield, which might be reached by further upgrades of the UCN source referring to an increased neutron guide diameter and a larger premoderator volume.

A Additional contents - Ultracold neutron source at beamport D

Contents supplementary to the Mainz ultracold neutron source at beamport D are provided in the following. The reader is especially advised to consider Ch. A.1, which serves as an introduction to the measurement principles and techniques relevant throughout the entire main part. Furthermore, an overview over the majority of presently active ultracold neutron (UCN) sources is provided in Ch. A.2. Details on the saturating UCN yield increase of the UCN D source after its upgrade are given in Ch. A.3. Chapter A.4 discusses the use of Raman spectroscopy to determine the rotational energy states of hydrogen and deuterium, which has a considerable impact on UCN production. Lastly, the low-energy UCN fraction available in the spectrum, the sensitivity of the UCN yield to the beam line height, and the reactor pulse energy distributions, and various other analyses are summarised in Ch. A.5.

A.1 Basics on ultracold neutron characterisation measurements

For various measurements testing UCN components and characterising UCN sources, storage bottles of different materials and volumes are used. The idea is to fill UCN into a storage volume in which they are materially confined. The upper storable energy, $E_{\mathrm{UCN,\,max}}$, is defined by the material's Fermi potential, V_{F}. V_{F} values typically used in UCN experiments are listed in Tab. A.1.

For performing an experiment, the UCN are extracted from the source by neutron guides ('beam line'). In case of the Mainz UCN D source, the UCN minimum energy corresponds to the Fermi potential of solid deuterium, *i.e.,* $E_{\mathrm{UCN,\,min,\,sD2}} = V_{\mathrm{F}}(\mathrm{sD_2}) = 105\,\mathrm{neV}$ ([ADF$^+$08]. In order to increase the amount of storable UCN, the beam line is elevated by $\Delta h \geq 1\,\mathrm{m}$ over the source exit (cf. Fig. A.1 a), which decreases the UCN energy by $\geq 102\,\mathrm{neV}$ due to the gravitational deceleration (cf. Ch. 3.2.1). Then, the UCN are filled into a storage bottle with two shutters S_1 and S_2 to fill and empty the bottle. Storing UCN in a material bottle is a straightforward measurement procedure. The subsequent steps are graphically depicted in Fig. A.2 a) and summarised as follows:

(i) Filling: Shutter S_1 is open for filling time t_{f} to fill UCN into the storage volume.

(ii) Storage: UCN are stored, while S_1 and S_2 remain closed for a defined storage time t_{s}.

Table A.1: Fermi potential values V_F relevant for UCN physics. Values were taken from [GRL91, ADF+08, ABB+09, Lau11, BDK+17, CBL+19]. For ^{10}B, the given value is valid for an enrichment of 96 %. For nickel molybdenum, the concentration is 85 % Ni and 15 % Mo.

Material	V_F (neV)
Titanium (Ti)	-48
Boron-10 (^{10}B)	2.5
Aluminium (Al)	54
Silicate glass (SiO_2)	90
Solid deuterium (sD_2)	105
Copper (Cu)	168
Stainless steel (VA)	190
Nickel molybdenum (NiMo)	220
Nickel-58 (^{58}Ni)	335

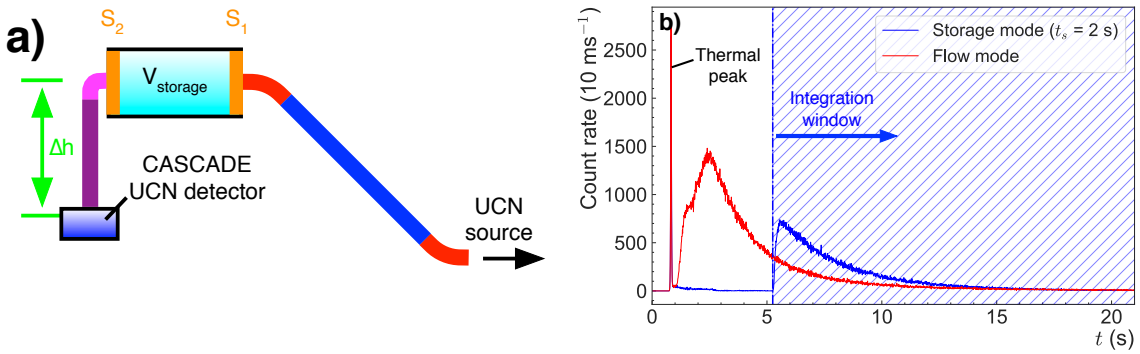

Figure A.1: Beam line setup and UCN time-of-flight (TOF) spectra. (a) Typical beam line used for UCN characterisation measurements at the Mainz UCN D source. After exiting the source, the UCN are gravitationally decelerated. The mechanical shutters S_1 and S_2 are used to fill the UCN in the storage volume and later empty the volume for counting in the CASCADE detector, which is placed at a lower gravitational level due to its aluminium entrance window. (b) The CASCADE TOF spectra were measured using a stainless steel storage bottle at height $\Delta h = 1.35$ m over source exit. For the 2 s storage measurement (blue line), an optimum filling time of 3.25 s was used. UCN within the integration window are counted. The red line shows the TOF spectrum in flow mode, during which both shutters S_1 and S_2 remain open.

(iii) Counting: Shutter S_2 is opened, which leads to the UCN leaving the trap and reaching the UCN detector. The resulting UCN time-of-flight (TOF) spectrum for $t_s = 2$ s is shown in Fig. A.1 b (blue line).

For UCN detection, the commercial CASCADE detector[1] is typically used, which captures UCN in the ^{10}B(n, $\alpha/^7$Li) reaction. The decay products are detected by gas electron multiplier (GEM) foils, whereby a UCN detection efficiency ~ 85 % is achieved [KS11]. Since the CASCADE detector includes an aluminium entrance window with V_F(Al) = 54 neV, the UCN are gravitationally accelerated (cf. Fig. A.1 a) to get an energy boost $\Delta E \geq V_F$(Al) in order to reach the gas volume behind the GEM foil.

[1]The CASCADE detector is built by CDT GmbH (`http://n-cdt.com`).

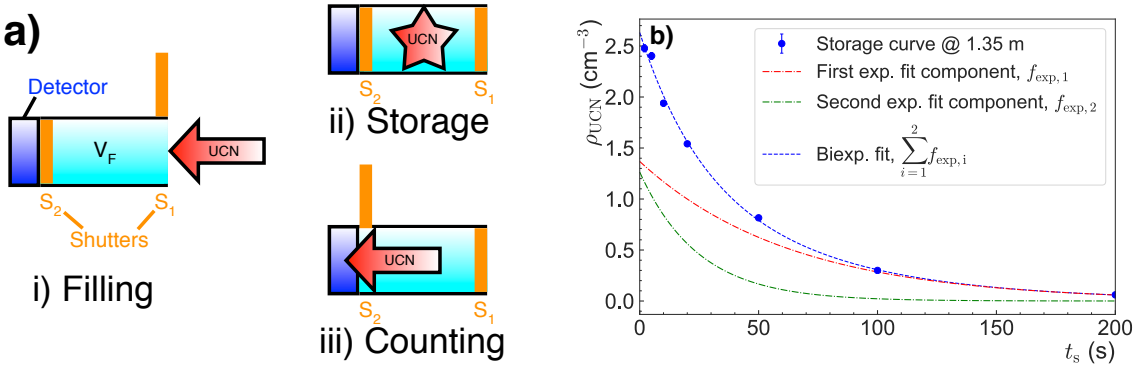

Figure A.2: Storage curve measurement in a material bottle. (a) First, the UCN are filled into the material bottle by opening shutter S_1 for a previously optimised filling time, t_f. During the storage process, both shutters S_1 and S_2 remain closed for the storage time t_s, while the bottle's Fermi potential V_F defines the maximum storable UCN energy. S_2 is opened for counting the UCN in a detector. (b) Plotting the UCN density ϱ_UCN against t_s results in the storage curve with biexponential fit (blue dashed line). The individual exponential functions are illustrated by the red and green dash-dotted lines.

Before the actual storage measurement, a filling time optimisation is performed. Using a typical storage time of $t_\mathrm{s} = 5\,\mathrm{s}$, t_f is varied until the value with maximal UCN counts is found. Having determined optimal filling conditions, the storage measurement starts. For this, t_s is typically varied from 2 - 200 s, which gives a TOF spectrum in which integration window all UCN are counted (cf. blue line in Fig. A.1 b). The storage curve is determined by plotting the UCN density (ϱ_UCN), *i.e.,* the number of stored UCN in storage volume V_storage, against t_s (cf. Fig. A.2 b).

After the measurement, the data is fitted using a biexponential function to account for UCN losses due to a non-cleaned spectrum[2] at small t_s [GRL91],

$$\varrho_\mathrm{UCN}(t_s) = \underbrace{A_1 \exp\left(t_s/\tau_1\right)}_{\text{'non-cleaned' spectrum}} + A_2 \exp\left(t_s/\tau_2\right) \ . \tag{A.1}$$

Assuming a storage bottle with comparably small loss terms, the UCN spectrum can be characterised according to the τ_2 value. Longer τ_2 times imply a 'softer' UCN spectrum with lower average energy, which is preferred for neutron lifetime experiments.

If not otherwise noted, measured UCN density $\varrho_\mathrm{UCN}(t)$ is normalised to the average pulse energy of the respective beam time, $\overline{E}_\mathrm{pulse}$:

$$\varrho_{\mathrm{UCN,\,norm},\,i} = \frac{\varrho_{\mathrm{UCN},\,i}}{E_{\mathrm{pulse},\,i}} \cdot \overline{E}_\mathrm{pulse} \ . \tag{A.2}$$

Additional typical measurements include:

- 'Flow mode' measurement, during which both shutters S_1 and S_2 remain open during the entire measurement (Fig. A.1 b) for TOF spectrum (red line)). This allows for consistency checks and also gives hints on the UCN capture efficiency of the measured setup. The integral number of counts measured in a specified time interval give C_flow,

[2] A 'cleaned' spectrum implies that only UCN are stored with energies corresponding to the Fermi potential of the material bottle, *i.e.,* $E_\mathrm{UCN} \leq V_\mathrm{F}$. Without cleaning, the upper limit of the stored energy spectrum is not defined since it contains 'marginally-trapped' UCN with energies higher than V_F.

which is also commonly referred to by the term 'transmission'. Depending on the beam line configuration, not only UCN contribute to C_{flow}, but also VCN (very cold neutrons with energies $\gtrsim 350\,\text{neV}$).

- Determination of the horizontal/vertical (h/v) ratio. Using a CASCADE detector with aluminium entrance window, a horizontal extraction at the same gravitational level as the storage bottle cuts out all UCN with energies below $V_{\text{F}}(\text{Al}) = 54\,\text{neV}$. In the vertical extraction, these low-energy UCN are detected due to the gravitational acceleration. Therefore, (1 - h/v) gives the proportion of UCN with $E_{\text{UCN}} \geq 54\,\text{neV}$ in the energy spectrum.

A.2 Ultracold neutron sources compared

The performance of all world-wide active UCN sources with the exception of the Los Alamos National Laboratory source (USA) has recently been compared with a standardised measurement setup [BDK+17]:

(i) PSI (Paul-Scherrer-Institut, Switzerland [Lau14])

(ii) PF2 (Institut Laue-Langevin (ILL), France [SNS+86])

(iii) SUN-2 (ILL, France [LIP+16])

(iv) UCN D (University of Mainz, Germany [KSB+14])

Among given UCN sources, the UCN D source is the only pulsed source. All remaining sources are run in DC mode. For comparing the sources' performance, the UCN were stored in a nickel molybdenum (NiMo)-coated stainless steel volume with a volume of $\sim 32\,\text{l}$ and a Fermi potential of $V_{\text{F}} = 220\,\text{neV}$ [BBD+16]. The beam line for UCN transport and the filling time were optimised at the respective facility before storage curves were taken (for an overview over the measurement process, cf. Ch. A.1). To evaluate the performance, the UCN density at a storage time of $t_{\text{s}} = 2\,\text{s}$ as well as the storage time constant τ_2 (extracted from a biexponential fit) were taken into account.

The result of the comparison measurements is shown in Fig. A.3. The currently best UCN sources at ILL (PF2) and Paul-Scherrer-Institute (PSI) achieve UCN densities of $\sim 20\,\text{cm}^{-3}$. The lowest-energetic UCN spectrum is provided by the SUN-2 source at ILL with $\tau_2 \sim 107\,\text{s}$. Although offering a competitive τ_2 value of $\sim 76\,\text{s}$, the Mainz UCN D source at the TRIGA research reactor [EG19]) could only offer a disappointing UCN density of $\sim 2.4\,\text{cm}^{-3}$. It should be considered, however, that cited measurements have compared the UCN spectrum with high maximum UCN energies defined by the Fermi potential of NiMo ($\sim 220\,\text{neV}$, cf. Tab. A.1). For lower-energetic UCN required for neutron lifetime experiments relying on magnetic storage ($E_{\text{UCN}} \lesssim 60\,\text{neV}$), the sources might compare differently.

As the energy-dependent UCN density can be approximated by a Maxwellian distribution, the production of lower-energetic UCN is heavily suppressed compared to higher-energetic UCN. Therefore, achieved densities for lower-energetic UCN are notably lower. To improve the number of storable UCN with energies $\lesssim 47\,\text{neV}$ for the τSPECT experiment, the Mainz UCN D source has been recently upgraded (cf. Ch. 4.2). This measure was another main goal for a successful operation of the τSPECT experiment, since sufficient UCN statistics is needed for measuring a storage curve and investigating systematic effects in manageable time.

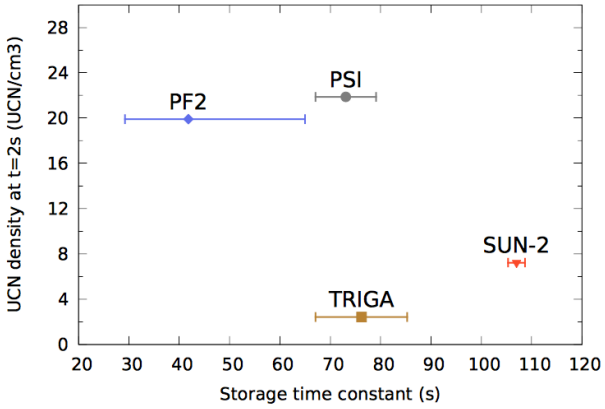

Figure A.3: Performance comparison of active UCN sources. All active UCN sources with the exception of the source at Los Alamos National Laboratory were compared in terms of their UCN density ϱ_{UCN} at $t_{\mathrm{s}} = 2\,\mathrm{s}$ (y-axis) and their storage time constant τ_2 (x-axis). Figure taken from [BDK+17].

A.3 Increasing ultracold neutron yield by pulsing

After the source upgrade, an increase in the UCN yield was discovered. Since the argumentation has already been published in [KRR+17], a short summary on the experimental findings along with the relevant plots is provided. As opposed to the behaviour of the UCN D source before the upgrade (cf. Fig. A.4 a), height over source exit $h = 125\,\mathrm{cm}$), an increase in the measured UCN density measured at 2 s storage time after the upgrade (cf. Fig. A.4 b), $h = 142\,\mathrm{cm}$) was observed.

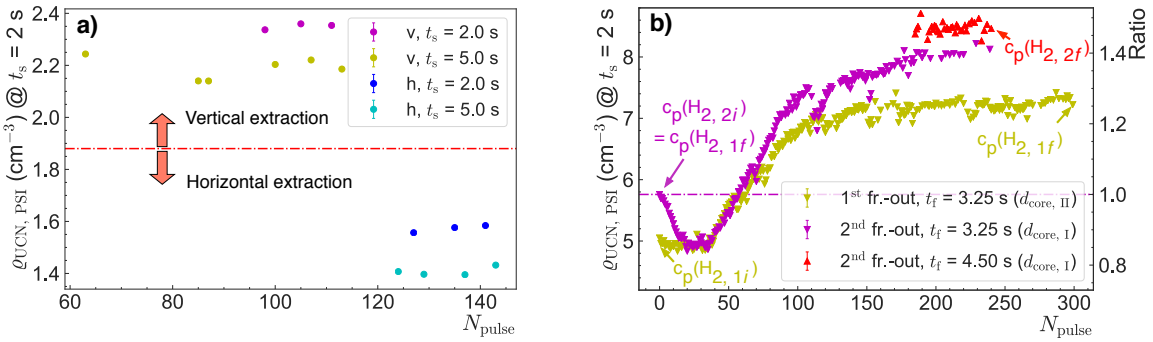

Figure A.4: UCN density in PSI storage bottle ($\varrho_{\mathrm{UCN,\,PSI}}$) as a function of reactor pulses (N_{pulse}) before and after source upgrade. (a) No change in the UCN yield was observed before the upgrade (v = vertical extraction, h = horizontal extraction, t_{s} = storage time). (b) After the upgrade, $\varrho_{\mathrm{UCN,\,PSI}}$ increases by $\sim 40\,\%$. The yield was measured after two consecutive freeze outs of the sD_2 crystal (first freeze-out (1), dark yellow data points: H_2 para concentration increased from initial (i) value $c_p(H_{2,1i}) = 30.8(4)\,\%$ to final (f) value $c_p(H_{2,1f}) = 89.8(2)\,\%$). Prior to the second freeze-out (2), the distance to the reactor was decreased from $d_{\mathrm{core,\,II}} = 30\,\mathrm{mm}$ to $d_{\mathrm{core,\,II}} = 0\,\mathrm{mm}$. The para concentrations before the second freeze-out (magenta and red data points for optimised filling time $t_{\mathrm{f}} = 4.5\,\mathrm{s}$) corresponds to $c_p(H_{2,1f})$, with final value $c_p(H_{2,2f}) = 89.0(6)\,\%$.

During the first freeze-out of the sD_2 converter, normal H_2 was used for the premoderator, which increased its para content to $\sim 90\,\%$ during pulsing[3]. A measurement with the $\sim 90\,\%$ para-H_2 frozen out as premoderator led to a quick decrease in the UCN yield (cf. Fig. A.5 a). The decrease can be explained by a deterioration of the sD_2 crystal, which is invoked by the ~ 10 times higher thermal conductivity of the para-converted H_2 [GKK+00]. Frozen out with a high para concentration, the heat absorbing properties of the premoderator are therefore limited. Adding $5\,\%$ D_2 in the premoderator decreased the thermal conductivity to levels comparable with natural H_2 [GKK+00]. This gas admixture was used from the second freeze-out on. For the measurements, a filling time of 3.25 s was used, which after the second freeze-out was increased to 4.50 s due to an additional filling time optimisation. In-between the first and the second freeze out, the distance of the front end of the nose containing the sD_2 crystal to the reactor core was decreased from 30 mm to 0 mm.

As Fig. A.4 b) shows, a similar yield pattern is found for the UCN densities at both freeze outs. After an initial decrease, the yield starts to rise after ~ 40 reactor pulses. After ~ 150 pulses, a saturation with $\sim 40\,\%$ increased UCN density is reached. A first possible explanation of the yield increase was based on the growing H_2 para concentration during pulsing. Para-converted H_2 (rotational quantum number $J = 0$) is more efficient than its ortho counterpart ($J = 1$) in moderating incoming neutrons. By inelastic scattering, the neutrons lose 14.7 meV energy, which is absorbed by the H_2 molecule to induce a conversion to the $J = 1$ state [Wür73]. A temporarily increasing para-H_2 concentration could therefore explain the rising UCN yield by a better matching to the sD_2 phonon energy spectrum. Since the UCN yield remained temporarily constant despite the increasing para-H_2 concentration before the upgrade (cf. Fig. A.4 a), and no clear evidence of higher UCN yields with higher para-H_2 concentrations at the upgraded source is found (cf. Fig. A.4 b), another process must be dominantly responsible for the observed behaviour.

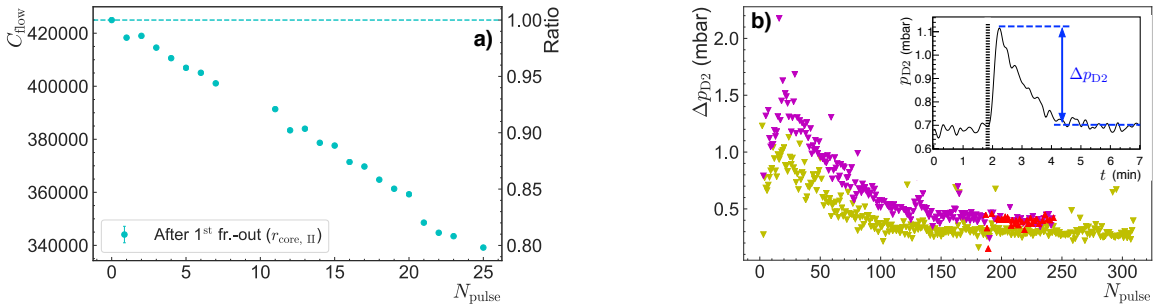

Figure A.5: Decreasing UCN yield during freeze-out of premoderator with high para concentration and evolution of deuterium pressure increase. (a) After the first freeze-out, the premoderator was frozen out with para concentration $c_p(H_{2,1f}) = 89.8(2)\,\%$, which led to a $\sim 20\,\%$ decrease of the counts in flow mode (C_{flow}) during the first 25 pulses (N_{pulse}) after freeze-out. (b) The converter pressure increase in D_2 (Δp_{D2}, cf. inset), which is caused by the thermal impact of the reactor pulse, shows a reciprocal behaviour when compared to the evolution of the UCN density (cf. Fig. A.4 b), also for colour coding).

A closer look on the D_2 pressure curves has given clear indications on reshaping effects of the sD_2 crystal due to the thermal impact of the reactor pulses. The D_2 pressure was

[3]The para concentration of the premoderator was determined in gaseous form by using a Raman spectrometer before the freeze-out and afterwards. More details on the rotatial energy levels and the measurement by the Raman technique are given in Ch. A.4.

measured by a pressure gauge attached to the neutron guide volume right of the vacuum separation foil (cf. Fig. 4.4) and continuously written to a file. An exemplary D_2 pressure curve is depicted in the inset of Fig. A.5 b). For the data analysis, the pressure increase Δp_{D2} caused by the thermal impact of the reactor pulse ('heat load') was evaluated and plotted against the number of pulses in accordance with Fig. A.4 b). In a first-order approximation, the Δp_{D2} values evolve reciprocal to the UCN density. Thus, similar to the UCN density, the pressure increase due to pulsing saturates after ~ 100 pulses (first freeze-out) and after ~ 150 pulses (second freeze-out), respectively. The reason for the later saturation after the second freeze-out is due to the by 30 mm decreased distance to the reactor core, which leads to an increased heat load. Furthermore, the increased heat load is reflected by the overall higher p_{D2} values during the second freeze-out. The dynamics of the heat load, which is characterised by a temperature increase in the nose, *i.e.,* the position of the sD_2 crystal, is depicted in Fig. A.6. At the occurrence of the reactor pulse, the nose temperature is increased to $T_{nose} \sim 25$ K before returning to thermal equilibrium ($T_{nose} \sim 5$ K) after ~ 30 s.

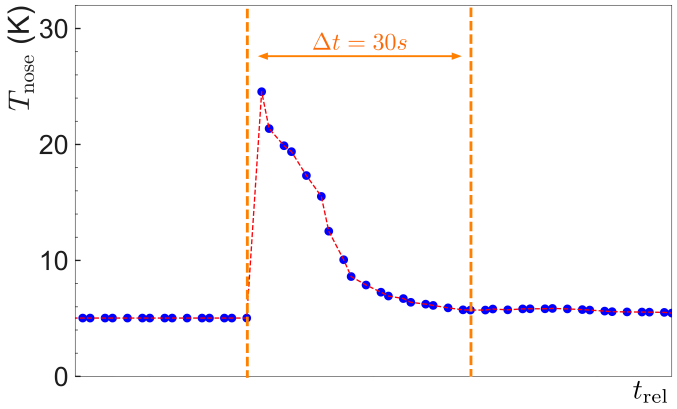

Figure A.6: Increase in nose temperature after reactor pulse. The reactor pulse (left orange dashed line) increases the local nose temperature at the position of the sD_2 crystal from $T_{nose} \sim 5$ K to ~ 25 K. After ~ 30 s, the source is in thermal equilibrium again. The red dashed line guides the eye.

To conclude, the current hypothesis states that the UCN yield increases due to reshaping effects of the sD_2 crystal, which are caused by the thermal heat load induced by the reactor pulses. After ~ 150 pulses, the reshaping represented by no more changes in Δp_{D2} stops, leading to a saturating UCN yield. When saturation is reached, the crystal form seems to be optimised for a effective UCN extraction from the sD_2. Dependencies on the UCN yield on thermal effects were also found at the UCN sources of Paul Scherrer Institute (PSI) and the Los Alamos National Laboratory (LANL). At both sources, which also use sD_2 as the converter material, the UCN yield decreases with the number of pulses, N_{pulse}. Thermal cycling, *i.e.,* exposing the sD_2 crystal to thermal heat, is applied to restore the source's performance at $N_{pulse} = 1$ [ABB+18]. Observations at the UCN source at North Carolina State University (NCSU) have demonstrated a decrease in optical transparency (build up of 'frost layers') after pulsing [ABB+18], which was used to model the UCN yield decrease at the PSI and LANL source. The increasing UCN yield of the Mainz source is therefore contrary to the UCN yield development at PSI and LANL.

A.4 Investigating radiation-induced para-ortho and ortho-para conversions

At the end of each beam time, the ortho and the para concentration of the solid deuterium (sD_2) converter and the solid hydrogen (sH_2) premoderator were found to be increased relative to their concentration prior to the beam time. First, the terms ortho and para concentration are explained while discussing Raman spectroscopy for the experimental determination (cf. Ch. A.4.1). Presenting common para and ortho concentrations during beam times (cf. Ch. A.4.2), the calculation of the associated conversion constants along with a comparison to literature values is provided in Ch. A.4.3. Ch. A.4.4 discusses the impact of the ortho concentration of the solid deuterium crystal during freeze-out on the UCN yield.

A.4.1 Raman spectroscopy for determination of the ortho and para concentration

In their ground state, hydrogen and deuterium molecules form a characteristic ratio in the alignment of the nuclear spins, defined by the rotational quantum number, J. The ratio in natural H_2 is ${}^3/_4$ $J = 1$ and ${}^1/_4$ $J = 0$ [Sou86]. The two spin configurations are referred to ortho-H_2 ($o(H_2)$) and para-H_2 ($p(H_2)$), respectively. In natural D_2, the ratio is defined as ${}^1/_3$ $J = 1$ (para-D_2, $p(D_2)$) and ${}^2/_3$ $J = 0$ (ortho-D_2, $o(D_2)$) [Sou86]. If hydrogen and deuterium molecules are exposed to energy in the range of several meV[4], a transition in the rotational energy levels can occur, which leads to a ortho-para transition in hydrogen and a para-ortho transition in deuterium. Possible energy contributions leading to a J transition can either stem from thermal energy, neutron scattering, or ionising radiation. In the case of ionising radiation, it is assumed that free ions and electrons are formed in the solid which transfer energy onto the individual molecules [Sou86].

The Raman spectroscopy relies on the excitation of a molecule's rotational energy states by laser light[5]. Thus, the para and ortho states of D_2 and H_2 can be identified by using a Raman spectrometer. For determining the para/ortho concentration, a $\sim 800 - 900\,\mathrm{mbar}$ sample of D_2 or H_2[6] was guided into spectrometer of type Bruker Sentinel II-532. Gas samples for the Raman spectrometer can be extracted before and after the freeze-out of the UCN-converting sD_2 crystal and the premoderating sH_2 crystal (cf. Ch. 4.2.1), which implies that para/ortho concentrations during pulsing can only be interpolated.

Fig. A.7 a) shows the resulting Raman spectrum of D_2. The peak structure representing the different rotational quantum numbers J can be clearly identified. In case of D_2, the ortho-calibration is determined by calculating the areas under the $J = 1$ (para state at $d_{\mathrm{Raman}} \sim 297\,\mathrm{cm}^{-1}$) and $J = 0$ (ortho state at $d_{\mathrm{Raman}} \sim 179\,\mathrm{cm}^{-1}$) peaks[7].

As demonstrated in Fig. A.7 b), the areas under the peaks (I_p for para state and I_o for ortho state) are extracted from a Gaussian fit to the data. With the calibration factor k, the ortho content in D_2, c_{o}, is calculated[8]:

$$c_o = \frac{1}{1 + \frac{k \cdot I_{\mathrm{p}}}{I_{\mathrm{o}}}}\,. \tag{A.3}$$

[4] For an ortho-para transition in H_2 ($J = 0 \rightarrow J = 1$), an energy of 14.5 meV is needed [GABP+15].

[5] Further details on Raman spectroscopy are given in [Sou86] and [GG89].

[6] Note that from November 2016 onwards, 5 % D_2 has been admixed to the H_2 used for the freeze-out of the premoderator.

[7] For hydrogen, the para content is inferred from $J = 0$ (para state at $d_{\mathrm{Raman}} \sim 354\,\mathrm{cm}^{-1}$) and $J = 1$ (ortho state at $d_{\mathrm{Raman}} \sim 587\,\mathrm{cm}^{-1}$).

[8] The equation is based on theory found in [Sil80, Lau10].

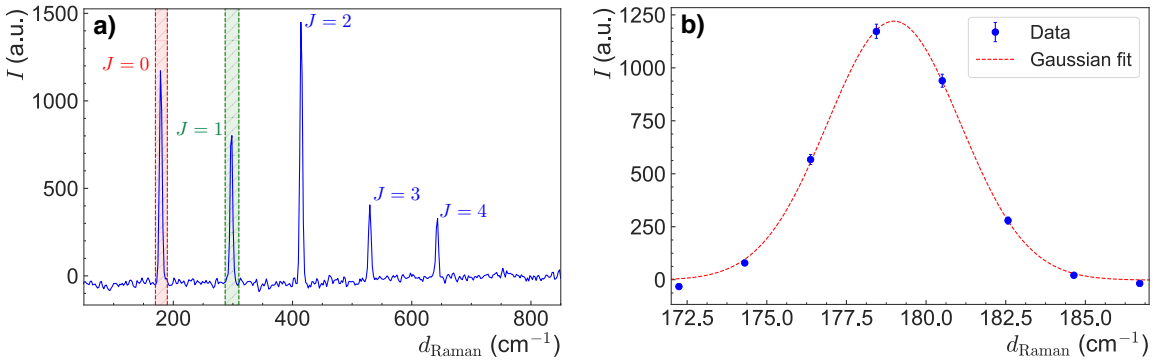

Figure A.7: Raman spectrum of deuterium (D_2) and Gaussian fit for determining the ortho concentration (c_o). (a) The Raman shift d_{Raman} as a function of intensity, I. For even rotational quantum number J, D_2 is in the ortho state, while para states are characterised by an uneven J value. For the determination of c_{o}, the areas under the peaks representing the rotational quantum states $J = 0$ (red shaded area at $d_{\mathrm{Raman}} \sim 179\,\mathrm{cm}^{-1}$) and $J = 1$ (green shaded area at $d_{\mathrm{Raman}} \sim 297\,\mathrm{cm}^{-1}$) are taken into account. (b) Due to the limited resolution of the spectrometer, the data in these regions (blue data points) is fitted by a Gaussian function, from which the area is extracted by the fit routine (red dashed line) relying on a Gaussian distribution.

Likewise, the para content in H_2, c_p, results from

$$c_p = \frac{1}{1 + \frac{k \cdot I_{\mathrm{o}}}{I_{\mathrm{p}}}} \,. \tag{A.4}$$

Associated errors were computed by performing a Gaussian error propagation on the errors of I_{o} and I_{p}, respectively. The errors resulted from the fit routine, which was implemented in the data analysis framework CERN ROOT v5.34/37.

Setting Eq. (A.3) equal to the theoretical value of $^2/_3$, the calibration factor k can be inferred, yielding

$$k = 0.724(25) \,. \tag{A.5}$$

The value is thus slightly shifted from the 2010 value ($k = 0.76$ [Lau10]), which might be due to aging processes of the spectrometer's components. The updated calibration factor has been applied to all analyses discussed in this work.

A.4.2 Para and ortho concentrations during beam times

The determination of the para/ortho concentrations was only possible until July 2018 due to a defect of the Bruker Sentinel II-532 spectrometer during the November 2018 beam time. Note that under normal conditions, D_2 is converted to a high ortho concentration at the beginning of the beam time prior to freeze-out of the sD_2 crystal. The para-ortho conversion is performed by using Oxisorb®[9], which catalyses the para-ortho conversion due to its paramagnetism. Unlike D_2, H_2 is filled in in its current para concentration, which initial concentration thus differs in-between beam times.

[9]The gas purification system Oxisorb® consists of silica gel and chromium oxide [mes18] and is produced by Messer Industriegase GmbH, `https://www.messer.de`.

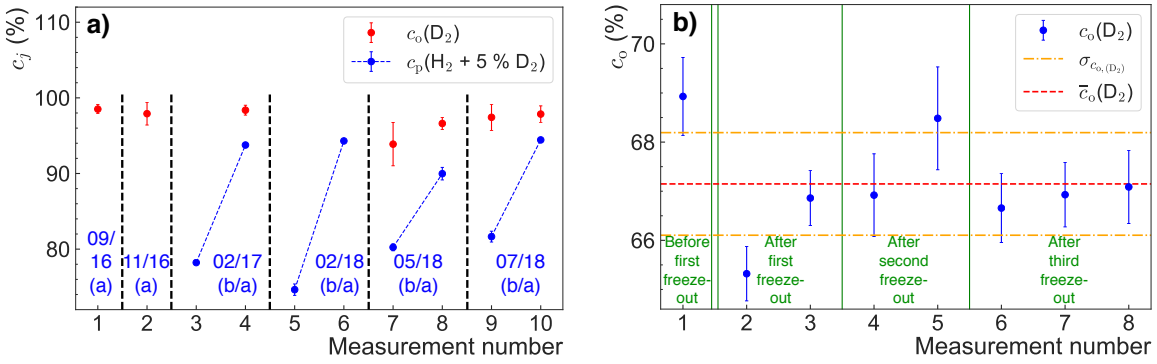

Figure A.8: Para and ortho concentration of deuterium (D_2) and hydrogen (H_2) during selected beam times and influence of the freeze-out procedure on the deuterium ortho concentration. (a) Para and ortho concentrations c_j with $j = o, p$ for ortho ($j = o$, red data points) and para concentration ($j = p$, blue data points) for various beam times. The blue dashed lines demonstrate the increasing premoderator para concentration before and after a beam time (b/a). The vertical black dashed lines segment the values of different beam times. (b) The D_2 ortho concentration, $c_o(D_2)$, before and after three consecutive freeze-out procedures within two days without the presence of reactor pulses. Multiple data points during one condition (segmented by vertical black lines) refer to re-measurements within short time spans. The mean $\bar{c}_o(D_2)$ is given by the horizontal red dashed line, while $\sigma_{c_{o,(D2)}}$ denotes the standard deviation (orange dashed horizontal line). It agrees well with the D_2 ortho concentration at room temperature, *i.e.*, $c_o(D_2) = {}^2/_3$ [Sou86]. Within the frozen-out sD_2 crystal, the para-ortho conversion is described by a time constant of $\tau_{\text{natural, D2}} = 1900\,\text{h}$ (assuming a temperature of 4.2 K [Sou86]).

Fig. A.8 a) shows the ortho concentration of D_2, which has been fairly stable throughout beam times to - despite one outlier in May 2018 - reach the goal of an ortho concentration $c_o(D_2) \geq 98\,\%$ in the sD_2 crystal for an efficient UCN downscattering process (cf. Ch. A.4.3). Furthermore, no significant change can be seen when determining c_o before and after the beam time - therefore the exposure of the sD_2 crystal to reactor pulses does not affect $c_o(D_2)$. The result of another important investigation is shown in Fig. A.8 b), for which non-converted D_2 was filled into the gas system. Without any exposure to reactor pulses, the sD_2 crystal was frozen out three times within two days. The plot clearly demonstrates that the freeze-out procedure does not impact the $c_o(D_2)$ concentration, with the measured values agreeing with the concentration at room temperature, *i.e.*, $c_o(D_2) = {}^2/_3$ [Sou86]. At a temperature $T = 4.2\,\text{K}$, which is close to the conditions in the sD_2 crystal, the para-ortho conversion would be described by a time constant $\tau_{\text{natural, D2}}$ [Sou86] (cf. Ch. A.4.3).

Returning to the para-concentration of H_2 as depicted in Fig. A.8 a), a ortho-para conversion can be clearly measured, which at first sight is proportional to the number of pulses the sH_2 premoderator is exposed to. Since the number of pulses is also correlated to the lifetime of the sH_2 premoderator, it had to be found out whether the conversion results from natural conversion or reactor pulse-induced processes.

A.4.3 Calculation of conversion constants

In the following, a detailed analysis is presented to determine whether the observed para-ortho and ortho-para conversions in D_2 and H_2 during beam times are invoked by reactor pulse-induced processes. Besides production of free ions and electrons due to ionising radi-

ation [Sou86], the solid D_2 (sD_2) and sH_2 crystals are also exposed to a rapidly increasing thermal heat during a reactor pulse, which in case of D_2 is reflected in the observed pressure increase (cf. Ch. A.3).

The required ortho concentration for D_2 was obtained from performing a Raman spectroscopy at the beginning and at the end of the February 2018 beam time, during which the ortho D_2 concentration, $c_o(D_2)$, initially was in its natural state of $^2/_3$. In total, the sD_2 crystal was exposed to $N_{\text{pulse}} = 194$ reactor pulses in the February 2018 beam time within $\Delta t_{\text{conv}} = 243\,\text{h}$[10]. For the investigation of the ortho-para conversion in H_2, the para concentration, $c_p(H_2)$, was slightly above its natural state of $^1/_4$ at the beginning of the beam time. While the time between the Raman measurements was comparable for H_2 ($\Delta t_{\text{conv}} = 237\,\text{h}$), it was exposed to $N_{\text{pulse}} = 245$ pulses in November 2016.

It is important to note that both D_2 and H_2 undergo natural conversion processes. At a temperature of 4.2 K, D_2 converts from para into ortho state within $\tau_{\text{natural, D2}} = 1900\,\text{h}$, while the ortho-para conversion in H_2 is significantly faster with $\tau_{\text{natural, H2}} = 135\,\text{h}$ [Sou86]. Consequently, assuming exponential saturation, the conversion process can be modelled by the following equation,

$$c_j(\Delta t_{\text{conv}}) = c_{\text{final}} + (c_j(\Delta t_{\text{conv}}) - c_{\text{final}}) \cdot \exp\left(-\Delta t_{\text{conv}}/\tau_{\text{natural, }k}\right) \,, \tag{A.6}$$

with para/ortho concentration as a function of conversion time, $c_j(\Delta t_{\text{conv}})$ ($j = o, p$), ortho/para concentration in final state, $c_{\text{final}} \equiv 1$, and natural conversion constant $\tau_{\text{natural, }k}$ ($k = D_2, H_2$).

To calculate the conversion constants τ_k ($k = D_2, H_2$) from the measurement data, the same model can be used. With para/ortho concentration as a function of pulse number, $c_j(N_{\text{pulse}})$ ($j = o, p$), the equation reads as follows:

$$c_j(N_{\text{pulse}}) = c_{\text{final}} + (c_j(N_{\text{pulse}} = 0) - c_{\text{final}}) \cdot \exp\left(-N_{\text{pulse}}/\tau_k\right) \tag{A.7}$$

The respective conversion constants,

$$\tau_k(N_{\text{pulse}}) = \frac{N_{\text{pulse}}}{\ln\left(\frac{c_j(N_{\text{pulse}}=0) - c_{\text{final}}}{c_j(N_{\text{pulse}}) - c_{\text{final}}}\right)} \,, \tag{A.8}$$

could then be extracted from fitting Eq. A.7 to the measured data, while associated errors were computed according to Gaussian error propagation.

The experimental results for the conversion of sD_2 and sH_2 in comparison with the associated natural conversion processes are depicted in Fig. A.9 (a) and (b), respectively. Deuterium was freshly filled into the gas system. Thus, the initial deuterium ortho concentration was $c_o(D_2) = 66.67(77)\,\%$. After exposing the sD_2 crystal to 194 reactor pulses, the measured concentrations were $c_o(D_2) = 73.01(35)\,\%$. According to Eq. A.8, the experimentally deduced conversion constant for the para-ortho conversion in sD_2 in units of pulse number, N_{pulse}, is $\tau_{D_2}(N_{\text{pulse}}) = 919.05(115.56)$. Since the $c_o(D_2)$ value agrees fairly well with the predicted value assuming natural conversion (red dashed line in Fig. A.9 a), no radiation-induced conversion processes could be found. The slight deviation of $\sim 1\,\%$ from the predicted $c_o(D_2)$ value stemming from natural conversion might be due to the inaccuracy of the used $\tau_{\text{natural, D2}}$ value.

[10] The given time Δt_{conv} refers to the time span between the Raman spectroscopy measurements before freeze-out and after dewing. Therefore, the freeze-out and dewing times need to be subtracted.

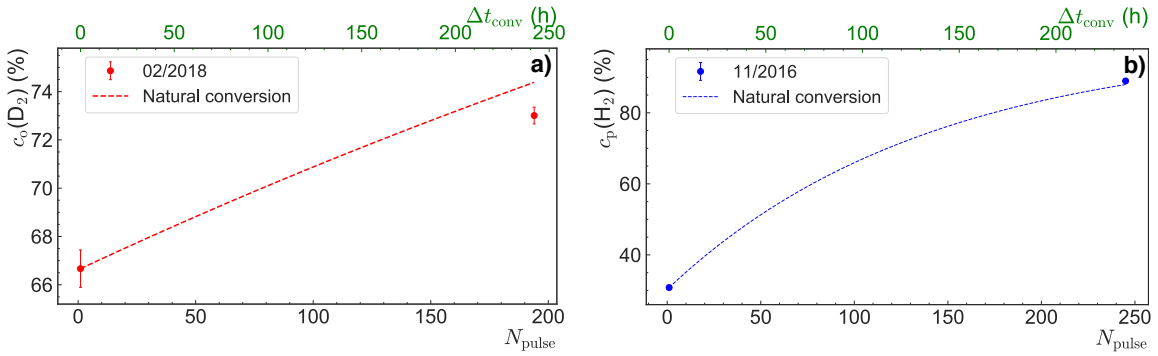

Figure A.9: Observed para-ortho conversion in deuterium and ortho-para conversion in hydrogen compared to natural conversion. (a) Ortho concentration of deuterium, $c_o(\mathrm{D_2})$, as a function of number of pulses, N_{pulse} (bottom x-axis) and as a function of conversion time, Δt_{conv}. The red dashed line represents the natural conversion according to Eq. A.6 with $\tau \equiv \tau_{\mathrm{natural,\ D2}}$. (b) Para concentration of hydrogen, $c_p(\mathrm{H_2})$, as a function of N_{pulse} and Δt_{conv}. The natural conversion is indicated by the blue dashed line ($\tau \equiv \tau_{\mathrm{natural,\ H2}}$, cf. Eq. A.6). Note the different scales on the y-axis.

For hydrogen, the initial para concentration was $c_p(\mathrm{H_2}) = 30.81(40)\,\%$, which is well above the ground state configuration. After exposure to 245 reactor pulses, the measured concentrations were $c_p(\mathrm{H_2}) = 88.97(8)\,\%$. Assuming natural conversion provides an accurate description of the observed measurement results (blue dashed line in Fig. A.9 b). Therefore, the ortho-para conversion in $\mathrm{sH_2}$ can also be explained by natural conversion. For comparison, the conversion constant in units of pulse number according to Eq. A.8 is $\tau_{\mathrm{H_2}}(N_{\mathrm{pulse}}) = 168.29(83)$.

Consequently, no radiation-induced processes leading to an accelerated para-ortho or ortho-para conversion in $\mathrm{sD_2}$ and $\mathrm{sH_2}$ could be identified. Instead, the observed conversions can be explained by natural conversion.

A.4.4 Impact on the UCN yield

Along with the experimental determination of the para-ortho conversion in solid deuterium ($\mathrm{sD_2}$) as performed in the February 2018 beam time (cf. Fig. A.9 a), the associated UCN yield has been monitored using the 'standard' beam line setup in flow mode configuration[11]. Since in regular operation, $\mathrm{D_2}$ is almost fully converted to its ortho state (initial ortho concentration $c_0(\mathrm{D_{2},}_i) \geq 98\,\%$) using OXISORB (cf. Ch. A.4.2), data from three beam times in February 2017, November 2017, and May 2018 could be used for comparison. It has to be noted that in May 2018, the para-ortho conversion has not been working reliably, yielding an initial (i) value of 93.88(2.85)%.

Fig. A.10 a) shows the that when freezing out a natural and thus non-converted $\mathrm{sD_2}$ crystal, the UCN yield is only $\sim 40\,\%$ (red data points) relative to the yield using OXISORB-converted $\mathrm{sD_2}$. Even after conversion to $c_o(t_1) = 73.01(35)\,\%$, the yield has not increased notably. Furthermore, the yield pattern which involves an initial 'dip' followed by a saturation after ≈ 150 pulses also shown in the yield developments of February and November 2017 could not be observed. As Fig. A.10 b) indicates, Monte Carlo simulations predict a yield of $\sim 77\,\%$ when using natural instead of ortho-converted $\mathrm{D_2}$. Therefore, additional

[11] The beam line setup is depicted in Fig. 4.9), with a stainless steel bottle of $\sim 10\,\mathrm{l}$ volume installed. For an explanation of the flow mode configuration in UCN measurements, refer to Ch. A.1.

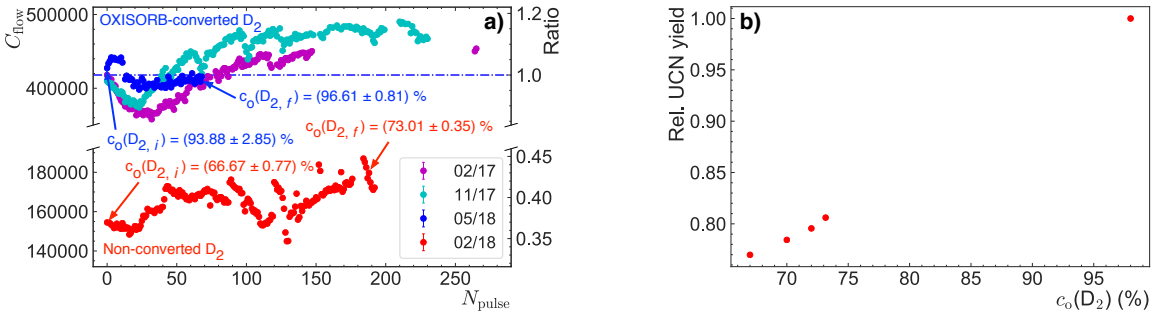

Figure A.10: UCN yield dependence on deuterium ortho concentration, $c_o(\mathrm{D_2})$. (a) UCN yield represented by counts in flow mode, C_{flow}, as a function of reactor pulse number, N_{pulse}, for different initial/final ortho concentrations, $c_o(\mathrm{D}_{2,i})/c_o(\mathrm{D}_{2,f})$. The red data points indicate the UCN yield development after freezing out the $\mathrm{sD_2}$ crystal with initial natural ortho concentration ($c_o(\mathrm{D}_{2,i}) = 66.67(77)\,\%$). Compared to the freeze-out of OXISORB-converted $\mathrm{sD_2}$, the relative UCN yield is only $\sim 40\,\%$ (blue dashed horizontal line indicates the mean value of all shown C_{flow} values measured with ortho-converted $\mathrm{sD_2}$). (b) Monte Carlo simulation of the relative UCN yield as a function of $c_o(\mathrm{D_2})$. The results predict a yield of $\sim 77\,\%$ when using natural instead of ortho-converted $\mathrm{D_2}$, which implies that additional processes decreasing the yield need to be considered.

processes such as different thermal conditions during freeze-out might lead to the larger observed decrease in the UCN yield.

A.5 Further UCN D source characterisation measurements

The following sections contain further analyses to characterise the UCN D source after its upgrade and provide supplementary information to discussions in the main part. First, the height dependence for different UCN energies and their respective maximum values are evaluated (cf. Ch. A.5.1). Consequently, the measured and simulated low-energy proportion of the stored UCN is given (cf. Ch. A.5.2). Afterwards, the reproducibility of the UCN yield is investigated (cf. Ch. A.5.3) and measurements characterising beam line elements are presented (cf. Ch. A.5.4). The next two sections deal with the effect of the solid deuterium crystal reformation on lower (cf. Ch. A.5.5) and higher UCN energies (cf. Ch. A.5.6). The last section provides the reactor pulse energy distributions of all beam times (cf. Ch. A.5.7).

A.5.1 Further measurements with the Mainz storage bottle

Further source characterisation measurements were performed using the Mainz storage bottle. It offers a storage volume of $V_{\mathrm{storage}} \sim 10\,\mathrm{l}$ and the possibility to vary the Fermi potential V_{F} from $54 - 190\,\mathrm{neV}$ (cf. Tab. A.1) by exchanging the central cylindrical tube. The used storage volumes ($\varnothing_{\mathrm{inner}} = 150\,\mathrm{mm}$ [Lau10]) include aluminium ($V_{\mathrm{F}}(\mathrm{Al}) = 54\,\mathrm{neV}$, $V_{\mathrm{storage,\,Al}} = 9.696(16)\,\mathrm{l}$), fused silica ($V_{\mathrm{F}}(\mathrm{SiO_2}) = 90\,\mathrm{neV}$, $V_{\mathrm{storage,\,SiO2}} = 10.381(15)\,\mathrm{l}$), and stainless steel ($V_{\mathrm{F}}(\mathrm{VA}) = 190\,\mathrm{neV}$, $V_{\mathrm{storage,\,VA}} = 10.227(15)\,\mathrm{l}$). To evaluate the dependence of the filling process on the storage volume, a stainless steel tube with $\varnothing_{\mathrm{inner}} = 6.6\,\mathrm{cm}$ and $l = 50\,\mathrm{cm}$ was additionally used as a storage bottle with volume $V_{\mathrm{storage,\,VA,\,small}} = 1.710(12)\,\mathrm{l}$.

The storage measurements with the Mainz storage bottle were performed and compared to data previously measured at the non-upgraded source by J. Karch. The measurement setup is shown in Fig. 4.9. Before the upgrade, a $l = 120\,\mathrm{cm}$ HE4 Nocado tube was used

($h = 116\,\mathrm{cm}$[12]), which was replaced by two HE5 Neumo tube segments with $l = l_1 + l_2 = 150 + 28\,\mathrm{cm}$ after the upgrade ($h = 155\,\mathrm{cm}$). All measurements were preceded by a filling time (t_f) optimisation, which implies a variation of t_f while storing UCN for 5 s. Deviations of only 0.5 s from the optimal filling time lead to up to 12 % decreased UCN densities (cf. Fig. A.13 b), which underlines the importance of its determination. Again, a storage time of $t_\mathrm{s} = 2\,\mathrm{s}$ was chosen.

A.5.1.1 Height dependence for different UCN energies

Before the source upgrade, an optimal height over source exit of $h = 116\,\mathrm{cm}$ was determined experimentally (cf. Fig. 3.26 in [Kar17], with $V_{\mathrm{storage,\ VA,\ small}}$), although MC simulations have pointed to an optimum height of $\sim 70 - 80\,\mathrm{cm}$ with $V_{\mathrm{storage,\ VA,\ small}}$ (cf. Fig. 3.26 in [Kar17]) and $V_{\mathrm{storage,\ VA}}$ (cf. Fig. 8 in [KSB+14]). A clear tendency to obtain higher densities at higher heights was inferred from the shifted energy spectrum caused by the ^{58}NiMo coating (cf. Ch. 4.2.2).

Fig. A.11 a) shows the ratio of the UCN yield at $t_s = 2\,\mathrm{s}$ for $h = (93, 121, 135, 155)\mathrm{cm}$[13] relative to the density measured at $h = 93\,\mathrm{cm}$. The increase in ϱ_UCN with increasing h is very striking for UCN stored in aluminium (gain factor ~ 2). For UCN stored in fused silica, a gain factor of ~ 1.55 is seen. The gain factors in both aluminium and fused silica seem to show first signs of saturation, which is more pronounced in the fused silica-stored UCN. Saturation effects stem from the increasing proportion of transmission losses at higher h levels, since longer tubes are installed in the beam line. A notably smaller gain factor (~ 1.2) was measured for UCN stored in stainless steel. Already at $h = 121\,\mathrm{cm}$, a saturation effect is clearly visible, while increasing the height to 155 cm leads to a minor gain of $\sim 5\,\%$. Due to spatial limitations in the reactor hall, mounting the storage bottles at $h > 155\,\mathrm{cm}$ was not possible. The storage curves measured at $h = 155\,\mathrm{cm}$ are depicted in Fig. A.11 b) (cf. Figs. A.12 a)/b) and A.13 a) for all individual storage curves of VA/SiO_2 and Al, respectively).

The detailed storage curves for UCN stored in Al, VA, and SiO_2 at different heights are shown in Figs. A.12 a)/b) and A.13 a). In addition, finding the optimum filling time is relevant for achieving a high UCN density. Fig. A.13 b) depicts the sensitivity of the different Mainz storage bottle configurations to variations of the filling time by $\pm 0.5\,\mathrm{s}$ for different heights over beam exit.

A.5.1.2 Maximum UCN densities

In the following discussion, the UCN densities with the Mainz storage bottle with different Fermi potentials have been evaluated and compared to data before the source upgrade. Tab. A.2 gives the results on the achieved UCN densities for $t_\mathrm{s} = 2\,\mathrm{s}$ after the upgrade ($h = 155\,\mathrm{cm}$, $d_{\mathrm{core,\ I}}$) compared to the non-upgraded source ($h = 116\,\mathrm{cm}$, $d_{\mathrm{core,\ II}}$). For $V_{\mathrm{storage,\ VA}}$, a ~ 2.9 times higher UCN density is achieved for the upgraded source. The gain factor reduces to ~ 1.7 when storing UCN in a smaller stainless steel volume of $V_{\mathrm{storage,\ VA,\ small}} \sim$

[12] The heights over the source exit achieved with the HE4 Nocado $l = 120\,\mathrm{cm}$ tube (surface roughness $R_\mathrm{a} \leq 0.4\,\mu\mathrm{m}$) and the HE5 Neumo tube (surface roughness $R_\mathrm{a} \leq 0.25\,\mu\mathrm{m}$) can deviate by $\pm 3\,\mathrm{cm}$.

[13] To achieve given heights relative to the source exit, a tilted HE5 Neumo tube with lengths $l = (80, 120, 150, (150 + 28))\mathrm{cm}$ were used for the beam line (cf. Fig. 4.9). The HE5 standard implies a surface roughness of $R_\mathrm{a} \leq 0.25\,\mu\mathrm{m}$.

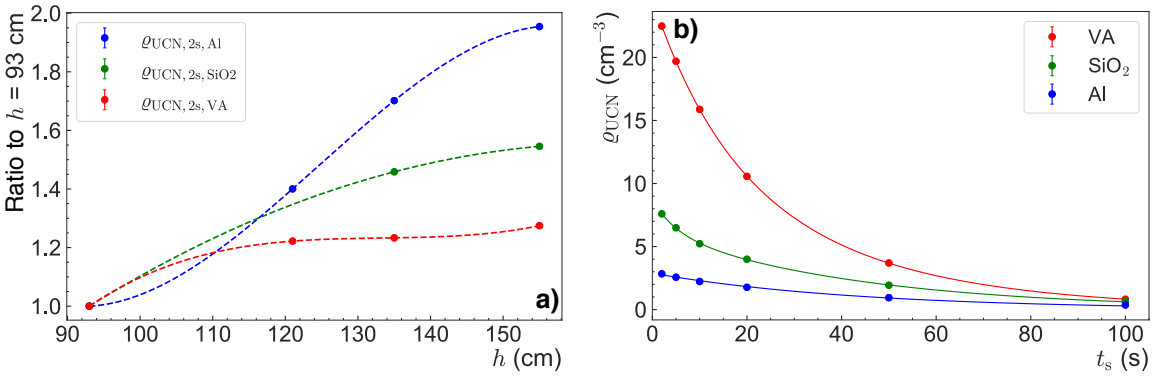

Figure A.11: Height dependence of UCN yield after upgrade and storage curve comparison Mainz storage bottle. (a) Gain in UCN density after 2 s storage time as a function of height over source exit (h) for UCN stored in $\sim$ 10 l of aluminium (Al, blue), fused silica (SiO_2, green), and stainless steel (VA, red). The dashed lines represent third-order spline fits to the data. (b) UCN density ϱ_{UCN} as a function of storage time (t_s) at $h = 155\,\mathrm{cm}$, with formerly mentioned colour coding and normalisation according to Eq. (4.8). The lines represent the biexponential fit to the data, with values $\tau_2 = 51.06(2.14)$ s, $\rho_{\mathrm{UCN,\,0\,s}} = A_1 + A_2 = 24.16(15)\,\mathrm{cm}^{-3}$ (VA), $\tau_2 = 51.23(1.31)$ s, $\rho_{\mathrm{UCN,\,0\,s}} = 8.01(9)\,\mathrm{cm}^{-3}$ (SiO_2), and $\tau_2 = 68.03(4.61)$ s, $\rho_{\mathrm{UCN,\,0\,s}} = 2.94(26)\,\mathrm{cm}^{-3}$ (Al).

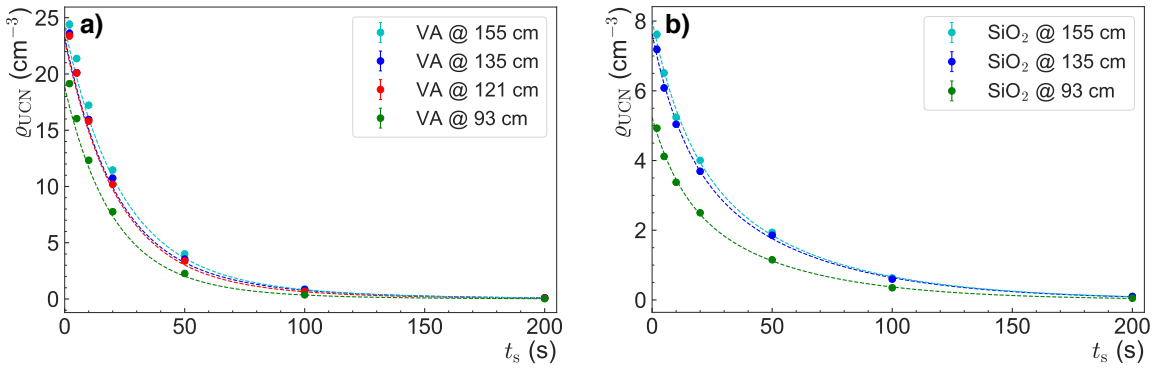

Figure A.12: Height-dependent storage curves for UCN stored in the (a) stainless steel (VA, $V_{\mathrm{storage,\,VA}} = 10.227(15)\,\mathrm{l}$) and (b) fused silica ($SiO_2$, $V_{\mathrm{storage,\,SiO2}} = 10.381(15)\,\mathrm{l}$) Mainz storage bottle. In both cases, the UCN density ϱ_{UCN} is plotted against the storage time, t_s. The measurements have been performed for different heights relative to the source exit (cf. legends).

1.71[14].

No data for UCN stored in fused silica and aluminium at the used storage volumes was available. In case of aluminium, the UCN density resulting from a 2 s storage measurement with a storage volume of 3.420(12) l was considered. The value was first scaled with volume

[14] With the non-upgraded source, a capture efficiency $\varepsilon_{\mathrm{capture}}$ of 54 % was measured for $V_{\mathrm{storage,\,VA}}$, which decreased by a factor of 2 to 27 % for $V_{\mathrm{storage,\,VA,\,small}}$ (cf. Tab. 3.11 in [Kar17]). The UCN capture efficiency is defined by the ratio between stored UCN in storage mode (C_{UCN}) and UCN in flow mode (C_{flow}): $\varepsilon_{\mathrm{capture}} = C_{\mathrm{UCN}}/C_{\mathrm{flow}}$. The result for $\varrho_{\mathrm{UCN,\,VA,\,2\,s}}$ in $V_{\mathrm{storage,\,VA,\,small}}$ and the non-interpolated value of $\varrho_{\mathrm{UCN,\,Al,\,2\,s}}$ is found in [Kar17].

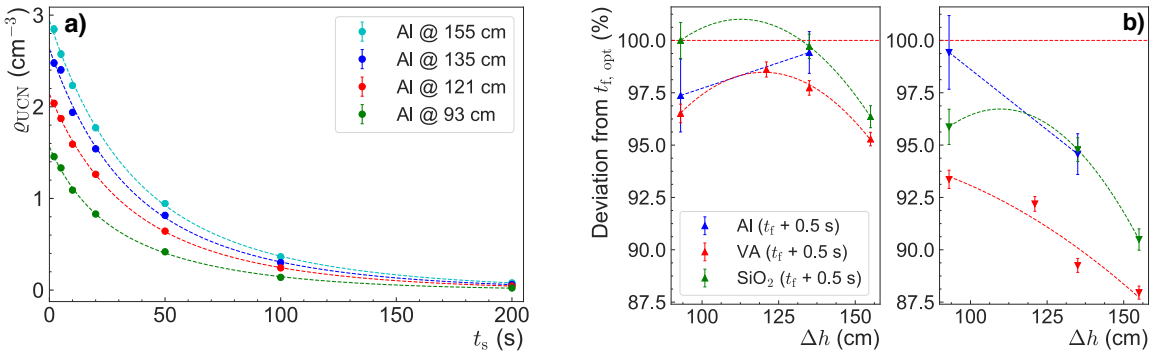

Figure A.13: Height-dependent storage curves for UCN stored in the aluminium (Al, $V_{\text{storage, Al}} = 9.696(16)\,\text{l}$) Mainz storage bottle and sensitivity to filling time. (a) UCN density ϱ_{UCN} as a function of storage time, t_s and for different heights relative to the source exit, Δh (cf. legend). (b) Deviations in the measured UCN density at $t_s = 2\,\text{s}$ if selecting a filling time t_f 0.5 s longer (left subplot) or shorter (right subplot) as the optimum filling time. The measurement results are plotted as a function of Δh.

Table A.2: Comparison of achieved UCN densities stored in the Mainz storage bottle ($V_{\text{storage, VA}} \sim 10\,\text{l}$ if not indicated otherwise) with different Fermi potential (vertical extraction mode). The measured UCN densities ϱ_{UCN} before (height over source exit $h = 116\,\text{cm}$) and after the upgrade ($h = 155\,\text{cm}$) were compared for storage times of 2 and 20 s in aluminium (Al), fused silica (SiO_2), and stainless steel (VA). For the third column, the used filling time is given in brackets. The first row always contains the UCN density normalised to a pulse energy of 10 MW s, while in case of the upgraded source, the second row provides the value according to the renewed normalisation procedure (cf. Eq. (4.8)). The results for the upgraded source were measured after the UCN yield had saturated (cf. Ch. A.3). The asterisk (∗) indicates an interpolated value.

UCN density	Before upgrade ($h = 116\,\text{cm}$)	After upgrade ($h = 155\,\text{cm}$)	Ratio
$\varrho_{\text{UCN, VA, 2 s}}$	$8.06(3)\,\text{cm}^{-3}$	$23.26(31)\,\text{cm}^{-3}$ (2.5 s) $22.56(31)\,\text{cm}^{-3}$	2.89(1)
$\varrho_{\text{UCN, VA, 2 s}}$ ($\sim 1.7\,\text{l}$)	$23.75(12)\,\text{cm}^{-3}$	$40.55(15)\,\text{cm}^{-3}$ (2.0 s) $38.24(15)\,\text{cm}^{-3}$	1.71(1)
$\varrho_{\text{UCN, Al, 2 s}}$	$1.09(16)\,\text{cm}^{-3}$ (∗) $0.32(5)\,\text{cm}^{-3}$	$3.03(4)\,\text{cm}^{-3}$ (3.0 s) $2.85(4)\,\text{cm}^{-3}$	$\sim 2.78(15)$
$\varrho_{\text{UCN, SiO2, 2 s}}$	/ /	$8.02(10)\,\text{cm}^{-3}$ (3.0 s) $7.62(10)\,\text{cm}^{-3}$	/

(scaling factor $k_{\text{scale, Al}} = 3.41(14)$). Also, a 20(5) % improved value for the capture efficiency $\varepsilon_{\text{capture}}$ was taken into account (cf. Tab. 3.11 in [Kar17]), giving an interpolated density of $\varrho_{\text{UCN, Al, 2 s}} = 1.09(16)\,\text{cm}^{-3}$. Thus, an interpolated gain factor of ~ 2.8 was found.

Over all measurements, smaller gain factors than measured with the $\sim 32\,\text{l}$ PSI storage bottle (gain factor 3.51(2)) have been obtained. A possible reason for the observation might be an increasing UCN capture efficiency at higher storage volumes, which has been analysed with the non-upgraded source in [Kar17]. Moreover, the similar gain factor for UCN stored in aluminium and stainless steel along with the constant h/v ratio for different storage

volumina (cf. Fig. A.14 b), are clear indicators for an unchanged energy spectrum.

A.5.2 Low-energy part of the UCN spectrum

The low-energy UCN proportion is an important parameter for describing the energy spectrum of a UCN source. Using a CASCACE neutron detector with its aluminium entrance window (cf. Ch. A.1) and storing the UCN in a stainless steel bottle, a distinction between UCN of minimum/maximum energies $E_{\mathrm{UCN,\,min,\,h}} \geq V_{\mathrm{F}}(\mathrm{Al}) = 54\,\mathrm{neV}$ / $E_{\mathrm{UCN,\,max,\,h}} \leq V_{\mathrm{F}}(\mathrm{VA}) = 190\,\mathrm{neV}$[15] (horizontal h extraction with UCN density $\varrho_{\mathrm{UCN,\,h}}$) and $E_{\mathrm{UCN,\,min,\,v}} = 0\,\mathrm{neV}$ / $E_{\mathrm{UCN,\,max,\,v}} \equiv E_{\mathrm{UCN,\,max,\,h}}$ (vertical v extraction with $\varrho_{\mathrm{UCN,\,v}}$) can be made. The low-energy proportion referring to $E_{\mathrm{UCN}} < 54\,\mathrm{neV}$ thus follows by

$$E_{\mathrm{UCN,\,low}} = 1 - (\varrho_{\mathrm{UCN,\,h}}/\varrho_{\mathrm{UCN,\,v}}) \;; \tag{A.9}$$

it can be determined for different storage times t_{s}, and storage volumes, V_{storage}. Throughout all measurements, the 'standard' beam line (cf. Fig. 4.9) was used.

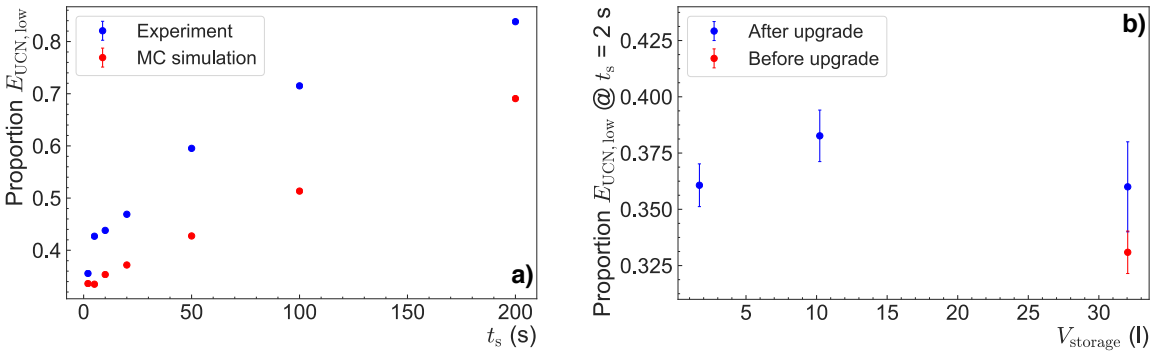

Figure A.14: Low-energy UCN proportion $E_{\mathrm{UCN,\,low}}$ as a function of storage time, t_{s}, and storage volume, V_{storage}. (a) $E_{\mathrm{UCN,\,low}}$, calculated according to Eq. (A.9) for the $\sim 32\,\mathrm{l}$ PSI storage volume, as a function of t_{s}. The experimental data represented by the blue data points is compared to the results from a Monte Carlo (MC) simulation (red data points). (b) $E_{\mathrm{UCN,\,low}}$ as a function of V_{storage} for $t_{\mathrm{s}} = 2\,\mathrm{s}$. The blue data points refer to the measured $E_{\mathrm{UCN,\,low}}$ values after the upgrade of the UCN source. For $V_{\mathrm{storage}} \sim 32\,\mathrm{l}$ (PSI storage volume), $E_{\mathrm{UCN,\,low}}$ has also been determined prior to the upgrade (red data point).

Fig. A.14 a) depicts the increase in $E_{\mathrm{UCN,\,low}}$ for larger storage times t_{s}, which implies that the UCN spectrum becomes increasingly low-energetic with increasing t_{s} due to energy-dependent loss mechanisms[16]. The deviations between the Monte Carlo (MC) data and the measured data becomes apparent at $t_{\mathrm{s}} > 2\,\mathrm{s}$, which indicates that the simulation does not fully account for the loss mechanisms. Moreover, $E_{\mathrm{UCN,\,low}}$ stays constant for different storage volumes (cf. Fig. A.14 b). Lastly, $E_{\mathrm{UCN,\,low}}$ has not significantly changed after upgrading the UCN D source.

A.5.3 Reproducibility of the UCN yield

In the following, the UCN yield after the source has reached saturation are compared for the same setups during different beam times. Observed fluctuations might *e.g.* occur due

[15] The terms $V_{\mathrm{F}}(\mathrm{Al})$ and $V_{\mathrm{F}}(\mathrm{VA})$ represent the Fermi potentials of aluminium and stainless steel, respectively. For an overview over all relevant Fermi potentials, refer to Tab. A.1.

[16] For more insights on UCN loss mechanisms during storage in material bottles, consider [GRL91].

to differences in the freeze-out procedure of both the sH_2 and the sH_2 crystals as well as a non-constant UCN transmission resulting from the beam line being entirely rebuilt for each beam time.

The superposition of all mentioned effects gives the overall UCN yield reproducibility. The used setup was the Mainz storage bottle with the 'standard' beam line (cf. Fig. 4.9) at height $h = 135\,\mathrm{cm}$ over source exit. The UCN were stored for 2 s in a stainless steel (VA, for higher-energetic UCN) or aluminium (Al, for lower-energetic UCN) bottle. For comparison, $N = 2$ measurements were taken with the source in saturation (VA: measurement after number of pulses $N_{\mathrm{pulse}} > 200$, Al: $N_{\mathrm{pulse}} > 150$[17]).

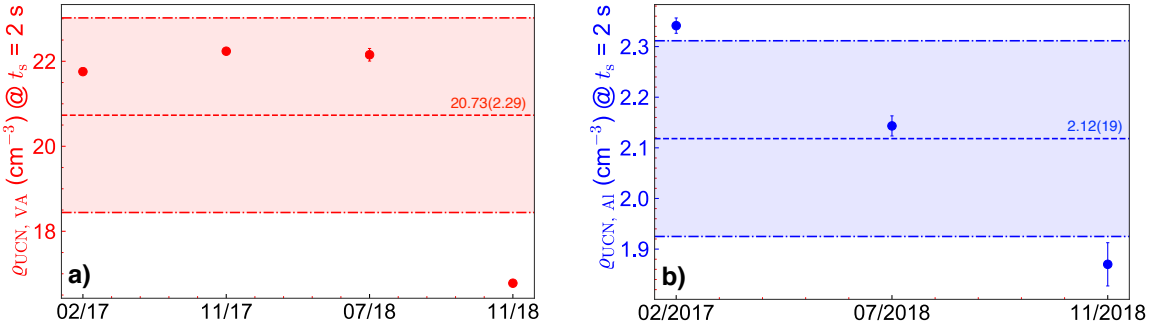

Figure A.15: Reproducibility of UCN densities at $t_s = 2\,\mathrm{s}$ storage time stored in the stainless steel ($\rho_{\mathrm{UCN,\,VA}}$) and the aluminium Mainz storage bottle ($\rho_{\mathrm{UCN,\,Al}}$). For the measurements, a height of $h = 135\,\mathrm{cm}$ was chosen. (a) The UCN densities stored in stainless steel (red data points) fluctuate on average by $\sim 11\,\%$ across 4 beam times (mean given by red dashed line, standard deviation represented by dash-dotted line: $\overline{\varrho}_{\mathrm{UCN,\,VA}} = 20.73(2.29)\ \mathrm{cm}^{-3}$). (b) The UCN densities after storage in aluminium (blue data points, $\overline{\varrho}_{\mathrm{UCN,\,Al}} = 2.12(19)\,\mathrm{cm}^{-3}$) show an average fluctuation of $\sim 9\,\%$.

The fluctuations in the UCN densities (ϱ_{UCN}) across beam times are shown in Fig. A.15 a) for 2 s storage time in stainless steel and b) in aluminium. Stored in a stainless steel bottle, $\varrho_{\mathrm{UCN,\,VA}}$ fluctuates by $\sim 11\,\%$ on average. The average fluctuations for UCN stored in aluminium are comparable ($\sim 9\,\%$). With regards to peak-to-peak fluctuations in one beam time, both show again similar fluctuations of $\sim 25\,\%$. When the UCN yield has saturated after $N_{\mathrm{pulse}} > 150$, observed average fluctuations are $\mathcal{O}(1-2\,\%)$ (cf. Figs. A.4 b, A.18). These fluctuations are in line with the fluctuating reactor pulse energy.

A.5.4 Beam line characterisations

The position of τSPECT within the reactor hall and its 90° orientation to the output tube of the UCN D source give stringent geometric constraints to the beam line design. Keeping these constraints in mind, several relevant measurements to find the optimum beam line for the geometric conditions (cf. Ch. A.5.4) were performed. Moreover, the final beam line used for τSPECT experiment has been characterised (cf. Ch. A.5.4).

Influence of beam line radii

One parameter which had to be optimised was the dependence of UCN transmission on the beam line radii. Former measurements relying on either flow mode or storage in stainless steel bottles preferred large beam line radii (typically, $r_{\mathrm{entry}} = 80\,\mathrm{cm}$ and $r_{\mathrm{top}} = 40\,\mathrm{cm}$ was

[17] No comparison data with higher N_{pulse} was available for UCN stored in aluminium.

used for the source characterisations [KRR+17]). This assumption was based on earlier characterisation measurements with the UCN source before its upgrade. To systematically check the impact of the beam line radii, a simple measurement setup was constructed, in which the neutron guide forms an 'S-shape' which allows for exchanging the entry and top radii while keeping the height relatively constant ($h_{\text{flow}} = 1.26(3)$ m for the flow mode measurements and $h_{\text{storage}} = 1.35(5)$ m for the storage measurements). The commercial CASCADE detector for UCN detection[18] was either directly connected to the top bend ('flow mode' configuration) or plugged into the 'waterfall tube' when pre-storing the UCN in an aluminium bottle. The beam line configurations are shown in Fig. A.16 a) and b).

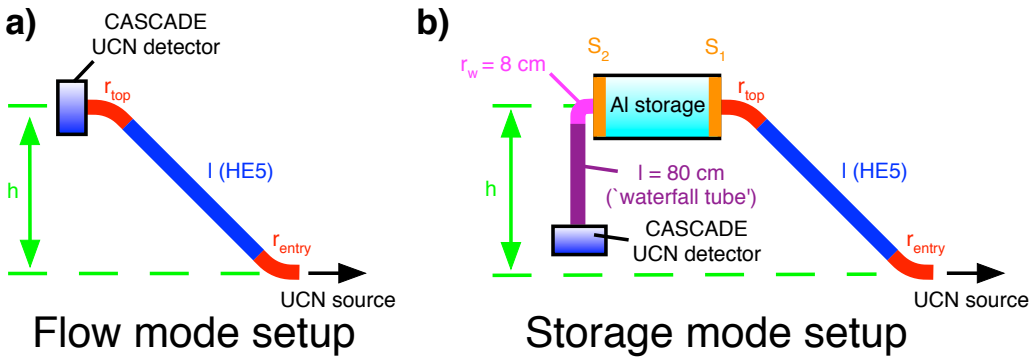

Figure A.16: Measurement setup for radius-dependent UCN transmission and final beam line. (a) In flow mode, the CASCADE was immediately connected to the last bend of the 'S-shaped' beam line with radius $r_{\text{top}} = 40\,\text{cm} = \text{const.}$, while r_{entry} was varied between measurements. To keep the height h constant at a ± 0.03 m level, l was adapted. (b) In storage mode, the UCN were stored in the aluminium bottle for 2 s and then counted by passing the 90° bend with $r_{\text{w}} = 8\,\text{cm} = \text{const.}$ connected to the 'waterfall' tube. Both r_{entry} and r_{top} were varied; h was kept constant at a level of ± 0.05 m through the adaption of l.

Fig. A.17 a) shows an improved transmission for larger entry radii for high-energetic UCN and VCN passing the neutron guide and being detected in flow mode[19]. Increasing r_{entry} from 25 cm to 80 cm leads to $\sim 25\,\%$ more UCN/VCN passing the beam line (cf. Fig. A.17 a). The top radius remained constant at $r_{\text{top}} = 40$ cm, with resulting height differences compensated by using different tube lengths in-between the bends.

Since τSPECT can only store UCN with energies ≤ 47 neV and the aforementioned spectrum measured in flow mode measurement contains non-storable UCN, beam line characterisations with storage of UCN in an aluminium bottle ($E_{\text{UCN}} \leq V_{\text{F}}(\text{Al}) = 54$ neV, $V_{\text{storage, Al}} = 9.696(16)$ l) were carried out. As opposed to the flow mode measurements, optima were found for $r_{\text{entry}} = 25$ cm and $r_{\text{top}} = 40$ cm ($r_{\text{top}} = \text{const.} = 40$ cm, cf. Fig. A.17 b), $r_{\text{entry}} = \text{const.} = 25$ cm, cf. Fig. A.17 c)). The short storage time of $t_{\text{s}} = 2$ s already ensures a cleaned spectrum, *i.e.,* no UCN with energies above $V_{\text{F}}(\text{Al}) = 54$ neV are present in the stored spectrum. This is due to the high surface roughness of the used aluminium

[18] For additional details on the CASCADE detector, refer to Ch. A.1.

[19] No clear distinction between UCN and VCN can be made in flow mode, since very cold neutrons (VCN) with energies $\gtrsim 350$ neV also contribute to the integral counts, C_{flow} (cf. Ch. A.5.6). Thus, aluminium storage bottle measurements providing defined UCN energies are additionally required.

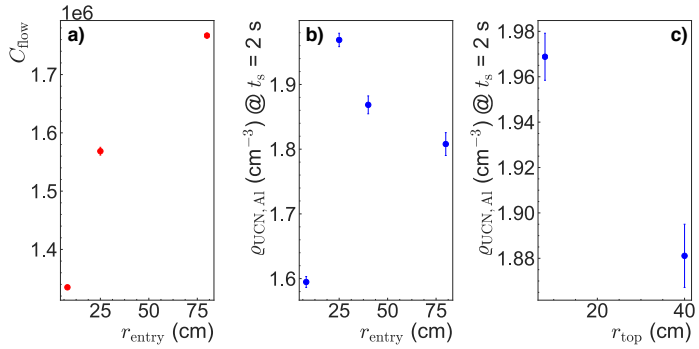

Figure A.17: UCN transmission and storage depending on beam line radii, with number of UCN in flow mode (C_{flow}) and UCN density stored in an aluminium bottle, $\varrho_{\mathrm{UCN,\,Al}}$. (a) In the flow mode measurement, the number of transmitted UCN significantly increases with larger entry radii r_{entry}. (b) This is not the case for low-energetic UCN, in which an optimum was found for $r_{\mathrm{entry}} = 25\,\mathrm{cm}$. (c) The favouring of smaller radii due to less transmission distance for low-energetic UCN is also reflected in the optimum at $r_{\mathrm{top}} = 8\,\mathrm{cm}$. In a) and b), $r_{\mathrm{top}} = 40\,\mathrm{cm} = \mathrm{const.}$, and in c), $r_{\mathrm{entry}} = 25\,\mathrm{cm} = \mathrm{const.}$ Heights were $h_{\mathrm{flow}} = 1.26(3)\,\mathrm{m}$ for a) and $h_{\mathrm{storage}} = 1.35(5)\,\mathrm{m}$ for b) and c).

storage bottle[20], which leads to the UCN being dominantly diffusely reflected off the aluminium walls, with a high loss probability at each wall collision μ [GRL91]. Thus, UCN with energies $> V_{\mathrm{F}}(\mathrm{Al})$, which corresponds to a velocity $\gtrsim 3.2\,\mathrm{m\,s^{-1}}$, are exposed to $\gtrsim 6$ collisions per second[21]. The cleaned spectrum also allows for using a simple exponential fit function for describing the stored spectrum - a biexponential fit taking higher-energetic, *i.e.,* non-cleaned, UCN into account (cf. Ch. A.1) is not required.

Comparison with height-optimised standard beam line

A comparison measurement to the 'standard' beam line at the previously-optimised height ($h_{\mathrm{opt}} = 1.53\,\mathrm{m}$, cf. Ch. 4.4.1) was made. The 'standard' beam line is 'S-shaped', with $r_{\mathrm{entry}} = 80\,\mathrm{cm}$, $l = l_1 + l_2 = 150\,\mathrm{cm} + 28\,\mathrm{cm}$ tube and $r_{\mathrm{top}} = 40\,\mathrm{cm}$ (cf. Fig. A.16 b). Due to time limitations, no full storage curve with the τSPECT beam line was measured - instead, the UCN density in aluminium after 2 s storage time was determined. For counting, the commercial CASCADE detector was used[22].

Due to geometric constraints, the τSPECT beam line depicted in Fig. 6.10 a) is quite complex compared to the standard beam line. A 45° bend with $r = 25\,\mathrm{cm}$ is followed by two tube pieces with total length 98 cm, after which a second 45° bend with $r = 25\,\mathrm{cm}$ is placed. A vertical tube with $l = 44\,\mathrm{cm}$ is inserted, resulting in a height over source exit of $h_{\tau\mathrm{SPECT}} = 1.59\,\mathrm{m}$. A 90° bend with $r = 8\,\mathrm{cm}$ follows, which is connected to a tube with $l = 31\,\mathrm{cm}$ to connect the beam line to the τSPECT beam entry shutter. Compared

[20] The surface roughness R has not been quantitatively determined, but shows no optical specular light reflection.

[21] The given assumption of 6 collisions per second refers to UCN traveling the maximum distance within the storage bottle until reaching the wall. For the shortest available distance, the UCN are exhibited to ~ 22 collisions per second with the material wall.

[22] During the characterisation measurements of the τSPECT beam line, the CASCADE reference voltage point was set to value 100 instead of the otherwise-used value 108. According to M. Klein, the head of CDT CASCADE Detector Technologies GmbH (`http://www.n-cdt.com`), this has a negligible effect on the counting efficiency of $\leq 0.1\,\%$.

to previously used beam lines, a heavy segmentation with various changes in direction is needed, which introduces many possibilities for slids and an overall reduced transmission due to many bends.

Results show that only $\sim 40\,\%$ of the UCN reach the beam entry of τSPECT when compared to the 'standard' beam line after 2 s and 10 s storage time (cf. Tab. A.3). In flow mode, the transmission is even lower ($\sim 30\,\%$), which points to a worse transmission for higher-energetic UCN. After 2 s of storage in the aluminium volume ($V_{\text{storage, Al}} = 9.696(16)\,\text{l}$), 10 758(104) UCN were detected.

Table A.3: τSPECT-specific beam line ($h_{\tau\text{SPECT}} = 1.59\,\text{m}$) compared to 'standard' beam line at $h_{\text{opt}} = 1.55\,\text{m}$. Given are counts ($C_{\text{UCN}}$) and densities ($\varrho_{\text{UCN}}$) stored in the aluminium bottle ($V_{\text{Al}} = 9.70\,\text{l}$) for storage times $t_{\text{s}} = 2/10\,\text{s}$ and counts in flow mode, C_{flow}. The counts and densities were normalised to the average pulse energy.

Beam line	$t_{\text{s}} = 2\,\text{s}$	$t_{\text{s}} = 10\,\text{s}$	Flow mode
τSPECT (I)	$C_{\text{UCN}} = 10\,758(104)$	$C_{\text{UCN}} = 8718(93)$	$C_{\text{flow}} = 57\,738(240)$
	$\varrho_{\text{UCN}} = 1.11(1)\,\text{cm}^3$	$\varrho_{\text{UCN}} = 0.90(1)\,\text{cm}^3$	
Standard (II)	$C_{\text{UCN}} = 27\,589(166)$	$C_{\text{UCN}} = 21\,640(148)$	$C_{\text{flow}} = 190\,970(436)$
	$\varrho_{\text{UCN}} = 2.85(2)\,\text{cm}^3$	$\varrho_{\text{UCN}} = 2.23(2)\,\text{cm}^3$	
Ratio I/II	$\sim 39\,\%$	$\sim 40\,\%$	$\sim 30\,\%$

Due to the disappointing result, additional attempts should be made to build a beam line with improved UCN transmission by *e.g.* lowering the geometrical complexity, which requires purchasing additional stainless steel beam line components. As measurements have shown, an entry radius of $r_{\text{entry}} = 25\,\text{cm}$ as well as a top radius of $r_{\text{top}} = 8\,\text{cm}$ were found to offer an optimal UCN transmission.

A.5.5 Effect of crystal reformation on lower ultracold neutron energies

Using the Mainz aluminium storage volume, the yield development for lower-energetic UCN was investigated. Again, the 'standard' beam line was used (cf. Fig. 4.9). A storage time of 2 s and a height over source exit of $h = 135\,\text{cm}$ was chosen.

Fig. A.18 shows the yield development in Al. Similar to the former observations with the PSI setup, the UCN density increases, until it eventually saturates. The lack of data in-between does not permit an accurate determination of a saturation, but similar to Fig. A.4 b), it is likely to saturate around pulse number 150. Unlike the yield development observed in stainless steel storage bottles (cf. Fig. A.4 b) for PSI setup, Fig. A.5 a) for Mainz storage bottle), no initial dip is seen. Additionally, only a gain of $\sim 17\,\%$ is measured, which corresponds to less than half the gain factor observed in stainless steel. More statistics, which implies another measurement of the UCN yield curve stored in aluminium, would be needed to investigate this behaviour further and rule out effects due to a non-efficient freeze-out of the sD_2 crystal.

A.5.6 Effect of crystal reformation on higher-energetic ultracold and very cold neutrons

In the next measurement, the yield development in two different energy regimes was monitored simultaneously. For the measurement, the 'standard' beam line (cf. Fig. 4.9) was used, with the CASCADE detector connected to the 45° bend with radius 40 cm by a HE5

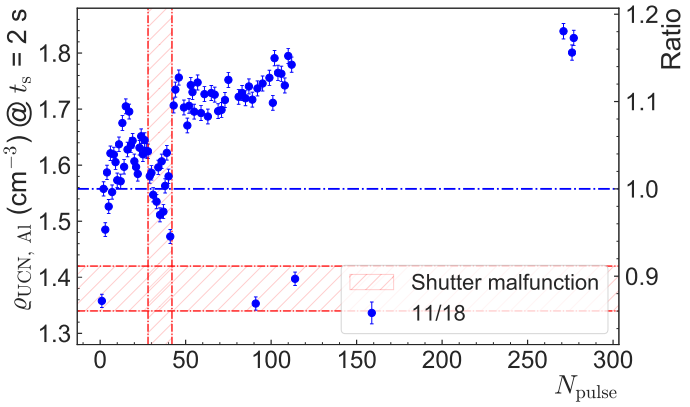

Figure A.18: UCN density $\varrho_{\mathrm{UCN,\ Al}}$ after 2 s storage in aluminium as a function of reactor pulses, N_{pulse}. Shutter malfunctions are indicated by the red areas. The blue dash-dotted line represents $\varrho_{\mathrm{UCN,\ Al}}(N_{\mathrm{pulse}} = 1)$, to which the ratio is calculated (right y-axis). The data has been normalised to the reactor pulse energy.

Neumo stainless steel tube (28 cm length, surface roughness $R_{\mathrm{a}} \leq 0.25\,\mu$m). In this configuration at $h = 135$ cm, the detector is therefore directly exposed to the UCN spectrum (flow mode measurement). To discriminate between neutron energies, two foil halves (1 μm AlMg3 and 1 μm AlMg3 coated with 400 nm NiMo 85/15) put inside a stainless steel foil holder were mounted in front of the CASCADE detector. The two foils allow for an energy discrimination: Neutrons with $E_{\mathrm{n}} > 54$ neV can penetrate through the AlMg3 foil, while only high-energetic UCN and VCN region with $E_{\mathrm{n}} > 220$ neV reach the detector when passing through the AlMg3-NiMo foil.

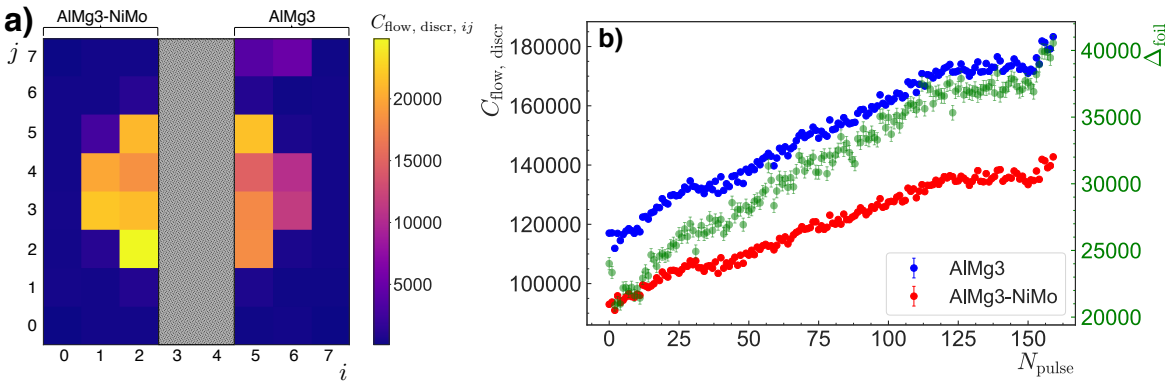

Figure A.19: Neutron transmission through AlMg3 and AlMg3-NiMo foil in comparison. (a) 8×8 pixel map of CASCADE detector, the number of detected counts is given by the colour scale right of the matrix. Due to a foil overlap, the two middle rows ($i = 3, 4$) were excluded from the analysis. (b) Number of neutrons transmitted through AlMg3 and AlMg3-NiMo foil ($C_{\mathrm{flow,\ discr}}$) as a function of reactor pulses, N_{pulse}. At $N_{\mathrm{pulse}} > 150$, the number of neutrons passing the AlMg3 foil has increased by $\sim 80\,\%$ (blue data pointss), while a gain of $\sim 50\,\%$ was measured for the transmission through the AlMg3-NiMo foil (red data points). The difference $\Delta_{\mathrm{foil}} = C_{\mathrm{flow,\ discr,\ AlMg3}} - C_{\mathrm{flow,\ discr,\ AlMg3\text{-}NiMo}}$ of both neutron counts is depicted by the green data points.

In the middle of the foil holder, the foils had a tiny overlap, which is why the two central

rows of the CASCADE 8 × 8 matrix were excluded in the data analysis (cf. Fig. A.19 a). To get rid of neutrons with high angles passing the AlMg3 foil, a neutron-absorbing pinhole aperture made of titanium with 2 mm thickness was installed before both foils, with circular openings leaving an area ∼ 70 % of each detector pixel open for neutron passage. The counts $C_{\text{flow, discr}}$ were determined by integrating the CASCADE time-of-flight files for each respective channel while subtracting the thermal peak. For detecting the neutron flow through AlMg3-NiMo, the three leftmost columns were used. The three rightmost columns were used in case of AlMg3. Summing over the integrals of all relevant channels, the number of counts $C_{\text{flow, discr}}$ were determined. The difference between both integral counts, $\Delta_{\text{foil}} = C_{\text{flow, discr, AlMg3}} - C_{\text{flow, discr, AlMg3-NiMo}}$, carries information about neutrons with energies $54\,\text{neV} \leq E_{\text{UCN}} \leq 220\,\text{neV}$. The ratio of Δ_{foil} to $C_{\text{flow, discr, AlMg3}}$ gives the ratio of neutrons in aforementioned energy interval relative to the total number of neutrons with $E_{\text{n}} \geq 220\,\text{neV}$ reaching the detector.

The yield development of the neutrons transmitted through both foils is depicted in Fig. A.19 b). Similar to prior observations, the number of neutrons increases with pulsing. While at $N_{\text{pulse}} = 150 \sim 80\,\%$ more neutrons pass the AlMg3 foil, the respective increase in neutrons penetrating the AlMg3-NiMo foil is ∼ 50 %. In principle, two conclusions can be drawn from the measurement. First, despite an approximately constant thermal flux (cf. Ch. 4.2.3), the overall number of neutrons increases on average. The increase is more prominent for neutrons with energies ≤ 220 neV, which is another indication for the UCN yield changing due to crystal reformation effects. Second, at the entry of the storage bottle, the proportion of neutrons with energies > 220 neV is ∼ 4.5 higher than UCN with $54\,\text{neV} \leq E_{\text{UCN}} \leq 220\,\text{neV}$. Assuming a $E_{\text{UCN}}^{3/2}$ dependency [GRL91], this factor translates into neutrons with an average energy of ∼ 350 neV reaching the detector after the standard 'S-shaped' beam line with two 45° bends of radii $r_{\text{entry}} = 80\,\text{cm}$ and $r_{\text{top}} = 40\,\text{cm}$ (cf. Fig. 4.9). This is an experimental proof for the presence of high-energetic UCN and VCN ($E_{\text{VCN}} \gtrsim 350\,\text{eV}$) in the Maxwellian-distributed spectrum after the source upgrade, which should be taken into account when analysing flow-mode measurements.

A.5.7 Pulse energy distributions of all beam times

The reactor pulse energy for 2 $ pulses is relevant for the UCN production, since it is directly proportional to the thermal neutron flux impinging on the UCN D source's solid hydrogen premoderator and solid deuterium crystal. Strong fluctuations in the pulse energy, which were mostly caused by malfunctions of the pulse rod creating the excess reactivity, thus lead to larger-than-ordinary fluctuations of the UCN yield. A striking example of a fluctuating pulse energy is depicted in Fig. A.20, the data was taken throughout the beam time in June 2019.

Apart from the strong outlier, the pulse energy distributions of the remaining beam times show less fluctuations. The following figures (Figs. A.21-A.26) show the pulse energy distributions along with mean and standard deviation provided in the legend for the beam times from November 2015 until June 2019.

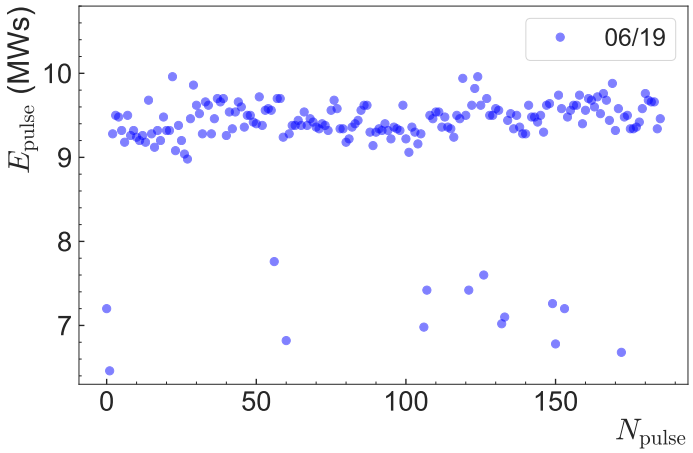

Figure A.20: Pulse energy E_{pulse} as a function of number of pulses, N_{pulse}, during the June 2019 beam time.

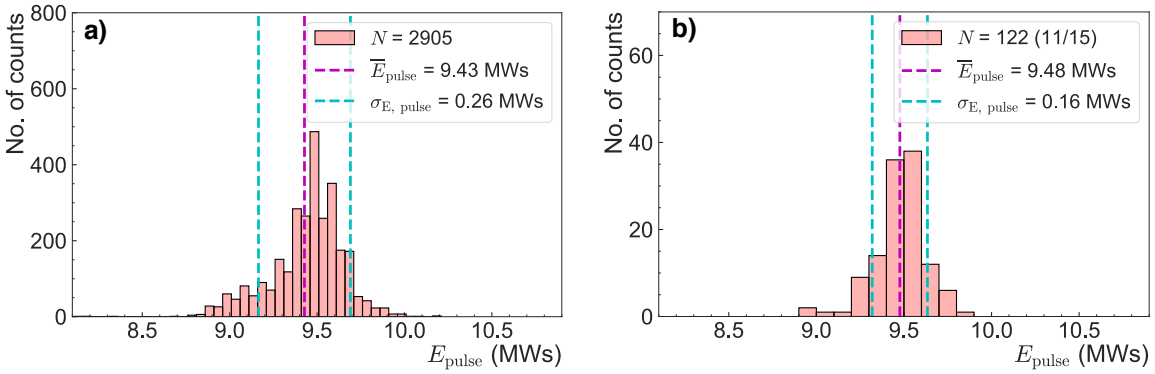

Figure A.21: Distribution of the pulse energy E_{pulse} for all beam times (a) and the November 2015 beam time (b). In the legend, the number of pulses (N), the mean value ($\overline{E}_{\mathrm{pulse}}$, magenta line), and the standard deviation ($\sigma_{\mathrm{E,\ pulse}}$, cyan lines) are given.

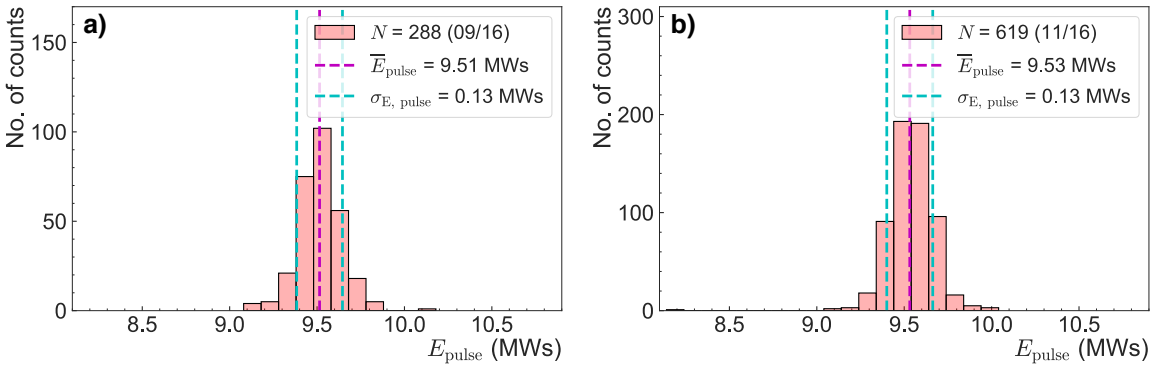

Figure A.22: Distribution of the pulse energy E_{pulse} for the September (a) and the November 2016 (b) beam times. The number of pulses is given by N, while the magenta line represents the mean value ($\overline{E}_{\mathrm{pulse}}$) and the cyan lines the standard deviation, $\sigma_{\mathrm{E,\ pulse}}$.

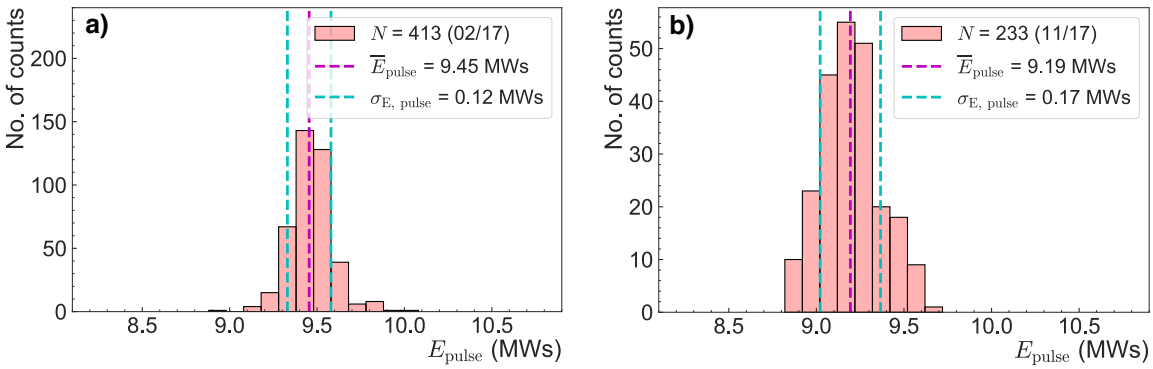

Figure A.23: Distribution of the pulse energy E_{pulse} for the February and the November 2017 beam times with number of pulses, N, mean value ($\overline{E}_{\text{pulse}}$, magenta line) and standard deviation, $\sigma_{\text{E, pulse}}$.

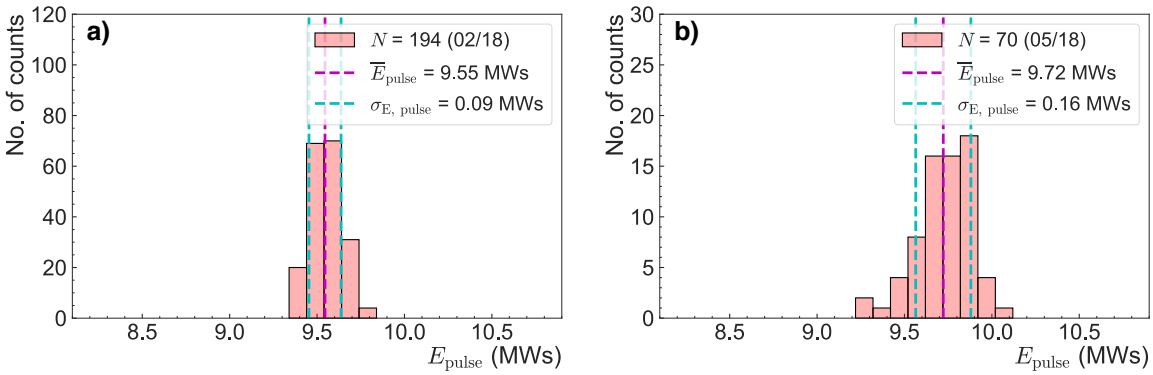

Figure A.24: Distribution of the pulse energy E_{pulse} for the February and the May 2018 beam times. The legend provides the number of pulses (N), the mean ($\overline{E}_{\text{pulse}}$, magenta line), as well as the standard deviation, $\sigma_{\text{E, pulse}}$.

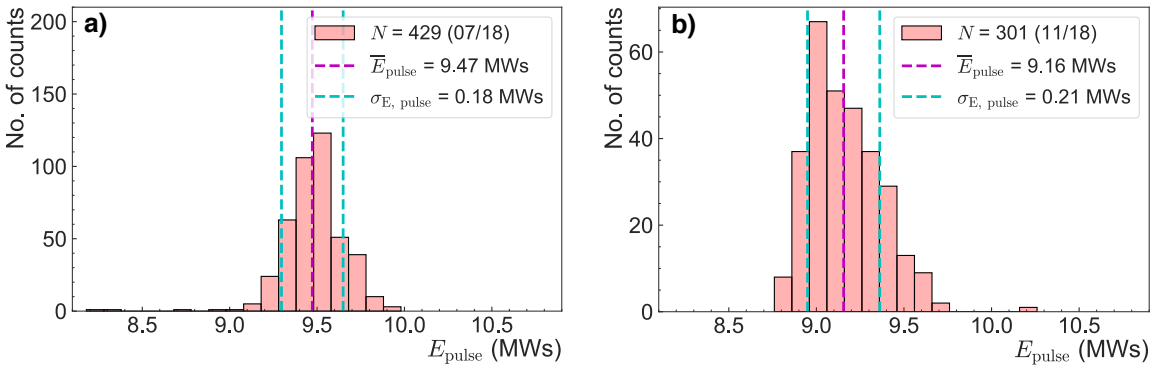

Figure A.25: Distribution of the pulse energy E_{pulse} for the July and the November 2018 beam times. The legend provides details on the number of pulses N, the mean value $\overline{E}_{\text{pulse}}$ (magenta line), and the standard deviation, $\sigma_{\text{E, pulse}}$.

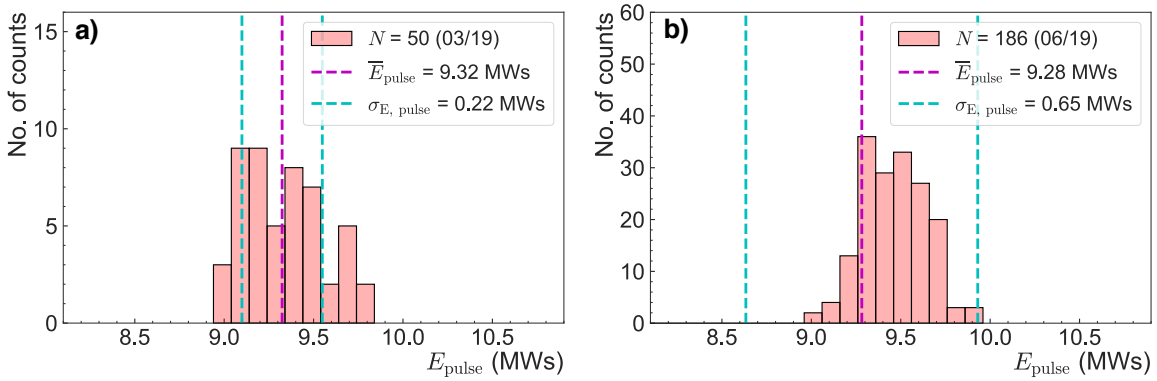

Figure A.26: Distribution of the pulse energy E_{pulse} for the March and the June 2019 beam times. The number of pulses forming the distribution are given in the legend (N). The magenta line refers to the mean value ($\overline{E}_{\mathrm{pulse}}$), while the standard deviation, $\sigma_{\mathrm{E,\ pulse}}$, is represented by the cyan lines.

B Additional contents - Setup of the τSPECT experiment

This chapter gives additional contents to Ch. 5. First, the accuracy of the positioning of the spin flipper and the neutron detector are laid out, which is affected by deviations between the computer aided design (CAD) model and the actual assembly (cf. Ch. B.1). Second, details on the detector concept are discussed in Ch. B.2, which includes simulations and calculations concerning the photon transmission inside the light cone and several aspects relevant to the UCN detection efficiency. Chapter B.3 provides further insights into the development and the finalisation of the detector read-out electronics. The detector characterisation setup, the algorithm used for event reconstruction, as well as first attempts to detect UCN are found in Ch. B.4.

B.1 Accuracy of positioning compared to mechanical design

For τSPECT, the actual position of the spin flipper and the UCN detector might deviate from the accuracy of the model implemented in computer aided design (CAD[1]). Possible deviations are due to imperfections in the mechanical realisation, *e.g.* caused by the manual welding of the flanges in the vacuum chamber system and the neutron guide system. To determine the mechanical accuracy, the two 1-axis Hall probes installed in proximity to the spin flip position and the detector's boron-10 layer[2] were used to determine the position of the relevant components relative to the longitudinal magnetic field with a resolution of $\Delta z = 5\,\mathrm{mm}$[3]. From the Hall probe measurement data, which contain the measured magnetic flux density in longitudinal direction (z), the gradient $\nabla_z B$ was also determined. It was calculated by computing the derivative of a spline fit to the measured data points.

For estimating the accuracy of positioning, the measurement data of both Hall probes as well as the computed magnetic flux density gradients were compared to the simulated longitudinal magnetic field density and the corresponding gradients. The simulated data,

[1] After upgrading from the 2016 version, the CAD software Inventor 2018 by Autodesk (`https://www.autodesk.com`) was used for the final design process.

[2] The Hall probe types and positions are provided in Chs. 5.4.1 and 5.5.1. According to the manufacturer, the calibrated Hall probes suited for cryogenic operation exhibit a $> 0.2\,\%$ linearity error up to a magnetic field of 1 T at $T = 300\,\mathrm{K}$ [are08].

[3] The readout system was developed by K. Franz.

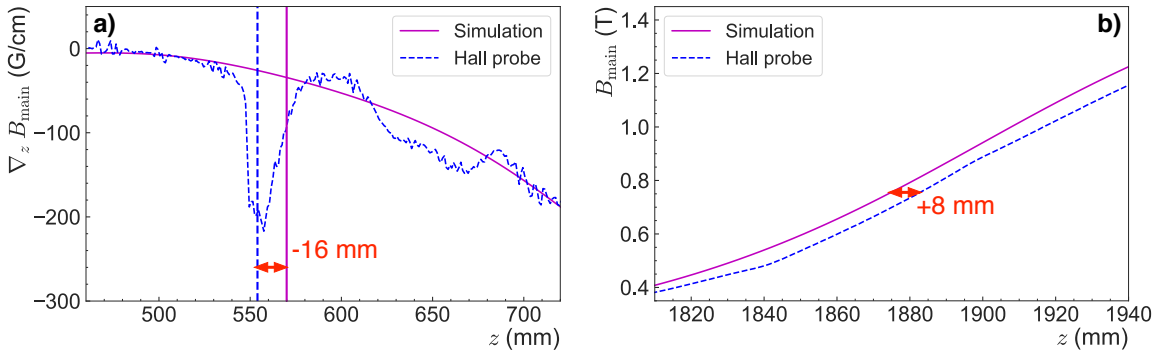

Figure B.1: Identification of offsets between the CAD design and the final mechanical implementation based on Hall probe measurements in z-direction. (a) For the neutron guide side, the gradient $\nabla_z B$ was computed from the magnetic flux density measured by the Hall probe (blue dashed line, superposition of the longitudinal magnetic field and the respective Halbach octupole field component). The resulting gradient was compared to the gradient calculated from the simulated data (magenta line, no consideration of the Halbach octupole). In the measured data, a kink is identified, which middle was taken as a reference point for the octupole position by considering earlier measurement data (middle of the kink represents the beginning of the Halbach octupole at $z = 570\,\mathrm{mm}$). Thus, a deviation of $-16\,\mathrm{mm}$ is deduced. (b) The average deviation of $+8\,\mathrm{mm}$ for the detector position can be concluded from comparing the longitudinal magnetic field shape, B_z, of the measured data (blue dashed line) to the simulated data (magenta line).

which did not consider the Halbach octupole, were considered as the reference point for all considerations laid out in this chapter and consequently all mechanical designs leading to implementing full-magnetic storage. To evaluate the accuracy of the detector position, the measured data was directly compared to the simulated data (cf. Fig. B.1 b). From the observed deviation in the field shape, an offset of

$$\Delta z_{\mathrm{corr,\ detector}} \sim +8\,\mathrm{mm} \tag{B.1}$$

was inferred, implying that the detector is actually 8 mm further retracted than given by the respective CAD position.

In case of the neutron guide side, comparing the measured absolute flux density data to the simulated data did not provide sufficient information to determine the offset. Instead, the gradient $\nabla_z B$ was computed for both the measured and the simulated data (cf. Fig. B.1 a). In the gradient depiction of the measured data (blue dashed line), a kink was identified due to the Hall probe measuring a superposition of the $z-$components of the longitudinal and the Halbach octupole field. After analysis of dedicated octupole measurement data, the position of the kink relative to the octupole position could be determined with $\sim 1\,\mathrm{mm}$ accuracy. Thus, the observed kink in the figure was taken as a reference point of the actual octupole position within the cryostat, which was within a precision of 1 mm at its design position (cf. Eq. (5.3)). As a result, an offset of

$$\Delta z_{\mathrm{corr,\ spin\ flipper}} \sim -16\,\mathrm{mm} \tag{B.2}$$

was found, which denotes that at the position of the AFP spin flipper, the neutron guide is actually $\sim 16\,\mathrm{mm}$ shorted than planned.

Since the operation of both the spin flipper and the UCN detector are highly sensitive to the longitudinal magnetic field, given offsets with respect to the dimensions given in CAD need to be considered when performing measurements. In case of the spin flipper, an accurate position is crucial to matching the required Larmor frequency and performing the spin flip. Also, the detector's energy sensitivity is affected by its positioning within the longitudinal magnetic field.

B.2 The detector concept

This section introduces the reader to the general detection principle based on neutron capture and detection of scintillation photons (cf. Ch. B.2.1) and discusses essential preconsiderations during the design phase (cf. Ch. B.2.2).

B.2.1 General detection principle

For detection, the UCN are captured in a boron-10 (^{10}B) layer. After the capture, a lithium-7 (^{7}Li)/α pair is produced. Depending on the angular orientation, either a ^{7}Li or α particle produce photons in a silver-doped zinc sulfide (ZnS:Ag) scintillator, which are detected in a silicon photomultiplier (SiPM array. Details are given in the following.

Combining boron-10 with a silver-doped zinc sulfide scintillator

Over the past decades, helium-3 (^{3}He) proportional counters containing ^{3}He gas were typically used for thermal neutron detection. The detection relies on the ^{3}He(n, p) reaction and provides a high thermal neutron cross section of 5330 b [Kno89]. With the onset of the ^{3}He shortage from 2001 onwards [SM10], the research has led to promising alternatives such as the solid compounds lithium-6 (^{6}Li) and boron-10 (^{10}B), which have also previously been used for detecting low-energy neutrons. Coupled with a scintillator, the neutron capture in mentioned solids leads to a generation of photons, which can easily be detected.

Compared to ^{6}Li, ^{10}B offers the advantage of a higher neutron cross section ($\sigma_{10\mathrm{B}} \sim 4\sigma_{6\mathrm{Li}}$ for neutron energy $E_\mathrm{n} = 10^{-2}\,\mathrm{eV}$[4] [Kno89]). The ^{10}B(n, $\alpha/^{7}$Li) reaction with the probability P to find the product ^{7}Li in ground or excited state reads [Kno89, CBL^{+}19]:

$$^{10}\mathrm{B} + {}^{1}\mathrm{n} \rightarrow {}^{7}\mathrm{Li} + {}^{4}\alpha \;\; \text{(ground state with } Q = 2.792\,\mathrm{MeV}, P = 6\,\%) \tag{B.3}$$

$$^{10}\mathrm{B} + {}^{1}\mathrm{n} \rightarrow {}^{7}\mathrm{Li}^{*} + {}^{4}\alpha + \gamma \;\; \text{(excited state with } Q = 2.310\,\mathrm{MeV}, P = 94\,\%)\,. \tag{B.4}$$

Due to the large Q values, the energy of the incoming neutron becomes negligible, leading to an angle $\theta = 180°$ between the ^{7}Li nucleus and the α particle upon ^{10}B neutron capture (cf. Fig. 5.20). Thus, a ^{7}Li or α carries the information of a neutron capture event with following energies [CBL^{+}19]:

$$E_{^{7}\mathrm{Li}} = 1.014\,\mathrm{MeV},\; E_\alpha = 1.775\,\mathrm{MeV} \text{ (ground state with } P = 6\,\%) \tag{B.5}$$

$$E_{^{7}\mathrm{Li}} = 0.841\,\mathrm{MeV},\; E_\alpha = 1.471\,\mathrm{MeV} \text{ (excited state with } P = 94\,\%)\,. \tag{B.6}$$

To convert the ^{7}Li nucleus and the α particle to photons, the inorganic scintillating material zinc sulfide with silver doping (ZnS:Ag) offers promising properties. It has been recently used for neutron detection in combination with ^{10}B (ultracold neutron detection in the qBounce [JCF^{+}13] and the UCNτ experiment [WHM^{+}15]) and ^{6}Li (cold neutron detection [OPYZ^{+}18, OPZ^{+}18], thermal neutron detection [MST^{+}15]). The scintillator offers a high

[4] For ^{10}B, the neutron cross section at $E_\mathrm{n} = 10^{-2}\,\mathrm{eV}$ is $\sim 4 \times 10^{4}\,\mathrm{b}$. Assuming the $1/v$ law, the relation between the cross sections of ^{10}B and ^{6}Li also holds for neutrons in the UCN energy range ($10^{-9}\,\mathrm{eV}$).

light output of $\sim$ 49 000 photons/MeV[5]. The Ag-doping causes the UV spectrum to be shifted into the visible range, with its peak intensity at $\lambda_{\text{peak}} \sim 450\,\text{nm}$, as shown in Fig. B.2 a). At the ZnS:Ag emission range, the photon transmission through the scintillator is $T \geq 90\,\%$ (cf. Fig. B.2 b).

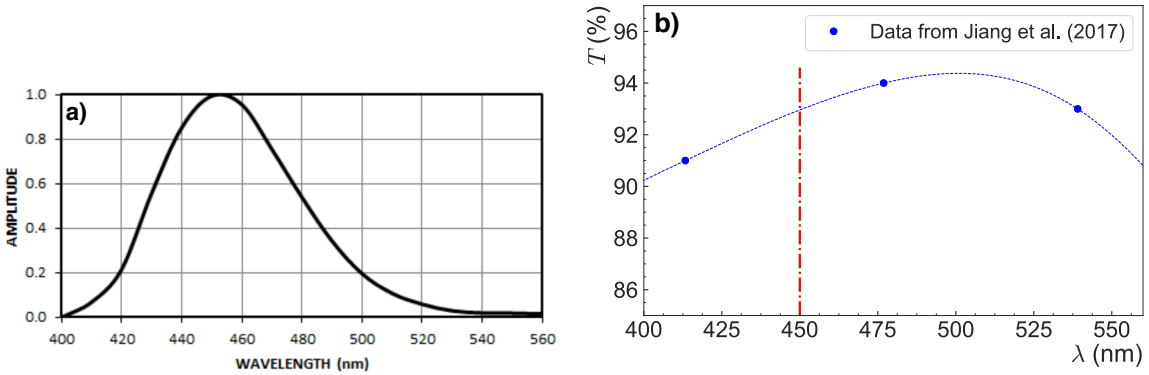

Figure B.2: Emission spectrum and reflectivity of ZnS:Ag. (a) Amplitude of light output plotted against wavelength (λ). The scintillator emits photons with peak intensity around $\lambda_{\text{peak}} = 450\,\text{nm}$. Figure taken from [elj16]. (b) The transmission T is above 90 % across the emission range with wavelength λ. The plot is based on data from [JZL+17], the blue dashed line represents a spline fit for interpolation. The red dash-dotted line gives the transmission at λ_{peak}.

Especially compared to organic liquid scintillators with decay constants $\sim 2-4$ ns, ZnS:Ag is a relatively slow scintillator with $\tau_{\text{decay, ZnS:Ag}} = 200\,\text{ns}$ [Kno89]. For thermal neutrons of energies $E_{\text{n}} = 2-6$ MeV, a biexponential decay with constants $\tau_{\text{n, decay,1}} = 130(20)\,\text{ns}$ and $\tau_{\text{n, decay,2}} = 340(40)\,\text{ns}$ was experimentally found [BP58], which is in the range of $\tau_{\text{decay, ZnS:Ag}}$. For lower-energetic neutrons, no data is presently available. Using the 5.5 MeV α particles emitted by americium-241 (^{241}Am), longer decay times than $\tau_{\text{decay, ZnS:Ag}}$ are observed. 84 % of the photons' decay is described by $\tau_{\alpha,\text{decay,1}} = 4520(70)\,\text{ns}$, while 14 % decay according to $\tau_{\alpha,\text{decay,2}} = 17\,300(1600)\,\text{ns}$[6] [MHH+12].

For UCN detection in τSPECT, a ^{10}B/ZnS:Ag layer with $\varnothing_{\text{neutron}} = 99\,\text{mm}$ is used, which is sufficient to cover the storage volume with $\varnothing_{\text{outer}} \sim 94\,\text{mm}$ while permitting a free movement inside the Halbach octupole ($\varnothing_{\text{Halbach, inner}} = 108\,\text{mm}$). Due to the low range of ^{7}Li and α particles ($R \lesssim 4\,\mu\text{m}$ [WMB+14]), the ZnS:Ag scintillator is directly glued to the ^{10}B layer, which is sputtered onto a PE substrate (cf. Ch. 5.5.1).

Photon detection in high magnetic fields

Moving into the storage volume to collect surviving UCN, the neutron detector is exposed to high magnetic fields ranging from $\sim 0.3\,\text{T}$ up to $\sim 1.7\,\text{T}$. During movement, the neutron detector is actively measuring, which excludes the usage of a conventional photomultiplier tube. As an alternative, a silicon photomultiplier (SiPM) array can be used, which is not affected by magnetic fields of given magnitude.

A SiPM electrically combines an array of avalanche photodiodes (APDs, which are junc-

[5] The light output has been calculated from [Kno89], according to which ZnS:Ag provides a 30 % higher light yield than NaI:Tl with a light output of 38 000 photons/MeV.

[6] The remaining 2 % of the intensity distribution are characterised by $\tau_{\alpha,\text{decay,3}} = 82\,000(10000)\,\text{ns}$.

tions with either p-on-n or n-on-p structure[7]). The bias voltage of the individual APDs is slightly set above their breakdown voltage ('Geiger mode'), such that the electron-hole pair created by an incoming photon experiences a high local electric field [OBD+05]. Accelerated by the electric field, the created charge carriers cause an avalanche process, in which multiple additional charges are released leading to high gain factors ('Geiger discharge'). Shortly afterwards, the avalanche process is stopped by a current flowing through a quenching resistor, which restores the initial bias voltage ('passive quenching'). The sum of the generated currents in all individual APDs is then proportional to the number of incoming photons.

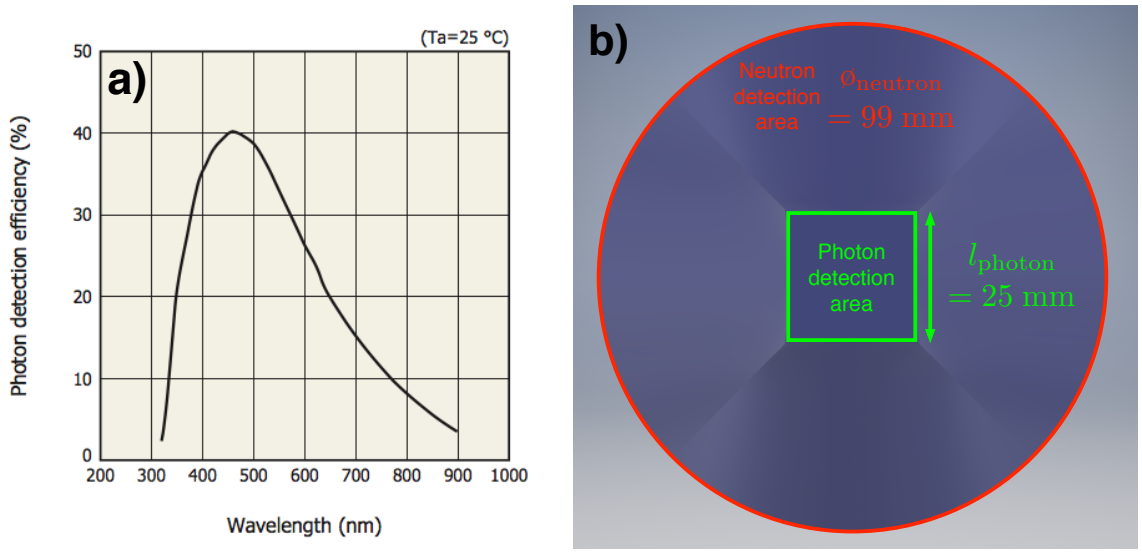

Figure B.3: Photon detection efficiency (PDE) of SiPM array and comparison of detection surfaces. (a) The PDE of the Hamamatsu S13361-6050AE-04 array as a function of wavelength λ at room temperature shows the good matching to the emission curve of ZnS:Ag with its maximum intensity at $\lambda_{\text{peak}} = 450\,\text{nm}$ (cf. Fig. B.2). Figure taken from [ham16b]. (b) The photons generated at the neutron detection area with $\varnothing_{\text{neutron}} = 99\,\text{mm}$ have to be guided to the photon detection area (top view), which dimensions are given by the SiPM array.

For τSPECT, a SiPM array of type Hamamatsu S13361-6050AE-04 is used[8], which in principle is a combination of 16 individual SiPM in a 4 x 4 array with a total area of $(25 \times 25)\,\text{mm}^2$. The specified Hamamatsu SiPM array was chosen since its spectral response range optimally matches the ZnS:Ag emission spectrum shown in Fig. B.3 a). Further relevant properties of the SiPM array are given in Tab. B.1.

Before reaching the SiPM array for detection, the difference in shape and size of the neutron detection area compared to the photon detection area as depicted in Fig. B.3 b) requires an effective photon guidance. For this, a PMMA light cone has been developed and thoroughly characterised by ray-tracing simulations. Details are given in the next section.

B.2.2 Relevant pre-considerations

During the detector design, several aspects needed to be taken into account. First, the photon guidance inside a light cone had to be characterised (cf. Ch. B.2.2.1). Since the UCN

[7]For photons with short wavelenghts, the p-on-n structure provides a higher photon detection efficiency. At longer wavelenghts, the n-on-p structure is preferred [RC11].

[8]The commercial name of the SiPM array given by Hamamatsu is MPPC (multi-pixel photon counter).

Table B.1: Main properties of the Hamamatsu SiPM array (type S13361-6050AE-04) [ham16b].

Channels	16 (4 × 4)
Total area	(25 × 25) mm^2
Fill factor (photosensitive area)	74 %
Number of pixels	14336 (896 per channel)
Refractive index epoxy window	1.55
Gain @298 K	1.7×10^6
Dark count rate @298 K	2 - 6 MHz
Bias voltage @298 K	53(5) V

detection inside the cryostat occurs at low temperatures, its impact had to be considered (cf. Ch. B.2.2.2). Of further significance for the detection efficiency is the thickness of the ^{10}B layer (cf. Ch. B.2.2.3) and the UCN reflection probability at the detector surface (cf. Ch. B.2.2.4).

B.2.2.1 Details on the photon guidance inside the light cone

Understanding the photon guidance inside the light cone, *i.e.,* estimating the photon guidance efficiency $\varepsilon_{\text{photon}}$, is another factor which is relevant for the detection efficiency. Furthermore, its characterisation is needed for matching the detector electronics to the expected light output caused by a neutron signal. The building of the PMMA light cone in the mechanical workshop of the Mainz Institute of Physics was initiated by J. Karch, while a detailed characterisation was part of this work. The side view of the light cone is depicted in Fig. B.4, with radial distance d_{centre} from the optical axis.

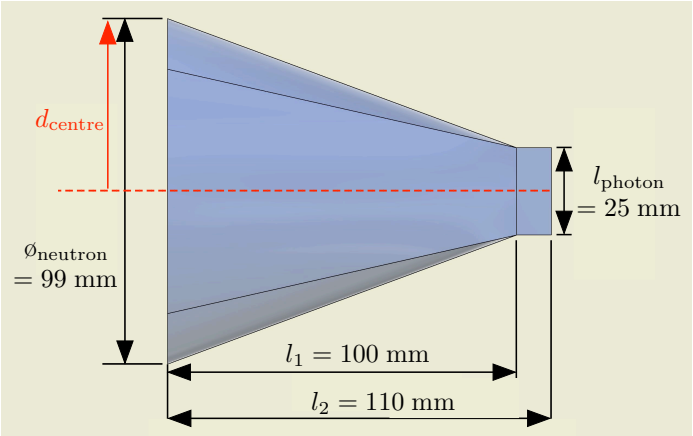

Figure B.4: Side view of light cone (CAD drawing). The UCN are converted into α particles/^{7}Li nuclei at the ^{10}B front side of the light cone ($\varnothing_{\text{neutron}}$ = 99 mm). The resulting photons from the scintillation process in the ZnS:Ag layer are then guided with efficiency $\varepsilon_{\text{photon}}$ to the rightmost side (l_{photon}), to which the SiPM array is attached for photon transmission. In ray-tracing simulations, the photon origin's distance from the optical axis (d_{centre}) (red dashed line) was shown to be relevant for photon transmission.

Laser transmission

After receiving the light cone from the mechanical workshop, the surface was mechanically polished for several hours using polishing paste specifically tailored for PMMA. For a first estimation on the photon guidance, the light cone was installed in the laser laboratory of the research group of Prof. K. Wendt. The available titanium-sapphire grating laser [TBC+10], which was set to power $P_{\text{laser}} = 80\,\text{mW}$ and wavelength $450.0(4)\,\text{nm}$[9], was shone perpendicular to the surface of the plain light cone surface (cf. Fig. B.5 a), which corresponds to the neutron detection side. A power meter was loosely attached to its rectangular end, which equals the SiPM array position in the final assembly.

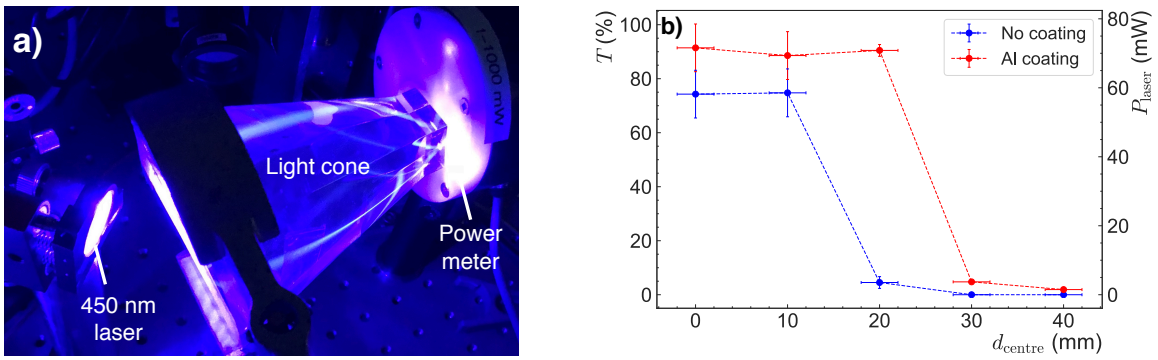

Figure B.5: Laser transmission through light cone. (a) The light cone was installed at the laser laboratory of Prof. K. Wendt to measure the transmitted laser power for $\lambda_{\text{laser}} = 450\,\text{nm}$. Using this setup, the transmitted laser power P_{laser} with laser light shone perpendicular to the light cone surface ($\alpha = 90°$, picture shows $\alpha = 45°$) was measured using a power meter for various distances from centre, d_{centre}. The picture shows the photons hitting the light cone surface with an angle. (b) The transmission T decreases towards the edge of the light cone, and could be improved by wrapping the light cone in aluminium foil (red data points). Already at $d_{\text{centre}} = 30\,\text{mm}$, no transmitted power could be measured with the uncoated light cone (blue data points).

In the measurement, the distance of the point-like laser centre was moved towards increasing distances from the light cone centre ($d_{\text{centre}} = (0, 10, 2030, 40)$ mm). Fig. B.5 b) shows the decreasing photon transmission T with increasing distance from centre, d_{centre}. The photon transmission is defined as the ratio of the measured power to the laser power,

$$T = P_{\text{measured}}/P_{\text{laser}} \,. \tag{B.7}$$

The measurement was repeated after wrapping the light cone in aluminium foil, which has led to significant transmission improvements due to better reflection. Without the aluminium coating, no photon detection was possible from $d_{\text{centre}} = 30\,\text{mm}$ onwards. With aluminium coating, T remained at $\sim 90\,\%$ until $d_{\text{centre}} = 20\,\text{mm}$ and dropped significantly to $\sim 5\,\%$ and $\sim 2\,\%$ at $d_{\text{centre}} = 30\,\text{mm}$ and $40\,\text{mm}$, respectively. Keep in mind that in the laser transmission measurements, only photons perpendicular to the light cone surface were considered. Ray-tracing simulations taking all photon incident angles into account give a more accurate view on the photon transmission.

[9]The set laser wavelength corresponds to the ZnS:Ag peak intensity (cf. Fig. B.2).

Ray-tracing simulations

The laser transmission measurement was quite limited to model the photon transmission inside the light cone, since the photons produced by the ZnS:Ag scintillator are emitted in 4π direction. Also, the photon transmission near the edge of the light cone ($d_{\text{centre}} = 49.5\,\text{mm}$) could not be determined. Therefore, the average transmission over all angles of incidence needs to be calculated, which is due to the light cone shape also dependent on the (x, y) position of the photon origin. For this, ray-tracing simulations based on Gaussian beam propagation were performed using the FRED software[10].

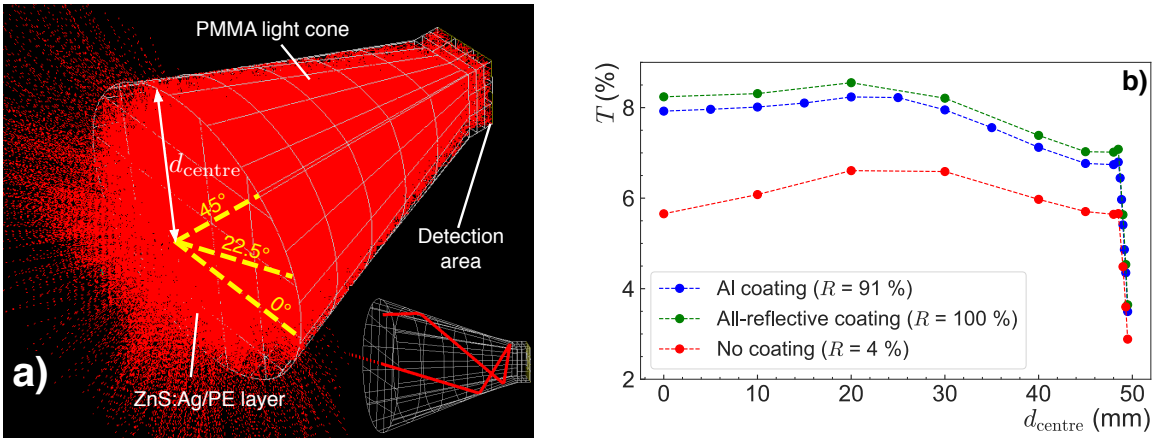

Figure B.6: Ray-tracing simulations of the photon transmission. (a) The light rays inside the light cone during ray-tracing are shown, with the wireframe model on the lower right depicting a back-reflected light ray. The photon origin position is varied radially along d_{centre} and according to the relative position to the square cutout ($\beta = 0°, 22.5°, 45°$, dashed yellow lines) on the ZnS:Ag surface. A detected photon with $\lambda = 450\,\text{nm}$ is counted if a light ray hits the detection area. (b) Transmission T as a function of the radial position, d_{centre}, for an aluminium coating (reflectivity $R = 91\,\%$, blue data points), a perfect coating ($R = 100\,\%$, green), and an uncoated PMMA surface ($R = 4\,\%$, red), assuming $\beta = 0°$. Towards the edge of the light cone ($d_{\text{edge}} = 49.5\,\text{mm}$), T decreases to $\sim 3.5\,\%$.

The CAD model of the light cone could be fully implemented in the software. Additionally, the ZnS:Ag layer (with PE substrate of 0.25 mm thickness) was implemented with transmission values shown in Fig. B.2 b) and regarded as the photon starting point[11]. The photons were programmed to have a fixed wavelength of 450 nm[12] and to be emitted into 4π direction, taking all possible incident angles $\theta_{\text{photon, incident}}$ into account. Also, associated material properties were defined, the refractive index of the detector window was considered ($r = 1.55$, cf. Table B.1), and no air gap between ZnS:Ag and PMMA surface was assumed. The influence of air gaps on the photon transmission is depicted in Fig. B.7.

As shown in Fig. B.6 a), ray-tracing simulations of the light cone were performed with

[10] The software is distributed by Photon Engineering (`https://photonengr.com/fred-software/`). For research purposes, the manufacturer provided a time-limited free version of FRED 16.112.

[11] Preliminary simulations have shown that the ZnS:Ag thickness of $t_{\text{ZnS:Ag}} \sim 22.6\,\mu\text{m}$ affects the total transmission by $< 0.5\,\%$ in a worst-case estimation (comparison of $t = 0.5\,\mu\text{m}$ vs $t_{\text{ZnS:Ag}}$). The middle of the scintillator thickness ($t_{\text{ZnS:Ag, middle}} = 11.3\,\mu\text{m}$) was therefore chosen as the photon origin.

[12] FRED simulations have shown a transmission dependency on the wavelength across the entire ZnS:Ag spectrum for $\lambda = [400, 550]$ nm (cf. Fig. B.2 a)) of $< 0.1\,\%$.

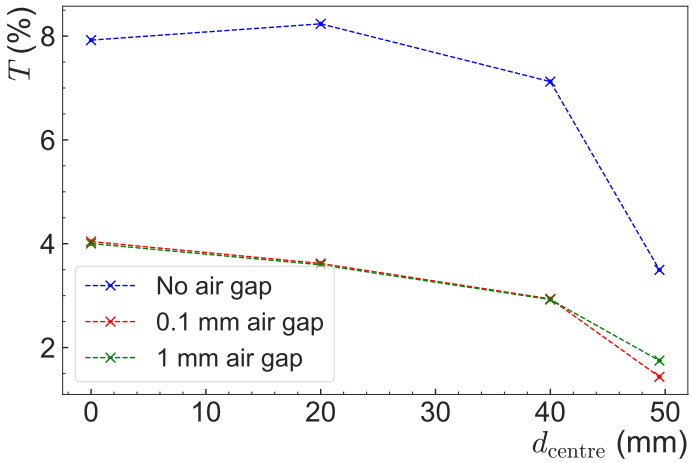

Figure B.7: Impact of air gaps on the light cone transmission.

10^7 photons and for a certain position of the light source from $d_{\text{centre}} = 0\,\text{mm}$ until the edge of the light cone, $d_{\text{edge}} = 49.5\,\text{mm}$. A random number generator was used to determine the photon incident angle $\theta_{\text{photon, incident}}$ from 0° until 90° relative to the surface normal. The square cutout for coupling the SiPM array ('detection area') leads to a 'symmetry breaking' of the light paths. At $\beta = 0°$ relative to the square cutout orientation, the transmission might behave differently than at $\beta = 22.5°$ and $\beta = 45°$ (yellow dashed lines), so these possibilities were included in additional simulation runs. The transmission T is defined as the ratio of the number of detected rays in the detection area, N_{detected}, and the number of emitted rays, N_{emitted},

$$T = \frac{N_{\text{detected}}}{N_{\text{emitted}}} \,. \tag{B.8}$$

Due to the simulation settings, given T values are already the average over all photon emission angles.

The simulations could confirm the observation made in the laser measurement, which implies that coating the light cone with aluminium foil increases T due to an increase in the reflectivity from $R = 4\,\%$ to $R = 91\,\%$[13]. On average, an increase of $\sim 2\,\%$ was found (cf. Fig. B.6 b). Also, a strong dependence on the radial position of the light emission can be seen. For aluminium and $\beta = 0°$, T decreases below 6 % at 0.5 mm before the edge ($d_{\text{centre}} = 49.0\,\text{mm}$) and decreases to $\sim 3.5\,\%$ at the edge, which implies that photon detection is possible at all distances from centre. The transmission curves for $\beta = 0°$ in Fig. B.6 b) differ from the results of the laser transmission measurements (cf. Fig. B.5 b), which have only considered laser light shone perpendicular on the light cone surface. Also, the results in Fig. B.6 b) depict the worst case, since T decreases less rapidly towards $d_{\text{edge}} = 49.5\,\text{mm}$ for $\beta = 22.5°$ and $\beta = 45°$ (cf. Fig. B.8 a). At $\beta = 45°$, the radial dependence of T even vanishes, which underlines the importance to include all β angles into account.

To further understand the photon transmission, the transmission dependence on the photon incident angles, $\theta_{\text{photon, incident}}$, was simulated (cf. Fig. B.8 b). For this, an upper

[13]The reflectivity values have been extracted from the data base found in the FRED simulation software for a wavelength of 450 nm.

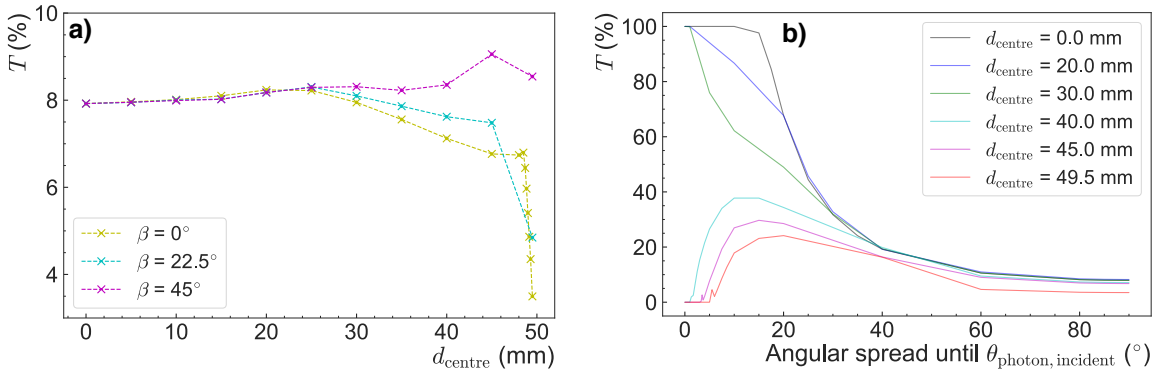

Figure B.8: Light cone transmission for different photon origin positions and impact of incident photon angle. (a) Transmission T as a function of the radial position (d_{centre}) for different photon origins with respect to the square cutout of the light cone, which is described by the angle β (cf. Fig. B.6 a). It can be seen that for $\beta = 0°$, *i.e.,* parallel to the square cutout, T decreases more rapidly towards the edge of the light cone, $d_{\text{edge}} = 49.5\,\text{mm}$. For $\beta = 22.5°$, the radial dependence of T decreases, while it nearly vanishes for $\beta = 45°$. (b) T plotted against the available angles up to an incident photon angle, $\theta_{\text{photon, incident}}$ for $\beta = 0°$. From an angular spread of 40° onwards, the integral transmission for all radial photon origins is comparable, while strong influences on the photon origin are seen for a lower angular spread. All simulations were run with $\lambda = 450\,\text{nm}$ and included aluminium light cone coating.

limit on the possible values for $\theta_{\text{photon, incident}}$ was defined, and varied in 5° steps from 5° until 90°[14]. As a result, each simulation with increasing upper limit on $\theta_{\text{photon, incident}}$ included all available angles from 0°. The transmission dependence on the incident angle is very striking for incident photon angles $< 40°$, while for $> 40°$, the integral transmission slowly decreases to $\sim 8\,\%$ ($\sim 4\,\%$ at d_{edge}), which is reflected by the results in Fig. B.6 b). For $d_{\text{centre}} = (0.0 - 30.0)\text{mm}$, integral T is $> 50\,\%$ up to angles of $\sim 20°$. The integral transmission curves for $d_{\text{centre}} = (40.0 - 49.5)\text{mm}$ form a second group with rising integral transmission until hitting a peak at $\theta = (10-20)°$. While none of this is of concern, it should be noted that no detection of photons with $\theta_{\text{photon, incident}} = (0-3)°$ (for $d_{\text{centre}} = 45.0\,\text{mm}$) and $(0-5)°$ (for $d_{\text{centre}} = 49.5\,\text{mm}$) is possible for photons generated near the edge of the light cone. This should be taken into account for later calculations of the detector efficiency.

To conclude, the light cone provides an overall photon detection efficiency of $\varepsilon_{\text{photon}} \equiv \overline{T} = 7.56\,\%$, which includes averaging over all incident photon angles $\theta_{\text{photon, incident}}$ and mentioned β angles. Additional simulations were performed to find possible improvements on the light cone transmission for later iterations of the UCN detector. A ~ 3.8 times better average transmission was found for a light cone with equal length ($l_1 = 100\,\text{mm}$) and front diameter ($\varnothing_{\text{neutron}} = 99\,\text{mm}$), but four times larger detection area (cf. Fig. B.9). As a result, the efficiency of the current light cone design scales almost linearly with detection area. Considering currently commercially-available SiPM arrays, this would imply electrically combining four SiPM arrays, which poses a challenge for later improvements of the detection system.

[14] A lower step size of 1° was chosen for the angular spread $\to 0°$ and $\to 90°$

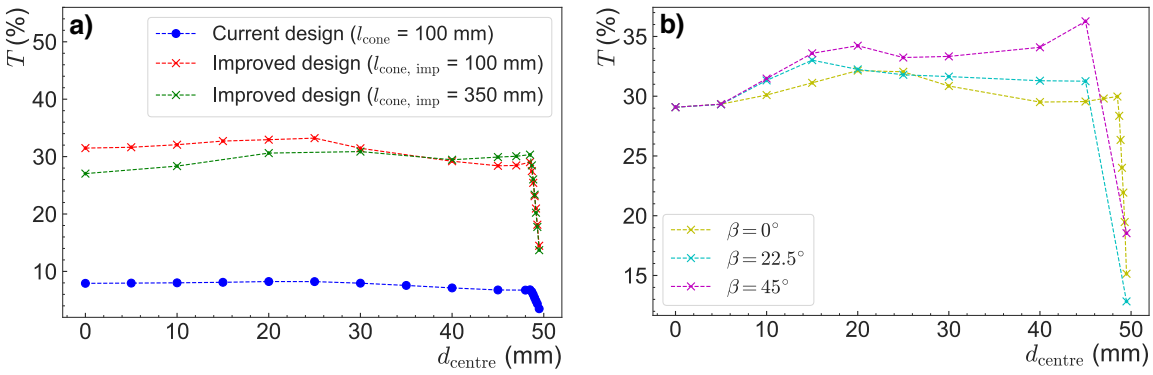

Figure B.9: Improved light cone with increased detection area. Raytracing simulations (a) show that by increasing the detection area from $25 \times 25\,\mathrm{mm}^2$ (current design, blue data points) to $50 \times 50\,\mathrm{mm}^2$ (improved design, red data points), the transmission can be increased by a factor > 3.8 on average. However, this would imply combining the signals of 4 SiPM arrays. Also, the dependence on the position with respect to the square light cone cutout has been varied for the light cone with improved design and $l_{\mathrm{cone,\ imp}} = 100\,\mathrm{mm}$ (b). The relative changes are comparable to the simulation results obtained with the current design (cf. Fig. B.8). All simulations have been performed with $\lambda = 450\,\mathrm{nm}$ and an aluminium-coated light cone.

Expected number of detectable photons

Based on discussed ray-tracing simulations and the properties of both the ZnS:Ag scintillator and the Hamamatsu SiPM array, an estimate on the number of detectable photons can be made. First, the ZnS:Ag light output ($\sim 49\,000$ photons/MeV, cf. Ch. B.2.1) was scaled to the energies of the ^{7}Li nuclei and the α particles. Their energies were weighted with the probability to find these in ground or in excited state (cf. Eqs. (B.5) - (B.6), giving $\overline{E}_{^7\mathrm{Li}} = 0.851\,\mathrm{MeV}$ and $\overline{E}_{\alpha} = 1.489\,\mathrm{MeV}$). Next, the light cone transmission averaged over all incident angles $\theta_{\mathrm{photon,\ incident}}$, all radial distances d_{centre}, and $\beta = 0°, 22.5°, 45°$[15] were taken into account. Also, the SiPM array's photon detection efficiency (PDE) of 40 % @ $\lambda = 450\,\mathrm{nm}$ (cf. Fig. B.3 a) was considered.

Table B.2: Estimation on the number of detectable photons per neutron capture, N_{photon}. Different effects were taken into account, while distinguishing between ^{7}Li nuclei and α particles, which lead to the emission of scintillation light with 50 % probability each per UCN capture event.

Effect	N_{photon} (^{7}Li)	N_{photon} (α)
ZnS:Ag light output	$\sim$ 41699	$\sim$ 72961
Light cone transmission	$\sim$ 3152	$\sim$ 5515
Photon detection efficiency SiPM array	$\sim$ 1260	$\sim$ 2206

Results are given in Tab. B.2. According to these calculations, a number of $\sim$ 1260 detectable photons for a ^{7}Li-induced scintillation process and $\sim$ 2206 for a scintillation

[15] For $\beta = 0°$, an average transmission of $\overline{T} = 6.77\,\%$ was found ($\beta = 22.5° \rightarrow \overline{T} = 7.66\,\%$, $\beta = 22.5° \rightarrow \overline{T} = 8.26\,\%$), yielding a total average of $\overline{T}_{\mathrm{light\ cone}} = 7.56\,\%$.

caused by an α particle is expectable. Due to the difference in the number of detectable photons ($\sim 75\,\%$ more in case of α-induced scintillation), a double-peak structure is expected to appear in the pulse height spectrum.

B.2.2.2 Impact of low temperature

Combining ^{10}B with ZnS:Ag has proven to be a highly-efficient UCN detector at room temperature in the UCNτ experiment [PCCW$^+$18]. At the neutron detector position of τSPECT, however, a local temperature of $\sim 180\,\mathrm{K}$ is reached. In a measurement with α particles of energy $E_\alpha = 5.5\,\mathrm{MeV}$ impinging on ZnS:Ag, the light output decreases by $\sim 17\,\%$ when cooling down from 300 K to 200 K [MHH$^+$12]. Although the α particle energy is a factor 3-7 larger than the energies of the ^{7}Li nuclei and α particles emitted in the ^{10}B(n, $\alpha/^7$Li) reaction (cf. Eqs. (B.5)-(B.6)), the light output impact should be comparable. The timing properties of ZnS:Ag slightly improve at 200 K, with a $\sim 18\,\%$ shorter first decay constant describing 84 % of the scintillation light [MHH$^+$12] (cf. Ch. B.2.1).

In a private communication with the manufacturer Hamamatsu, the suitability for the operation of our selected SiPM array up to liquid nitrogen temperature (77 K) was guaranteed. A considerable temperature effect on the SiPM bias voltage is present, which is also reflected by the manufacturer's recommendation to lower the bias voltage by $54\,\mathrm{mV\,K^{-1}}$ [ham16b], as the breakdown voltage decreases with decreasing temperature. The linear dependence of a similar SiPM array from room temperature down to $T = 238\,\mathrm{K}$ could be experimentally confirmed [DNP17]. Going further to $T = 180\,\mathrm{K}$, the linear approximation as depicted in Fig. B.10 a) still provides a sufficient description of measured data. For $T < 140\,\mathrm{K}$, the linear model overestimates the change in the breakdown voltage [CBM$^+$11, ZHJGF$^+$12]. Since prior temperature measurements could confirm that no such low temperatures are reached, a temperature regulation based on the linear approximation as shown in Fig. B.10 b) was implemented into the detector electronics (cf. Ch. B.3.2). Also, the recommended bias voltage is depicted by a red line in Fig. B.10 b), and refers to the optimum regarding the SiPM array's breakdown voltage.

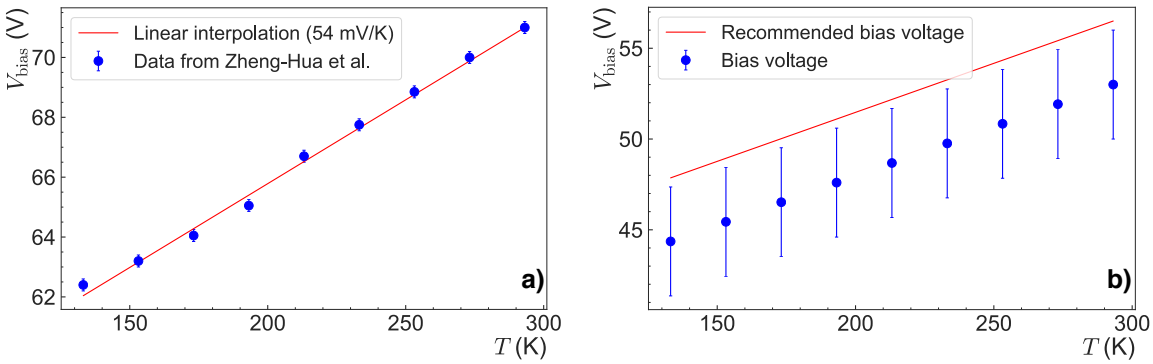

Figure B.10: Temperature dependence of the SiPM array bias voltage. (a) The measured linear dependence of the bias voltage V_{bias} on the temperature T (blue points, data from [ZHJGF$^+$12]). The red line represents the hypothetical linear interpolation of V_{bias} recommended by Hamamatsu for the SiPM array used in τSPECT ($54\,\mathrm{mV\,K^{-1}}$) [ham16b]. (b) Interpolation of the bias voltage applied to the τSPECT SiPM array in the final implementation (blue data points, with uncertainty $\sim \pm 3\,\mathrm{V}$) as a function of T. The red line represents the recommended value for the SiPM array bias voltage, which has been determined experimentally (cf. Ch. 5.5.2).

As experimentally determined in [ZHJGF+12], the gain of a one-channel $1 \times 1\,\mathrm{mm}^2$ Hamamatsu SiPM array with 100 pixels decreases by a factor ~ 2.3 from $\sim 2.03 \times 10^6$ to $\sim 0.9 \times 10^6$ when decreasing the temperature from room temperature to 180 K. A similar behaviour can be expected for our SiPM array and could inhibit the detection efficiency. The temperature dependence of the photodetection efficiency has not been experimentally determined yet.

A beneficial effect at low temperatures $\sim 180\,\mathrm{K}$ is the reduced dark count rate, which is found to be suppressed by two [BGK+18] or almost three orders of magnitude [CBM+11]. This is due to the reduced thermal noise, which accounts for the majority of the dark count rate [ZHJGF+12]. The specified dark count rate for our SiPM array is $\sim 2 - 6\,\mathrm{kHz}$ at $T = 298\,\mathrm{K}$ [ham16b].

B.2.2.3 Boron-10 layer thickness

A relevant factor for the detector efficiency is the thickness of the ^{10}B layer. While a thicker layer leads to a higher neutron absorption [Kno89], it also causes a decrease in the transmission probability of the ^{7}Li nucleus and the α particle. A higher transmission probability translates into a higher scintillation probability, since the ^{7}Li nucleus and the α particle are more likely to deposit their energy inside the scintillating material.

First, the UCN absorption mean free path and the probability for the UCN to be absorbed in ^{10}B was calculated, which is now referred to as the UCN conversion efficiency, ϵ_c. The UCN absorption mean free path, λ_{abs}, is given by the product of the UCN absorption time $\tau_{\mathrm{abs}} = 9\,\mathrm{ns}$ [WHM+15] and the velocity v_{UCN} [GRL91],

$$\begin{aligned} \lambda_{\mathrm{abs}} &= \tau_{\mathrm{abs}} v_{\mathrm{UCN}} \\ &= \tau_{\mathrm{abs}} \sqrt{\frac{2E_{\mathrm{UCN}}}{m_{\mathrm{n}}}} \,, \end{aligned} \tag{B.9}$$

with neutron mass m_n. The straightforward assumption based on [WMB+14] allows for the simple calculation of the conversion efficiency ϵ_c according to

$$\epsilon_c = 1 \cdot \exp\left(-k\right) \,, \tag{B.10}$$

with the ^{10}B layer thickness given by $d(^{10}\mathrm{B}) = k\lambda_{\mathrm{abs}}$. Thus, $d(^{10}\mathrm{B}) = \lambda_{\mathrm{abs}}$ ($k = 1$) gives $\epsilon_c \sim 63\,\%$ and $d(^{10}\mathrm{B}) = 5\lambda_{\mathrm{abs}}$ ($k = 5$) leads to $\epsilon_c \sim 99\,\%$. Following the recommendations in [WHM+15], a layer thickness of $d(^{10}\mathrm{B}) = 3\lambda_{\mathrm{abs}}$ ($k = 3$) should be reached in the final implementation, which yields $\epsilon_c \sim 95\,\%$. The dependence on λ_{abs} on the UCN energy E_{UCN} for different ϵ_c values is shown in Fig. B.11 a). To achieve the design goal of $\epsilon_c \sim 95\,\%$ ($k = 3$), an optimal layer thickness of $\sim 80\,\mathrm{nm}$ is found for the maximum storable UCN energy of $\sim 47\,\mathrm{neV}$.

The drawback of a thicker ^{10}B layer is a lower transmission probability of the ^{7}Li nuclei and the α particles. Although their range in ^{10}B, $R_{10\mathrm{B}}$, fulfils the condition $R_{10\mathrm{B}} \sim (2 - 4)\,\mu\mathrm{m} \gg d(^{10}\mathrm{B})$[16], trajectories with steep angles to the surface normal are affected by $d(^{10}\mathrm{B})$. To fully understand the transmission behaviour, SRIM[17] simulations were performed. For this, a total number of 10^6 ions with energies corresponding to the ^{7}Li/α

[16] The maximum ranges of ^{7}Li and α in ^{10}B are $R_{\mathrm{max},\,^7\mathrm{Li}} = 1.84\,\mu\mathrm{m}/2.06\,\mu\mathrm{m}$ and $R_{\mathrm{max},\,\alpha} = 3.55\,\mu\mathrm{m}/4.39\,\mu\mathrm{m}$, for excited/ground state (cf. Eqs. (B.5)-(B.6)), respectively [JCF+13].

[17] SRIM ('The Stopping and Range of Ions in Matter') is a common tool for simulating ion-matter interactions [ZZB10]. For these simulations, the 2008 version was used.

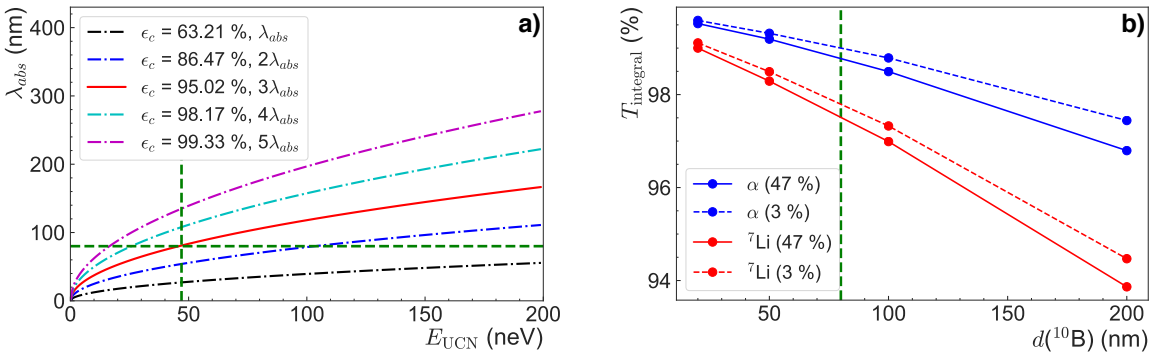

Figure B.11: Influence of ^{10}B layer thickness on neutron conversion and decay product transmission. (a) The UCN absorption mean free path, λ_{abs}, as a function of the UCN energy, E_{UCN}. The dash-dotted and the continuous line represent the different UCN conversion efficiencies, ϵ_c. For the maximum storable UCN energy of τSPECT, an optimum of $\lambda_{\text{abs}} = 26.7\,\text{nm}$ could be found (green dashed line), which translates to a layer thickness of $d(^{10}\text{B}) \sim 80\,\text{nm}$ at $\epsilon_c = 95.02\,\%$ (red line). (b) Simulated transmission probabilities T_{integral} for ^{7}Li and α (47 %/3 % denote the excited/ground state), averaged over incident angles $\theta_{\text{incident}} \in [0°, 90]°$ for different $d(^{10}\text{B})$. The green dashed line represents $d(^{10}\text{B}) = 80\,\text{nm}$), at which the highest ϵ_c was achieved.

energies in excited/ground state (cf. Eqs. (B.5)-(B.6)) were generated impinging on a ^{10}B layer with density $2.17\,\text{g}\,\text{cm}^{-3}$ and atomic weight 10.013 u (values similar to [JCF+13]). All other values such as atom displacement energy and lattice binding energies remained unchanged. The simulations were run for $d(^{10}\text{B}) = 20, 50, 100, 200\,\text{nm}$ and all incident angles $\theta_{\text{incident}} = [0°, 90]°$, with increasing precision from $\theta_{\text{incident}} \sim 88°$ onwards.

The effect of $d(^{10}\text{B})$ on the transmission can be seen in Fig. B.11 b), in which the integral transmission T_{integral} implies averaging over all incident angles θ_{incident} relative to the surface normal, *i.e.*, $\theta \in [0°, 90]°$. The ^{7}Li nuclei have a lower transmission probability, which is due to their lower kinetic energy obtained in the neutron capture process. Still, transmission at $d(^{10}\text{B}) = 80\,\text{nm}$ is $\geq 97.5\,\%$ in all cases and is maximally decreased by $\sim 1.5\,\%$ when compared to a thin layer of 20 nm thickness.

A detailed look on the incident angle-dependent transmission is provided in Fig. B.12, for α particles (a) and ^{7}Li nuclei (b). Assuming imperfections in the ^{10}B sputtering on the substrate, which yields to an uncertainty in the planned thickness $d(^{10}\text{B}) = 80\,\text{nm}$, the results of the SRIM simulation with 100 nm thickness are taken for a worst case estimation. The critical angle, which defines the boundary for total reflection, is calculated by referring to the maximum range of ^{7}Li and α in ^{10}B ($R_{10\text{B}}$),

$$\theta_{\text{critical}} = \cos^{-1}\left(\frac{d(^{10}\text{B})}{R_{10\text{B}}}\right), \tag{B.11}$$

with $R_{10\text{B}}$ being the respective ranges in ^{10}B. As Fig. B.12 shows, θ_{critical} is $> 88°$ for α particles and $> 86°$ for $d(^{10}\text{B}) = 100\,\text{nm}$. A thin layer of 20 nm would increase the angular acceptance towards 90°, which is however at the cost of a decreased conversion efficiency. Due to the higher significance of ϵ_c, it was agreed on using a layer thickness of 80 nm, after measurements have confirmed a significantly higher detection efficiency than when using a 20 nm layer (cf. Ch. 5.5.2).

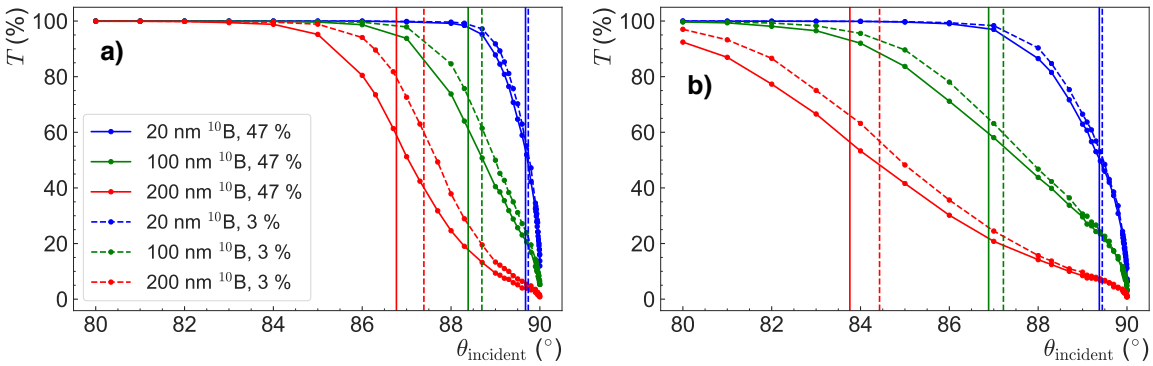

Figure B.12: Influence of ^{10}B layer thickness on angular acceptance. The transmission T as a function of incident angle θ_{incident} is plotted for α particles (a) and ^{7}Li nuclei (b), with the legend in a) being also valid for b). The transmission curves are plotted for $d(^{10}\text{B}) = 20, 100, 200\,\text{nm}$. A further distinction is made between α and ^{7}Li in excited/ground state with probabilities 47 % / 3 % (continuous line/dashed line). Corresponding critical angles θ_{critical} (cf. Eq. (B.11)) are represented by vertical lines.

B.2.2.4 UCN reflectivity

While transmission losses in the ^{10}B layer with thickness $d(^{10}\text{B})$ have been simulated to be mostly negligible, UCN reflections on the detector surface occur when taking the complex form of the Fermi potential $V_{\text{F}} = V - iW$ with real part V and imaginary part iW [GRL91] into account. The calculation is based on [WHM+15], in which the reflection theory found in [Lek87] has been applied to UCN. The Fermi potential allows the UCN to be reflected from the detector's ^{10}B surface under certain angles of incident, θ_{incident}, as depicted in Fig. B.13 a).

A shift in the real part V from negative $-3.4\,\text{neV}$ (neutron-absorbing) to positive value $5.8\,\text{neV}$ (neutron-reflecting for $E_{\text{UCN}} \leq 5.8\,\text{neV}$) is caused by a contamination with 3.5 % oxygen and 1 % carbon[18] [WHM+15]. The imaginary part with value $W = 36.3\,\text{neV}$ is not affected [WHM+15]. Under the condition $d(^{10}\text{B}) \gg \lambda_{\text{abs}}$ (with UCN absorption mean free path λ_{abs}), which in our case is valid due to $d(^{10}\text{B}) = 3\lambda_{\text{abs}}$, the reflection coefficient R is calculated [Lek87] (in [WHM+15][19]),

$$R = \frac{(k_0 - k_r)^2 + k_i^2}{(k_0 + k_r)^2 + k_i^2} \,, \tag{B.12}$$

which depends on θ_{incident}, V, W, the UCN energy E_{UCN}, and the neutron mass, m_n. The critical angle for total reflection is then given by [WHM+15]

$$\theta_{\text{critical, r}} = \cos^{-1}\left(\sqrt{\frac{V}{E_{\text{UCN}}}}\right) \,, \tag{B.13}$$

with average reflectivity

$$\overline{R} = \int_0^{\frac{\pi}{2}} d\theta_{\text{incident}}\; R \sin\theta_{\text{incident}} \,. \tag{B.14}$$

[18] The contamination is characteristic for the used sputtering facility, as it *e.g.* depends on the end pressure. For comparison, Tab. B.3 therefore also contains an analysis without surface contamination.

[19] For a detailed description of the coefficients, refer to [WHM+15].

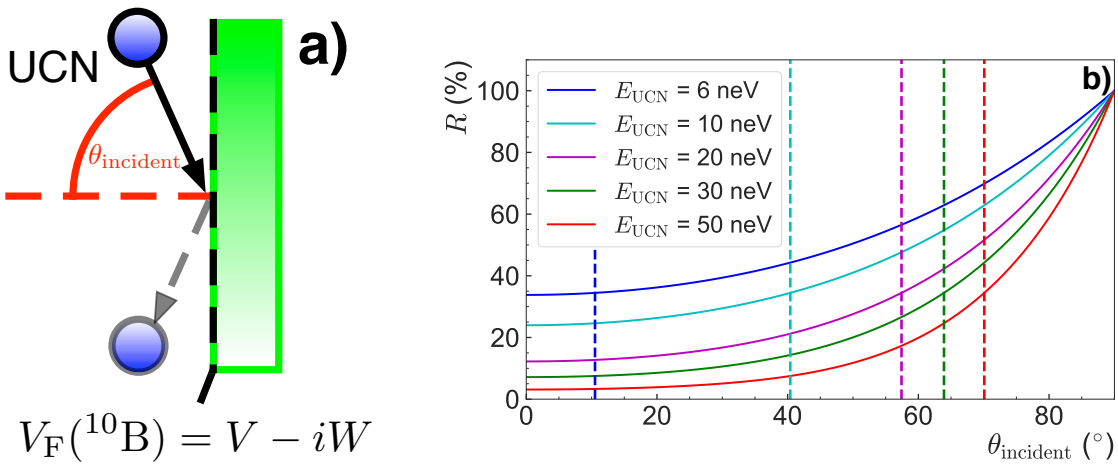

Figure B.13: Reflectivity of UCN on the neutron detector surface. (a) UCN impinging on the ^{10}B layer with incident angle θ_{incident} relative to the surface normal (red dashed line) have a certain probability to be reflected. (b) Reflection probability R of UCN with different energies impinging on a surface-contaminated ^{10}B layer as a function of θ_{incident}, calculated according to Eq. (B.12). Especially for lower-energetic UCN with energies $E_{\text{UCN}} \sim V(^{10}\text{B})$, high reflection probabilities for all incident angles are observed. For $\theta_{\text{incident}} \to 90°$, $R \to 100\,\%$. The vertical dashed lines depict the respective critical angle for total reflection, $\theta_{\text{critical, r}}$.

Table B.3: Reflection properties neutron detector with and without surface contaminants. Given are the average reflectivity, $\overline{R}$, and the critical angle, $\theta_{\text{critical, r}}$, for different UCN energies, E_{UCN}. For comparison, $\overline{R}_{\text{pure}}$ has been added, which is the average reflectivity for a pure ^{10}B surface with no contaminants.

E_{UCN} (neV)	$\theta_{\text{critical, r}}$ (°)	$\overline{R}$ (%)	$\overline{R}_{\text{pure}}$ (%)
6	10.52	53.69	49.84
10	40.40	45.48	41.72
20	57.42	34.24	31.07
30	63.92	28.17	25.53
50	70.09	21.63	19.65

As Fig. B.13 b) shows, the reflectivity of UCN has a considerable impact on the neutron capture efficiency. For low UCN energies just above $V = 5.8\,\text{neV}$, reflection dominates over transmission from $\theta_{\text{incident}} \sim 50°$ onwards, which is also reflected by $\theta_{\text{critical, r}}$. Table B.3 shows that even for $E_{\text{UCN}} = 50\,\text{neV}$, which approximately corresponds to the maximum storable UCN energy in τSPECT (47 neV), the average reflection is $\overline{R}_{\text{pure}} \sim 20\,\%$, with only little impact by the assumed surface contaminants oxygen and carbon.

It should be noted that a UCN reflection does not necessarily translate to a UCN loss, since reflected UCN bouncing back and forth at the magnetic potential well have a high probability to reach the detector surface again. For an accurate evaluation of the resulting detection efficiency, the energy distribution of the UCN stored inside the τSPECT storage volume needs to be simulated.

B.3 Properties of the detector read-out electronics

The read-out electronics involves a preamplification and a shaper stage. This section gives an overview on how the electronics were iteratively matched to the ZnS:Ag light output, starting with pre-tests with a single SiPM (cf. Ch. B.3.1), which have led to the final design (cf. Ch. B.3.2). The development was conducted in collaboration with electrical engineer H. Lenk, who was responsible for the implementation of the electronics.

B.3.1 Pre-tests with silicon photomultiplier diode

Before ordering the 4×4 SiPM array, tests with the corresponding 1×1 SiPM Hamamatsu S13360-3050CS with similar properties were performed[20]. The primary aim was to investigate the influence of the light cone on the pulse height in order to evaluate if a sufficient photon detection is possible and thus in line with the ray-tracing simulation results.

For the characterisation measurements, the Mainz Institute of Nuclear Chemistry provided an americium-241 (^{241}Am) source in liquid form with a low activity of 68(7) Bq[21]. The ^{241}Am solution was dripped onto the ZnS:Ag side of an uncoated ZnS:Ag/PE foil [22] with outer dimensions ($25 \times 25\,\mathrm{mm}^2$). After drying the ^{241}Am solution for $\sim 6\,\mathrm{h}$ under UV light, the middle of the foil was covered with a $\varnothing_{\text{outer, Am-241}} = 5\,\mathrm{mm}$ layer of ^{241}Am. Due to the resulting dual-layer structure, only 50 % of the α particles emitted in 4π direction hit the scintillator and therefore cause an emission of photons, which has been considered during the calibration measurements (cf. Ch. 5.5.2).

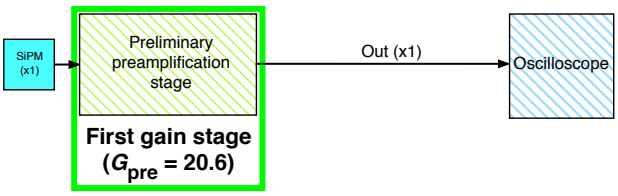

Figure B.14: Electrical circuit scheme precharacterisation SiPM.

Fig. B.14 shows the electrical circuit scheme which was used for the first test measurement. The electrical circuit is shown in Fig. B.15. The SiPM was electrically connected to the preliminary amplification stage containing the operational amplifier Analog Devices AD8099[23], which provided a gain factor of 20.6. The output signal was fed into an oscilloscope of type Tektronix TDS540, which worked as an analogue-digital converter (ADC) to save data to a floppy disk for typical durations of $\sim 10\,\mu\mathrm{s}$ due to low storage capabilities. Furthermore, the oscilloscope offered a 'peak detection mode', which could be used to display and save events exceeding a pre-defined peak threshold.

For the measurement, the ^{241}Am-covered ZnS:Ag/PE foil was optically coupled to the front of the aluminium foil-coated light cone by using the optical grease Saint-Gobain BC-630 (cf. Fig. B.16 a). The same grease was used for coupling the SiPM to the centre of

[20] The properties can be found in Tab. B.1, with following adaptions: 1 channel, photosensitive area of $3 \times 3\,\mathrm{mm}^2$, 3600 pixels, refractive index 1.41, and dark count rate 0.5−1.5 MHz [ham16a]. The wavelength-dependent detection efficiency is similar to the dependence shown in Fig. B.2 a).

[21] The source activity was measured by D. Renisch using a γ detector.

[22] The used ZnS:Ag foil was from the same batch as the boron-coated scintillation foils.

[23] The AD8099 operational amplifier was chosen due to its low noise of $0.5\,\mathrm{nV}/\sqrt{\mathrm{Hz}}$ and its operability with 5 V supply voltage [ana16].

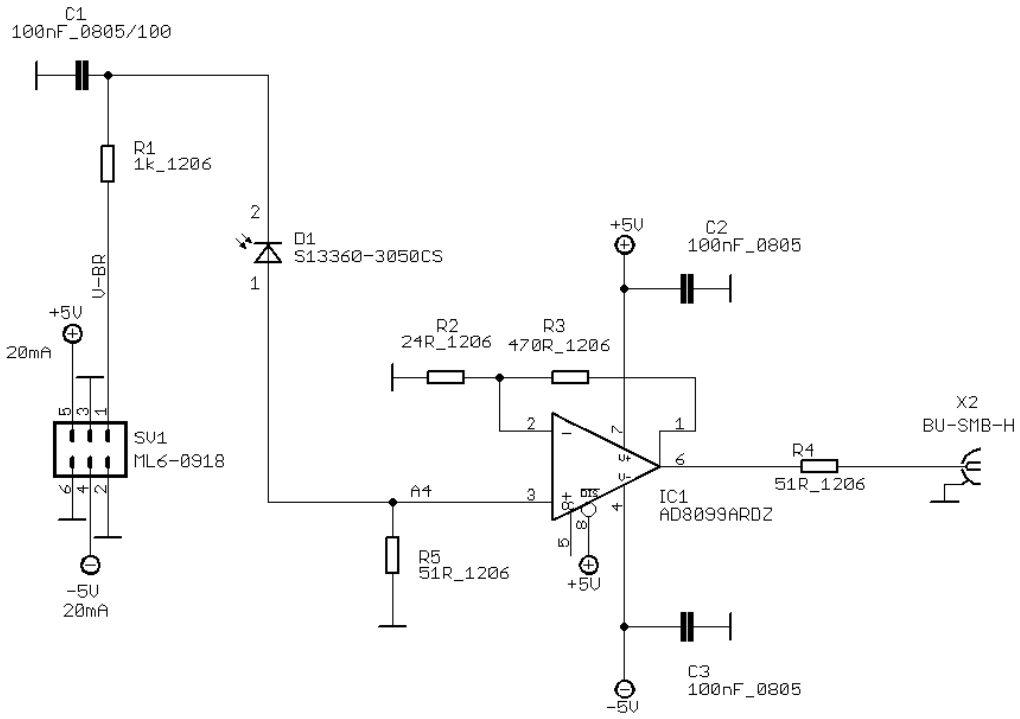

Figure B.15: Electrical circuit precharacterisation SiPM for Hamamatsu S13360-3050CS (courtesy of H. Lenk). The test circuit only contains a preamplification stage with preamplifier Analog Devices AD8099 which provides a gain factor of 20. A shaper stage with further signal amplification had not been developed yet.

the light cone bottom. The preamplification board was read out by the oscilloscope to save the signals. Later, the measurement was repeated without the light cone. For this, the ZnS:Ag/PE foil was directly coupled to the SiPM.

A comparison of the pulse height maxima with and without including the light cone (cf. Fig. B.16 b) gives a ratio of $\Delta V_{\text{max, w/}} / \Delta V_{\text{max, w/o}}$ of 0.083[24]. Although the SiPM only covers $\sim 1.6\,\%$ of the area covered by the SiPM array, a similar transmission dependence to the ray-tracing simulations were obtained, which predicted a transmission of $\sim 8\,\%$ for $\beta = 0°$ and $d_{\text{centre}} = 0\,\text{mm}$ (cf. blue line in Fig. B.2 b).

B.3.2 Characterisations of the silicon photomultiplier array for final implementation

During the pre-tests with the 1×1 SiPM, the PCB containing the connectors for the SiPM array and the integrated preamplification stage for each of the 16 SiPM array channels was designed by H. Lenk and custom-made by Beta Layout GmbH[25]. In the meantime, the prototype shaper box which combined the individual signals to a single output signal was finished. Photographs of the PCB and the shaper box are depicted in Fig. B.17 a) and b), respectively.

[24] Repeated measurements have confirmed this value to $\sim \pm 10\,\%$ accuracy.
[25] Beta Layout GmbH (`https://de.beta-layout.com`) is a manufacturer specialised in PCB prototypes.

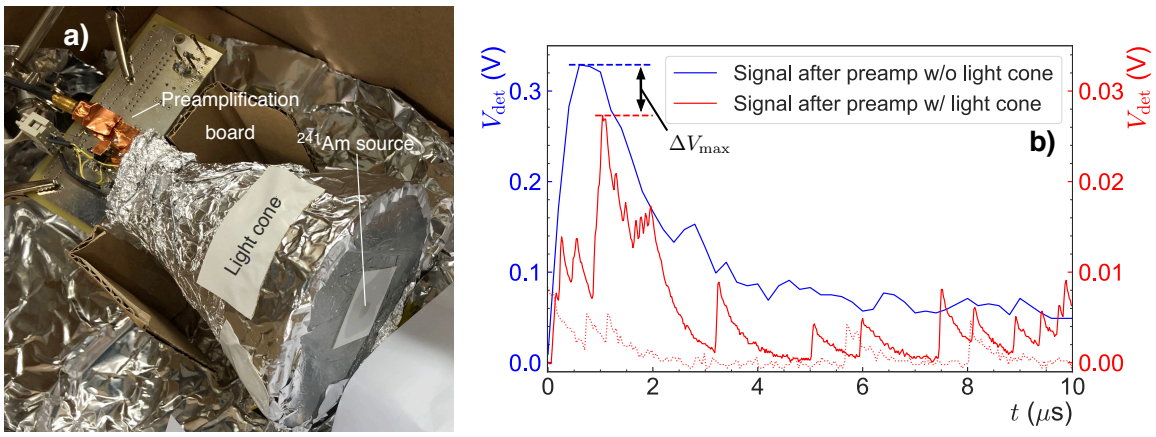

Figure B.16: Measurement setup SiPM characterisation and influence of light cone on the pulse height, after the preamplification stage. Note that these measurements were carried out using the single-channel SiPM Hamamatsu S13360-3050CS, which differs from the 4 x 4 SiPM array later used in the final τSPECT neutron detector. Furthermore, the preamplification stage was not finalised yet and the signals were not undergoing any pulse shaping. All factors combined lead to a different signal shape with a different timing behaviour. (a) Measurement setup for measuring the impact of the light cone on the photon transmission. The ^{241}Am source on the scintillation foil is optically coupled to the light cone centre, the SiPM signal is preamplified before being sent to the oscilloscope. (b) Detector voltage V_{det} after preamp without light cone (left $y-$axis, resolution of 0.5 MHz) and with light cone (right $y-$axis, 5 MHz resolution) plotted against time. With the light cone, the pulse height maximum is decreased by $\gtrsim$ 90 %. The red dashed line shows the signal with no ^{241}Am source, which is presumably dominated by thermal noise ($\mathcal{O}$(1 MHz)).

At first, a concise overview over the UCN detector electronics is given in Fig. B.18. The depiction is based on the virtual test circuit which was implemented in LTSpice[26]. Additional details on the electronics are given in this section and can be found in the documentation by H. Lenk [Len16]. The SiPM array is modeled by the Corsi model [CDM+07], which is commonly used to describe the internal SiPM electronics[27]. It approximates the entire SiPM array at bias voltage V_{bias} by a RC network, in which a current I_C is generated being proportional to the number of photons hitting the SiPM array. The current, which stems from the discharging of small capacitors inside a hit SiPM cell, causes a voltage at the 51 Ω resistance. Already at the PCB level, to which the SiPM array is mounted with 2 x 80 pin Samtec SS4-40-3.00-L-D-K-TR connectors, this voltage is fed into an AD8099 operational amplifier. In the original design, all 16 channels of the SiPM array were read out and preamplified individually, with a total of 16 AD8099 amplifiers. The electrical circuit model in Fig. B.18 simplifies the preamplification stage and the first shaper stage to one channel only.

After the signal of each channel is preamplified by a gain factor of 20.6, it is sent to the shaper box using a RG58 coaxial cable. All 16 cables are connected to one of the 16 SMB

[26] LTSpice is an analog circuit simulator based on SPICE ('Simulation Program with Integrated Circuit Emphasis'). The software is maintained by Analog Devices, Inc. (`https://www.analog.com/en/design-center/design-tools-and-calculators/ltspice-simulator.html`).

[27] The Corsi model parameters (left side) of the similar SiPM array S13360-6050VE are given by the manufacturer [ham18].

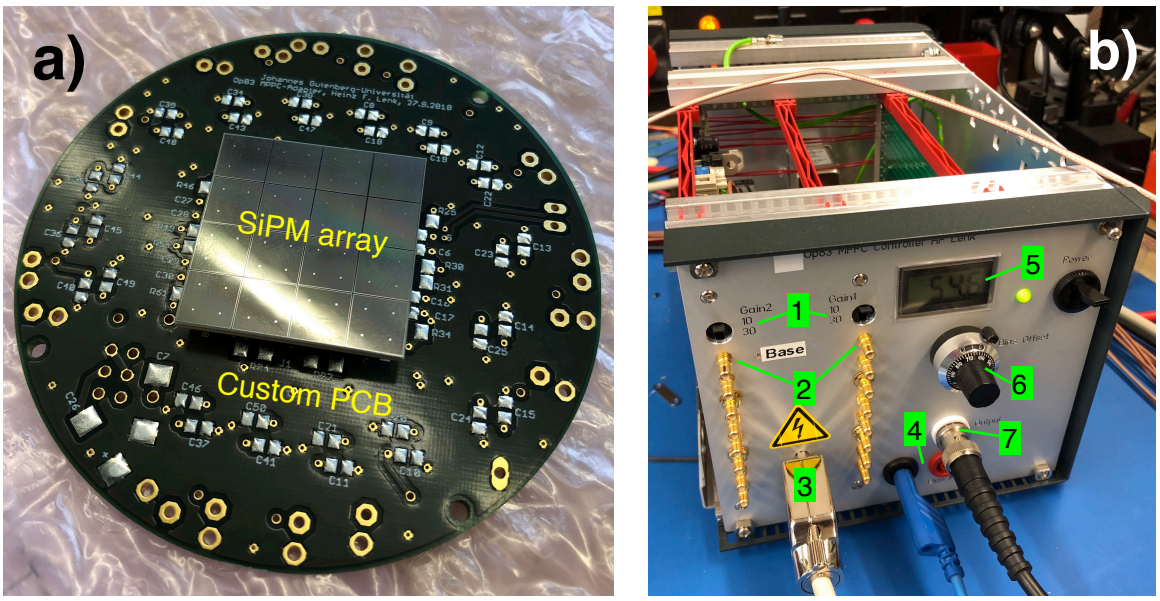

Figure B.17: SiPM array on PCB and shaper box. (a) SiPM array mounted on the custom PCB, which mainly contains the electronics for preamplifying the output signal. (b) Shaper box with the front panel characteristics: Toggle for gain stage 1 and 2 in shaper box (1), SMB inputs (2), D-Sub 9 connector PCB supply (3), external bias voltage read out (4), bias voltage display (5), potentiometer for bias voltage setting (6), BNC output (7).

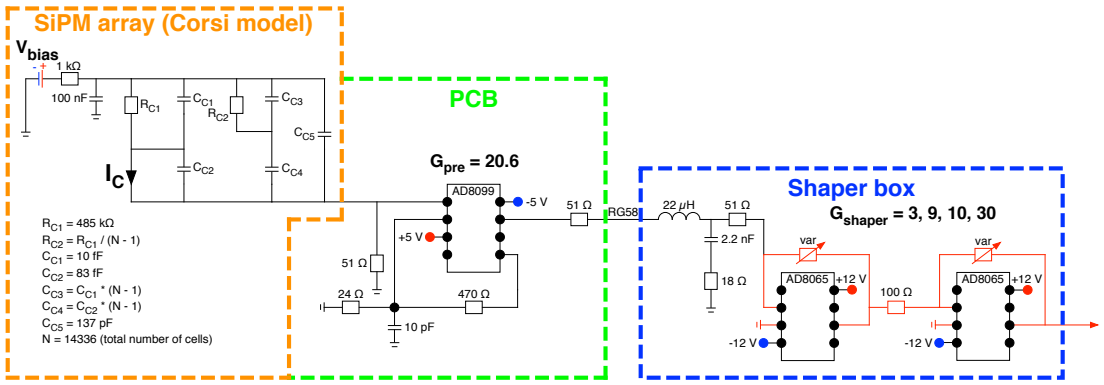

Figure B.18: Electrical circuit model of neutron detector. The electronics is divided into the Corsi-modelled SiPM array (orange), the PCB with the preamplification stage (green) and into the shaper box (blue), in which all signals are shaped, combined and further amplified. Until reaching the beginning of the shaper box, the signals from all 16 channels are separated. The combined signals in the shaper box are represented by red lines.

inputs. Each signal is first shaped by the resonator parts (22 μH coil, 2.2 nF capacitor) along with the damping resistances (18 Ω, 51 Ω). From now on, the signals of all channels behind their 51 Ω resistances are combined. The summed signals enter the first AD8065 operational amplifier with variable gain, which can be adapted by a toggle switch at the shaper box. Next, a second stage gain with variable gain factor and otherwise same properties follows.

In the first iteration, the shaper box offered gain factors of $G_{\text{shaper}} = 30, 100, 300$, which was later decreased to $3, 9, 10, 30$. The output signal is sent to a BNC connector. At gain 100, a shaper bandwidth of 600 kHz is achieved.

The circuit model does not show additional electronics, which is able to regulate the bias voltage according to a temperature change. The implementation is based on the voltage change measured over a Pt1000 resistor at the PCB front side through which a constant current of 134 μA flows. Assuming linear interpolation, the bias voltage is changed by $54\,\text{mV}\,\text{K}^{-1}$ (cf. Ch. B.2.2.2). At 293.15 K (20 °C), the bias voltage is set to 53.0 V. The Pt1000 resistor can be additionally read out and written to hard disk by using an Arduino Uno board.

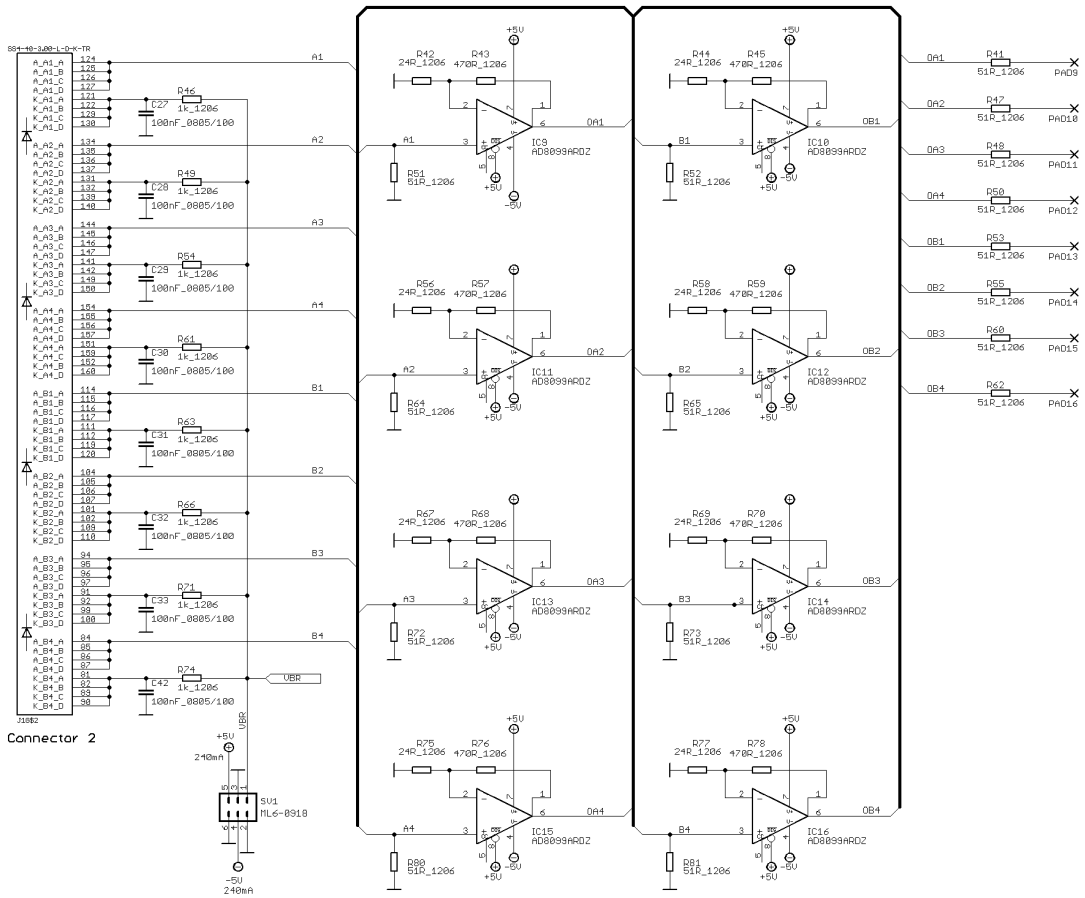

Figure B.19: Electrical circuit PCB neutron detector (courtesy of H. Lenk). On the PCB, one operational amplifier for each of the 16 channels provides an amplification of the signal by a factor 20.6.

The bias voltage can be offset by up to +10 V to meet the SiPM array's breakdown voltage[28]. Also not shown is the possibility to perform a base level adjustment by ±1 V before the combined signal enters the first shaper stage.

In the following, the associated electrical circuits are provided. Fig. B.19 depicts the

[28]The breakdown voltage of the SiPM array is characteristic for each 'channel' and is typically measured by performing a current-voltage scan ('*IV* curve', [DNP17]). Due to time constraints, the breakdown voltage has not been determined.

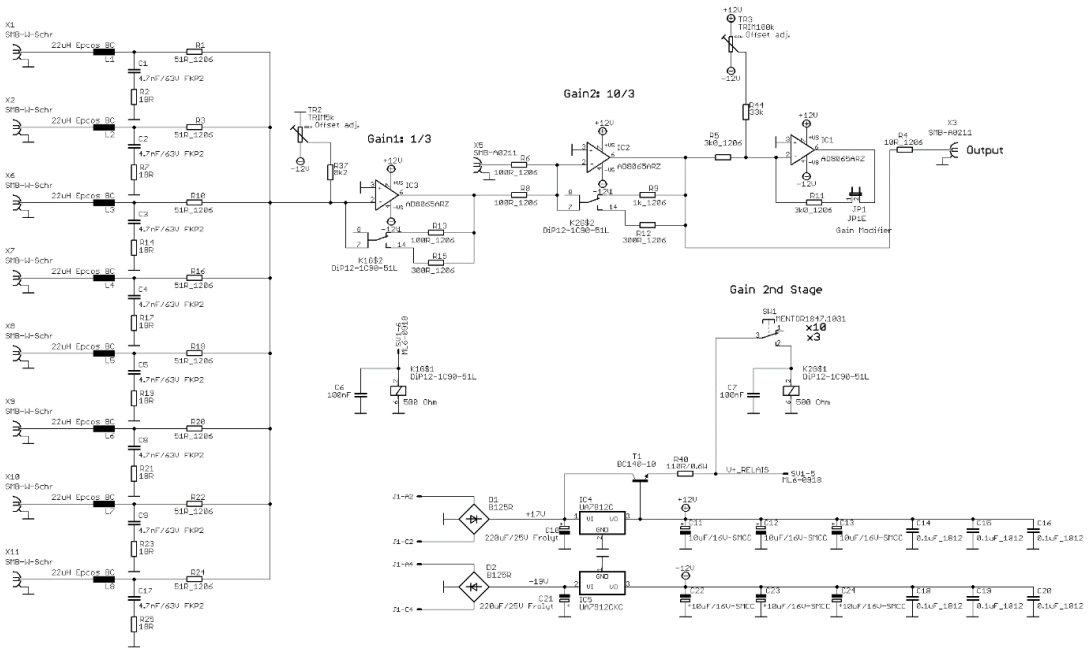

Figure B.20: Electrical circuit shaper box neutron detector (courtesy of H. Lenk). After shaping the signal, two adaptable gain stages amplify the signal by factors $3, 9, 10, 30$. The operational amplifier IC1, which is shown after the second gain stage, is obsolete in the final design.

electrical circuit of the detector PCB. The electrical circuits for the shaper box and the bias voltage regulation are provided in Figs. B.20 and B.21.

Radial intensity distribution after preamplification stage

Determining the radius of a UCN capture event would be of interest for τSPECT, since it would possibly allow for the reconstruction of the UCN energy. This is due to the shape of the radial magnetic field of the Halbach octupole (cf. Fig. 5.10 a), which radially confines UCN according to their energy. Thus, UCN with higher energy have a higher probability to be detected towards at larger distances from the centre of the ^{10}B layer.

To test the radial dependence, the ^{241}Am source on the smaller-cut ZnS:Ag/PE sheet was optically coupled to a position near the edge of the light cone at $d_{\text{centre}} = 45\,\text{mm}$ (displacement in direction of rectangular cutout, $\beta = 0°$, cf. Ch. B.2.2.1). All 16 channels were read out individually and the preamplified signals were recorded using the formerly used Tektronix TDS540 oscilloscope. The intensity distribution is shown in Fig. B.22 a) (matrix form) and b) (histogram). In general, it was found that higher pulse heights are more likely in SiPM array cells closer to the scintillator. Since these results only model a special case, raytracing simulations were run to fully understand the radial dependence.

The ray-tracing simulations have yielded a clearer picture on the distribution of the intensities. For placing the photon origin parallel to the light cone cutout ($\beta = 0°$) and 45° relative to it ($\beta = 45°$), finding the SiPM array cell with the maximum intensity allows for a simple reconstruction on the radius (cf. Fig. B.23 a), the distributions per cell are given in Figs. B.23 b) and B.24 b). This was not the case for $\beta = 22.5°$ (cf. Fig. B.24 a). For $\beta = 0°$ and $\beta = 45°$, a simple reconstruction was thus possible by finding the maximum in

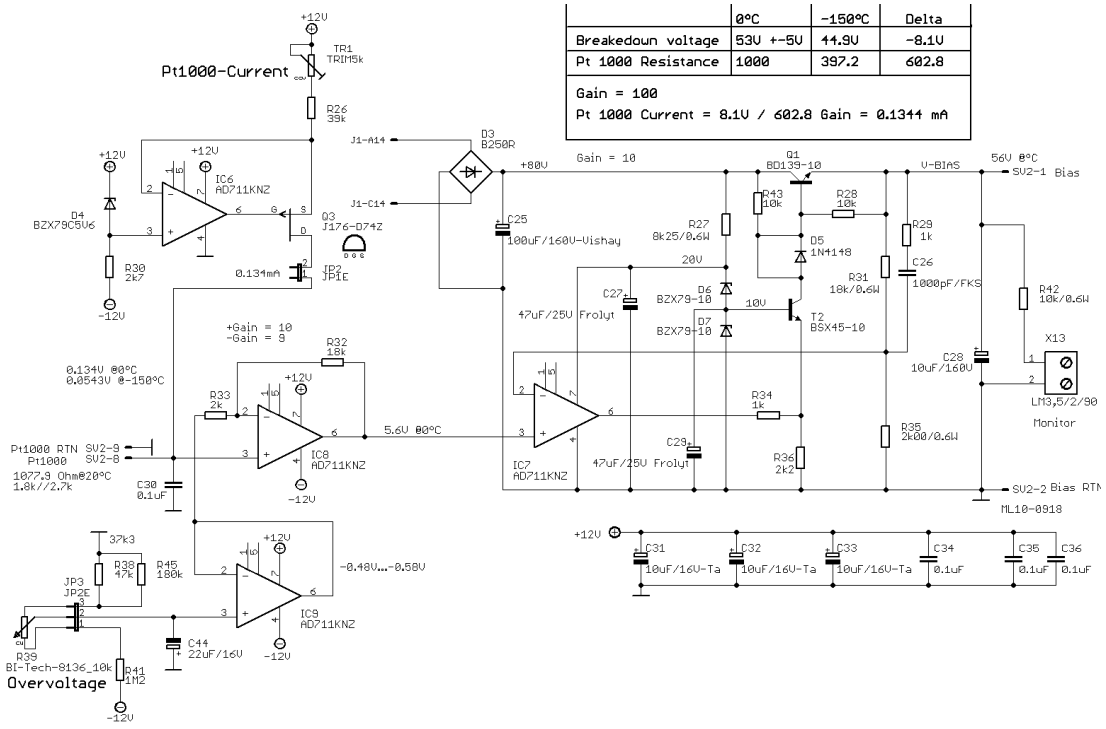

Figure B.21: Electrical circuit bias voltage regulation neutron detector (courtesy of H. Lenk). The bias voltage is varied with temperature ($54\,\mathrm{mV\,K^{-1}}$), which is determined by a Pt1000 resistor at the PCB. Also, the bias voltage can be increased by $+10\,\mathrm{V}$ using a potentiometer.

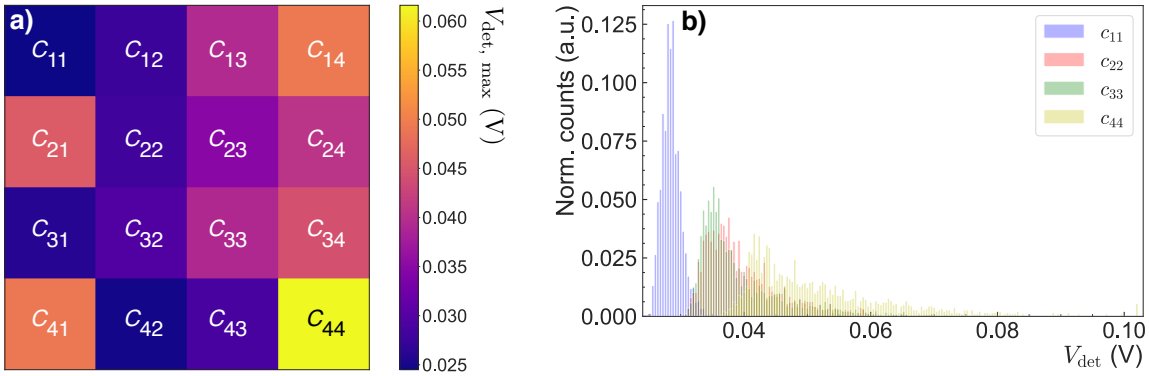

Figure B.22: Distribution of maximum pulse heights over all SiPM array channels after preamplification. (a) Distribution of the maximum pulse heights $V_{\mathrm{det,\,max}}$ over the entire SiPM array area. During the measurement, the scintillator was positioned at $d_{\mathrm{centre}} = 45\,\mathrm{mm}$, with closest distance to the cells c_{24} and c_{34}. (b) Histogram of the pulse heights V_{det} across the diagonal from c_{11} to c_{44}. It becomes apparent that higher detector voltages V_{det} are reached towards the position of the scintillator. The histogram has been normed to 1 to compare the pulse height distributions.

all cells. Again, this did not work for $\beta = 22.5°$.

To summarise, the current light cone design does not allow for the reconstruction of the radial distribution of UCN events and therefore offers no conclusive information on the UCN

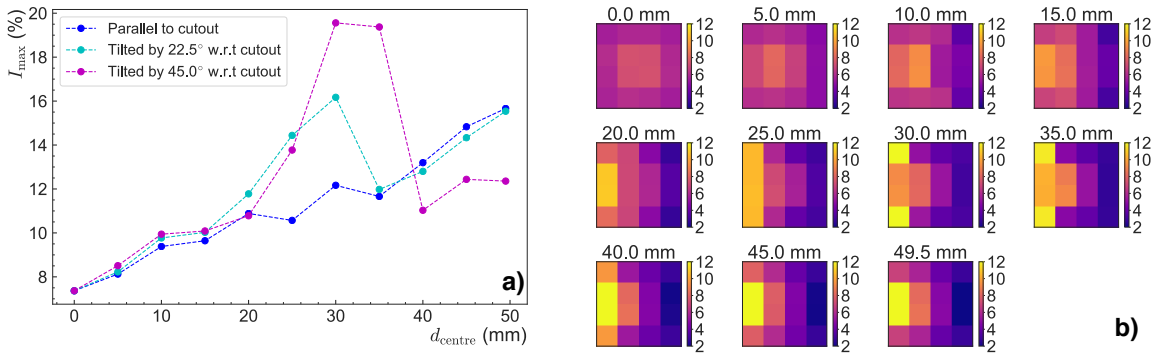

Figure B.23: Maximum intensity and intensity distribution for $\beta = 0°$. (a) The maximum intensity $I_{\max}$ across all cells for increasing radial distances (d_{centre}) is plotted. (b) Intensity distribution in detector for different radial distances at $\beta = 0°$.

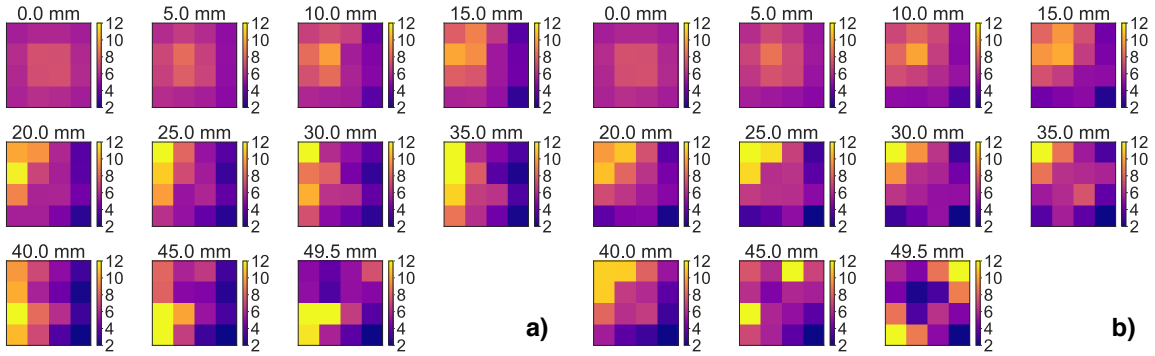

Figure B.24: Intensity distribution for (a) $\beta = 22.5°$ and (b) $\beta = 45°$.

energy distribution inside the storage volume.

Shaping of the signal

To measure the impact of the shaper on the signal shape, the ^{241}Am source on the ZnS:Ag sheet was repositioned at the centre of the light cone. The output signal of the shaper was displayed and recorded using the oscilloscope Tektronix TDS540. The results of the pulse shaping on the signal in a preliminary version are depicted in Fig. B.25 a). It shows the clear smoothing of the signal by the shaper electronics, without affecting the noise considerably (cf. Fig. B.25 b).

Since the signal output at $G_{\text{shaper}} = 30$ was with maximum values $\gtrsim 10\,\text{V}$ too high for the commercial ADC's input tolerance of $\pm 2.5\,\text{V}$ (cf. Ch. B.4.1), the first and second gain stage of the shaper box were later modified to provide possible gain factors of $3, 9, 10, 30$ instead of $100, 300, 900$. Before implementation into the final detector electronics, further fine-tunings were performed to optimise the pulse shaping.

Combination of channels for vacuum feedthrough

An effective vacuum separation made it necessary to include the SiPM array and the PCB electronics into the main vacuum, which was not considered in the primary design. This required a total of 9 lanes to be guided through a vacuum feedthrough, if all 16 SiPM array

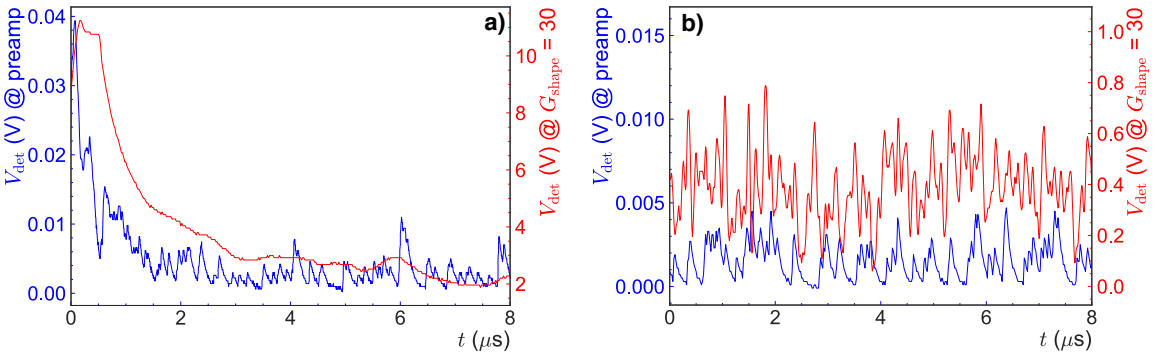

Figure B.25: Preliminary shaping of the pre-amplified signal and resulting noise level, with detector voltage V_{det} after preamp (left $y-$axis) and after shaper with gain $G_{\mathrm{shape}} = 30$ (right $y-$axis). The shown plots depict the shaper in an early development stage, which implies that the timing properties of the pulses was not final yet. (a) The shaped signal (red) is clearly smoothed when compared to the signal after the preamp (blue). (b) The noise peak structure has not been affected by the pulse shaping.

channels were combined into a single channel before entering the preamplification stage[29]. The inclusion of the Hall probe and the thermal wire for local heating increased the number of required lanes to 15. Therefore, a 15-pin D-Sub 15 vacuum feedthrough on a CF40 flange was used, which provided the maximum available number of electrical lanes within the mechanically available space (cf. Fig. B.26 and Tab. B.4 for the connection schemes). Thus, all 16 signals were combined after the SiPM array channel's individual 51 Ω resistors and fed into a single AD8099 operational amplifier. The combined preamplified signal was then transmitted to the shaper box via a single SMB input. Apart from adaptions to the Corsi model, Fig. B.18 represents the new circuit well.

The first drawback of combining the signals was losing the information on the radial distribution of the photon signals, which was hoped to be used to reproduce the UCN energy spectrum. Since ray-tracing simulations found no convincing radial dependence, this drawback is of no concern. Another drawback is a slowdown of the detection system. By combining the output signals of the individual SiPM channels, the capacities of the SiPM cells are also combined ($C_{\mathrm{SiPM,\,total}} = 16 \cdot \tau_{\mathrm{cell,\,individual}} = 16 \cdot 1.3\,\mathrm{nF} = 20.8\,\mathrm{nF}$ [ham16b]). After 5τ, the count rate capability in terms of a SiPM cell ready to fire again decreases by this measure from 3.0 MHz to 0.2 MHz, which is however still ~ 25 times faster than typically-observed UCN count rates ~ 8 kHz (cf. Fig. 6.8). Therefore, the decreased count rate capability does not inhibit the UCN detection efficiency.

Saturation effects of the detector electronics were noticed for counts $\gtrsim 10^5\,\mathrm{s}^{-1}$, which is close to the approximated count rate capability of the SiPM array (~ 0.2 MHz). The saturation leads to a 'gap' in the data plotted in Fig. 5.29. The high counts rates were reached when the detector was directly exposed to thermal neutrons of the reactor during the CASCADE comparison measurements (cf. Ch. 5.5.2).

[29] Without combining all SiPM array channels, a total of 25 pins just for the detector signals along with additional 6 pins for Hall probe/thermal wire would have been required, which was technically not possible.

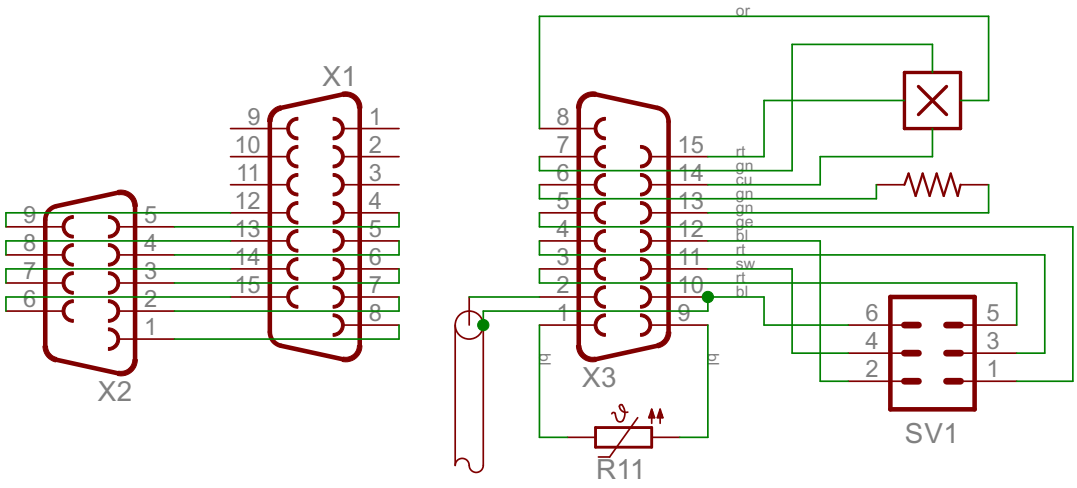

Figure B.26: Connections scheme 15-pin SUB-D vacuum feedthrough neutron detector (courtesy of T. Gerhardt). On the right hand side, viewed from top to bottom, the Hall probe, the thermal wire and the PCB connections (SV1) are depicted. R11 denotes the Pt1000 temperature sensor, which is read out to regulate the SiPM array's bias voltage.

Table B.4: Pin connection mapping between 15-pin SUB-D connection in vacuum feedthrough flange and MIL-DTL-26482 at pre-vacuum flange.

Pin assignment MIL-DTL-26482	Pin assignment 15-pin SUB-D
A	1
C	3
D	4
E	5
F	6
G	7
H	8
J	9
K	10
L	11
M	12
N	13
P	14
R	15

B.4 Detector characterisation and data analysis

After purchasing a fast analogue-digital converter (ADC) and building a test chamber (cf. Ch. B.4.1), detector characterisation measurements were performed. First, the response to an ^{241}Am source was measured for inferring an event count rate from the spectrum with a suitable algorithm (cf. Ch. B.4.2, the measurements are discussed in Ch. 5.5.2). Later, the detector's radial dependency (cf. Ch. B.4.3) and its capability to detect UCN at room temperature was tested for the first time (cf. Ch. B.4.4, a comparison to the performance of a commercial CASCADE detector is found in Ch. 5.5.2).

B.4.1 Measurement setup for detector characterisation

For the characterisation measurements, the output signal from the shaper box was recorded by a commercial ADC system. The FPGA (Field Programmable Gate Array)-based system[30] is able to continuously stream its data with 14 bit resolution[31] to a personal computer over its gigabit ethernet port. A time resolution of $\Delta t = 100\,\mathrm{ns}$ (corresponding to a sampling rate of 10 MHz) is achieved, with a data transfer rate of 20 MB/s written to the computer's hard disk.

In the discussed measurements, the ADC channels were converted to a voltage V_{det}, with integer 16384 representing an input voltage of +2.5 V and -16384 representing −2.5 V. Note that the 'zero point' of the detector voltage, *i.e.*, $V_{\mathrm{det}} = 0$, can be set by an external potentiometer at the shaper box. An adaption of this zero point has not been made in all measurements, which is why the baseline fluctuates in-between measurements. Up to a certain limit, at which the noise sharply increases, a higher bias voltage leads to a higher detection efficiency, since the detector bias voltage is brought closer to the breakdown voltages of the individual APD cells (cf. Ch. B.3.2). The associated connection scheme for all characterisation measurements is depicted in Fig. B.27 a), along with a picture of the shaper box feeding its output signal into the ADC (b).

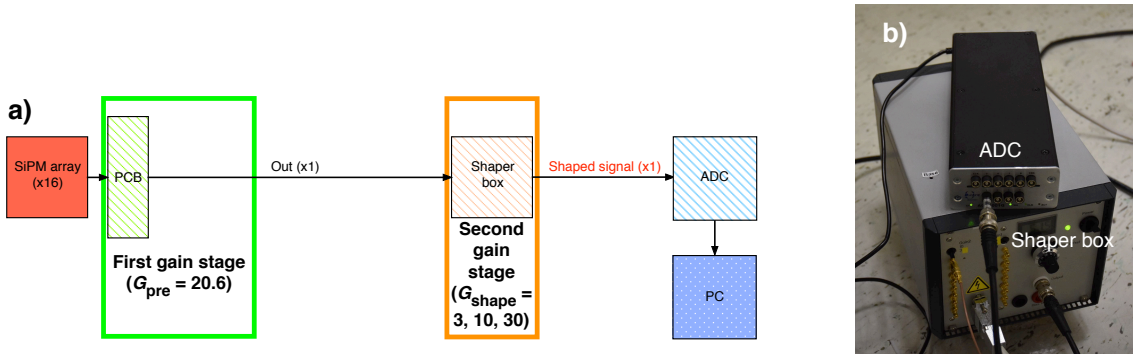

Figure B.27: Electrical circuit scheme detector characterisation measurements and ADC. (a) The scheme shows how the electrically-combined signal of the SiPM array is preamplified in the PCB and later shaped and further amplified in the shaper box. The output signal is digitised by an ADC, which streams the data to a connected PC with $\Delta t = 100\,\mathrm{ns}$ time resolution. (b) The picture illustrates the shaper box and the ADC during a measurement phase.

Additionally, a test chamber was developed, which was usable throughout all characterisation measurements with an americium-241 (^{241}Am) source as well as neutrons. A CAD rendering of the vacuum-tight test chamber with included detector assembly is depicted in Fig. B.28 and shows that the assembly is screwed to the bottom CF100 flange, which permitted mounting the test chamber in vertical and horizontal direction. The pump outlet allowed for an even pumping of the chamber's interior and the connected tube system to decrease the local pressure on the ZnS:Ag scintillator foil. Similar to the final design (cf. Ch. 5.5.1), the electrical signals are sent to ambient conditions using a CF40 flange with integrated vacuum feedthrough.

[30] The Linux-programmable ADC system of type ACQ480ELF was provided by D-TACQ Solutions Ltd (`http://www.d-tacq.com`), which offers 8 input channels with LEMO connectors [dta16].

[31] For a specified input voltage of ±2.5 V, this corresponds to the signal being represented by ±16384 integers. The maximum offset on the input voltage is specified by ±3 mV [dta16].

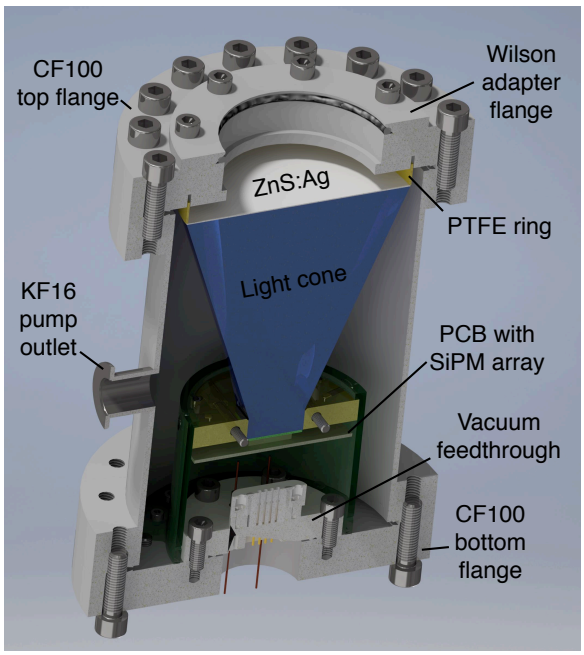

Figure B.28: CAD rendering of the test chamber used for UCN detector characterisation measurements. The top flange of the vacuum-tight test chamber is prepared for UCN characterisation measurements.

At the CF100 top flange used during the UCN characterisation measurements, a PTFE ring is inserted, which closes the 5 mm gap to prevent UCN from escaping. Also, a Wilson adapter flange is screwed to the top flange to connect a stainless steel neutron guide with $\varnothing_{\text{outer, guide}} = 70\,\text{mm}$. During the ^{241}Am calibration measurements (cf. Fig. 5.23), the top flange was replaced by a common CF100 blind flange.

B.4.2 Finding peaks for event counting

For event counting, a peak finding algorithm was tested and optimised, with the input data generated with the calibrated ^{241}Am source of 68(7) Bq. A first peak counting algorithm written in the programming language C was implemented by D. Ries, which has the capability to read in the ADC output consisting of 16 bit unsigned integers and detect a signal reaching a pre-defined pulse height ('peak threshold') - for the final data analyses, an updated automated algorithm was written in Python as part of this work (cf. later in this section).

Fig. B.29 a) shows the noise (red) and the ^{241}Am signal with distinctive peaks (blue) and an increase of the average detector voltage, if the detector is exposed to the ^{241}Am source. The shift in the average detector voltage by $\sim$ factor 2 is inferred from comparing the average voltages $\overline{V}_{\text{det}}$ for signal and noise. This characteristic was observed in all detector characterisation measurements at room temperature. It likely occurs due to the signal integration in the shaper, which did not inhibit peak detection. By setting a peak threshold over noise level, a good discrimination between signal and noise is achieved.

In Fig. B.29 b), an individual ^{241}Am peak from the zoomed-in spectrum is depicted, along with the attributes considered by the algorithm. After setting the peak threshold V_{thr} (green dashed line) manually, the algorithm created an output file containing the time stamp

when the signal exceeds the peak threshold and the duration until the signal falls below the peak threshold again ('time over threshold', Δt_{thr}). Also, the peak integral ('integral area'), *i.e.,* the sum of all recorded integers while the peak threshold is exceeded, is written to the output file. For event counting, the 'time over threshold' is significant, since it provides an additional constraint. By setting a 'time over threshold' filter to $\Delta t_{\mathrm{thr}} = 1\,\mu\mathrm{s}$, signals representing noise are not counted as events.

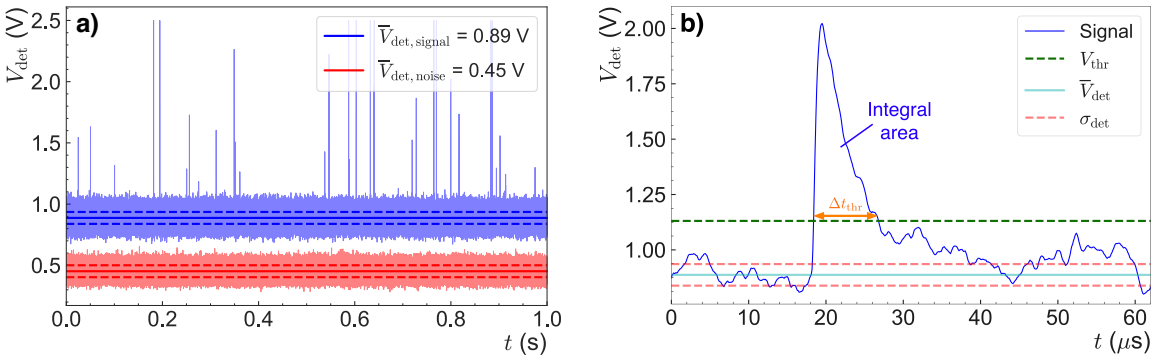

Figure B.29: Peak structure of americium-241 calibration measurement and illustration of peak finding attributes, with detector voltage V_{det} plotted against time. (a) Signal with distinctive peaks (blue) and the noise (red), with the average detector voltage shifted by a factor $\sim$ 2 compared to noise level (comparison of respective average values, $\overline{V}_{\mathrm{det}}$). (b) Zoomed-in peak of the signal spectrum along with the peak threshold V_{thr} and integral area of the peak. Additionally, the algorithm also determines the 'time over threshold' (Δt_{thr}) value, which allows for excluding parts of the signal from event counting. The mean ($\overline{V}_{\mathrm{det}}$, light cyan line) and the standard deviation of the signal (σ_{det}, light red dashed line) are displayed for demonstration purposes. The signals were measured with detector bias voltage set to 57.2 V and in case of the signal measurement, the ^{241}Am source placed in the middle of the light cone ($d_{\mathrm{centre}} = 0\,\mathrm{mm}$). The gain in the pulse shaping stage was set to $G_{\mathrm{shape}} = 9$.

The simple algorithm was heavily extended to offer an automated peak analysis free from user input. This measure made the results inferred from different spectra comparable to each other. For better adaptability and extendibility, the algorithm was first rewritten in the programming language Python, while a low performance led to an implementation in Cython, which is a Python variation with added type declaration to compile the underlying code to C code. Thus, a bearable performance loss compared to C is reached[32], while maintaining most of the advantages of the Python language.

The principle of the peak finding according to the newly-developed code, which has been used for all analyses presented from now on, is discussed in the following. The peak finding consists of two analysis steps:

(i) Finding the peak threshold V_{thr},

[32] In a test setting with an Intel CPU of type i5-6360U@3.1 GHz and an internal NVMe-connected SSD with 1.3 GB/s read speed, the C implementation took 50.1(1.4) s for finding peaks with a pre-defined threshold (*i.e.,* corresponding to one iteration) in a file of 2 GB size. The Cython (`https://cython.readthedocs.io`) implementation was $\sim$ 80 % slower with 90.4(2.6) s, with each speed measurement repeated 3 times. For comparison, the Python implementation (`https://www.python.org`) was more than a factor 11 slower than C code.

(ii) applying a time threshold Δt_{thr}.

In a first step (i), the algorithm finds the mean of the whole signal, $\overline{V}_{\mathrm{det}}$, and the corresponding standard deviation, σ_{det} (cf. Fig. B.30 a). Then, the code starts at $\overline{V}_{\mathrm{det}} - \sigma_{\mathrm{det}}$ and iterates 'downwards' in m 0.2σ steps until no signal occurences are found:

$$\widetilde{V}_{\mathrm{thr,\ intermediate}}(k) = \overline{V}_{\mathrm{det}} - k\sigma_{\mathrm{det}} \quad \text{with } k = m \cdot 0.2\ . \tag{B.15}$$

This is defined as the 'negative peak threshold' $\widetilde{V}_{\mathrm{thr}}$, which in the given example equals $\overline{V}_{\mathrm{det}} - 5.0\sigma_{\mathrm{det}}$. Assuming a symmetry of the signal shape, as demonstrated by the Gaussian distribution of the V_{det} values (cf. Fig. B.30 b), the 'negative peak threshold' is applied in positive direction, giving

$$V_{\mathrm{thr,\ intermediate}}(k) = \overline{V}_{\mathrm{det}} + k\sigma_{\mathrm{det}} \quad \text{with } k = m \cdot 0.2\ . \tag{B.16}$$

Plot b) shows how the number of events below $\widetilde{V}_{\mathrm{thr}}$ and above V_{thr} decreases for k increasing from 4 to 5 in the given ^{241}Am spectrum. At $k = 5$, no more events below $\widetilde{V}_{\mathrm{thr}}$ are detected, which implies that the value for the peak threshold V_{thr} has been found.

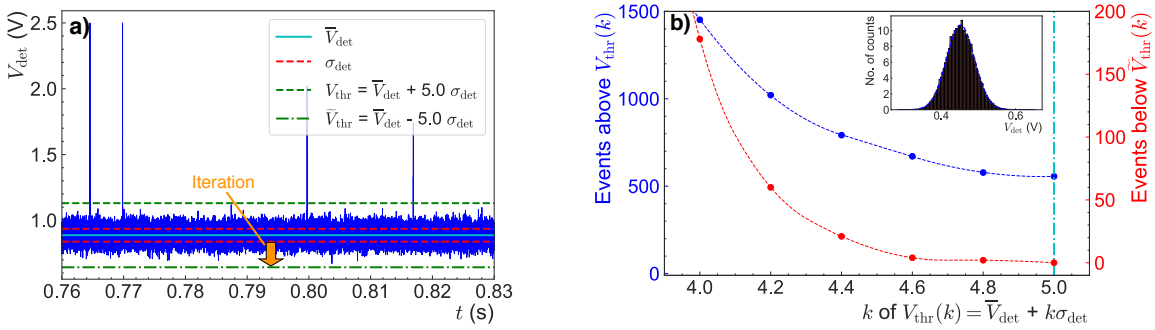

Figure B.30: Principle of the extended peak finding algorithm. (a) After finding the detector voltage signal mean ($\overline{V}_{\mathrm{det}}$, cyan line and standard deviation (σ_{det}, red dashed line), the algorithm iterates in negative V_{det} in $0.2\sigma_{\mathrm{det}}$ steps (direction of orange arrow), until no more peaks are counted at negative threshold $\widetilde{V}_{\mathrm{thr}}$ (green dash-dotted line). Due to the symmetry in the signal shape (cf. inset in b), the negative threshold is applied in the positive direction (V_{thr}, green dashed line). (b) Number of events above V_{thr} (blue data points and left axis) and below $\widetilde{V}_{\mathrm{thr}}$ (red data points and right axis) as a function of iterations, k. At $k = 5$, no more events below $\widetilde{V}_{\mathrm{thr}}$ are found, which defines the peak threshold value $V_{\mathrm{thr}} = \overline{V}_{\mathrm{det}} + 5\sigma_{\mathrm{det}}$.

In a second step (ii), the algorithm takes the fixed V_{thr} value calculated in (i) to run over a dedicated measurement file, in which the background is contained[33]. Reading in the newly-generated output file for the fixed V_{thr} value, increasing cuts to the time over threshold values, Δt_{thr}, are made with $0.2\,\mu$s iteration, until no more events are detected in the background measurements. Fig. B.31 shows the decreasing background count rate as a function of Δt_{thr} cuts. For this example, an Δt_{thr} value of $0.6\,\mu$s was found, meaning that only events with 'over peak duration' $\Delta t \geq 0.6\,\mu$s are counted.

To sum up, the algorithm counts an event if the determined peak threshold V_{thr} is exceeded for a duration $\Delta t \geq \Delta t_{\mathrm{thr}}$.

[33] Taking an additional measurement file for background determination is only valid for the ^{241}Am calibration and the UCN DC measurements. In case of the stored UCN and τSPECT measurements, the background was determined at the end of each measurement, when no more UCN could be detected.

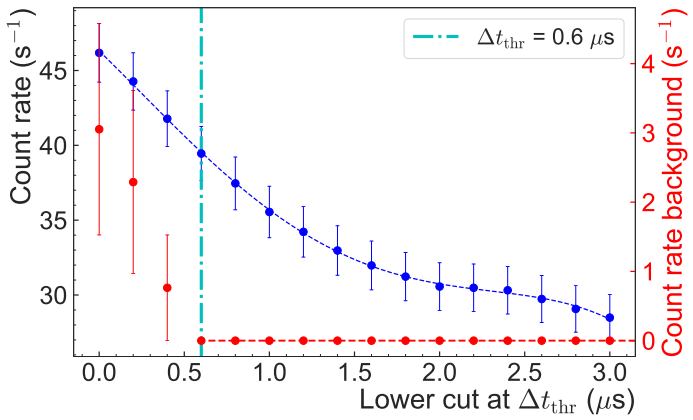

Figure B.31: Determination of the time threshold for event determination. The lower cut for $\Delta t_{\mathrm{threshold}}$ was increased in 0.2 μs steps, until the background count rate (red data points) vanished. This gives the time threshold of $\Delta t_{\mathrm{thr}} = 0.6\,\mu$s, which was applied as a filter on the signal count rate (blue data points). Thus, events were only counted if they exceed the peak threshold for $\Delta t \geq 0.6\,\mu$s.

B.4.3 Determination of the detector efficiency on the radial position of a calibrated Americium-241 source

To investigate the dependence of the signal detection on the radial position of the ^{241}Am source on the light cone front, which has been previously simulated in ray-tracing simulations (cf. Fig. B.6 b), the scintillator was positioned at different distances from the centre of the light cone ($d_{\mathrm{centre}} = 0.0\,$mm) to $d_{\mathrm{centre}} = 47.5\,$mm, which was the closest possible position from the edge of the light cone ($d_{\mathrm{edge}} = 49.5\,$mm). The bias voltage was set at the determined optimum of 57.2 V (cf. Fig. 5.25, and the scintillator position was shifted in the direction parallel to the quadratic light cone cutout[34].

As Fig. B.32 shows, a radial dependency of the count rate could be identified, with a decreasing detection efficiency from $d_{\mathrm{centre}} = 30\,$mm onwards. From 30 mm to 47.5 mm, the extracted detection efficiency does not change significantly, with the count rate matching the expectations of the α decay. Apart from the outlier at 30 mm, the results moreover agree fairly well with the transmissions predicted by the ray-tracing simulations (cf. Fig. B.8 a). Spatial limitations prevented shifting the ^{241}Am source to the region in which the ray-tracing simulations yield a worse photon transmission ($d_{\mathrm{centre}} > 45\,$mm). In summary, the detection efficiency does have a radial dependence, which might be explained by the radial dependence of the photon transmission in the light cone.

B.4.4 First neutron detection at the UCN C source

In a first measurement setup, the neutron detector was connected to a beam line at the UCN C source. As opposed to the pulsed UCN D source, which is normally used for UCN measurements, the source at beamport C offers the advantage of providing a constant neutron flow. This property made the UCN C source suitable for performing a bias voltage scan. The experimental setup is illustrated in Fig. B.33 a), along with a stainless steel adapter flange to connect the 'standard' beam line with $\varnothing_{\mathrm{outer}} = 70\,$mm to the UCN C source

[34] The direction parallel to the light cutout is defined as $\beta = 0.0°$. Ray-tracing simulations show that increasing the distance from the light cone centre for angles of $\beta = 22.5°$ or $\beta = 45.0°$ relative to the cutout impacts the photon transmission (cf. Fig. B.6 b).

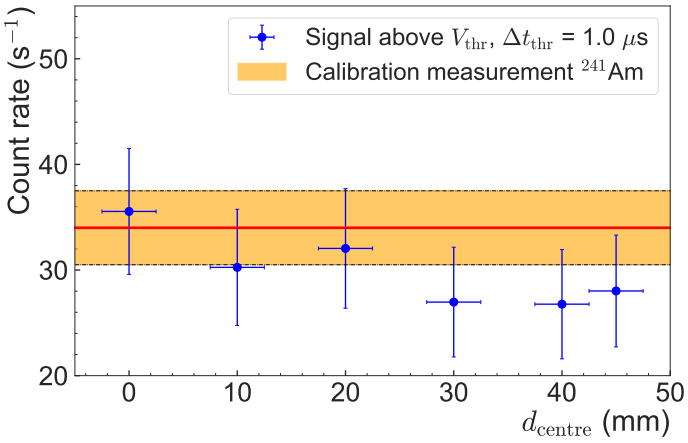

Figure B.32: Detector count rate as a function of radial distance to the centre during ^{241}Am calibration measurements. When moving away from the light cone centre, the count rate decreases. The error bars for d_{centre} represent the 5 mm spread of the ^{241}Am source, while the error in the count rate is given by the standard deviation.

($\varnothing_{outer}$ = 80 mm). The total height was h = 1.35 m. To prevent signal clipping, which was observed in some ^{241}Am spectra (cf. Fig. B.29 b), the gain was reduced to G_{shape} = 3 in order to decrease the ADC input voltage. As in the ^{241}Am calibration measurements, the highest count rate was again found for a bias voltage of 57.2 V (cf. Fig. B.33 b).

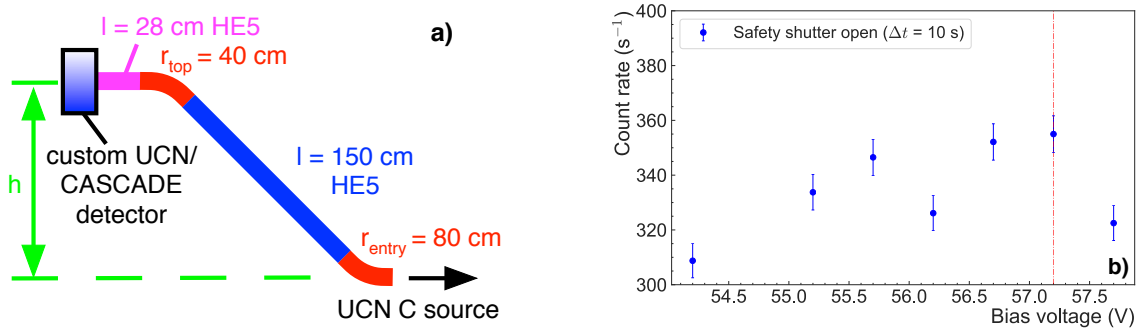

Figure B.33: Measurement setup UCN C source measurements and detector count rate dependence on bias voltage. (a) The UCN detector was mounted horizontally to the 'standard' beam line at h = 1.35 m and was in the meantime exchanged with the commercial CASCADE detector. (b) The highest count rate was achieved by setting the bias voltage to 57.2 V, red dash-dotted line).

The same setup was used to compare the UCN detector's performance with an optically coupled 20 nm ^{10}B layer to a commercial CASCADE UCN detector[35]. In horizontal extraction, the UCN detector counted an almost 4 times lower count rate than the CAS-

[35]The Mainz variant of the CASCADE detector has a ^{10}B layer of 200 nm.

CADE[36]. The low detection efficiency of the custom UCN detector is due to the presence of high-energetic UCN and VCN in the UCN C spectrum[37]. The horizontal mode combined with the used beam line allows for a transmission of higher-energetic neutrons, which would have been suppressed by mounting the custom UCN detectors vertically, since the required 90° bend would have reduced the amount of transmitted higher-energetic neutrons. In the higher-energy regime, the CASCADE is significantly more efficient due to its 200 nm ^{10}B layer, while the 20 nm ^{10}B layer of the custom UCN detector does not suffice for efficient neutron conversion. As shown in Fig. B.11 a), a ^{10}B layer with ~ 160 nm thickness is needed to achieve a conversion efficiency of $\sim 95\,\%$ for UCN with $E_{\mathrm{UCN}} = 200$ neV. This is the reason for the almost 4 times better counting efficiency of the CASCADE detector.

[36]For the neutron detector, a count rate of 355.00(6.67) s^{-1} with a background of 57.20(12.50) s^{-1} was measured. The CASCADE measured a significantly higher count rate of 1380.98(37.53) s^{-1} on day 1 (N = 4), and of 1371.81(37.04) s^{-1} on day 2 (N = 1), with an average background of 142.10(11.31) s^{-1}. For the background measurements, the safety shutter was closed, while the reactor was still running at $P = 100$ kW. All given figures are background-subtracted.

[37]VCN are very cold neutrons with energies $\gtrsim 350$ neV. To undermine this notion, the measurement was repeated with the CASCADE in vertical extration. At vertical extraction (UCN detection after $r = 8$ cm 90° bend), a count rate of 881.88(29.70) s^{-1} was measured, which implies that only $\sim 63\,\%$ of the UCN had sufficiently low energy to pass the 90° bend mounted before the CASCADE. The UCN reaching the detector were due to the source design and the absence of a storage volume of notably higher energy than the maximum storable UCN energy in τSPECT (47 neV).

C Additional contents - First τSPECT measurements

This chapter provides contents supplementary to Ch. 6 in terms of the temperature conditions during the first measurements (cf. Ch. C.1).

C.1 Temperatures in the cryostat

Subsequently, the detailed temperature conditions are presented, starting with the temperature sensor positions inside the cryostat (cf. Ch. C.1.1). Lastly, a depiction of all temperature curves during cooldown is provided in Ch. C.1.2.

C.1.1 Positions of cryostat temperature sensors

Below, the positions of the permanently-installed temperature sensors inside the former aSPECT cryostat are given (cf. Fig. C.1). Note that the sensors 8, 9, 11, 14, 19 are broken.

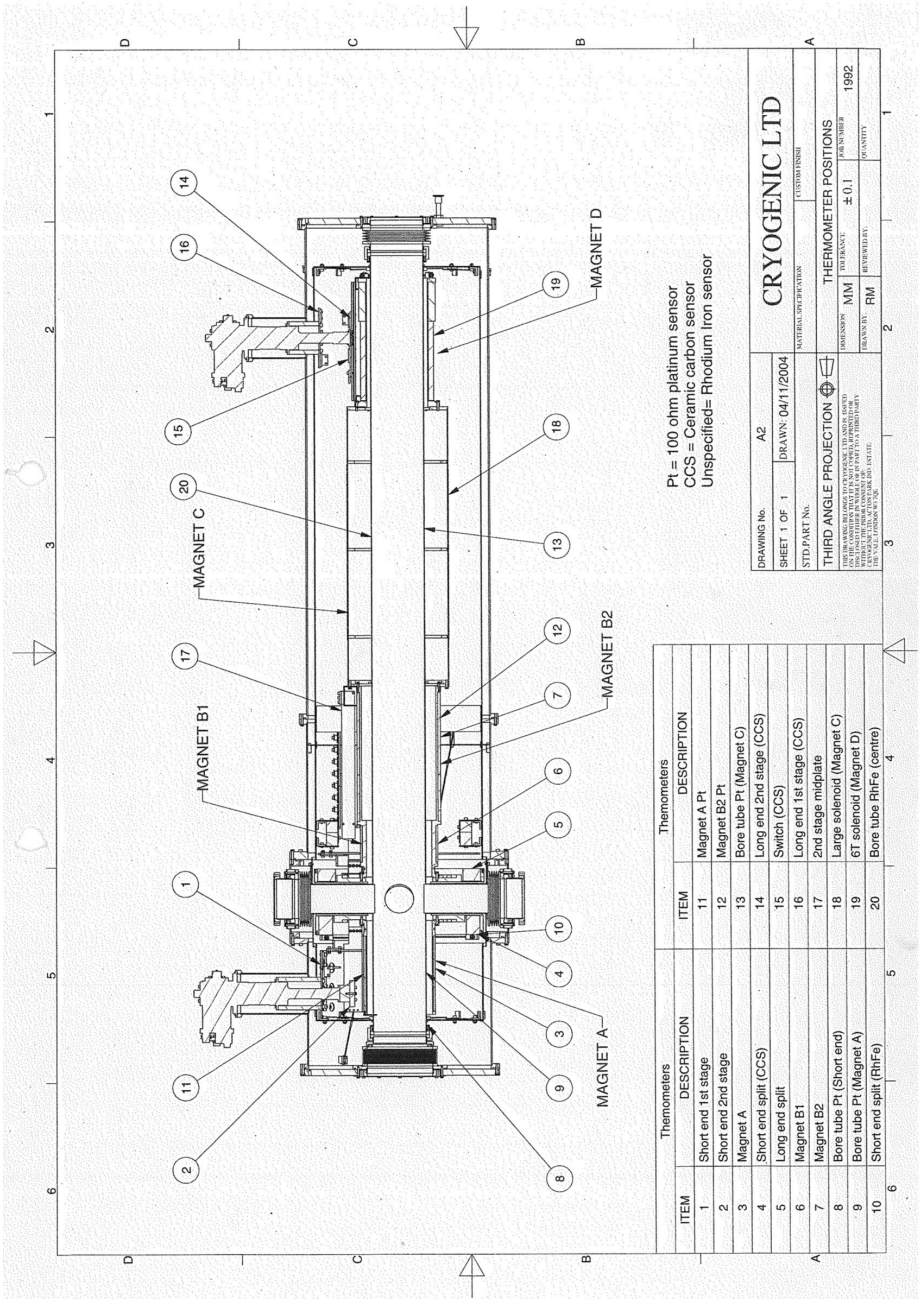

Figure C.1: Pre-installed temperature sensors in the aSPECT cryostat. Figure taken from [cry04].

C.1.2 Cooldown temperature curves

While the most relevant data on the temperature curves during cooldown are presented in Ch. 6.1.1, this section provides a full depiction of the readings of all temperature sensors. The detailed cooldown temperature curves of all inner cryostat sensors are given in Figs. C.2 a)/ b) and Fig. C.3 a). Fig. C.3 b) contains the temperature readings of the PT1000 sensors mounted on the outer stainless steel tube (cf. Tab. 5.1 for positions).

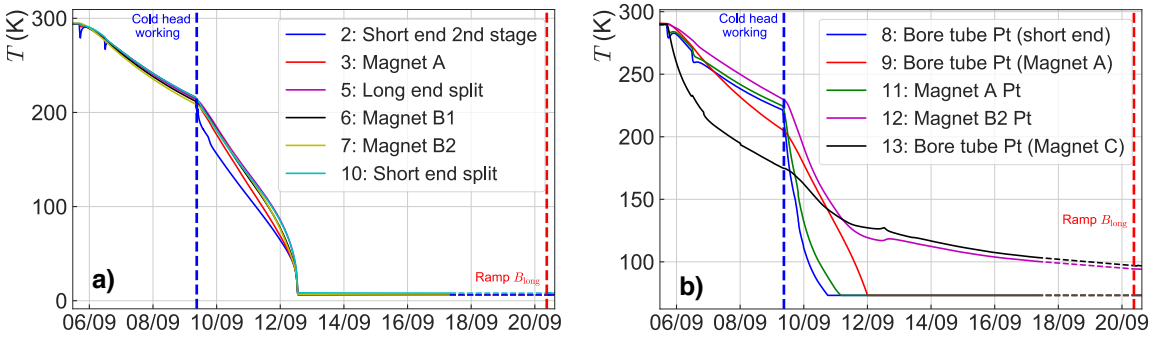

Figure C.2: Detailed cooldown temperatures 09/2019 (1) in (a), (2) in (b).

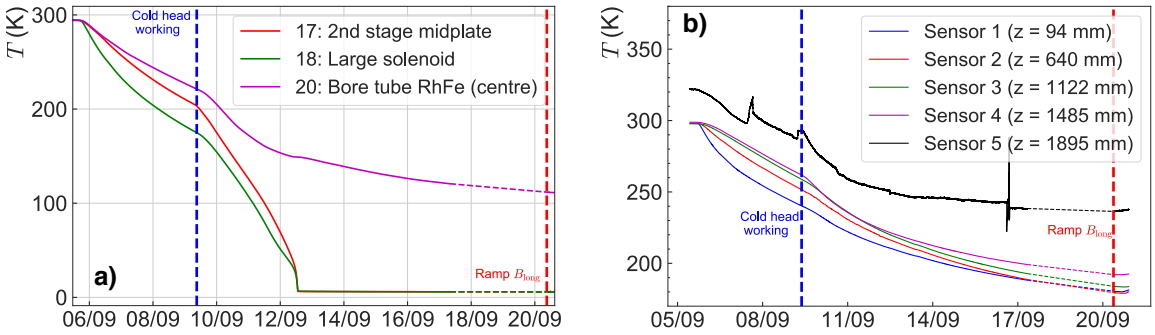

Figure C.3: Detailed cooldown temperatures 09/2019 (3) and temperatures development on outer stainless steel tube. (a) Temperature development of sensors 17, 18, 20. (b) Temperatures on outer stainless steel tube near outer Halbach octupole diameter. Sensor 5 exhibits a strange behaviour compared to earlier cooldowns and should therefore be ignored. Sensors 1-4 show a decreasing temperature, which points to a temperature gradient $\sim 20\,\mathrm{K}$ over the length of the Halbach octupole. Dashed lines show interpolation (failure of the readout system).

Bibliography

[AAA+12] G. Aad, T. Abajan, B. Abbott, *et al.* Phys. Lett. B **716** (2012), 1.

[AAA+19] S. Ahmed, E. Altiere, T. Andalib, *et al.* Phys. Rev. C **99** (2019), 025503.

[AAA+20] C. Abel, S. Afach, N. J. Ayres, *et al.* Phys. Rev. Lett. **124** (2020), 081803.

[ABB+09] I. Altarev, G. Ban, G. Bison, *et al.* Nucl. Instrum. Methods A **611** (2009), 133.

[ABB+18] A. Anghel, T. L. Bailey, G. Bison, *et al.* Eur. Phys. J. A **54** (2018), 148.

[ABC+15] S. Arzumanov, L. Bondarenko, S. Chernyavsky, *et al.* Phys. Lett. B **745** (2015), 79.

[ABD+04] H. Abele, E. Barberio, D. Dubbers, *et al.* Eur. Phys. J. C **33** (2004), 1.

[Abe08] H. Abele. Prog. Part. Nucl. Phys. **60** (2008), 1.

[ADF+08] I. Altarev, M. Daum, A. Frei, *et al.* Eur. Phys. J. A **37** (2008), 9.

[AGR+11] E. G. Adelberger, A. Garcia, R. G. H. Robertson, *et al.* Rev. Mod. Phys. **83** (2011), 195.

[AHB+02] H. Abele, M. A. Hoffmann, S. Baeßler, *et al.* Phys. Rev. Lett. **88** (2002), 211801.

[AMG+78] P. Ageron, W. Mampe, R. Golub, *et al.* Phys. Lett. **66A** (1978), 469.

[ana16] *Data sheet AD8099.* URL: `https://www.analog.com/media/en/technical-documentation/data-sheets/AD8099.pdf` (2016). Technical note Analog Devices, Inc.

[AOS15] E. Aver, K. A. Olive, and E. D. Skillman. JCAP **07** (2015), 011.

[are08] *High linearity Hall probes for room and cryogenic temperatures.* URL: `http://www.arepoc.sk/uploaded/download/HallProbes.PDF` (2008). Product data sheet AREPOC s.r.o.

[arn03] *Using permanent magnets at low temperatures.* URL: `https://www.arnoldmagnetics.com/wp-content/uploads/2017/10/TN_0302_rev_150715.pdf` (2003). Technical note Arnold Magnetic Technologies Corp.

[arn14] *RECOMA - The complete range of $SmCo_5$ and Sm_2Co_{17} alloys.* URL: `https://www.arnoldmagnetics.com/wp-content/uploads/2017/10/Recoma-Combined-160301.pdf` (2014). Technical note Arnold Magnetic Technologies Corp.

[BBD+16] G. Bison, F. Burri, M. Daum, *et al.* Nucl. Instrum. Methods A **830** (2016), 449.

[BBF89] J. Bernstein, L. S. Brown, and G. Feinberg. Rev. Mod. Phys. **61** (1989), 25.

[BCD+17] V. Bondar, S. Chesnevskaya, M. Daum, *et al.* Phys. Rev. C **96** (2017), 035205.

[BDH+96] J. Byrne, P. G. Dawber, C. G. Habeck, *et al.* EPL **33** (1996), 187.

[BDK+17] G. Bison, M. Daum, K. Kirch, *et al.* Phys. Rev. C **95** (2017), 045503.

[Ber19a] Z. Berezhiani. Eur. Phys. J. C **79** (2019), 484.

[Ber19b] Z. Berezhiani. *The CKM unitarity problem: A trace of physics at the TeV scale?* (2019). Physics of Fundamental Symmetries and Interactions (PSI 2019).

[BGB+08] S. Baeßler, F. A. Guardia, M. Borg, *et al.* Eur. Phys. J. A **38** (2008), 17.

[BGB+19] M. Beck, F. A. Guardia, S. Baeßler, *et al.* arXiv:1908.04785 (2019).

[BGK+18] L. Baudis, M. Galloway, A. Kish, *et al.* JINST **13** (2018), P10022.

[BMS+80] J. Byrne, J. Morse, K. F. Smith, *et al.* Phys. Lett. B **92** (1980), 274.

[Bod78] E. Bodenstedt. *Experimente der Kernphysik und ihre Deutung Teil 2.* B.I.-Wissenschaftsverlag, 2nd edition (1978).

[BP58] G. M. Bailey and J. R. Prescott. Aust. J. Phys. **11** (1958), 135.

[BP05] J. D. Bowman and S. I. Penttila. J Res Natl Inst Stand Technol **110** (2005), 361.

[BS85] A. M. Boesgaard and G. Steigman. Annu. Rev. Astron. Astrophys. **23** (1985), 319.

[Byr02] J. Byrne. *An overview of neutron decay* (2002). Proceedings of the two-day-workshop quark mixing, CKM unitarity Heidelberg.

[Byr11] J. Byrne. *Neutrons, nuclei and matter - An exploration of the physics of slow neutrons.* Dover Publications, Inc. (2011).

[Cab63] N. Cabibbo. Phys. Rev. Lett. **10** (1963), 531.

[CBL+19] B. Clement, A. Bes, A. Lacoste, *et al.* JINST **14** (2019), P09003.

[CBM+11] G. Collazuol, M. G. Bisogni, S. Marcatili, *et al.* Nucl. Instrum. Methods A **628** (2011), 389.

[CDM+07] F. Corsi, A. Dragone, C. Marzocca, *et al.* Nucl. Instrum. Methods A **572** (2007), 416.

[CFO+16] R. H. Cyburt, B. D. Fields, K. A. Olive, *et al.* Rev. Mod. Phys. **88** (2016), 015004.

[CGH13] V. Cirigliano, S. Gardner, and B. R. Holstein. Prog Part Nucl Phys **71** (2013), 93.

[CKS+12] S. Chatrchyan, V. Khachatryan, A. M. Sirunyan, *et al.* Phys. Lett. B **716** (2012), 30.

[CMS04] A. Czarnecki, W. J. Marciano, and A. Sirlin. Phys. Rev. D **70** (2004), 093006.

[CMS18] A. Czarnecki, W. J. Marciano, and A. Sirlin. Phys. Rev. Lett. **120** (2018), 202002.

[CMS19] A. Czarnecki, W. J. Marciano, and A. Sirlin. Phys. Rev. D **100** (2019), 073008.

[CNB+72] C. J. Christensen, A. Nielsen, A. Bahnsen, *et al.* Phys. Rev. D **5** (1972), 1628.

[cod19a] *NIST standard reference database.* URL: `https://physics.nist.gov/cgi-bin/cuu/Value?mn|search_for=neutron+mass` (2019). Neutron mass 2018 CODATA recommended value.

[cod19b] *NIST standard reference database 121.* URL: `https://physics.nist.gov/cgi-bin/cuu/Value?gnn` (2019). Neutron g factor 2018 CODATA recommended value.

[cry04] *Cryogen - Free Magnet System* (2004). Reference sheet Joc. No. 1992 Cryogenic Ltd.

[DAB+08] D. Dubbers, H. Abele, S. Baeßler, *et al.* Nucl. Instrum. Methods A **596** (2008), 238.

[DGN+03] M. S. Dewey, D. M. Gilliam, J. S. Nico, *et al.* Phys. Rev. Lett. **91** (2003), 152302.

[DNP17] N. Dinu, A. Nagai, and A. Para. Nucl. Instrum. Methods A **845** (2017), 64.

[Dra14] S. Dragisic. *Entwurf eines multipolaren Halbach-Arrays zur magnetischen Speicherung von ultrakalten Neutronen für das Lebensdauerexperiment tSPECT.* Master's thesis, University of Mainz (2014).

[DS11] D. Dubbers and M. G. Schmidt. Rev. Mod. Phys. **83** (2011), 1111.

[DSM+19] D. Dubbers, H. Saul, B. Märkisch, *et al.* Phys. Lett. B **791** (2019), 6.

[dta16] *ACQ480ELF product specification.* URL: `http://www.d-tacq.com/acq400ds/acq480elf-product-specification.pdf` (2016). Technical note D-TACQ Solutions Ltd.

[Dur15] R. Durrer. Class. Quantum Grav. **32** (2015), 124007.

[EAB+18] V. F. Ezhov, A. Z. Andreev, G. Ban, *et al.* JETP Lett. **107** (2018), 671.

[EG19] K. Eberhardt and C. Geppert. Radiochim. Acta **107** (2019), 535.

[EK94] V. L. Eletsky and I. I. Kogan. Phys. Rev. D **49** (1994), R3083.

[elj16] *Alpha detection EJ-440, EJ-442.* URL: `https://eljentechnology.com/images/products/data_sheets/EJ-440_EJ-442.pdf` (2016). Technical note Eljen Technology.

[ERM05] J. Erler and M. J. Ramsey-Musolf. Prog Part Nucl Phys **54** (2005), 351.

[Ezh19] V. Ezhov. *Neutron lifetime measuring experiments with UCN magnetic storage* (2019). Physics of Fundamental Symmetries and Interactions (PSI 2019).

[Fer34] E. Fermi. Z. Phys. **88** (1934), 161.

[FG18] B. Fornal and B. Grinstein. Phys. Rev. Lett. **120** (2018), 191801.

[FGM58] R. P. Feynman and M. Gell-Mann. Phys. Rev. **109** (1958), 193.

[FHI+98] Y. Fukuda, T. Hayakawa, E. Ichihara, *et al.* Phys. Rev. Lett. **81** (1998), 1562.

[Fix09] D. J. Fixsen. ApJ **707** (2009), 916.

[FSA+07] A. Frei, Y. Sobolev, I. Altarev, *et al.* Eur. Phys. J. A **34** (2007), 119.

[GABP+15] K. B. Grammer, R. Alarcon, L. Barrón-Palos, *et al.* Phys. Rev. B **91** (2015), 180301(R).

[GANCS19] M. Gonzalez-Alonso, O. Naviliat-Cuncic, and N. Severijns. Prog Part Nucl Phys **104** (2019), 165.

[Gar06] A. Garcia. Hyperfine Interact. **172** (2006), 23.

[GB83] R. Golub and K. Böning. Z. Phys. B. - Condensed Matter **51** (1983), 95.

[GBB+05] F. Glück, S. Baeßler, J. Byrne, *et al.* Eur. Phys. J. A **23** (2005), 135.

[GG89] D. J. Gardiner and P. R. Graves. *Practical Raman spectroscopy.* Springer (1989).

[GGS58] M. Goldhaber, L. Grodzins, and A. W. Sunyar. Phys. Rev. **109** (1958), 1015.

[GKK+00] B. Y. Gorodilov, O. A. Korolyuk, A. I. Krivchikov, *et al.* J. Low Temp. Phys. **119** (2000), 497.

[Gla61] S. L. Glashow. Nucl. Phys. **22** (1961), 579.

[GM58] M. Gell-Mann. Phys. Rev. **111** (1958), 362.

[Gol95] R. Golub. *Ultra-cold neutrons* (1995). Proceedings on dark matter in cosmology, clocks and test of fundamental laws.

[GP75] R. Golub and J. M. Pendlebury. Phys. Lett. **53A** (1975), 133.

[GP79] R. Golub and J. M. Pendlebury. Rep. Prog. Phys. **42** (1979), 439.

[GP13] S. Gardner and B. Plaster. Phys. Rev. C **87** (2013), 065504.

[GRL91] R. Golub, D. Richardson, and S. K. Lamoreaux. *Ultra-cold neutrons.* Adam Hilger (1991).

[GS22] W. Gerlach and O. Stern. Z. Phys. **9** (1922), 349.

[GT36] G. Gamow and E. Teller. Phys. Rev. **49** (1936), 895.

[Haa16] J. Haack. *Vollmagnetische Speicherung von ultrakalten Neutronen bei tSPECT.* Master's thesis, University of Mainz (2016).

[Hal80] K. Halbach. Nucl. Instrum. Methods **169** (1980), 1.

[ham16a] *MPPC (multi-pixel photon counter) - S13360 series.* URL: `https://www.hamamatsu.com/resources/pdf/ssd/s13360_series_kapd1052e.pdf` (2016). Technical note Hamamatsu Photonics K. K.

[ham16b] *MPPC (multi-pixel photon counter) arrays - S13361-6050 series.* URL: `https://www.hamamatsu.com/resources/pdf/ssd/s13361-6050_series_kapd1056e.pdf` (2016). Technical note Hamamatsu Photonics K. K.

[ham18] *CORSI model parameters (S13360-6050VE)* (2018). Reference sheet Doc. No. K30-I50329 Hamamatsu Photonics K. K.

[HBD+12] A. T. Holley, L. J. Broussard, J. L. Davis, *et al.* Rev. Sci. Instrum. **83** (2012), 073505.

[Hen19] A. Henriksson. arXiv:1905.06185 (2019).

[HES+69] C. E. Hayes, W. A. Edelstein, J. F. Sneck, *et al.* J. Magn. Reson. **63** (1969), 622.

[HT77] B. R. Holstein and S. B. Treiman. Phys. Rev. D **16** (1977), 2369.

[HT05] J. C. Hardy and I. S. Towner. Phys. Rev. C **71** (2005), 055501.

[HT15] J. C. Hardy and I. S. Towner. Phys. Rev. C **91** (2015), 025501.

[IAC+18] T. M. Ito, E. R. Adamek, N. B. Callahan, *et al.* Phys. Rev. C **97** (2018), 012501(R).

[IB06] T. Ito and J. D. Bowman. Los Alamos Science (2006), 30, 214.

[IHT+19] A. N. Ivanov, R. Höllwieser, N. I. Troitskaya, *et al.* Phys. Rev. D **99** (2019), 053004.

[JCF+13] T. Jenke, G. Cronenberg, H. Filter, *et al.* Nucl. Instrum. Methods A **732** (2013), 1.

[JS75] H. F. Jones and M. D. Scadron. Phys. Rev. D **11** (1975), 174.

[JTW57] J. Jackson, S. Treiman, and H. Wyld. Phys. Rev. **106** (1957), 517.

[JZL+17] D. Y. Jiang, Z. Zhang, R. X. Liang, *et al.* Nucl Sci Tech **28** (2017), 32.

[Kar17] J. Karch. *Design und Aufbau des Experiments tSPECT zur Messung der Neutronlebensdauer mittels magnetischer Wandspeicherung.* Ph.D. thesis, University of Mainz (2017).

[KGB+14] G. Konrad, F. A. Guardia, S. Baeßler, *et al.* Nucl. Instrum. Methods A **767** (2014), 475.

[KJM+19] M. Klopf, E. Jericha, B. Märkisch, *et al.* Phys. Rev. Lett. **122** (2019), 222503.

[KKMT80] Y. Y. Kostvintsev, Y. A. Kushnir, V. I. Morozov, and G. I. Terekhov. Sov. Phys. JETP Lett. **31** (1980), 236.

[Kle16] H. Kleinert. *Particles and quantum fields.* World Scientific Publishing (2016).

[KM73] M. Kobayashi and T. Maskawa. Prog. Theor. Phys. **49** (1973), 652.

[KMM+13] K. S. Kumar, S. Mantry, W. J. Marciano, *et al.* Ann. Rev. Nucl. Part. Sci. **63** (2013), 237.

[KMT86] Y. Y. Kostvintsev, V. I. Morozov, and G. I. Terekhov. Sov. Phys. JETP Lett. **44** (1986), 571.

[Kno89] G. F. Knoll. *Radiation detection and measurement.* John Wiley & Sons, 2nd edition (1989).

[Kra88] K. S. Krane. *Introductory Nuclear Physics.* John Wiley & Sons (1988).

[KRR+17] J. Kahlenberg, D. Ries, K. U. Ross, *et al.* Eur. Phys. J. A **53** (2017), 226.

[KS11] M. Klein and C. J. Schmidt. Nucl. Instrum. Methods A **628** (2011), 9.

[KSB+14] J. Karch, Y. Sobolev, M. Beck, *et al.* Eur. Phys. J. A **50** (2014), 78.

[Lau10] T. Lauer. *Investigation of a superthermal ultracold neutron source based on a solid deuterium converter for the TRIGA Mainz reactor.* Ph.D. thesis, University of Mainz (2010).

[Lau11] B. Lauss. J. Phys. Conf. Ser. **312** (2011), 052005.

[Lau14] B. Lauss. Phys. Procedia **51** (2014), 98.

[Lek87] J. Lekner. *Theory of reflection.* Martinus Nijhoff Publishers (1987).

[Len16] H. Lenk. *OP83 MPPC array preamplifier* (2016). Documentation detector electronics.

[Les09] A. Lesov. *The Weak Force: From Fermi to Feynman* (2009). Senior Thesis, University of South Carolina.

[LIP+16] K. K. H. Leung, S. Ivanov, F. M. Piegsa, *et al.* Phys. Rev. C **93** (2016), 025501.

[LPSS69] V. I. Luschikov, Y. N. Pokotilovsky, A. V. Strelkov, and F. L. Shapiro. Sov. Phys. JETP Lett. **9** (1969), 23.

[LT84] V. I. Luschikov and Y. V. Taran. Nucl. Instrum. Methods A **228** (1984), 159.

[LY56] T. D. Lee and C. N. Yang. Phys. Rev. **104** (1956), 254.

[LYL00] C.-Y. Liu, A. R. Young, and S. K. Lamoreaux. Phys. Rev. B **62** (2000), R3581(R).

[MAB+89] W. Mampe, P. Ageron, C. Bates, *et al.* Phys. Rev. Lett. **63** (1989), 593.

[MAB+17] C. L. Morris, E. R. Adamek, L. J. Broussard, *et al.* Rev. Sci. Instrum. **88** (2017), 053508.

[Mar07] B. R. Martin. *Nuclear and particle physics - An introduction.* John Wiley & Sons (2007).

[Mar09] W. J. Marciano. *High precision CKM unitarity and neutron decay* (2009). UCN Workshop Santa Fe.

[Mar12] W. J. Marciano. *Neutron lifetime theory* (2012). Proceedings of the 2012 workshop Next generation experiments to measure the neutron lifetime.

[MBM+93] W. Mampe, L. N. Bondarenko, V. I. Morozov, *et al.* JETP Lett. **57** (1993), 82.

[mes18] *Gas purification - For the highest level of purity at point-of-use.* URL: `https://www.messer.be/documents/20182/701258/Gasnachreinigung_en.pdf/d4ae95a1-249f-4471-b9ed-67c7e7dbc450` (2018). Advertisement document Messer Group GmbH.

[MHH+12] V. B. Mikhailik, S. Henry, M. Horn, *et al.* J. Lumin. **134** (2012), 63.

[MK02] T. Mayer-Kuckuk. *Kernphysik - Eine Einführung.* B. G. Teubner (2002).

[MMS+19] B. Märkisch, H. Mest, H. Saul, *et al.* Phys. Rev. Lett. **122** (2019), 242501.

[MPA+09] S. Materne, R. Picker, I. Altarev, *et al.* Nucl. Instrum. Methods A **611** (2009), 176.

[MPB+13] M. P. Mendenhall, R. W. Pattie, Y. Bagdasarova, *et al.* Phys. Rev. C **87** (2013), 032501.

[MS86] W. J. Marciano and A. Sirlin. Phys. Rev. Lett. **56** (1986), 22.

[MS06] W. J. Marciano and A. Sirlin. Phys. Rev. Lett. **96** (2006), 032002.

[MST+15] V. N. Marin, R. A. Sadykov, D. N. Trunov, *et al.* Tech. Phys. Lett. **41** (2015), 912.

[MTK75] H. Menke, N. Trautmann, and W.-J. Krebs. Kerntechnik **17** (1975), 281.

[Mum18] P. Mumm. Science **360** (2018), 605.

[nan10] *Stepping motor ST6018D4508-B.* URL: https://de.nanotec.com/fileadmin/files/Baureihenuebersichten/Schrittmotoren/Baureihenuebersicht_ST6018.pdf (2010). Data sheet Nanotec Electronic GmbH.

[nan13] *Stepping motor ST5909L3008.* URL: https://de.nanotec.com/fileadmin/files/Baureihenuebersichten/Schrittmotoren/Baureihenuebersicht_ST5909.pdf (2013). Data sheet Nanotec Electronic GmbH.

[NCGA13] O. Naviliat-Cuncic and M. Gonzalez-Alonso. Ann. Phys. (Berlin) **525** (2013), 600.

[NDG+05] J. S. Nico, M. S. Dewey, D. M. Gilliam, *et al.* Phys. Rev. C **71** (2005), 055502.

[NHI+17] N. Nagakura, K. Hirota, S. Ieki, *et al. Precise neutron lifetime experiment using pulsed neutron beams at J-PARC* (2017). Proc. of INPC2016 fundamental symmetries and interactions in nuclei.

[OBD+05] A. N. Otte, J. Barral, B. Dolgoshein, *et al.* Nucl. Instrum. Methods A **545** (2005), 705.

[OPYZ+18] A. Osovizky, K. Pritchard, Y. Yehuda-Zada, *et al.* J. Phys. Commun. **2** (2018), 045009.

[OPZ+18] A. Osovizky, K. Pritchard, J. Ziegler, *et al.* IEEE Trans. Nucl. Sci. **65** (2018), 1025.

[Pau09] S. Paul. Nucl. Instrum. Methods A **611** (2009), 157.

[PCCW+18] R. W. Pattie, N. B. Callahan, C. Cude-Woods, *et al.* Science **360** (2018), 627.

[Per82] D. H. Perkins. *Introduction to high energy physics.* Addison-Wesley Publishing Company, Inc., 2nd edition (1982).

[PFB+04] D. Pocanic, E. Friez, V. A. Baranov, *et al.* Phys. Rev. Lett. **93** (2004), 181803.

[pfe19] *PKR 251 Pirani/Kaltkathoden-Transmitter.* URL: https://www.pfeiffer-vacuum.com/filepool/file/measurement/bg5155bde_d.pdf?referer=1830&detailPdoId=3917&request_locale=de_DE (2019). Operating instructions Pfeiffer Vacuum GmbH.

[pfe20] *TPR 280, DN 16 ISO-KF.* URL: https://static.pfeiffer-vacuum.com/productPdfs/PTR26950.de.pdf (2020). Data sheet Pfeiffer Vacuum GmbH.

[Poc17] D. Pocanic. *Evaluating V_{ud} from neutron beta decays* (2017). Proceedings of the 9th International Workshop on the CKM Unitarity Triangle (CKM2016), Mumbai.

[PRS+09] B. Povh, K. Rith, C. Scholz, *et al. Teilchen und Kerne.* Springer, 8th edition (2009).

[PVS+10] A. Pichlmaier, V. Varlamov, K. Schreckenbach, *et al.* Phys. Lett. B **693** (2010), 221.

[Raj14] G. Rajasekaran. Resonance **19** (2014), 18.

[RC11] E. Roncali and S. R. Cherry. Ann Biomed Eng **39** (2011), 1358.

[RFG+00] D. Ridikas, G. Fioni, P. Goberis, *et al. On the fuel cycle and neutron fluxes of the high flux reactor at ILL Grenoble* (2000). 5th Workshop on Shielding Aspects of Accelerators, Targets and Irradiatiation Facilities.

[RFT80] V. C. Rubin, W. K. Ford, and N. Thonnard. ApJ **238** (1980), 471.

[RM09] M. J. Ramsey-Musolf. Nucl. Instrum. Methods A **611** (2009), 111.

[Rob51] J. M. Robson. Phys. Rev. **83** (1951), 349.

[Ros17] K. U. Ross. *Transport und Speicherung von ultrakalten Neutronen im Lebensdauerexperiment tSPECT*. Master's thesis, University of Mainz (2017).

[RRS54] I. I. Rabi, N. F. Ramsey, and J. Schwinger. Rev. Mod. Phys. **26** (1954), 167.

[SAB+14] D. J. Salvat, E. R. Adamek, D. Barlow, *et al.* Phys. Rev. C **89** (2014), 052501(R).

[Sal52] E. E. Salpeter. ApJ **116** (1952), 649.

[Sau19] A. Saunders. *Overview of neutron lifetime experiments* (2019). Physics of Fundamental Symmetries and Interactions (PSI 2019).

[SBNC06] N. Severijns, M. Beck, and O. Naviliat-Cuncic. Rev. Mod. Phys. **78** (2006), 991.

[Sch16] S. Scherer. *Symmetrien und Gruppen in der Teilchenphysik*. Springer (2016).

[Sch19] C. Schmidt. *Improved determination of the beta-neutrino angular correlation coefficient a in free neutron decayusing the aSPECT experiment*. Ph.D. thesis, University of Mainz (2019).

[SGPRM18] C.-Y. Seng, M. Gorchtein, H. H. Patel, and J. Ramsey-Musolf. Phys. Rev. Lett. **121** (2018), 241804.

[Sil80] I. F. Silvera. Rev. Mod. Phys. **52** (1980), 393.

[SKF+18] A. P. Serebrov, E. A. Kolomensky, A. K. Fomin, *et al.* Phys. Rev. C **97** (2018), 055503.

[SKL+17] W. Schreyer, T. Kikawa, M. J. Losekamm, *et al.* Nucl. Instrum. Methods A **858** (2017), 123.

[SM57] E. C. G. Sudarshan and R. E. Marshak. *The nature of the four-fermion interaction* (1957). Proc. of the Conference on Mesons and Newly-Discovered Particles.

[SM10] D. A. Shea and D. Morgan. *The helium-3 shortage: supply, demand, and options for congress* (2010). Congressional Research Service Report for Congress.

[SML04] R. M. Scanlan, A. P. Malozemoff, and D. C. Larbalestier. Proc. IEEE **92** (2004), 1639.

[Sno17] M. Snow. *Progress toward a new beam measurement of the neutron lifetime* (2017). INT Workshop INT-17-69W.

[SNS+86] A. Steyerl, H. Nagel, F. X. Schreiber, *et al.* Phys. Lett. A **116** (1986), 347.

[Sou86] P. C. Souers. *Hydrogen properties for fusion energy.* University of California Press (1986).

[SPC+16] L. Salvati, L. Pagano, R. Consiglio, *et al.* JCAP **2016** (2016), 55.

[Spi88] P. E. Spivak. Sov. Phys. JETP Lett. **94** (1988), 1.

[SPK+12] A. Steyerl, J. M. Pendlebury, C. Kaufman, *et al.* Phys. Rev. C **85** (2012), 065503.

[SSP+56] P. E. Spivak, A. N. Sosnovki, Y. A. Prokofiev, *et al.* Proc. Int. Conf. on Peaceful Uses of Atomic Energy, Geneva **2** (1956), 3.

[SSP+59] A. N. Sosnovki, P. E. Spivak, Y. A. Prokofiev, *et al.* Nucl. Phys. **10** (1959), 395.

[Ste69] A. Steyerl. Phys. Lett. B **29** (1969), 33.

[Ste01] A. Steyerl. *Use of Low-Temperature Fomblin for a Neutron Lifetime Experiment* (2001). Third UCN Workshop Pushkin.

[Suz66] M. Suzuki. Phys. Rev. **144** (1966), 1154.

[SVK+05] A. P. Serebrov, V. Varlamov, A. Kharitonov, *et al.* Phys. Lett. B **605** (2005), 72.

[SW59] A. Salam and J. C. Ward. Il Nuovo Cimento **11** (1959), 568.

[TBC+10] A. Teigelhöfer, P. Bricault, O. Chachkova, *et al.* Hyperfine Interact. **196** (2010), 161.

[TG75] S. R. Trout and C. D. Graham. AIP Conf. Proc, **29** (1975), 608.

[THH+18] M. Tanabashi, K. Hagiwara, K. Hikasa, *et al.* Phys. Rev. D **98** (2018), 030001.

[vat17] *HV gate valve series 140.* URL: `http://www.vatvalve.com/business/valves/catalog/A/140_1_V` > [Download] (2017). Product data sheet VAT Group AG.

[VWT15] K. K. Vos, H. W. Wilschut, and R. G. E. Timmermans. Rev. Mod. Phys. **87** (2015), 1483.

[WAH+57] C. S. Wu, E. Ambler, R. W. Hayward, *et al.* Phys. Rev. **105** (1957), 1413.

[Wei67] S. Weinberg. Phys. Rev. Lett. **19** (1967), 1264.

[Wei09] S. Weinberg. J. Phys. Conf. Ser. **196** (2009), 012002.

[WHM+15] Z. Wang, M. A. Hoffbauer, C. L. Morris, *et al.* Nucl. Instrum. Methods A **798** (2015), 30.

[Wie12] F. E. Wietfeldt. *Neutron Lifetime Experiments Using the Beam Method: Past, Present, and Future* (2012). Proceedings of the 2012 workshop Next generation experiments to measure the neutron lifetime.

[Wie18] F. E. Wietfeldt. Atoms **6** (2018), 70.

[Wil82] D. H. Wilkinson. Nucl. Phys. A **377** (1982), 474.

[WMB+14] Z. Wang, C. L. Morris, J. D. Bacon, *et al.* Nucl. Instrum. Methods A **764** (2014), 261.

[Wol83] L. Wolfenstein. Phys. Rev. Lett. **51** (1983), 1945.

[WTP+11] D. M. Webber, V. Tishchenko, Q. Peng, *et al.* Phys. Rev. Lett. **106** (2011), 041803.

[Wu64] C. S. Wu. Rev. Mod. Phys. **36** (1964), 618.

[Wür73] H. Würz. *Untersuchungen zur Neutronenthermalisierung an flüssigem Ortho- und Para-Wasserstoff.* Ph.D. thesis, Universität Karlsruhe (1973).

[YDG+13] A. T. Yue, M. S. Dewey, D. M. Gilliam, *et al.* Phys. Rev. Lett. **111** (2013), 222501.

[YMG86] Z. Yu, S. S. Malik, and R. Golub. Z. Phys. B. - Condensed Matter **62** (1986), 137.

[ZHJGF+12] A. Zheng-Hua, L. Jun-Guang, S. Feng, *et al.* Chin. Phys. C **36** (2012), 633.

[Zim14] O. Zimmer. *Neutron lifetime experiment HOPE* (2014). Beta-decay weak interaction studies in the era of the LHC.

[ZZB10] J. F. Ziegler, M. D. Ziegler, and J. P. Biersack. Nucl. Instrum. Methods A **268** (2010), 1818.

Acronyms

AFP	Adiabatic fast passage
BBN	Big Bang nucleosynthesis
BNC	Bayonet Neill-Concelman
BSM	Beyond the Standard Model Physics
CAD	Computer-aided design
CF	ConFlat® flange
CKM	Cabibbo-Kobayashi-Maskawa
CMB	Cosmic microwave background
CN	Cold neutron
CPU	Central processing unit
CVC	Conserved vector current
DAQ	Data acquisition
FEM	Finite element method
FKM	Fluoroelastomer material
FPGA	Field Programmable Gate Array
ILL	Institut Laue-Langevin
J-PARC	Japan Proton Accelerator Research Complex
KF	Klein flange
LANL	Los Alamos National Laboratory
LHC	Large Hadron Collider
MC	Monte Carlo
MPPC	Multi-pixel photon counter®
NIST	National Institute of Standards and Technology
NMR	Nuclear magnetic resonance
PCAC	Partially-conserved axial vector current
PCB	Printed circuit board

PDG	Particle Data Group
PEEK	Polyether ether ketone
PMMA	Poly(methyl methacrylate)
PSI	Paul-Scherrer-Institut
PE	Polyethylen
POM	Polyoxymethylene
PTFE	Polytetrafluoroethylene
QCD	Quantum chromodynamics
SiPM	Silicon photomultiplier
SM	Standard Model of Particle Physics
SPICE	Simulation Program with Integrated Circuit Emphasis
SRIM	The Stopping and Range of Ions in Matter
TRIGA	Training, Research, Isotopes, General Atomic
TTL	Transistor-transistor logic
UCN	Ultracold neutron
VA	Stainless steel
VCN	Very cold neutron